A STUDY ON ELECTROCHEMICAL REPLICATION AND TRANSFER FOR FLEXIBLE ELECTRONICS

CHEN ZIJIAN

PhD

The Hong Kong Polytechnic University

2025

The Hong Kong Polytechnic University

School of Fashion and Textiles

A Study on Electrochemical Replication and Transfer for Flexible Electronics

CHEN Zijian

A thesis submitted in partial fulfillment of the
requirements for the degree of
Doctor of Philosophy

August 2024

CERTIFICATE OF ORIGINALITY

I hereby declare that this thesis is my own work and that, to the best of my knowledge and belief, it reproduces no material previously published or written, nor material that has been accepted for the award of any other degree or diploma, except where due acknowledgement has been made in the text.

_____________ (Signed)

CHEN Zijian (Name of student)

Abstract

With the rapid progress of science and technology, the concept of the Internet of Things (IoT) has gained significant prominence. The field of wearable electronics has become an essential part of the Internet of Things (IoT) and has sparked a great deal of curiosity and thorough investigation. The basic fabrication technical core of electronic devices on untraditional flexible and stretchable substrates largely relies on patterning techniques. Traditional methods of patterning, such as photolithography, electron beam lithography (EBL), and nanoimprinting lithography (NIL), serve as effective instruments in creating high-resolution integrated circuits on semiconductor substrates. However, they are not suitable for the direct patterning process on flexible substrates due to various problems including rough surfaces with low wettability, poor resistance to chemical solvents, and unstable to thermal treatment. In just the past few decades, miscellaneous advanced patterning techniques have been proposed to satisfy the requirements of fabricating electronic devices with different materials on arbitrary substrates, including transfer printing, 3D printing, inject printing and so on. However, there is still no one patterning technique that could satisfy most of the applications while achieving a great balance in the aspects of resolution, throughput and cost.

Recently, electrochemical replication and transfer (ERT), an advanced patterning technique had evolved. By combining the traditional patterning methods with the electroplating process, the high-resolution pattern could be easily replicated and peeled off by a UV-curable binder. The electrodeposited pattern could be therefore transferred to various flexible substrates like fibers, papers, and polymers. Furthermore, it could achieve a great balance between resolution, throughput and cost. However, the fabrication of nanoscale patterns is still a challenge. The fabrication of stretchable electronics and the construction of 3D structures have not been demonstrated. Therefore, to tackle the challenges and enhance the capability of ERT, various modifications to the template and binder material were proposed in this thesis. The applicability and potential applications of each template were demonstrated.

Firstly, a thin layer of SiO_2 was added to the original Si substrate which has the same thickness as the Au pattern in the following thermal evaporation process. By combining the photolithography and drying etching methods, the Au pattern could be embedded into the SiO_2 layer and protected by it. Therefore, during the next electrodeposition process, the target materials will only be deposited onto the up surface of the Au pattern. The adhesion force between the Au pattern and the target materials will be greatly reduced because of the decreasing contact area. This SiO_2-protecting template could be efficient in improving the robustness of the Au template and the resolution limits of ERT. Nanoscale patterns with various materials reaching sub-100 nm could be successfully fabricated with this template.

Secondly, the rigid UV-curable binder was replaced by a PVA solution. After drying, the PVA layer could serve as a strong adhesion layer to peel off and transfer the electrodeposited pattern. It is still applicable for large-area transfer of various materials patterns. Additionally, the dissolvability of the PVA layer allows an arbitrary transfer of

the replicated pattern to any substrates including hard surfaces, curved surfaces and stretchable substrates. The production of diverse stretchable electronic devices was showcased.

Thirdly, through conducting photolithography and drying etching process on a SiO_2/Si substrate, a 3D patterned Si template with different aspect ratios could be successfully fabricated. The electroplating process will be directly conducted on the Si substrate without deposition of the Au pattern. Instead of using PFDT, a silylating reagent will be used to conduct the surface modification of the template to minimise the interfacial adhesion force between the template and the electrodeposited substances. Both continuous and isolated patterns with different aspect ratios could be replicated and transferred to flexible substrates. Additionally, the growth of the target materials will be restricted to the 3D groove area, which mitigates the diminution of the resolution of the replicated pattern attributable to the isotropic deposition inherent in the electroplating process. This 3D architecture presents a significant advantage in the production of transparent electrodes.

Finally, we investigated the application prospect of ERT in the field of energy and biomedical engineering. Taking the fabrication of triboelectric nanogenerator (TENG) electrodes by ERT as an example, we conceived the idea of setting up the production line of ERT and characterize the performance of the devices in the view of electrochemical performance, stability and flexibility. The potential consumption of energy and money was evaluated using LCA in the aspect of sustainable production.

We also explored the biocompatibility of electrodes fabricated by ERT and showed the relating application of an electronic bandage in accelerating wound recovery.

In summary, this work focuses on the shortcomings of the original ERT methods, and proposed target improvements for each challenge through modification of the template and binder material. The applicability of each modification was detailly studied, and the related applications were demonstrated. The improved ERT method has great potential in the large-scale fabrication of diverse wearable electronic apparatuses and become an indispensable part of patterning techniques in the near future.

List of Publications

Related Journal Publications

[1] **Chen, Z.**, Lu, X., Wang, H., Chang, J., Wang, D., Wang, W., ... & Zheng, Z. Electrochemical replication and transfer for low-cost, sub-100 nm patterning of materials on flexible substrates. ***Advanced Materials***, 2023, 35(10), 2210778.

[2] **Chen, Z.**, Fu, J., Chen, F., Xie, C., Zhuang, Q., Huang, Q., Zheng, Z. Construction of three-dimensional patterns through modified electrochemical replication and transfer. ***Advanced Materials Technologies***, 2024, 9(21), 2301695.

[3] **Chen, Z.**, Zhang, C., Zheng, Z. Advancements in Transfer Printing Techniques for Flexible Electronics: Adjusting Interfaces and Promoting Versatility. ***International Journal of Extreme Manufacturing***, 2024, 6(5), 052005.

Papers in Preparation

[1] Fu, J.*, **Chen, Z.***, Xu, G.*, Zi, Y., …, Huang, Q., Zheng, Z. Rapid and Sustainable Fabrication of Flexible Triboelectric Nanogenerator via Electrochemical Replication and Transfer *(*Co-first Author)*. ***ACS Nano***, Under Review.

[2] **Chen, Z.**, Liang, J. Fu, J., Chen, F., Zheng, Z. (2024). Low-Cost, Self-Powered Electronic Bandage with Hybrid Pulsed Electric Field for Accelerating Wound Healing.

In Preparation.

Other Journal Publications

[1] Wang, P., Ma, X., Lin, Z., Chen, F., **Chen, Z.**, Hu, H., ... & Zheng, Z. Well-defined in-textile photolithography towards permeable textile electronics. ***Nature Communications***, 2024, 15(1), 887.

[2] Xie, C., Rong, M., Guo, Q., Wei, Z., Chen, Z., Huang, Q., & Zheng, Z. UV-Permeable 3D Li Anodes for in situ Fabrication of Interface-Gapless Flexible Solid-State Lithium Metal Batteries. ***Advanced Materials***, 2024, 36(33), 2406368.

[3] Chen, F., Zhuang, Q., Ding, Y. Zhang, C., Song, X., **Chen, Z.** … & Zheng, Z. Wet-Adaptive Electronic Skin. ***Advanced Materials***, 2023, 35(49), 2305630.

[4] Fang, L., Zhang, C., …, **Chen, Z.**, …, Huang, Q. Facile spinning of tough and conductive eutectogel fibers via Li+-induced dense hydrogen-bond networks. ***Chemical Engineering Journal***, 2023, 478, 147405.

[5] Hu, H., Guo, X., Zhang, Y., **Chen, Z.**, Wang, L., Gao, Y., ... & Zheng, Z. Elasto-Plastic Design of Ultrathin Interlayer for Enhancing Strain Tolerance of Flexible Electronics. ***ACS Nano***, 2023, 17(4), 3921–3930.

[6] Rong, M., Chen, D., …, **Chen, Z.**, …& Zheng, Z. Stretchable and Self-Healable Fiber-Shaped Conductors Suitable for Harsh Environments. ***Small***, 2023, 19(50), 2304353.

Acknowledgements

Firstly, I would like to extend my profound gratitude towards Prof. Zijian Zheng for his unwavering efforts in guiding me to acquire knowledge, explore research areas, and attain a PhD degree. He patiently trained me from being an undergraduate with no prior knowledge of academia to a doctoral student with a profound interest in scientific research and valuable insights. Moreover, he demonstrated a great example of maintaining a healthy balance between study, work, and life, which led me to complete the four-year study with a sound mind and body. He also demonstrated to me a serious and rigorous attitude towards academia and a consistent passion, which had a tremendous positive impact on my values for future research endeavours.

I would also like to convey my profound appreciation for the companionship and guidance of my colleagues in Prof. Zheng's group over these 4 years. I want to thank Prof. Qiyao Huang, Dr. Mingming Ron, Dr. Qianyi Guo, Dr. Chuan Xie, Dr. Pengwei Wang, Dr. Hailong Xu, Dr. Yuan Gao, Dr. Hong Hu, Dr. Ziran Wang, Dr. Pui Fai, Joanne, Ng, Dr. Lei Wang, Dr., Wenjiao Ge, Dr. Junling Xu, Dr. Wenshuo Wang, Dr. Yuqi Zhang, Dr. Dongdong Li, Dr. Lina Chen, Dr. Xi Lu, Dr. Chao Wang, Dr. Xian Song, Dr. Yufei Zhang, Dr. Jingjing Fu, Dr. Huimin Wang, Dr. Junhua Zhou, Dr. Chi Zhang, Dr. Yichun Ding, Dr. Yingsi Wu, Dr. Haining Fan, Dr. Yanpeng Guo, Dr. Yi Pei, Dr. Yufeng Luo, Dr. Sze Wing, Miya, Ng, Dr. Yaokang Zhang, Dr.Qiuna Zhuang, Dr. Leni Zhong, Dr. Fan Chen, Dr. Wancheng Yu, Dr. Zhenyao Wei, Dr. Youchao Qi, Mr. Pengxiang Zhang, Mr. Lingtao Fang, Mr. Xiaohao Ma, Mr. Lixi Chen, Mr. Jinxing Jiang, Mr. Jiaheng

Liang, Mr. Zhibo Li, Ms. Wudi Li, Ms. Huixin Wang, Ms. Jiehua Cai, Ms. Yuqing Shi, Ms. Shujing Wen, Ms Mengjia Zhu, Ms Zhizhi Wu, Ms. Huiming Wang. I am grateful for the valuable training, advice, and discussions provided by my lab colleagues, which have greatly contributed to my daily research activities.

I want to extend my gratitude to the technicians and staff at the School of Fashion and Textiles and the University Research Facility Management System (URFMS) for their invaluable assistance with the characterization and analysis of samples. Additionally, I acknowledge the financial backing from the Hong Kong Polytechnic University and project foundations provided by Prof. Zheng.

Most importantly, I want to thank my dear wife Ms. Na Xu. In the first two years of the epidemic closure process, she never abandoned me. When I was under huge pressure from scientific research and life, she accompanied me every day and enlightened me to get through that difficult and dark two years. After the end of the epidemic, she also gave up her original job for me and resolutely came to Hong Kong to accompany me for the remaining two years. I could never have gotten this PhD without her support and help. Finally, my parents, they also gave me great spiritual support and help during my doctoral study.

Table of Contents

List of Figures

List of Tables

List of Abbreviations

2D	Two dimensional
3D	Three dimensional
AFM	Atomic force microscopy
Ag	Silver
AR	Aspect ratio
ArF	Argon fluoride
Au	Gold
BMP	Beats per minute
CaF	Calcium fluoride
CD	Critical dimension
CMOS	Complementary metal-oxide-semiconductor
Cr	Chromium
Cu	Copper
CV	Cyclic voltammetry
DPI	Dots per inch
DPN	Dip-pen lithography
EBL	Electron beam lithography
ECG	Electrocardiogram
EDX	Energy Dispersive X-ray spectroscopy
ERT	Electrochemical replication and transfer

EUV	Extreme ultraviolet
FoM	Figure of Merit
FTE	Flexible transparent electrodes
IC	Integrated circuit
ICP	Inductively coupled plasma
IL	Interference lithography
IoT	Internet of things
IR	Infrared
ITO	Indium tin oxide
KrF	Krypton fluoride
LCA	Life cycle assessment
LED	Light-emitting diodes
LiCl	Lithium chloride
MoS_2	Molybdenum disulfide
MSCs	Micro-supercapacitors
NA	Numerical aperture
Ni	Nickel
NIL	Nanoimprint lithography
nTP	Nano-transfer printing
OLEDs	Organic light-emitting diodes
OM	Optical microscopic

PDMS	Polydimethylsiloxane
PET	Polyester
PFDT	1H,1H,2H,2H-perfluorodecanethiol (PFDT)
PI	Polyimide
PMMA	Polymethyl methacrylate
Pt	Platinum
PVA	Polyvinyl alcohol
SAM	Self-assembled monolayer
SEM	Scanning Electron Microscope
Si	Silicon
SiO_2	Silicon dioxide
SWNTs	Single-walled carbon nanotubes
TENG	Triboelectric nanogenerator
Ti	Titanium
UV	Ultraviolet
vdW	Van der Waals
XRD	X-ray Diffraction
μCP	Microcontact printing

Chapter 1: Introduction

1.1 Background and Challenges

Flexible and stretchable electronics have broadened the horizon for unconventional applications, presenting a plethora of possibilities, such as wearable electronics[1-3], biosensors[4, 5], and optical devices[6, 7]. Patterning technology is crucial in the manufacturing process of the circuits for the devices applied in these areas. Traditional patterning technologies such as photolithography[8], electron beam lithography[9], and nanoimprinting lithography[10] have undergone significant improvements over the years, particularly in the aspect of resolution[11]. However, these technologies are not only expensive and inefficient in throughput, but also unsuitable for the emerging applications mentioned above which require conducting of patterning process on unconventional substrates[12].

Conventional lithography techniques like photolithography are incompatible with the direct patterning process on flexible substrates due to issues like rough surfaces with low wettability, poor resistance to chemical solvents, and thermal instability[13]. To address this, advanced patterning techniques such as transfer printing[14-17], inject printing[18, 19], 3D printing[20, 21], and soft lithography[22, 23] have been developed. Yet, achieving patterns possess the characteristics of high-resolution and high-aspect ratio simultaneous on these flexible substrates using existing technologies remains a challenge, especially considering commercial requirements for high throughput and low cost[12, 24, 25].

In our previous work, we introduced a novel additive patterning technology named electrochemical replication and transfer (ERT), which allows for the repeatable and parallel fabrication of multi-scale patterns on flexible and stretchable substrates at the same time[26]. The ERT method uses a gold (Au) patterned template fabricated by conventional lithography techniques for the electrodeposition of target materials. The Au template is pre-treated with 1H,1H,2H,2H-perfluorodecanethiol (PFDT) solution to establish a self-assembled monolayer (SAM) which reduces the adhesion force between the Au template and the target materials during the following electrodeposition process. This allows the target materials pattern to be easily transferred to flexible substrates by a binder layer, without damaging the template. Thus, ERT strikes a great balance between resolution, throughput, and cost.

However, being a newly developed method, ERT still has several limitations. Firstly, while the resolution limits of the electro-replicated pattern are, in theory, solely constrained by the original template, which should be capable of achieving several nanometers, fabricating nanoscale patterns using ERT remains a challenge in the aspect of protecting the template. Secondly, the ultraviolet (UV)-curable binder used in ERT is a rigid polymer binder, which is non-stretchable, limiting its application in stretchable electronics. Thirdly, the replicated pattern is embedded in the binder layer, although improving the flexibility of the devices, it also restricts its use in some applications requiring three-dimensional structures such as metasurfaces[27], wearable sensors[28], tissue engineering[29], and energy harvesting and storage[30]. Lastly, the resolution of the fabricated pattern may decrease over time due to the isotropic growth of electroplated materials. Therefore, further research on ERT is needed to address these issues and expand its application in the fabrication of flexible electronics.

1.2 Research Objectives

To confront the aforementioned challenges associated with ERT, this research project focuses on the modification of the template structure and the binder material used in ERT to realize the improvement of ERT and expand its influence in flexible electronics. The research objectives of this research are delineated in detail as follows:

(1) To design and develop a new structure of the Au patterned template with an embedded structure for the fabrication of nanoscale patterns.

(2) To replace the rigid binder with another dissolvable material and realize the manufacturing of stretchable electronic devices.

(3) To design and develop a new structure of the bare Si substrate with a 3D structure pattern for the fabrication of 3D patterns and study the related applications.

(4) To investigate the potential applications of ERT including designing the production lines for mass manufacturing of triboelectric nanogenerator electrodes and evaluating the value of ERT in green production and biomedical engineering.

1.3 Research Originality

The patterning technique is crucial in the fabrication of wearable electronics. ERT, a potent patterning method, can fabricate diverse material patterns on a variety of flexible substrates, achieving an excellent balance between resolution, throughput, and cost. However, it has limitations, including the fabrication of nanoscale patterns, stretchable electronics, and 3D structure patterns. The potential for mass and green production remains unexplored. We designed and fabricated templates with varying structures to address these challenges and replaced binders with different materials. We also proposed design ideas for production lines of ERT for mass manufacturing and evaluated its potential in green production.

Initially, we added an extra 30 nm thick layer of SiO_2 to the original Si substrate. Photolithography and dry etching were performed on the SiO_2/Si substrate before the thermal vapour deposition of the Au pattern, which is also 30 nm thick. Consequently, the Au pattern is embedded into the SiO_2 layer, with only the upper surface exposed. During the subsequent electroplating process, the target materials are deposited solely on the upper surface of the Au pattern. This SiO_2-protecting structure template significantly enhances the durability of the template and extends the resolution limitation of ERT to the nanoscale.

Next, we replaced the UV-curable binder NOA 63 used in ERT with a polyvinyl alcohol (PVA) water solution. The adhesion force of the PVA binder is strong enough to detach the intended material pattern from the Au template. The dissolvability of PVA also facilitates the clean transfer of the replicated pattern to any substrate, including hard surfaces, curved surfaces, and stretchable substrates. This makes it suitable for various stretchable electronics, such as stretchable conductors and supercapacitors.

Additionally, we used a 3D structure template for the electroplating process during ERT. The 3D Si template with a SiO_2-protected surface can be fabricated through a simple photolithography and inductively coupled plasma (ICP) etching process, without additional Au deposition on the patterned template. The growth of conductive materials is selectively proceeding on the exposed Si surface during the electrodeposition process, replicating the 3D structure patterns on the template. Using the photocurable binder NOA 63, we can quickly peel off the 3D structure patterns of different materials. This 3D template can fabricate both continuous and isolated patterns with different conductive materials, with the highest aspect ratio reaching 4:1. The resulting 3D patterns also maintain the flexibility and reliability of ERT-fabricated devices.

Lastly, we conceptualized a production line for ERT, taking the manufacturing of triboelectric nanogenerator (TENG) electrodes as an example. We characterized the efficacy of the TENG devices fabricated by ERT including electrochemical performance, flexibility, and stability. We evaluated the potential energy and cost consumption in real production through PLC and proved that the ERT fabrication process is environment-friendly and highly efficient. Furthermore, the potential application in biomedical engineering of ERT has also been proved through the evaluation of an implantable electrical stimulation device.

1.4 Outline of the Thesis

The thesis is structured as follows:

Chapter 1 provides a succinct introduction to the background of the patterning technique and the evolution of ERT, outlining its challenges. It then presents the objectives and originality of this research project.

Chapter 2 offers a review of the progression of various patterning methods, encompassing both traditional and recently proposed advanced techniques. It includes a thorough comparison of these methods with ERT, focusing on resolution, throughput, and cost.

Chapter 3 encapsulates the methodologies employed in this research, detailing the materials, fabrication processes, and characterization equipment used.

Chapter 4 details the fabrication process of the SiO_2-protecting template for ERT, demonstrating its applicability in creating nanoscale patterns with different materials and substrates, and its potential for large-scale fabrication.

Chapter 5 explores the function of substituting UV-curable binders with water-dissolvable PVA binders, demonstrating its applicability to various materials and substrates, including stretchable substrates. It also proposes the fabrication of various stretchable electronics.

Chapter 6 investigates the fabrication of a 3D structure of Si substrates for creating 3D patterns using ERT. It showcases the advantages of 3D-ERT in maintaining resolution and constructing 3D structure electrodes, as evidenced by the application of flexible transparent electrodes and pressure sensors.

Chapter 7 proposes the idea of establishing an ERT production line for fabricating TENG devices and assesses the potential energy consumption and cost in the context of sustainable ERT production. The application prospect in the field of biomedical engineering has also been proven.

Chapter 8 concludes the research and discusses future research directions for ERT and other advanced patterning techniques, offering insights and suggestions.

Chapter 2 Literature Review of Patterning Techniques for Flexible Electronic Devices

In this era of technological explosion, we are heavily reliant on the utilization of electronic instruments and the Internet. The rise of the Internet of Things (IoT), which integrates physical objects into network platforms to help humans sense the world, reflects our evolving relationship with digital technology[31]. This shift has sparked intense debate about wearable electronic devices, which is a key component of IoT. The implementation of IoT requires the collection and exchange of diverse signals and data via the Internet. Wearable electronic devices play a vital role in monitoring and collecting data between physical objects and the human body[1, 3, 32-34].

Unlike traditional rigid electronics, wearable devices must be flexible or even stretchable, conforming to human skin or clothing. The deformation of the human body can range from 5% to 30% across different body regions, which also represents the limit of human skin[35]. This necessitates additional requirements for circuits, devices, and substrates that carry electrical components[36]. While it is feasible to find flexible, stretchable, and biocompatible materials for substrates, the real challenge lies in achieving the flexibility and stretchability of integrated circuits (ICs) and electrical components, while maintaining superior performance and long-term stability, to realize the integration of devices and substrates[37].

The fabrication of wearable electronics primarily involves the creation of ICs, which connect various electronic components and enable different functions. Patterning techniques are crucial in this process, as they can create and fabricate different circuit patterns onto target substrates. In the traditional semiconductor industry, commercial products are produced via a sequence of procedures encompassing photolithography, etching, deposition, cleaning, encapsulation, and testing, typically conducted on a silicon wafer[38]. This process is complex, costly, and potentially harmful due to the use of various chemicals[31]. While silicon wafers and metals could withstand the corrosion caused by these chemicals, things may be greatly different for flexible and stretchable substrates. These substrates, usually composed of polymers or fibers, can easily corrode or dissolve during the fabrication process[39]. The uneven surface of these substrates also brings tackles in maintaining resolution, negatively impacting electrical performance[40].

When evaluating the suitability of a patterning method for the fabrication of flexible electronics, three key factors must be considered: resolution, throughput, and cost[41]. Achieving a balance between these three aspects remains a challenge for all lithography methods. This chapter will provide a detailed overview of various conventional patterning methods, including photolithography, and discuss their pros and cons in the context of flexible electronics. It will also present a comprehensive literature review of emerging patterning techniques that have significantly improved flexible electronic devices. Finally, it will introduce a novel patterning method, called electrochemical replication and transfer (ERT), which can fabricate a range of metal, polymer, and metal oxide patterns on diverse flexible substrates, providing high throughput and cost-effectiveness.

2.1 Traditional Patterning Techniques

2.1.1 Photolithography

Photolithography is a famous patterning technology that serves a pivotal function in the fabrication of Integrated Circuit (IC) chips, the cornerstone of modern electronic devices such as computers and mobile phones[8]. IC chips comprise numerous transistors and other vital electronic components integrated into a semiconductor substrate, primarily silicon. The efficiency of an integrated circuit (IC), gauged by its computational speed, is directly linked to the count of transistors per unit area[42]. Go back to 1965, Gordon Moore, one of the founders of Fairchild Semiconductor and Intel, hypothesized that the count of semiconductors on an IC will increase twofold each year, a forecast famously known as Moore's Law[43]. This principle was later updated in 1975 to suggest a biennial doubling, a pattern that persists to the present day[44]. The continuous relevance of Moore's Law is intrinsically connected to the swift progression of photolithography technology, a crucial method in IC production[45].

Photolithography, a mature patterning technique which has been the subject of scholarly investigation for more than five decades, operates by using the light sensitivity of a specific chemical photoresist to transfer pre-designed patterns from a photomask to a target substrate, such as silicon. The solubility of the photoresist in a particular chemical solution will change after light exposure, allowing the pattern of target materials to be obtained through etching or filling with further chemical or physical treatment[46]. These two fabrication models are detailed in Figure 2.1. The etching model involves depositing the target materials layer onto the silicon surface, succeeded by the application and patterning of the photoresist layer via spin-coating on the target materials' surface[47]. The unpatterned area of the metal layer is then etched away using dry etching or a specific chemical solvent (wet etching). Finally, the residual photoresist will be cleaned with acetone or another organic solvent[48]. Dry etching is preferred in the semiconductor industry thanks to the extreme anisotropy, although it may cause some damage to the substrate or subbasement layer[49]. Conversely, the lift-off technique entails depositing the wanted material layer onto the resist surface following the exposure and development stages. Subsequently, the undesired portion is eliminated together with the photoresist layer using acetone. This process is preferable when the target material is difficult to dry etch, but it may also present problems such as incomplete removal of metals and 'ears' phenomena on sidewalls[50-52].

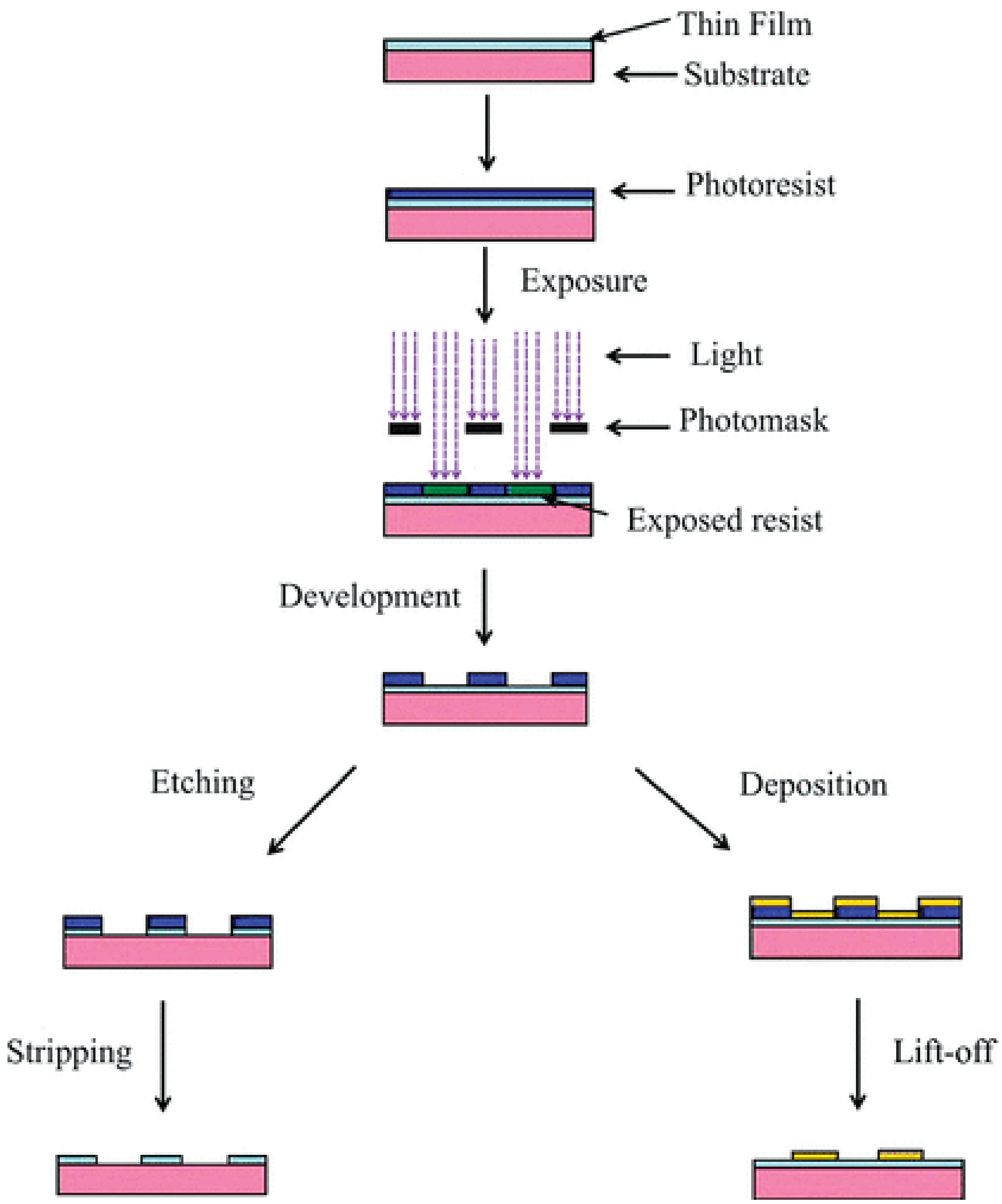

Figure 2.1 Two different fabrication models in photolithography including etching and lift-off processes[53].

The primary development direction of photolithography is improving the resolution limit to accommodate the increasing number of transistors on ICs[54]. The essence of lithography is image projection technology, and the minimum feature size, or critical dimension (CD), depends on three parameters: the k_1 factor, the wavelength of the light (λ), and the numerical aperture (NA) of the lens used in the lithography. These three parameters have a relationship shown in equation (2.1) below.

$$CD = k_1 \times \frac{\lambda}{NA} \tag{2.1}$$

The history of photolithography, summarized in Figure 2.2, shows an increase in resolution over time. Mercury lamps were the first light sources used in photolithography, and in the 1990s, the 248 nm Krypton Fluoride (KrF) excimer laser was introduced as the light source, increasing the resolution to 0.25 μm and 0.18 μm[55, 56]. The NA of the lens was also boosted from 0.60 NA to 0.93 NA[57].

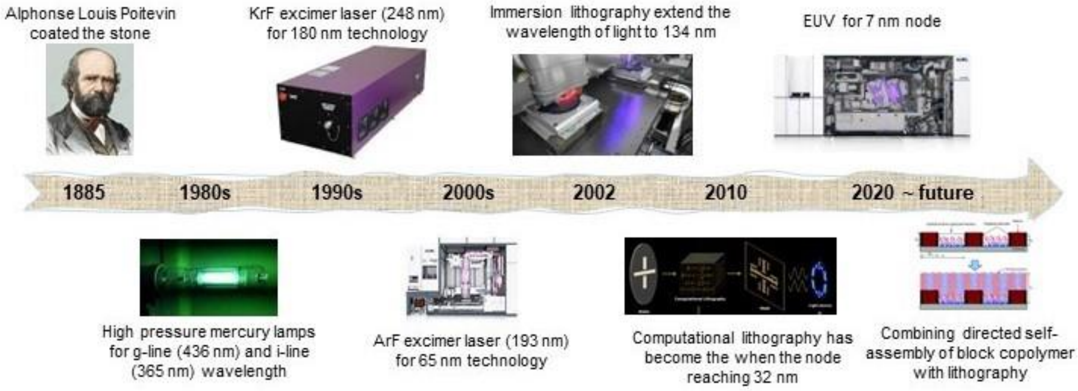

Figure 2.2 The history and important node for photolithography[55, 56, 58-62].

To enhance the resolution limit further, the Argon Fluoride (ArF) excimer laser was developed at the start of the 21st century[58]. This development enabled the fabrication of ICs with 65 nm / 55 nm line width. However, other gas excimer lasers with shorter wavelengths, such as fluorine (157 nm), are unsuitable for photolithography because UV light has a wavelength under 193 nm will be absorbed in air, necessitating a vacuum environment for light propagation. Moreover, only optical glass made from Calcium

Fluoride (CaF) crystals can transmit 157 nm UV light, which exhibits hygroscopy and high intrinsic birefringence[63, 64].

As a significant milestone, water-immersion lithography was developed, which involves filling the space between the optical source and the specimen with water (Figure 2.3)[65]. This method successfully extends the wavelength of light to 134 nm due to the refraction of light in water (possessing a refractive index of approximately 1.436 at 193.368 nm), a significant improvement over 157 nm[66-68]. Furthermore, it eliminates the need for a vacuum environment, making water-immersion lithography a widely used technique. The NXT1970ci machine developed by ASML can resolve a 38 nm linewidth, 76 nm period, and 2 nm embedding accuracy (3 standard deviations)[69].

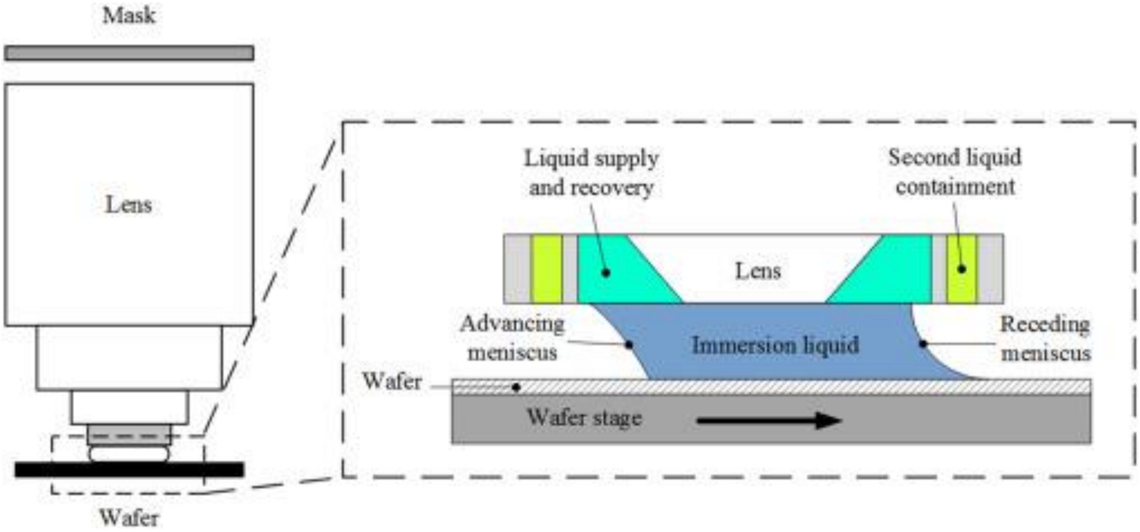

Figure 2.3 Schematic illustration of immersion lithography[65].

In addition to using light refraction to increase resolution, oblique illumination (also known as ionization illumination) and light diffraction can further increase the limit[70]. However, this may induce an optical proximity effect, necessitating the addition of a certain line width bias to the mask for compensation, known as optical proximity correction (Figure 2.4)[71-73]. This led to the birth of computational lithography, which uses optical and chemical models to theoretically explore methods of increasing resolution and process window of lithography, and guide process parameter optimization[60, 74]. Around 2010, the co-optimization of illumination conditions and mask graphics, along with inversion lithography, propelled computational lithography to new heights[75-77]. It is fair to say that computational lithography has become the core of the photolithography process when the node reaches 32 nm.

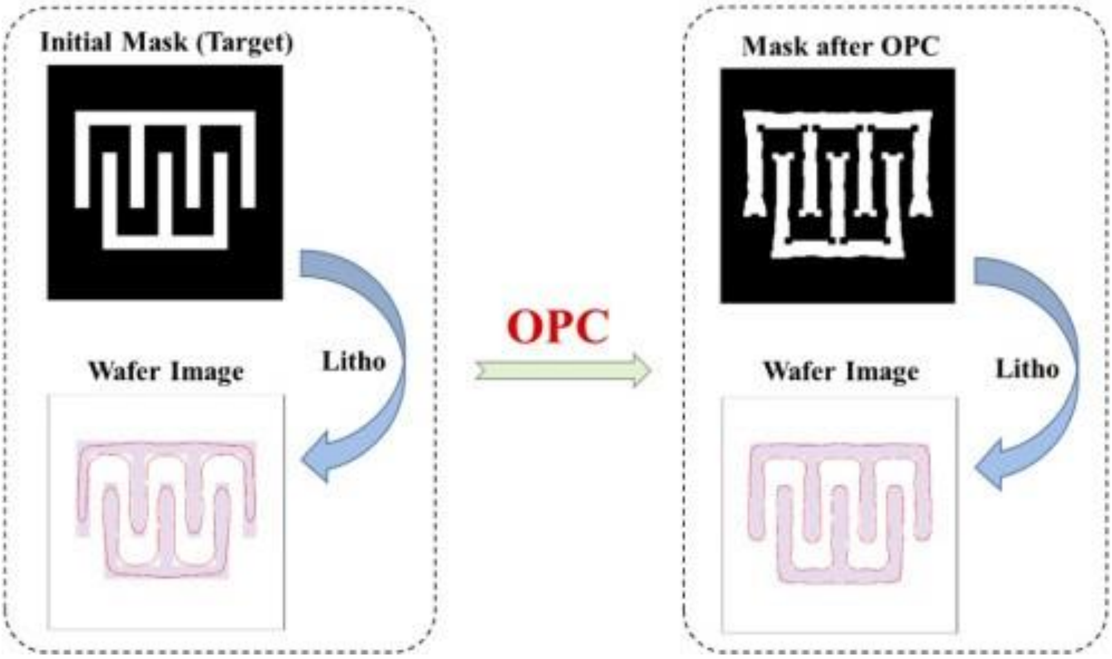

Figure 2.4 Comparison of the imaging quality with and without optical proximity correction[73].

In recent years, the development of another light source, extreme Ultraviolet (EUV), has significantly increased resolution[78, 79]. EUV lithography uses ultraviolet light which has a wavelength of 13.4 nm, emitted from the excitation of the K pole of the

UV tube with an electric current[61]. The optical system of EUV lithography differs significantly from traditional lithography methods owing to the potent absorption of extreme ultraviolet light at a wavelength of 13.4 nm by almost all optical materials. Therefore, the optical system can only use reflectors (Figure 2.5)[80, 81]. The main technical challenge of EUV is that the energy output of the light source struggles to meet productivity requirements compared to the 193 nm immersion lithography machine[82]. The limited energy absorption efficiency of photoresists to extreme ultraviolet hinders the productivity improvement of lithography machines and causes significant graphic edge roughness[83]. Additionally, due to the high vacuum system and complex systems, such as laser-excited isobaric light source, resulting in low equipment reliability, the utilization rate was only 60%~70% in 2017. In contrast, the utilization rate of the 193 nm immersion lithography machine is greater than 92%, generally around 95%. Therefore, extreme ultraviolet lithography is more suitable for the middle and back section lithography in logic circuits, which does not require high roughness of the graphic edge such as shear mask graphics, grooves, etc[84-86]. It was not widely used until 2020 and currently is used for cutting-edge processes below 7 nm[87].

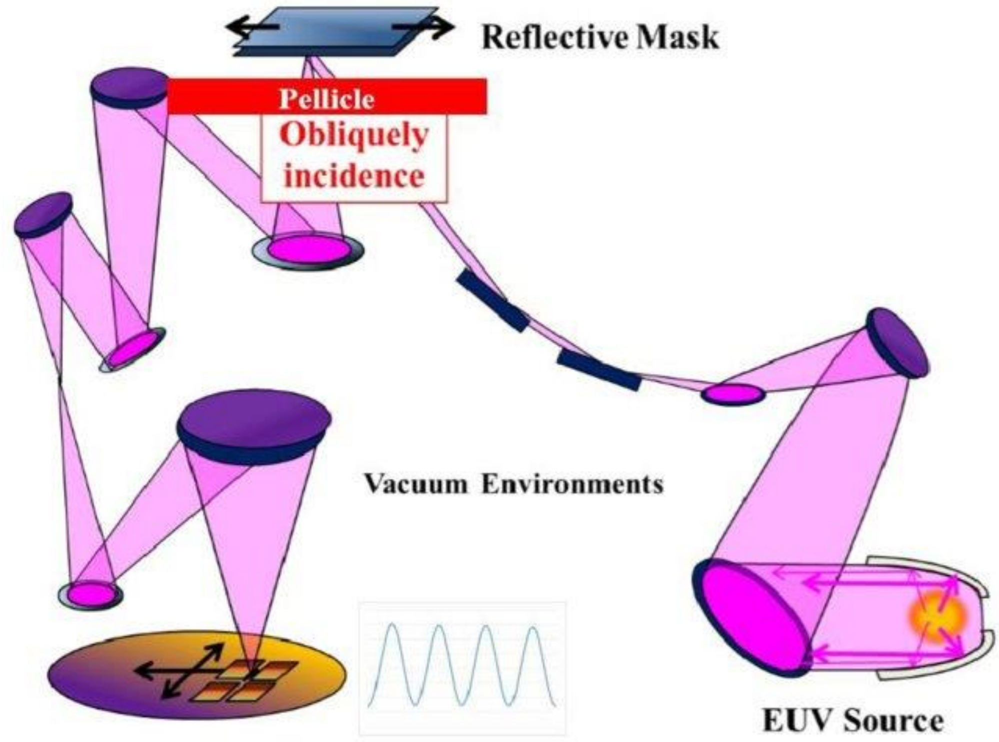

Figure 2.5 Schematic presentation of the function mechanism of EUV lithography[81].

The industry has shown significant interest in the intrinsic self-assembly of block copolymers, primarily due to its straightforward process and cost-effectiveness[69, 88-92]. Periodic pattern structures with characteristic features smaller than 10 nm could be obtained through self-assembly in thin films. Its low line-width roughness (lower than EUV and 193 nm immersion lithography) makes it a suitable choice for future logic circuit front processes[69, 90]. However, due to its high defect rate and graphical placement deviation, i.e., line edge roughness, it cannot be applied in mass production[62]. Alongside EUV lithography, block copolymer still has significant potential for growth.

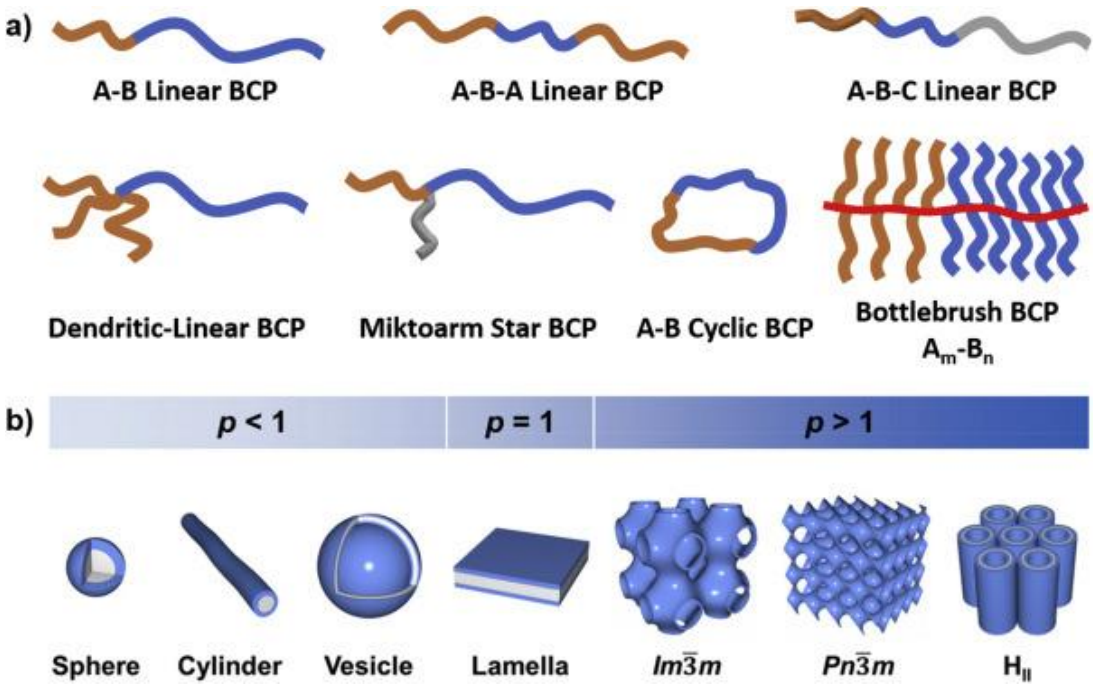

Figure 2.6 Various nanostructures constructed by directed self-assembly of block copolymer[92].

2.1.2 Electron Beam Lithography

Electron Beam Lithography (EBL) is a lithography method that employs an electron beam to create patterns on a resist layer. In accordance with de Broglie's theory of matter waves, electrons are perceived as waves possessing exceedingly short wavelengths[93]. This characteristic enables EBL to achieve high resolution, reaching up to 5 nm[94].

EBL utilizes two types of patterning models: the direct writing model and project printing[95]. Figure 2.7 below illustrates these two models. Project printing employs a modulator to project the pattern onto the substrate in parallel, similar to the mask used in photolithography. However, challenges such as the fabrication of the mask, integration of multi-scale patterns, aberration limitations, and other issues significantly hinder the development and widespread adoption of this projection model[96]. Conversely, the direct writing model, which is commonly used in practical production, follows a serial writing approach. This model uses a highly focused Gaussian round beam to expose each pixel on the substrate individually, creating the final high-resolution pattern without the need for an expensive mask. However, this characteristic also restricts its capacity for mass production and makes the process time-consuming. The cost of the machine and a single template can also be prohibitively high. As a result, EBL is primarily suitable for mask-making or small-volume high-resolution products in test and research labs[95].

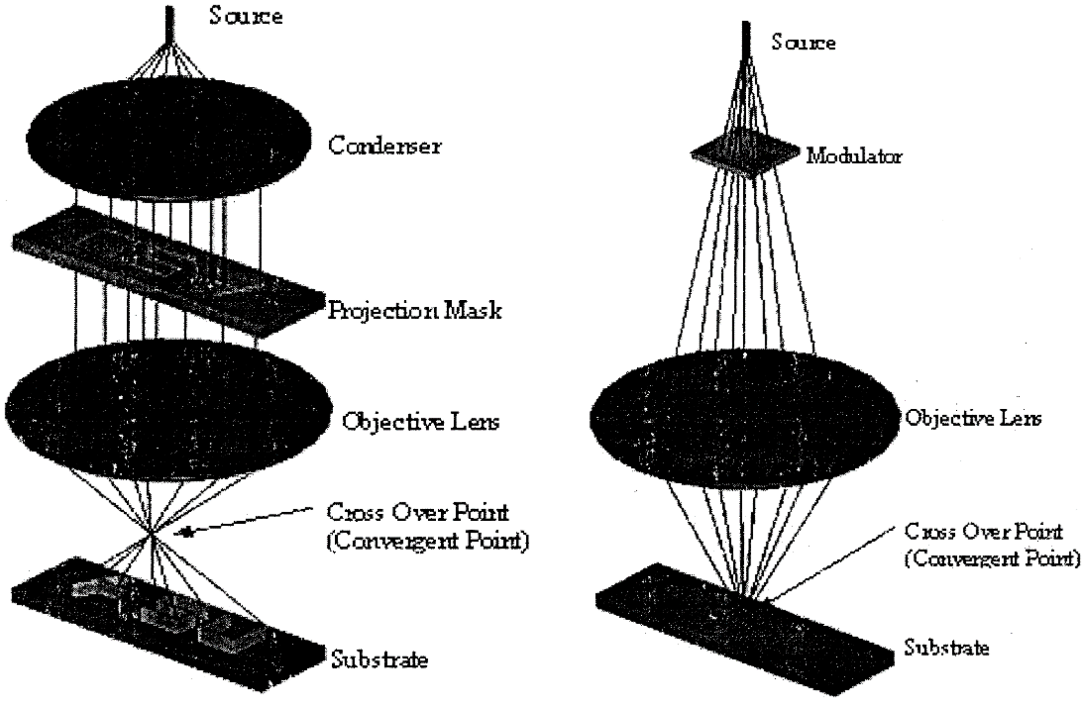

Figure 2.7 Sketch map of the direct writing (left) and project printing (right)[95].

EBL research primarily focuses on the study of the resist layer used in the process. The resolution of EBL is also significantly influenced by the kind of resist material utilized. Common resists can be categorized into two types: PMMA-contained resist (both organic and inorganic) and chemically amplified resists[97]. Different categories of resistance have varying sensitivities and contrasts, which significantly influence the developing dynamic. Consequently, the resolution for a particular resist has an upper limit. Figure 2.8 shows a bar chart of the resolution range of some common resists for EBL.

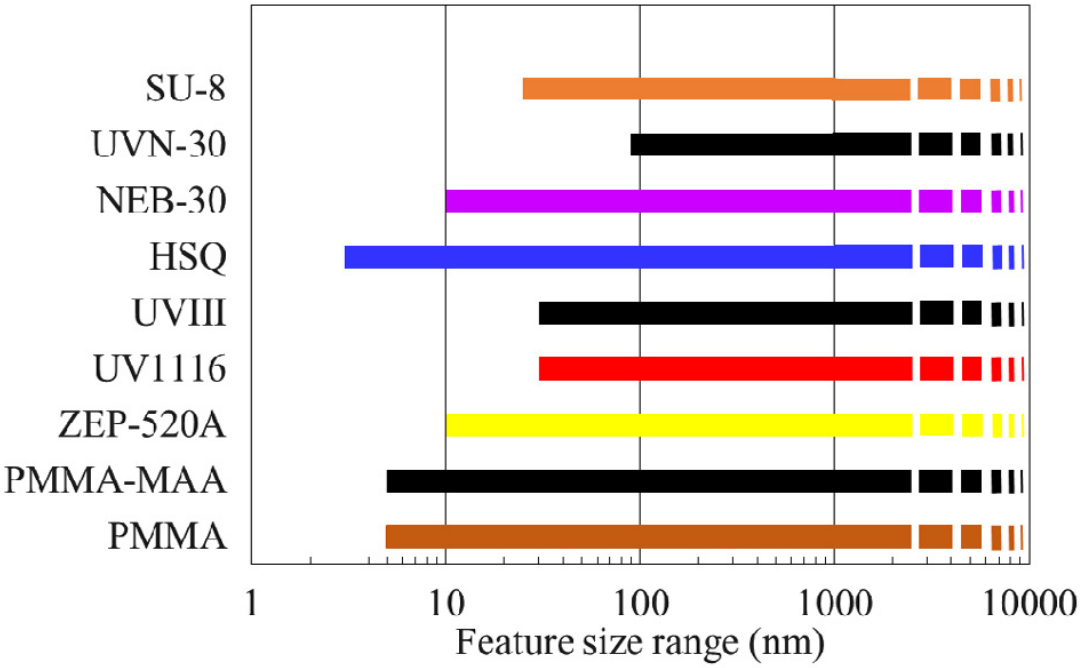

Figure 2.8 Bar chart of the range of resolution of some common resists for EBL[98-105].

The ability to use different layers of resist also provides the opportunity to fabricate multilayer nanostructure devices, including T-shaped gates (as shown in Figure 2.9)[106], metallic tunnelling junctions[97], chiral structures[107], and more. This has provided valuable insights for the fabrication of other nanodevices.

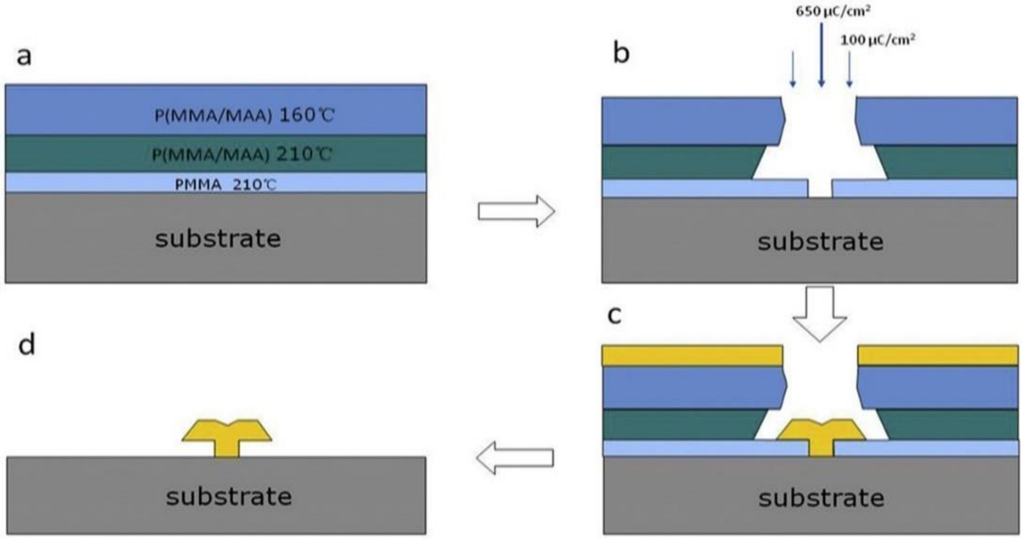

Figure 2.9 Example of application for T shape gates using EBL[106].

The limitations of EBL are similar to those of photolithography, particularly in the fabrication of flexible electronics. The elevated fabrication expenses and diminished throughput also curtail its applicability in large-scale production.

2.1.3 Nanoimprint Lithography (NIL)

Nanoimprint Lithography (NIL) differs slightly from the previously mentioned patterning techniques. While it also uses a resist layer in the lithography process, NIL generates patterns by combining mechanical force with heat or light. The pattern is replicated through mechanical contact and 3D material movement between the resist layer and a prefabricated mould. This process is not constrained by the wavelength of any kind of light, unlike photolithography or EBL. The crucial aspect of this technique is the subsequent curing of the resist layer, which is achieved through thermosetting or photosetting properties[108-110]. Figure 2.10 provides a schematic illustration of these two types of nanoimprint lithography.

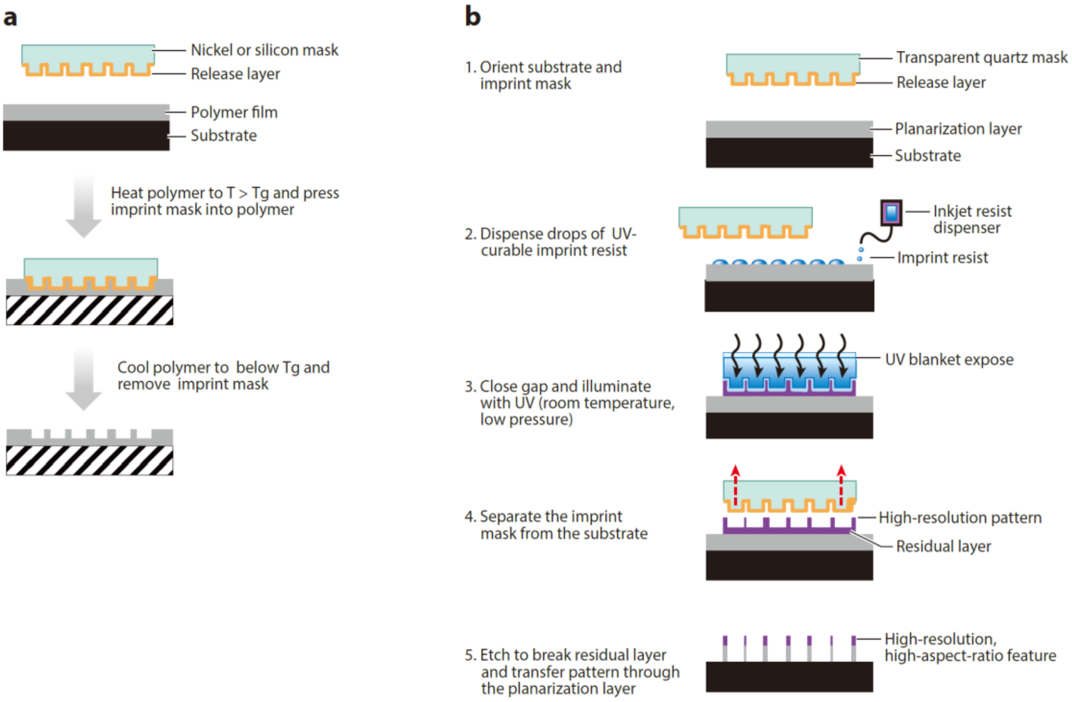

Figure 2.10 Comparison of (A) normal thermal NIL and (B) UV-curable NIL[111].

The production of patterns in NIL is similar to photolithography, as it follows the parallel replication of patterns. Consequently, the throughput of NIL can reach 10^{-5}-1 m^2/h, maintaining a low cost that is even more affordable than photolithography[112]. Since 1995, when Chou and his group proposed a three-structure pattern of sub-25 nm diameter and 100 nm depth, NIL has emerged as a dependable option for the fabrication of electronic devices on a scale of 11 to 15 nm[108, 113]. It has been applied in various industries, including the fabrication of ICs[114], hard disk drives[115], photonics[116], solar cells[117], and biological research[118]. However, NIL still faces some challenges in practical application, such as the need for specific production parameters to produce high-quality and multilayer products. One of the most significant challenges is the alignment of the template, especially when the scale is reduced to a few nanometers. It becomes increasingly difficult for a machine to precisely position the template relative to other features. This issue may limit the application of NIL only suitable in the production of single printing or patterns with low alignment requirements[119].

In conclusion, NIL has garnered increasing attention due to its potential to replace traditional photolithography and electron beam lithography. It presents the potential for simultaneously attaining high resolution, high efficiency, and cost-effectiveness.

2.1.4 Summary

As wearable electronics continue to evolve, a critical challenge is maintaining the advantages of traditional lithography techniques when fabricating electronic devices on flexible substrates. For photolithography, EBL, and NIL, a significant issue is that flexible substrates, unlike the ultra-flat and pristine rigid substrates employed in conventional photonic or electronic industries, have characteristics that present considerable challenges in the patterning process. These characteristics include a rougher surface, difficulty in wetting, incompatibility with strong solvents (such as developers and removers), and instability under thermal annealing.

2.2 Printing Techniques

2.2.1 Inject Printing

The applicability of any technique to large-scale manufacturing is a crucial factor in its market viability. Normal printing techniques continue to hold significant preponderances in the aspect of rapid fabrication and mass production. Among various printing technologies, Inject Printing distinguishes itself due to its non-contact mode[120].

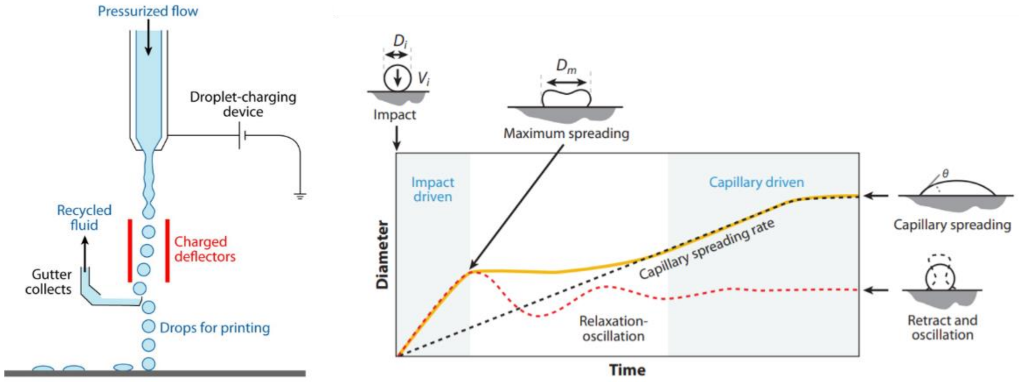

Figure 2.11 Diagram illustration of the creation of ink (left) and formation of the pattern (right)[121].

Figure 2.11 showcases the entire course of inject printing, including the ink creation and the subsequent events that occur once the ink droplets land on the substrate. Droplets are formed and ejected from the chamber, with an electric field or other force controlling the direction and speed of the droplets. The fundamental mechanism behind the pattern formation by these droplets is complex and will not be discussed in detail here. Notably, unlike other patterning techniques, the pattern in inject printing is composed of numerous droplets that act as pixels in the pattern. The resolution is typically determined by a parameter known as dots per inch (DPI), and the precise control of this process significantly influences the maximum resolution achievable[122]. However, due to its printing mode limitations, its resolution is not as impressive as other lithography methods. Typically, the resolution can only reach micrometres, with only a few researchers exploring its potential in nanoscale patterns, successfully achieving a scale of hundreds of nanometers[123].

2.2.2 Screen Printing

In contrast to inject printing, screen printing uses a mesh with various patterns as a mould for ink or dye to pass through (Figure 2.12). A squeegee is used to distribute the ink evenly. The desired pattern areas allow the ink to pass through and be printed on the target substrates, while the rest is blocked by the screen[124].

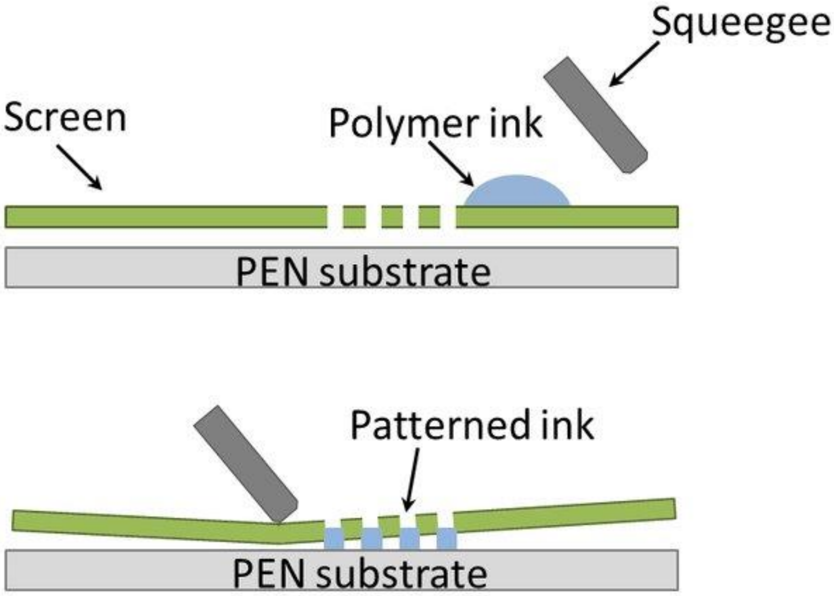

Figure 2.12 Schematic of the screen-printing[124].

Originally used for patterning clothes, screen printing is suitable for patterning on flexible substrates like textiles. However, due to the fluid properties of ink, the resolution of screen printing is difficult to exceed 50 μm, and the entire pattern has a thickness greater than a few micrometres, making it unsuitable for the fabrication of high-precision electronic devices[125, 126].

2.2.3 Summary

Despite their resolution limitations, printing techniques offer significant advantages in terms of throughput and production cost. It is common to combine printing techniques with a roll-to-roll process[127]. Figure 2.13 provides examples of the roll-to-roll process applied to printing techniques. By sacrificing resolution to a certain extent, this model can continuously generate patterns with an extremely high throughput of around 10^3 m^2/h or even higher. Scholars have also endeavoured to augment throughput by incorporating many nozzles into a single printer to create microvascular multi-nozzle arrays[128]. Other printing techniques, such as gravure printing[129], flexographic printing[130], and rotary screen printing[131], employ similar strategies. These technologies significantly increase production rates while maintaining low costs.

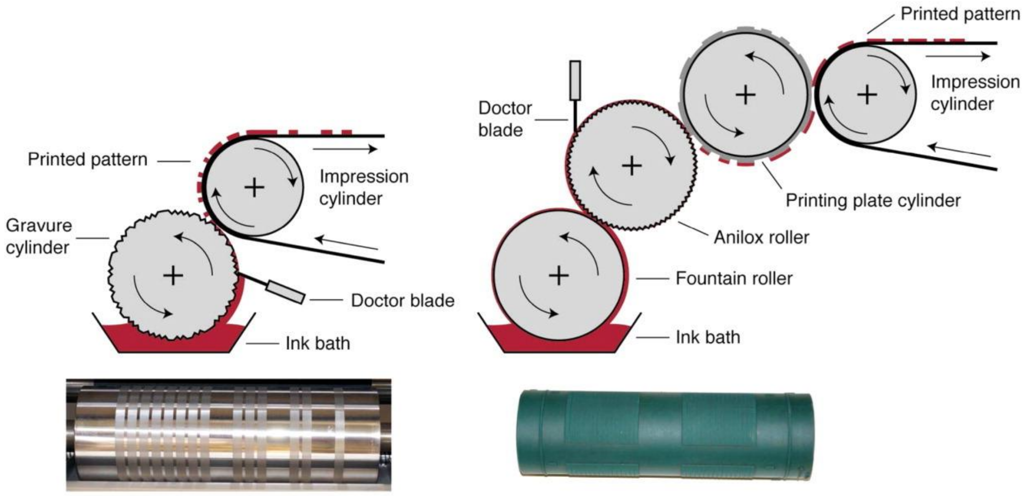

Gravure printing **Flexographic printing**

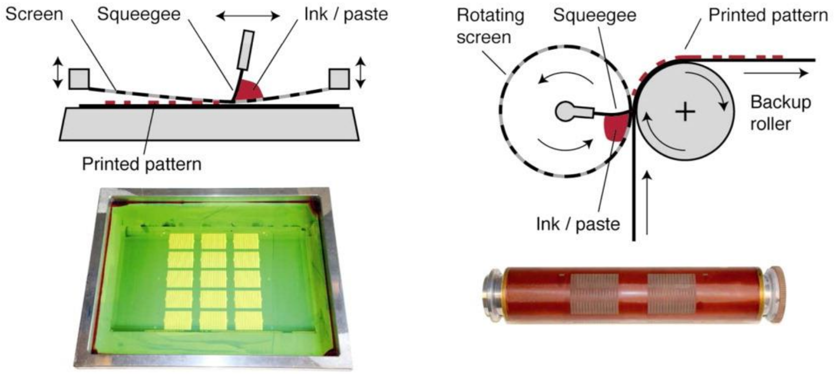

Screen printing **Rotary screen printing**

Figure 2.13 Diagram explanation of the roll-to-roll process in the application of printing technique[132].

2.3 Soft Lithography

2.3.1 Microcontact Printing (μCP)

Microcontact printing, an advanced pattern method, was invented by Whitesides and his team in 1993. This method made large-scale fabrication of high-resolution patterns possible[133]. It uses an elastomer, typically poly(dimethyl siloxane) (PDMS), as soft stamps derived from a hard Si template fabricated by traditional photolithography[134]. After the PDMS soft stamp is fabricated, ink forms on the surface of the stamp through immersion or direct casting. The high hydrophobicity of PDMS allows the ink to diffuse into the PDMS layer, enabling multiple uses of the stamp[135]. The printing process can be separated into two models: the lift-off and casting process, as revealed in Figure 2.14[136].

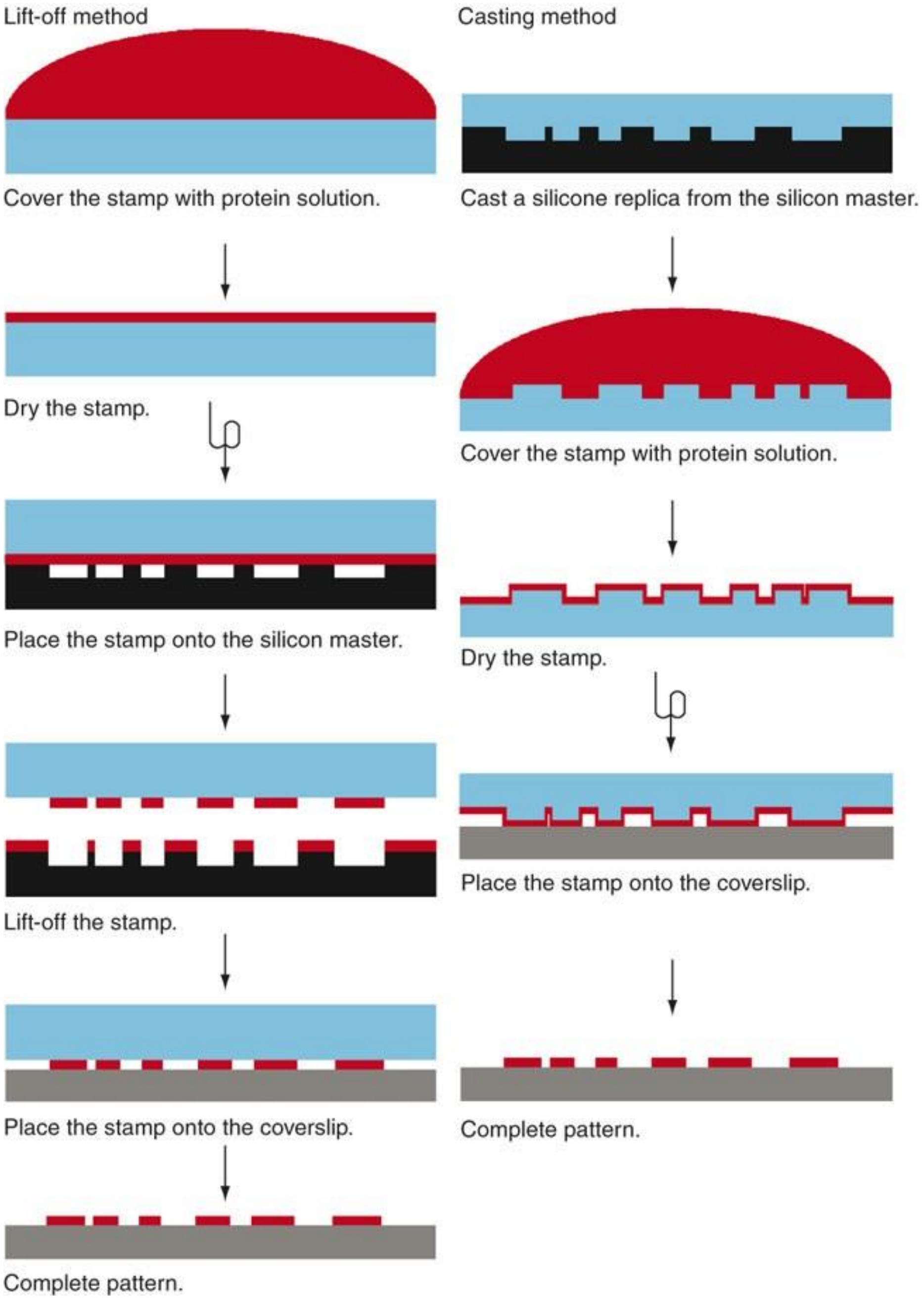

Figure 2.14 Diagram of two patterning models fabricated by PDMS stamps. Left: lift-off method. Right: Casting method[136].

The key to this printing technique is the self-assembly of ink materials on the surface of the target substrates. For example, the thiol group selectively forms on the Au surface[137]. It can also be used for biomedical applications through the self-assembly process of DNA molecules[138].

Despite the cost-saving and potential for a roll-to-roll fabrication process on a flexible substrate, the soft properties of PDMS stamps have several disadvantages. For instance, stamp deformation is a significant issue. As shown in Figure 2.15, the soft PDMS stamp can buckle, laterally collapse, and roof collapse under physical pressure, affecting the resolution and accuracy of the pattern[138]. Other issues like substrate contamination on the stamp, stamp shrinkage or swelling, and ink mobility can also hinder the application of μCP in some fields[22].

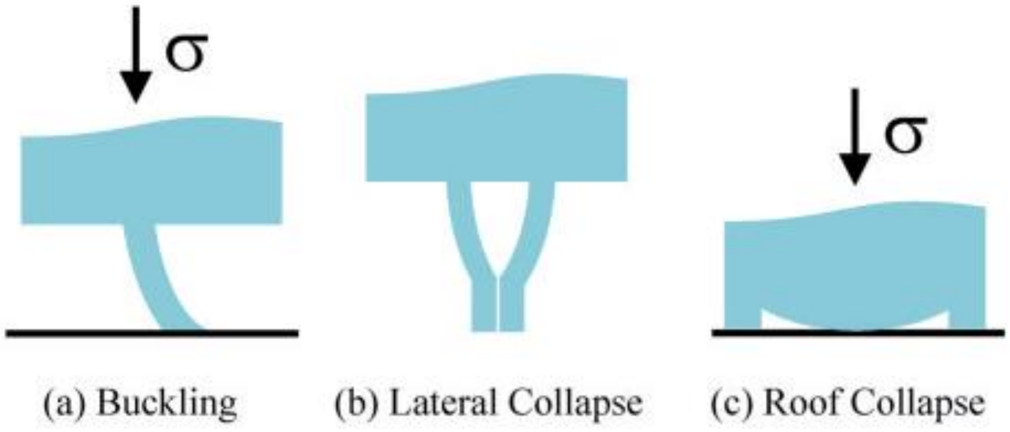

Figure 2.15 Schematic of the mechanical stamp deformation for PDMS stamps[138].

Over the years, many improvements have been made to μCP to address these issues. For example, increasing the printing speed can significantly reduce soft stamp deformation. Combining the printing process with a piezoelectric actuator can automate the process and increase the speed to milliseconds, improving the uniformity of the pattern[139]. Using a liquid medium can also enhance stability. Hydrophobic polymers can be printed by submerging the stamp in water with a high aspect ratio PDMS stamp reaching 15:1[140]. Other methods like using new stamp materials with high Young's modulus, using a magnetic field or plasma to assist the printing process, and special ink design have also been proposed to achieve high resolution on various substrates[141-144].

2.3.2 Nano-Transfer Printing (nTP)

Due to the limitations of traditional lithography methods on flexible substrates, the most common solution is to fabricate patterns on rigid substrates and then transfer the pattern onto the desired substrates. This process, known as transfer printing, can achieve high-resolution transfers reaching nanometer levels compared to μCP, hence it is also called nano transfer printing (nTP)[145, 146].

Unlike μCP, which uses the self-assembly property of molecules to transfer patterns, nTP utilizes the difference between the material-stamp and material-substrate interfaces. Different chemical or physical treatments are conducted to act as a 'release' or 'glue' layer[147]. Figure 2.16 illustrates the basic process.

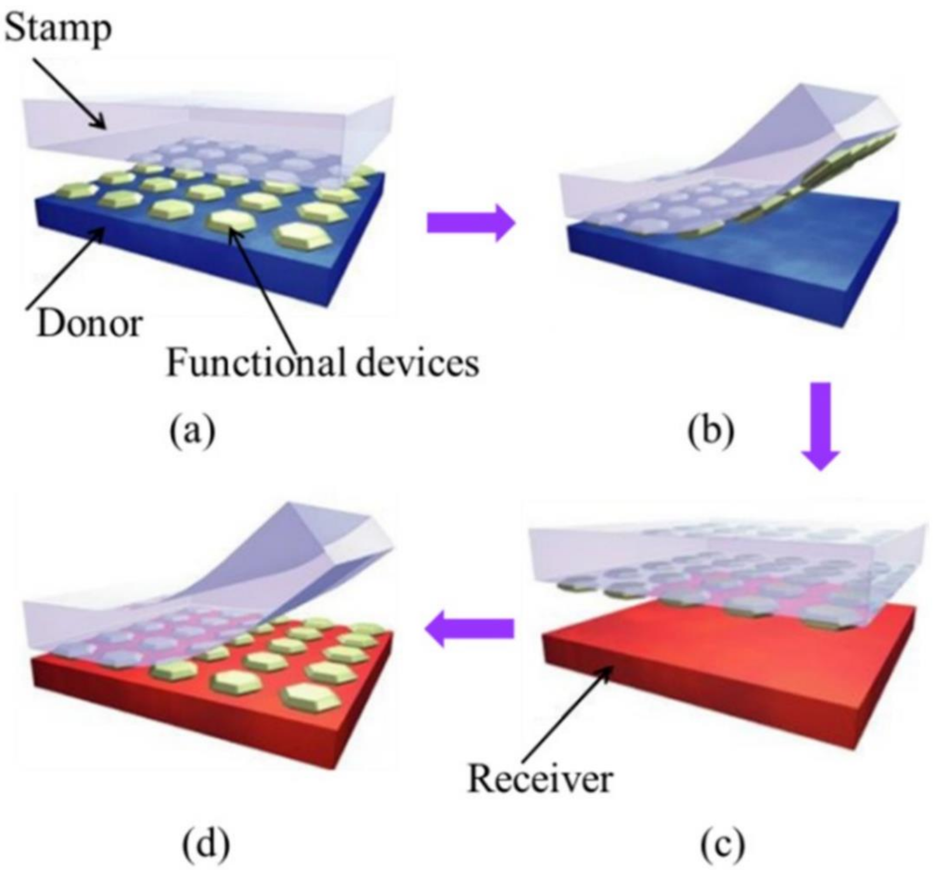

Figure 2.16 Schematic of nTP process including peeling-off and transfer process[14].

PDMS is also a primary stamp used in the transfer process. The mechanism of nTP is diverse, including kinetically controlled[14], thermal-assisted[148], water-assisted[149], surface relief structure-assisted[150], shear stress-assisted[151], and more.

As shown in Figure 2.17, the adhesion force between the PI tape and the polymer replica layer (PMMA) decreases as the temperature increases. Therefore, a hot roll is used as the transfer machine, providing uniform force and heat during the contact process. This enables large-scale fabrication (8-inch) of high-resolution line arrays (20 nm).

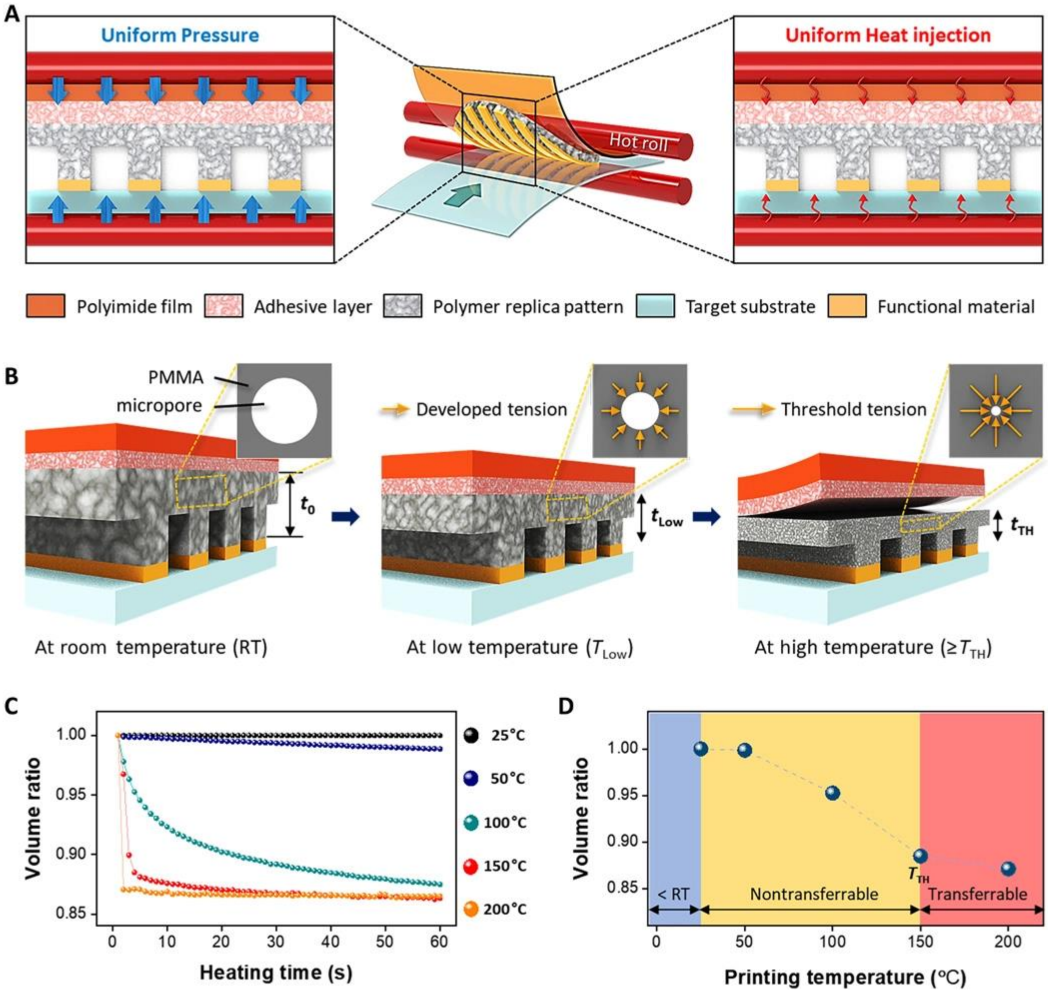

Figure 2.17 Thermal-assisted nano transfer printing for 20 nm resolution and 8-inch scale[148].

Since the adhesion force between the PDMS layer and target materials originates from the vdW force, which is related to the contact area, geometric control can also be used to facilitate the transfer process. Figure 2.18 showed a PDMS stamp with many protruding sharp corners is used to conduct the transfer process. During the first peeling-off process, an external force is exerted to induce deformation on the sharp corners. The extensive contact surface guarantees the successful execution of the detachment process. After leaving the surface of the template and retracting the external force, the rebound characteristic of PDMS causes a decrease in the contact area between the PDMS stamp and the target materials. The stamp with the pattern then contacts the target substrate slowly and gently, leaving the materials on the target substrate.

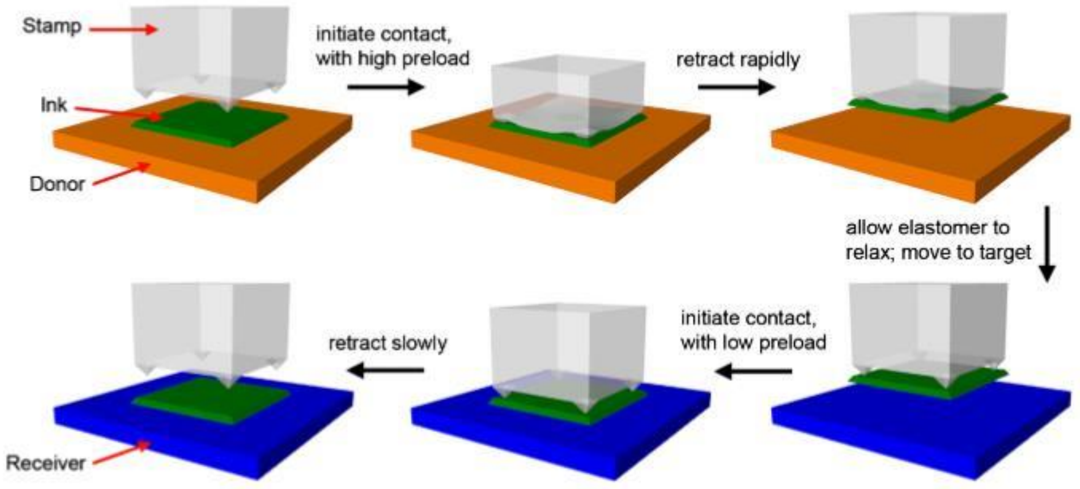

Figure 2.18 Illustration of surface relief structure-assisted nano transfer printing[150].

Apart from the PDMS stamp, many other materials can also be used as stamps to transfer patterns for the fabrication of different flexible electronic devices. PVA is a suitable choice due to its strong adhesion force, dissolvability, flexibility, and biocompatibility[152]. Di and his group reported that metals exhibiting either weak adhesion (such as Cu, Ag, Au) or strong adhesion (such as Pt, Ti, Ni) to the Si substrate can be effortlessly detached from the Si substrate through the utilization of PVA, facilitated by the presence of Graphene[153]. The metal dot array was fabricated by photolithography and electron-beam evaporation. Owing to the high-quality vdW force within the 3D metals and 2D materials, these metal objectives could be successfully moved to 2D material receivers like MoS_2 on a 4-inch wafer scale[154]. The yield could be close to 100%. Compared with direct metal deposition on the 2D material substrates, the transfer process could avoid creating defects caused by high-energy particles during the evaporation process[155]. Using this method, MoS_2 transistors with high and uniform electrical performance could be fabricated (Figure 2.19).

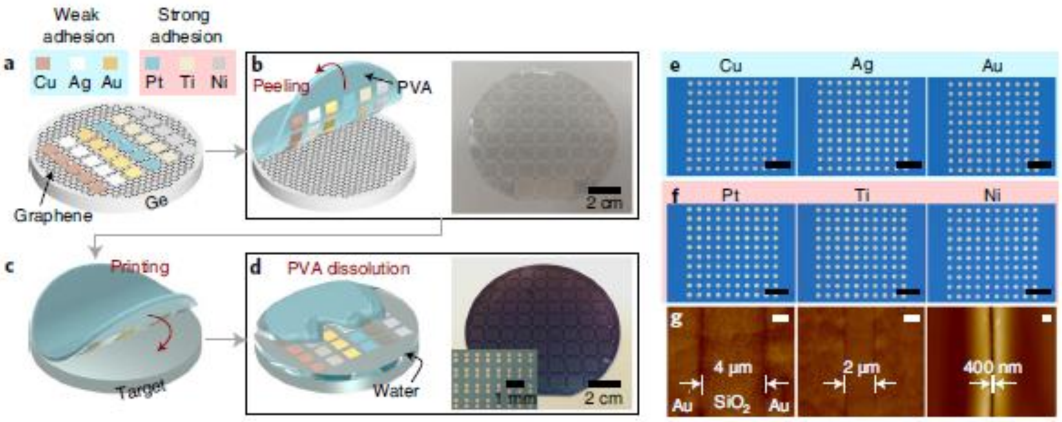

Figure 2.19 Utilizing PVA as glue to transfer various metal patterns with the assistance of graphene[153].

Ice is also a great candidate for transfer printing due to the nature that the adhesion force of ice increases as the temperature decreases[156]. By controlling the environmental temperature and surface wettability, the adhesion force between the target materials and the ice binder can be adjusted to realize the grab and release process of materials (Figure 2.20). This method is extremely suitable for the transfer process of various 2D materials such as MoS_2. One of the advantages of this method is that ice (water) is the only material used in the transfer process, which is highly pure and clean. Therefore, it also has the potential to clean the contamination during the fabrication process.

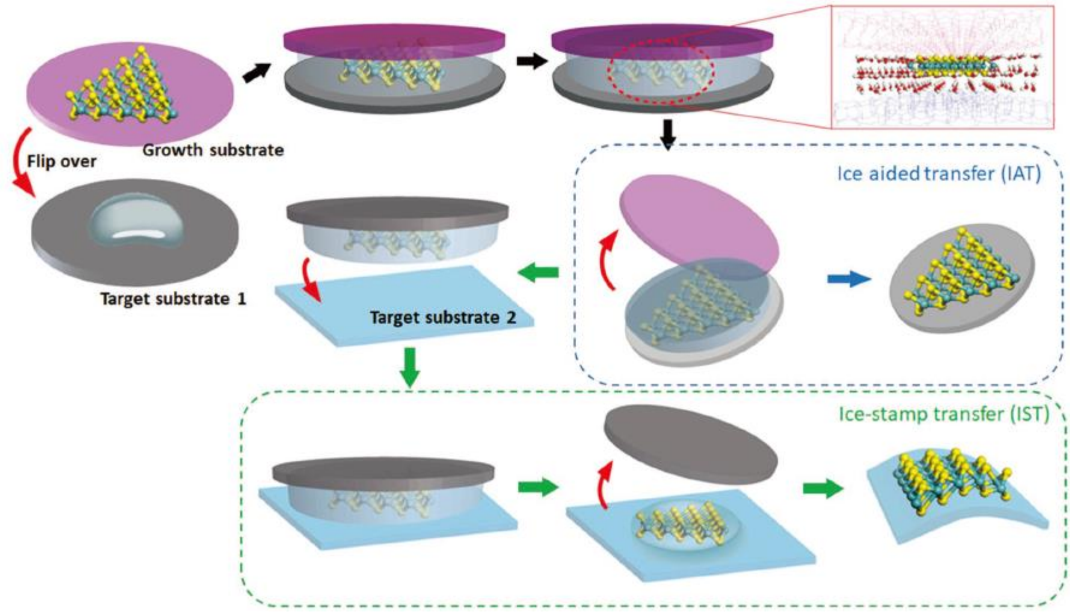

Figure 2.20 Illustration of ice-aided transfer (IAT) and ice-stamp transfer (IST) process[156].

The composite consisting of sugar and corn syrup can also be suitable for the transfer process[157]. Other existing materials or methods introduced before could only be compatible with limited curvatures. Compared with other materials, the sugar mixture has a unique reflow characteristic, which could converse between solid and liquid states freely. This offers better conformability to even nanoscale and complex surfaces as shown in Figure 2.21. It is able to be applied to almost all kinds of substrates including metals, polymers, papers, hydrogels, and even cells. The transfer precision could reach sub-10 nm and enable the transfer of multilayer patterns.

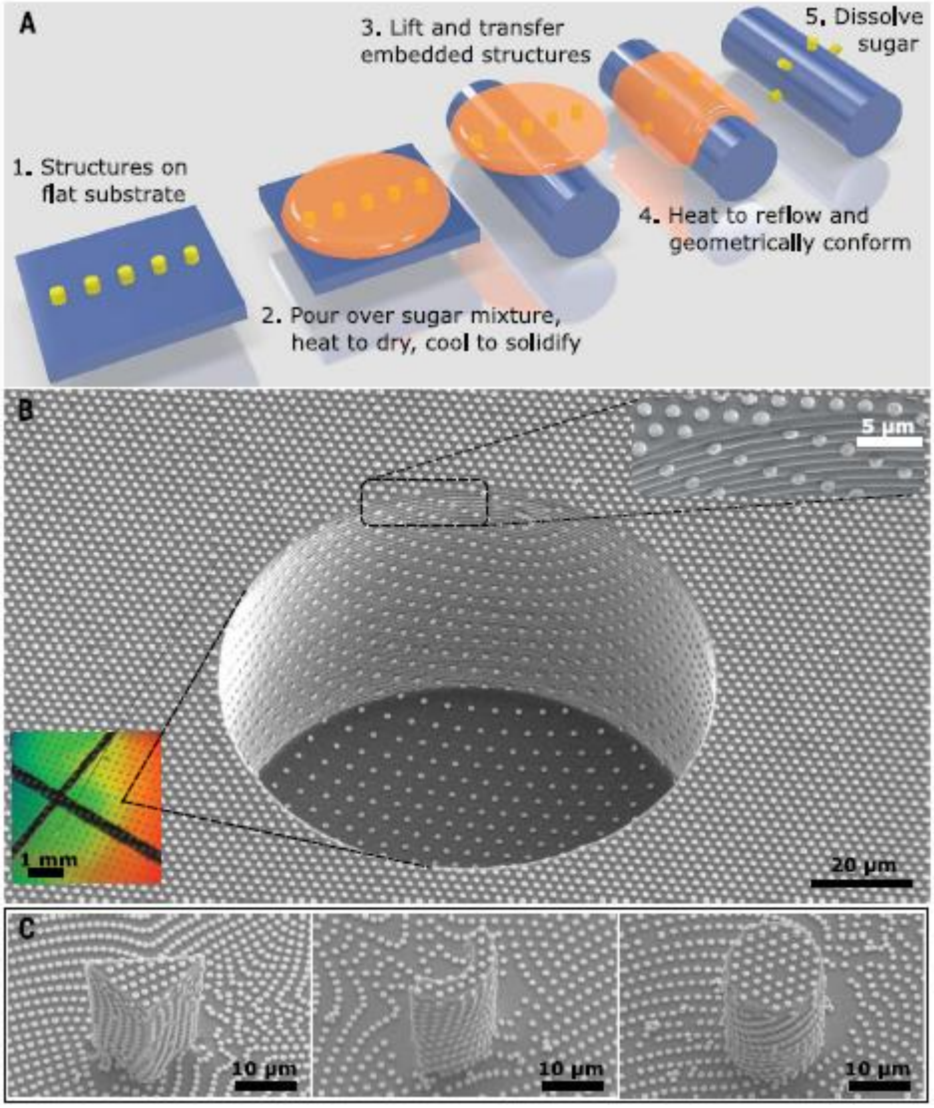

Figure 2.21 (A) Illustration of transfer printing process utilizing sugar mixture. (B-C) SEM images of nanodots array transferred to various 3D surface[157].

2.3.3 Dip-Pen Nanolithography (DPN)

Dip-pen nanolithography (DPN) is a variant of the normal contact printing technique. This new patterning technique, proposed by Prof. Chad A. Mirkin in 1999, uses an atomic force microscope (AFM) tip to write[158]. It utilized the adhesion force from gold-sulfur bonds to directly 'write' patterns on the gold surface. The molecules containing alkanethiol groups were delivered by the capillary force from the AFM tip. The whole machine and process are illustrated in Figure 2.22. Moreover, different kinds of molecules and substrates could be applied in this method, including fluorescent dyes, DNA, and metal salts on substrates of gold, silicon dioxide, gallium arsenide, and more[23, 158-166].

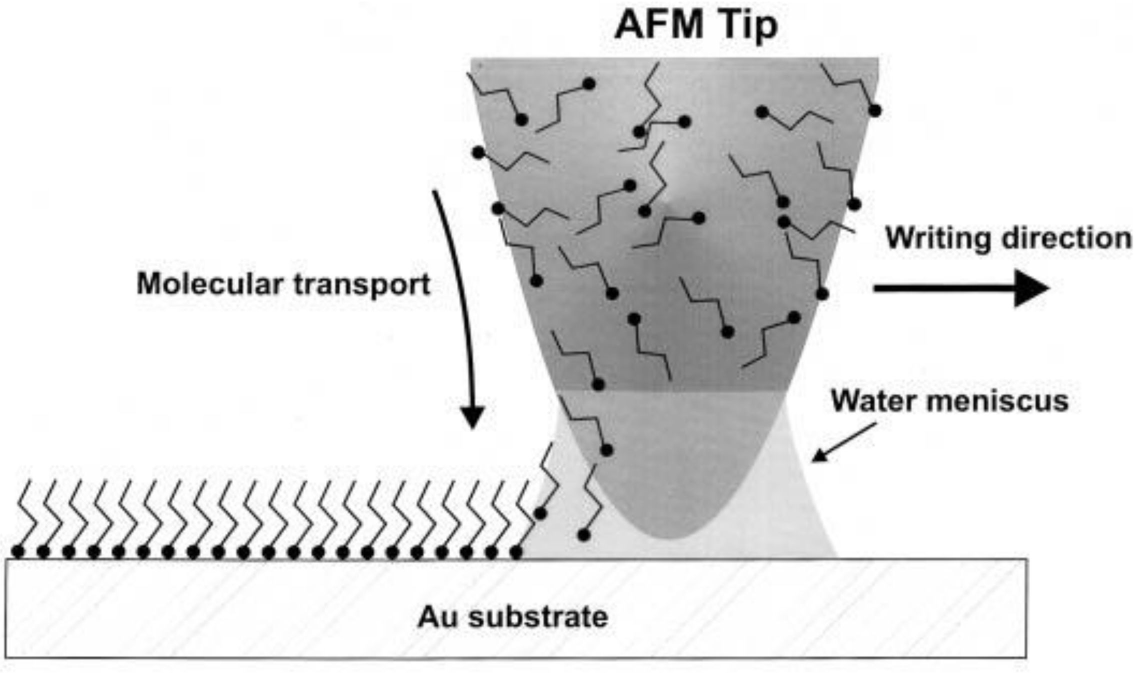

Figure 2.22 Diagram illustration of Dip-pen Nanolithography (DPN)[158].

Unlike conventional patterning techniques, the decisive factor of its resolution is different. The machine or the category of the molecule used will not influence the resolution. The key point is the control of the behaviors of the 'paper' and the 'ink'. These include the kind of substrate which has a specific grain size, the diffusion process which controls the dynamic performance after the contact, the writing and scan speed of the machine, and the process environment such as relative humidity[158]. To date, the resolution of DPN has been successfully improved from the original 30 nm to sub-2 nm, which is no less than photolithography or electron beam lithography[158, 167]. The disadvantages of DPN still lie in the low throughput and high cost. Although high throughput could be primarily realized by a large-scale cantilever array with more than 50000 pens[168], the extremely high cost of the machine still impedes its step to replace traditional patterning techniques.

2.4 3D Printing

3D printing, alternatively referred to as additive manufacturing, is a sophisticated technique that fabricates objects by sequentially depositing layers derived from digital model files. This process employs cohesive substances, such as powdered metal or plastic, functioning as the 'ink' in the construction of the desired object[169-172]. The special part of 3D printing that refers to other patterning techniques is its ability to create spatial, geometric, and complex patterns. As a result, it proves to be a powerful tool in various fields including architecture[173], aerospace[174], dental and medical industries[175], and biomedicine[171].

3D printing is able to be divided into several varieties according to the fabrication model, such as fused deposition modelling, binder jetting, directed energy deposition, powder bed fusion, and sheet lamination. These models can accommodate many materials including metals, polymers, alloys, resins, ceramics, etc[176]. Moreover, 3D printing can construct structures on any substrate, which is a significant advantage in the fabrication of flexible electronics (Figure 2.23).

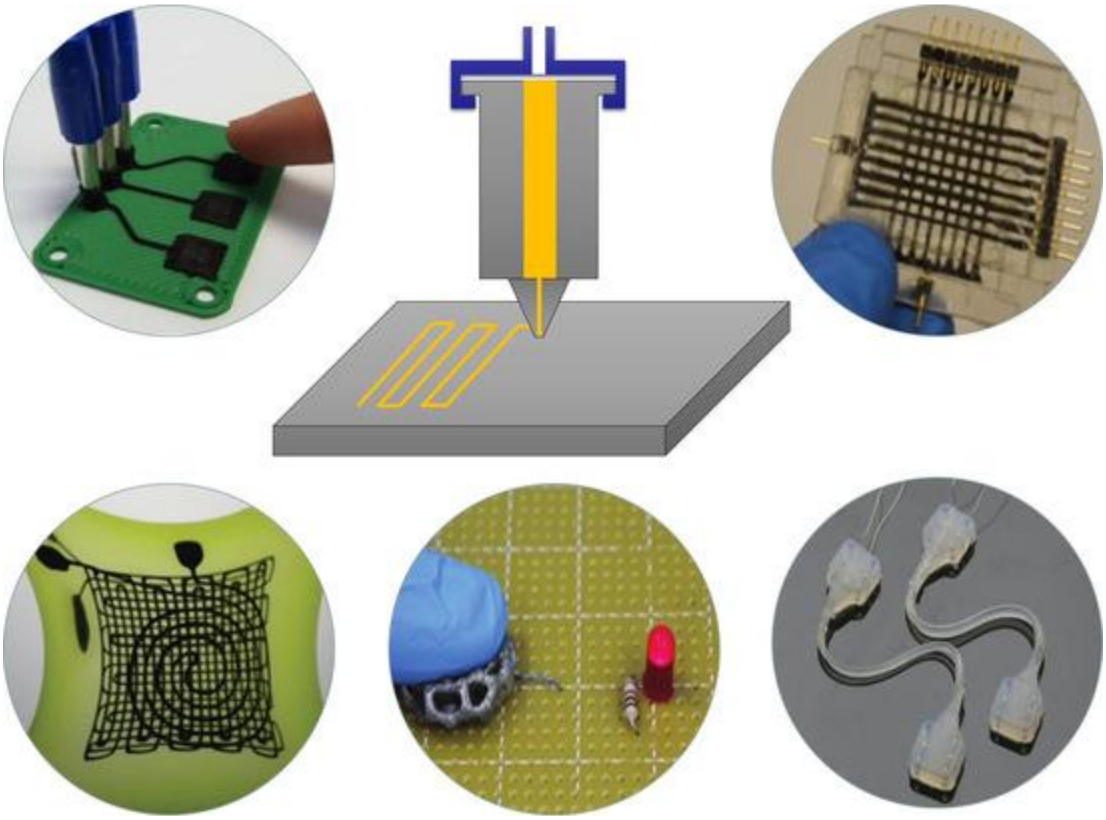

Figure 2.23 3D printing for flexible electronics[177].

Despite its strengths, 3D printing also has several limitations. The resolution of the printed object is constrained by the characteristics of the ink materials used, making it challenging to achieve a high resolution of a few micrometers. Additionally, as 3D printing is a traditional extrusion process, the printing speed is limited, which can hinder achieving a factory-level production rate. Material restrictions and high costs also pose challenges to its development[128, 178-181].

2.5 Electrochemical Replication and Transfer (ERT)

Based on the preceding introduction, it can be inferred that striking a perfect balance between resolution, throughput, and cost remains a challenge for existing techniques. Our team, led by Prof. Zheng Zijian, has proposed a novel patterning technique known as Electrochemical Replication and Transfer (ERT). This technique aims to enhance resolution and throughput while maintaining low costs[26].

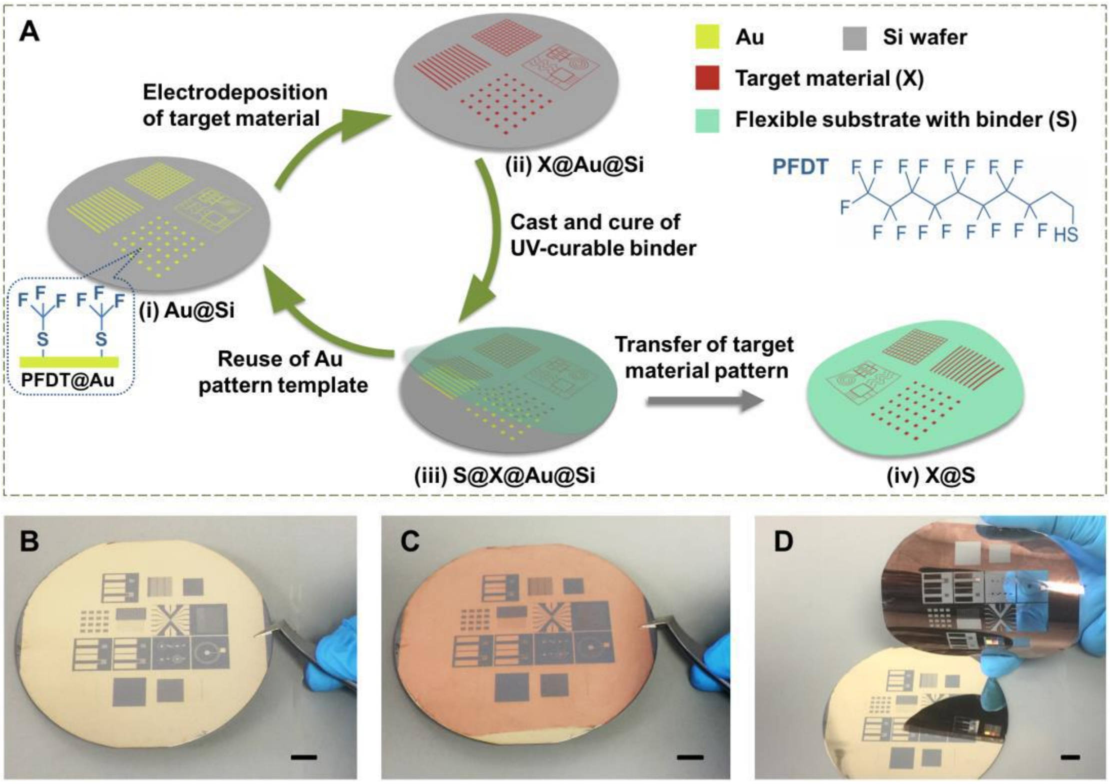

Figure 2.24 (A) Diagram of the manufacturing process of the ERT method. (B-D) Profile display of the process[26].

Figure 2.24 details the entire ERT process. Initially, a silicon template with a gold pattern is manufactured using traditional patterning techniques such as photolithography or electron beam lithography. The pattern on the template consists of a bilayer of Cr (5 nm) and Au (25 nm). The Cr layer serves as a bonding layer, connecting the silicon template and Au pattern, and also functions as a semiconductor layer to facilitate subsequent steps[182]. This template is then immersed in a PFDT solution to form a SAM on the pattern template. The formation process is conducted by the bonding process of the thiol groups at the chain terminals of PFDT and the gold pattern, creating gold-sulfur bonds on the Au surface[183, 184].

Next, the target material, such as Cu, Au, or Ag, is electrodeposited on the pattern area. Since the silicon template is a semiconductor, the target material will not be deposited on the area without patterns. At this point, the target material will not directly adhere to the gold template but will be separated by the monolayer PFDT. Finally, a UV-curable binder (e.g., NOA 63) is cast and cured on the Si surface. The binder layer is approximately 100 μm thick. After peeling off the NOA binder layer, the target materials pattern can be easily removed. Simultaneously, the PFDT layer protects the Au pattern template from being peeled off. This function was validated through a series of experiments, the achievements of which are listed in Figure 2.25.

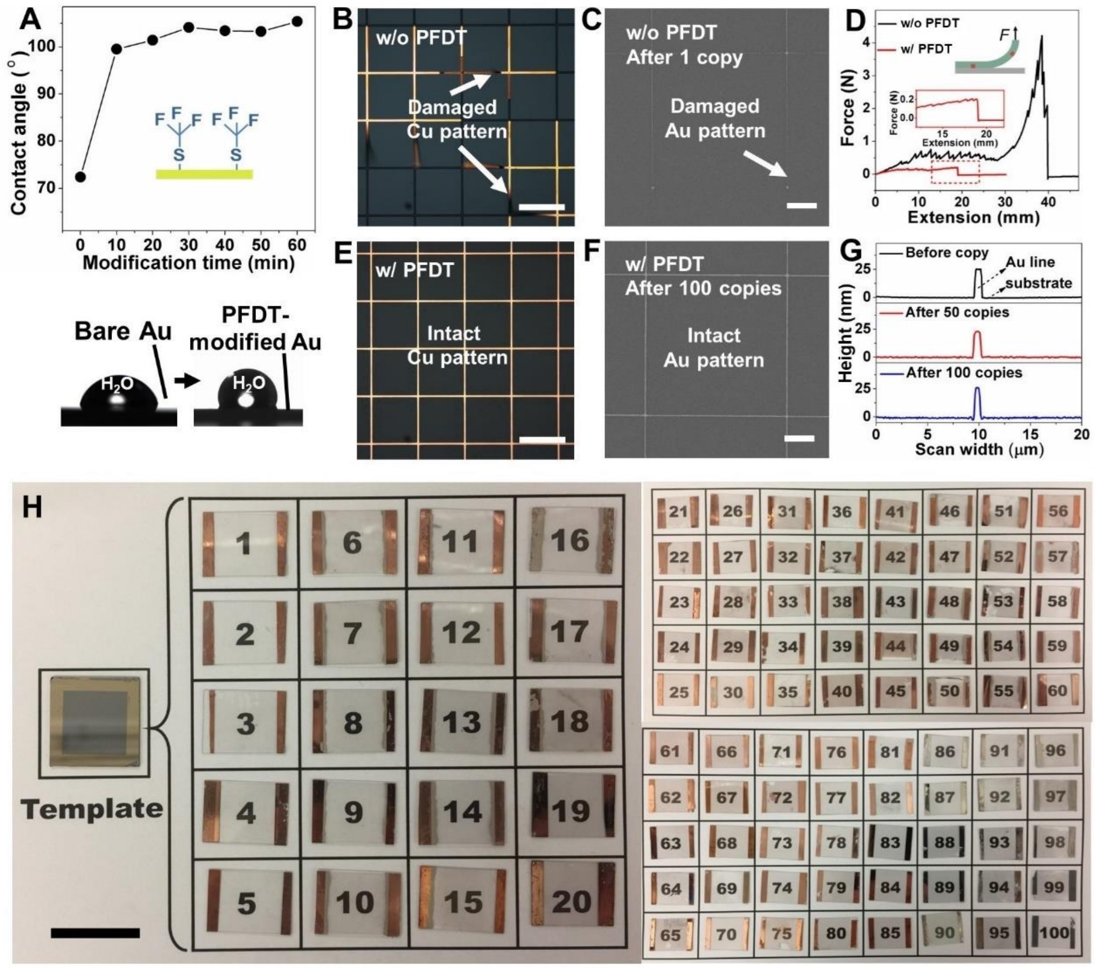

Figure 2.25 Experiments to prove the function of PFDT[26].

Figure 2.25 demonstrates the functionality of PFDT. In Figure 2.25 A, the change in hydrophobicity was tested by the contact angle (CA) of the interface between the template and water droplets. With the successful modification of PFDT, the Au template becomes hydrophobic due to the F terminals at the other side of the monolayer[185, 186]. Figure 2.25 B-G compare the template with and without PFDT modification, including differences in peeling force, the extent of damage to the Au pattern, and the integrity of the target materials pattern. Figure 2.25 H confirms that the template used in this method can be reused more than 100 times without any damage to the gold pattern.

This method is highly versatile for different patterns and materials, provided they can be fabricated by electroplating. Figures 2.26 and 2.27 display various geometric patterns and materials, respectively. The patterns range from a few micrometers, and the materials include metals, metal oxides, polymers, and more.

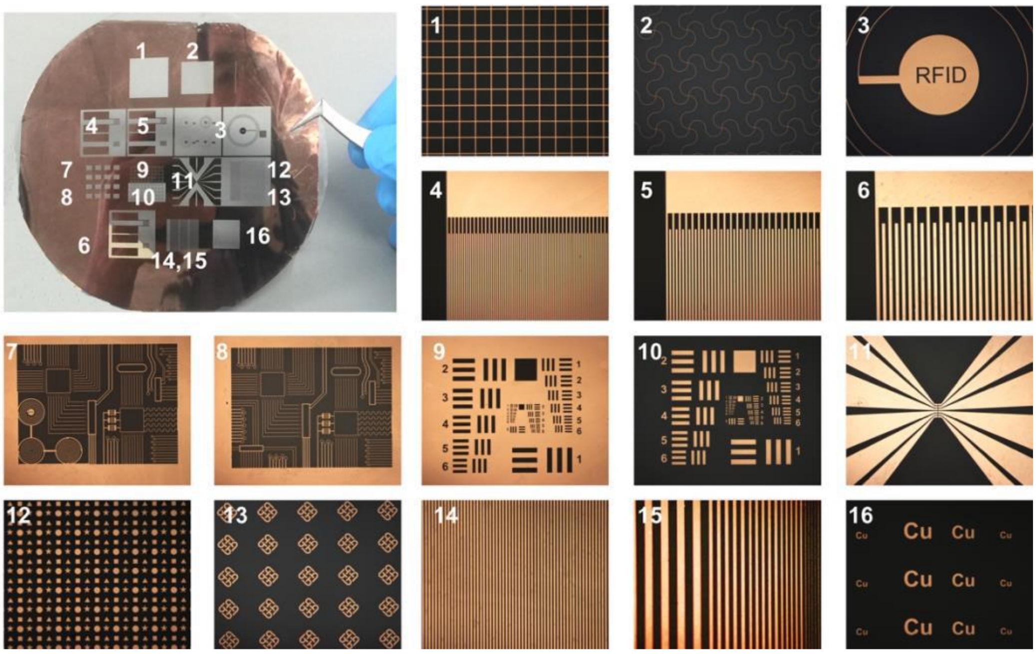

Figure 2.26 Different kinds of patterns fabricated by ERT method[26].

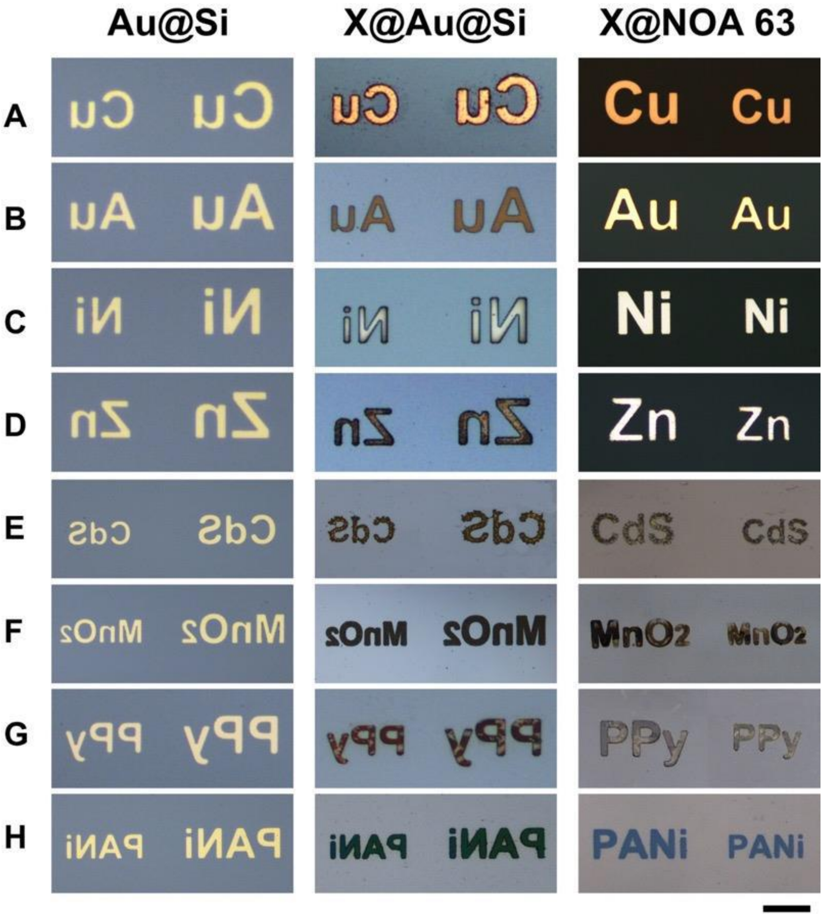

Figure 2.27 Different kinds of materials are deposited and transferred by ERT method[26].

Based on prior research, ERT has been successfully applied to various flexible electronics areas, including flexible transparent electrodes, touch screens, OLEDs, and micro-supercapacitors.

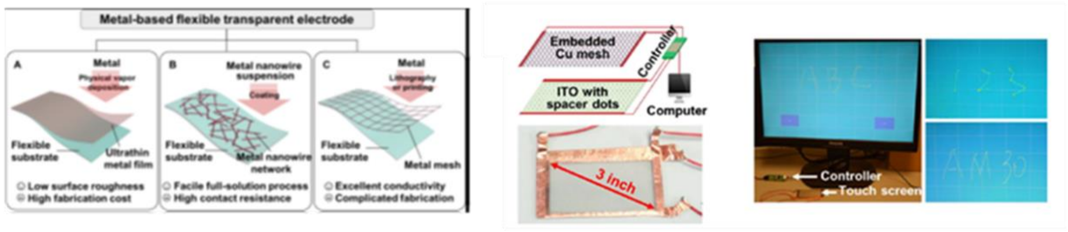

Flexible transparent electrode

Touch screen

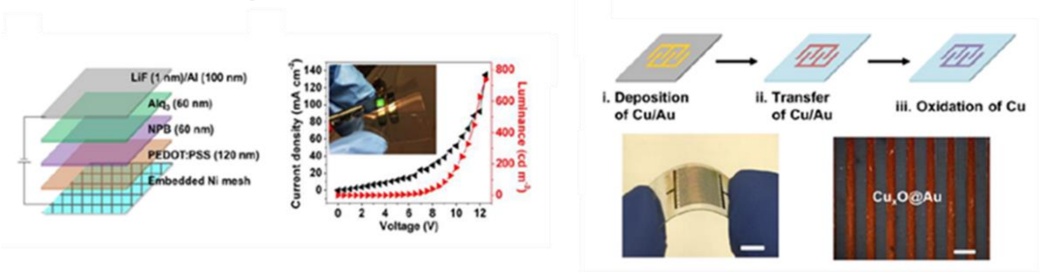

Organic Light-Emitting Diodes

Micro-supercapacitors

Figure 2.28 Applications enabled by ERT[26].

In conclusion, the unique aspect of the ERT method is the use of PFDT molecules to modify the template. Since the resolution of this method is theoretically determined by the original template fabricated by traditional patterning techniques, it can achieve extremely high resolution. Furthermore, PFDT helps protect the template, and the electrodeposition process is simple and quick. Therefore, the throughput of this method is also very high, reaching 10^{-1}-10^{2} m^2/h, and the cost is low due to the reusability of the template.

However, as a novel patterning technique, ERT still has some limitations. First, although various electronic devices, including OLEDs and touch screens, have been successfully fabricated using this method, it remains challenging to apply them to the fabrication of stretchable electronics because of the rigid characteristic of the UV-curable binder NOA used in the transfer process. Second, although theoretically, ERT could fabricate a high-resolution pattern determined by the original template, it is still impossible to increase the resolution to a few nanometers. This is because when the resolution reaches nanometers, the thickness parallel to the plate direction of the Au template will be smaller than the thickness in the vertical direction, which is 30 nm (5 nm Cr and 25 nm Au). This value cannot be reduced due to conductivity restrictions. If the thickness is thinner, it will hinder the electroplating process. Therefore, although PFDT can significantly protect the template, the Au pattern can still be easily damaged during the ERT process when the resolution reaches nanometers. Third, the entire as-deposited pattern is embedded into the binder layer. While this may be advantageous in specific applications that require low surface roughness and can improve the flexibility of electronic devices, it is impossible to construct a 3D structure on flexible substrates for certain applications such as meta-surface, pressure sensors, etc. Lastly, the specific advantages in terms of cost, energy consumption, and other aspects need to be clarified for specific applications.

2.6 Conclusions

The patterning technique plays an important role in the fabrication of flexible electronics. Some typical patterning methods have been proven to be powerful and efficient tools in the fabrication of integrated circuits such as photolithography, electron beam lithography and nanoimprint lithography. However, these patterning techniques are only powerful when fabricating patterns on rigid substrates like silicon wafers because of the rigorous requirements of the environment and substrate. The substrate should be ultra-flat, smooth and clean. It is difficult to fabricate patterns directly on flexible substrates because flexible substrates are often much rougher. They also have some characteristics like being difficult to wet, incompatible with strong solvents, and unstable to thermal annealing, which are indispensable steps in the classic lithography process. Therefore, traditional patterning methods are not preferable for the fabrication of flexible electronics, especially in the aspect of resolution and substrate requirements. Apart from that, the cost is also a problem.

Another big category of patterning techniques, printing methods, have been proven to be efficient in the fabrication of flexible electronics because they are cheap, user-friendly and most importantly, they are easy to fabricate patterns directly on the flexible substrates. Printing methods also have a good compatibility with the roll-to-roll fabrication process which means a high throughput. But they are still not perfect because the resolution of the printing methods is normally in the order of tens of micrometers, which cannot satisfy the needs for making micro- and nano-devices. This is an important problem regarding the miniaturization of the devices.

For newly developed soft lithography like transfer printing and micro-contact printing, although these techniques are advanced and powerful in some situations, they still exist problems such as the stamps are normally soft, which may be easily deformation during the printing process. The diffusion of ink may influence the resolution of the pattern.

Other problems like the capillary pressure of nanofluidic may influence the fluency of printing and it is difficult to control the contact uniformity over a large distance which influences the throughput.

In conclusion, there is still a lack of cost-effective techniques for high-throughput and high-resolution patterning of a wide variety of materials on flexible substrates to date. The proposed ERT method has the great potential to solve this balance problem after overcoming existing technical bottlenecks.

Chapter 3: Methodology

3.1 Materials

Pure gold (Au, 99.999%, China New Metal), pure chromium (Cr, 99.9%, China New Metal, China), doped silicon wafer (Si, <100>, Suzhou Crystal Silicon Electronic & Technology CO., Ltd, China), Si wafer with silicon oxide layer (SiO_2, 30/300/500 nm, Suzhou Crystal Silicon Electronic & Technology CO., Ltd, China), positive photoresist (AZ 5214E, Microchemicals GmbH, Germany), developer for AZ 5214E (AZ 300 MIF, Microchemicals GmbH, Germany), negative photoresist (NR9-1500P, Futurrex, Inc., USA), developer for NR9-1500P (DR6, Futurrex, Inc., USA), Au etchant (Transene Company, Inc.), Cr etchant (Sigma-Aldrich), methyl isobutyl ketone (99.5%, Sigma-Aldrich), acetone (99.9%, Sigma-Aldrich), ethanol (99.5%, Sigma-Aldrich), isopropanol (99.5%, Sigma-Aldrich), 1H,1H,2H,2H-Perfluorodecanethiol (PFDT, 97%, Sigma-Aldrich), commercial copper /gold/nickel/zinc plating solutions (Plug N Plate Cu Solution, Plug N Plate Au Solution, Plug N Plate Ni Solution, Plug N Plate Zn Solution, Caswell Inc., USA), sodium thiosulfate pentahydrate ($Na_2S_2O_3 \cdot 5H_2O$, 99.5%, Sigma-Aldrich), hydrochloric acid (HCl, >37%, Sigma-Aldrich), manganese(II) acetate tetrahydrate ($Mn(CH_3COO)_2 \cdot 4H_2O$, 99%, Sigma-Aldrich), sodium sulfate (Na_2SO_4, 99%, Acros), pyrrole (98%, Sigma-Aldrich), potassium nitrate (KNO_3, 99%, Uni-chem), aniline (99.5%, Acros), sulfuric acid (H_2SO_4, 99%, Sigma-Aldrich), Norland Optical Adhesive 63 (NOA 63, Norland Products Inc., USA) , polyethylene terephthalate (PET, Suzhou Dawan Plastic Electronics Co. Ltd., China), polyvinyl alcohol (PVA, Mw 89,000-8,000, 99+% hydrolyzed, Sigma-Aldrich), hydrogen peroxide 30% (H_2O_2 30%, VWR International, Belgium), ammonium hydroxide solution, ($NH_3 \cdot H_2O$, 28% NH_3 in H_2O, ≥ 99.99% trace metals basis, Sigma-Aldrich). dodecyl triethoxy silane ($C_{18}H_{40}O_3Si$, Nanjing UP Chemical Co. Ltd., China), commercial PDMS membrane (200 μm, 1 mm, BALD advanced materials, China), Ecoflex 00-30 Soft platinum silicone liquid rubber (Bentley Advanced Materials, UK), soda-lime Glass (Kaivo Optoelectronic Technology Co. Ltd., China), glass sample bottle (KAISHIDE, China), poly(vinyl alcohol) 0588 low-viscosity (PVA-205, alcoholysis degree 87.0～89.0 mol/mol, Sigma-Aldrich)

3.2 Fabrication of Templates

3.2.1 Etching Process.

A thin adhesive layer of Cr, measuring 5 nm, and a 25 nm layer of Au were thermally evaporated onto a Si or SiO_2 substrate. The substrate, now layered with Au, was subsequently processed with a positive photoresist AZ 5214, spin-coated at a speed of 4000 revolutions per minute for a duration of 30 seconds, and pre-heated at a temperature of 110 °C for 3 minutes. The photoresist was then exposed to Ultraviolet light through a photomask with a dosage of 40 mJ/cm^2, utilizing a mask aligner (MA6, SUSS MicroTec, Germany), post-baked at 90 d°C for 1 minute, and developed in the

AZ 300 MIF developer for a period of 70-80 seconds. The exposed Au was subsequently etched away in a solution composed of pristine Au etchant and water in a 1:5 ratio for a duration of 60-120 seconds. Following the rinsing of the photoresist in acetone and ethanol and drying with compressed N_2, an Au-pattern template was successfully obtained.

3.2.2 Lift-off Process.

The uncoated Si or SiO_2 substrate was subjected to spin-coating with negative photoresist NR9-1500P at a speed of 4000 revolutions per minute for a duration of 40 seconds, pre-baked at a temperature of 155 °C for 1 minute, exposed to ultraviolet light with a dosage of 170 mJ/cm^2 using the mask aligner MA6, post-baked at 105 °C for 3 minutes, and developed in the DR6 developer for a period of 10-15 seconds. Following the cleaning of the wafer in deionized water and drying it with flowing N_2, a thin adhesive Cr layer of 5 nm and a 25 nm Au layer were thermally evaporated onto either a Si or SiO_2 substrate on the photoresist-patterned substrate. The photoresist and any superfluous deposited metals were subsequently removed with acetone and ethanol.

3.2.3 Interference Lithography (IL).

A Silicon wafer, featuring a SiO_2 substrate of 30 nm thickness, underwent a treatment process using oxygen plasma (Harrick Plasma Cleaner, USA) for a duration of five minutes. Subsequently, the substrate was subjected to spin-coating with an 800-nm-thick layer of positive photoresist AZ MiR 701 at a speed of 3000 revolutions per minute, followed by a pre-baking process at 90 °C for 60 seconds. The sample was then exposed to a homemade interference lithography system (HIL-1000, InterLitho Technology Limited, Hong Kong SAR) utilizing a 405-nm laser. After a post-heating process at 110 °C for 60 seconds, the photoresist was developed in the AZ 726 MIF developer for 60 seconds and thoroughly cleaned with deionized water, resulting in gratings with a 700 nm period and a 200 nm linewidth. Utilizing the photoresist pattern as the etching mask, the underlying SiO_2 layer was directly etched using inductively coupled plasma reactive ion etching (ICP-RIE, Trion Phantom III, USA) with CF_4 gas at a flow rate of 40 sccm, an ICP power of 1500W, an RIE power of 32W, and an etching time of 30 seconds. Following the application of a thin adhesive Cr layer of 5 nm and a 25 nm Au layer to either a Si or SiO_2 substrate via thermal evaporation, a lift-off process was conducted with ultrasonic cleaning in RCA-1 solution ($NH_3 \cdot H_2O$: H_2O_2: H_2O = 1:1:5) at 80 °C for 3 minutes, resulting in a substrate with a periodic SiO_2/Au pattern.

3.2.4 3D-ERT Template.

To create patterns, the photolithography process was initially implemented on a bare SiO_2/Si substrate, adhering to the procedures outlined in sections 3.2.1 and 3.2.2. Subsequently, a 50-nm-thick Cr layer was deposited onto the photoresist-patterned substrate via thermal evaporation. The photoresist and any superfluous deposited metals were eliminated using acetone and ethanol, leaving the Cr pattern to serve as the mask for the dry etching process. The SiO_2 and Si layers were sequentially etched using ICP-

RIE, with CF_4 gas employed for SiO_2 and SF_6 gas for Si. Following the dry etching process, the residual Cr mask was removed using a Cr etching solution, and the 3D-ERT template was obtained after rinsing with deionized water and drying with compressed N_2.

3.3 Modified ERT Process

3.3.1 ERT with NOA Binder.

The freshly fabricated Au-patterned template was submerged in a 5 mM PFDT ethanol solution for a duration of 10-15 minutes to facilitate the formation of a SAM on the Au surface. The electrodeposition process was conducted using either a two-electrode setup on a source meter (Keithley 2400, Tektronix, Inc., USA) or a three-electrode setup on an electrochemical workstation (CHI 600e, CH Instruments, Inc., China). The SAM-modified Au-patterned template served as the working electrode in the electrochemical deposition, with the counter electrode being either a dissolvable pure target material or noble Pt foil. Following deposition, Norland Optical Adhesive 63 was cast on the template and cured under 365 nm Ultraviolet light with a dosage exceeding 4,500 mJ/cm^2. A transparent Polyethylene Terephthalate (PET) layer was applied on top before curing to assist in the removal of the target material pattern from the template. After transfer, the Au-patterned template was rinsed with deionized water and ethanol for reuse.

3.3.2 2D ERT with PVA Binder.

After electrodeposition, a PVA solution was poured onto the template surface and dried at 80 °C for 20 min. The PVA binder layer with metal pattern embedded into it was then detached from the template and attached to the receiver substrate immediately. At last, the PVA layer was dissolved by being immersed in deionized water for at least two hours to leave the pattern on the surface of the receiver substrate.

3.3.3 3D ERT with NOA Binder.

The freshly fabricated 3D-ERT template was submerged in a 20% dodecyl triethoxysilane solution for around ten to twelve minutes to create a molecular surface on the exposed Si surface. The Si template was then heated at 120 °C for 15 min and washed with ethanol before being used in the electroplating process, which followed the same steps as in 2D ERT.

3.4 Fabrication of Devices

Fabrication of stretchable micro-supercapacitors. To fabricate stretchable micro-supercapacitors, an interdigital electrode pattern was fabricated by consecutively depositing Au for 10 minutes and Cu for 5 minutes using a current density of 1 mA cm^{-2}. The Au layer served as a current collector. The whole device was transferred to a pre-stretched PDMS substrate together, which formed buckles on the PDMS surface after releasing the pre-strain. The device was then treated with oxygen plasma for five minutes. The Cu was oxidized to CuO_x, which served as active material. Finally, the electrolyte (20 wt.% LiCl and 10% wt.% PVA in H_2O) was cast on the surface of the interdigital electrode directly for an electrochemical test.

Fabrication of flexible transparent heater. For the fabrication of a flexible transparent heater, a 3D Cu mesh pattern was fabricated by the 3D-ERT method and served as the heating electrodes. The line width was 10 μm and the line gap was 200 μm. The height of the mesh pattern was 10 μm. Both sides of the transparent electrode were affixed with conductive copper tape as the two electrodes of the transparent heater. Then the whole transparent electrode was encapsulated by another layer of NOA 63 binder and cured with UV emission.

Fabrication of flexible TENG-based pressure sensors. To fabricate flexible TENG-based pressure sensors, a Cu-PDMS-Cu sandwich construction was used. The bottom layer of Cu consisted of a 3D circle dots array with different resolutions and heights fabricated by the 3D-ERT method and served as both an electrode and a friction material that encountered the middle PDMS layer. The top layer of Cu functioned as an electrode. The middle layer of PDMS was spin-coated on the surface of the top Cu layer with a rotating speed of 2000 rpm. The thickness of the PDMS is around 50 μm.

Fabrication of electronic bandage. The electronic bandage composed of three parts including the TENG power source, the interdigital electrode and the encapsulation layer. For the TENG layer, 8 g PEO is mixed with 92 mL deionized water and stirred at room temperature for 12 hours to form an 8%W/w PEO solution. Then 10mL PEO solution is poured onto a silicon wafer and spin-coated at 300 rpm for 1min. The silicon wafer is then baked at 80 °C for 10 min to form the PEO membrane. 5 g EC is mixed with 95 mL ethanol and stirred at room temperature for 12 hours to form a 5%W/w EC solution. Then 10mL EC solution is poured onto a silicon wafer and spin-coated at 300 rpm for 1min. The silicon wafer is then baked at 40 °C for 10 min to form the EC membrane. The conductive Cu layer was thermal evaporated on the PEO and EC membrane. Then, these two TENG electrodes were separated and connected by a PDMS framework. The Au interdigital electrode was fabricated by ERT while the encapsulation layer was fabricated by electrospinning.

3.5 Characterization Methods

Optical microscopic (OM): Optical pictures were captured using an optical microscope (Eclipse 80i, Nikon, Japan) with magnifications from 50× to 1000×.

Scanning electron microscopy (SEM): SEM images were acquired on a Field Emission Scanning Electron Microscope (FE-SEM, MAIA3, TESCAN, Czech Republic), Scanning Electron Microscope (SEM, VEGA3, TESCAN, Czech Republic) and Field Emission Scanning Electron Microscope (FE-SEM, MIRA, TESCAN, Czech Republic) with an Energy Dispersive Spectrometer (EDS, Oxford Instruments).

Atom force microscope (AFM): AFM images were obtained through AFM (XE-100, Park Systems, Korea) and characterized the topography (line width, thickness, 3D view morphology, and surface roughness) of patterns.

X-ray diffraction (XRD): XRD patterns were obtained using an X-ray diffractometer (Rigaku SmartLab 9 kW, Japan) with a Cu Kα X-ray source.

Surface Profiler: The surface topography of the samples was tested by a Surface Profiler machine (Bruker DektakXT).

Optical Surface Profiler: The optical surface topography of the samples was tested by an Optical 3D surface Profiler (TopMap Metro. Lab).

Contact angle (CA): CA images were obtained through an optical contact angle measuring device (SDC-350, Dynetech, Inc., China) using a DI water droplet.

Sheet resistance (R_s): R_s was measured by the four-probe method with a source meter (Keithley 2400 SourceMeter, Tektronix, Inc., USA).

Optical transmittance (T): Transparency was recorded on a UV-vis spectrometer (Cary 300, Varian, USA) with a wavelength from 340 nm to 800 nm.

Bending Tests: The flexibility of the devices was conducted on a stepper motor linear stage (TSA50-C, Zolix, China).

Infrared (IR): The IR images were mapped by an IR camera (E4, FLIR, USA).

Electrochemical Performance: The electrochemical performance of the micro-supercapacitor was characterized on an electrochemical workstation (CHI 600e, CH Instruments, Inc., China).

Electrocardiogram (ECG): The ECG results were recorded by replacing one of the electrodes of a commercial ECG device (BMD101, SICHIRAY, China).

Resistance of the conductors: The change of resistance was tested by a source meter (Keithley 2400 SourceMeter, Tektronix, Inc., USA).

Performance of TENG-based pressure sensors: The output of voltage and current were characterized by a source meter (Keithley 2400 SourceMeter, Tektronix, Inc., USA).

Digital images: Photos were taken with a commercialized single-lens reflex camera (D7200, Nikon, Japan).

Chapter 4: SiO_2-Protecting Structure Template for Nanoscale Pattern in ERT

This chapter proposes a template that uses SiO_2 as a protecting layer based on the original ERT template. This protecting layer almost eliminates the adhesion force on the Au template and the electrodeposited materials interface, preventing the Au template from being damaged during the creation of nanoscale patterns. Various patterns with sizes ranging from sub-100 nm to several cm are presented to demonstrate the feasibility of this SiO_2-protecting structure template for both micro and nano-scale patterns. The adaptability of isolated patterns, various materials including metals, oxides, and polymers, and large-scale fabrication are also proven.

4.1 Introduction

Fabrication of patterns and structures with a high resolution reaching sub-100 nm or even a few nanometers are an essential part of nanotechnology. For traditional chip fabrication, the reduction in the feature scale of the electronics could greatly improve the performance of device. Higher resolution often means more electronic components per unit area which could enhance the performance of the whole electronic devices[187]. It could also be applied to various emerging nanotechnologies including biosensors[188], plasmonic areas[189], nanoelectronics[190], nano energy[191], metasurface[192], and so on.

For the original template used in ERT, the protection of PFDT is efficient for the fabrication of microscale patterns based on previous experimental results. This conclusion could be expressed by a simple equation (4.1) as shown below:

$$F_P < F_A \tag{4.1}$$

F_P is the peeling force which is the force between the Au template and the electrodeposited target materials while F_A represents the adhesion force which relates to the interface between the Au template and the Si wafer.

Since the peeling force is great smaller than the adhesion force for microscale pattern fabrication, the electrodeposited pattern could be peeled off without damaging the Au template. These two forces could be further explained by equations (4.2) and (4.3):

$$F_P = F_0 \times \left(S_{up} + S_{side}\right) \tag{4.2}$$

$$F_A = F_1 \times S_{down} \tag{4.3}$$

F_0: Peeling force per unit area, F_1: Adhesion force per unit area, S_{up}: Upper surface area of the Au template, S_{side}: Lateral area of the Au template, S_{down}: Down surface area of the Au template, $S_{up} = S_{down}$.

As shown in Figure 4.1 (A), the electrodeposited materials will cover the top and lateral cover of the Au template. Since the area of the up surface is the same as the down surface, the contact interface of the peeling force is bigger than that of the adhesion force. Consequently, we could derive that:

$$F_0 < F_1 \tag{4.4}$$

For the fabrication of the microscale pattern, since the Au template is only 30 nm, the area of the upper surface is far larger than the lateral part as drawn in Figure 4.1 (B). In this situation, the factor of the force per unit area will count more compared to equation (4.2) with (4.3). Therefore, the peeling force is smaller than the adhesion force based on experiment results. However, when the pattern goes down to the nanoscale, that is, smaller than 30 nm, the acreage of the upper area will be far less than the lateral area as drawn in Figure 4.1 (C). For this situation, the area factor in equations (4.2) and (4.3) will count more. Therefore, the peeling force may exceed the adhesion force based on previous experiment results, which causes damage to the Au template.

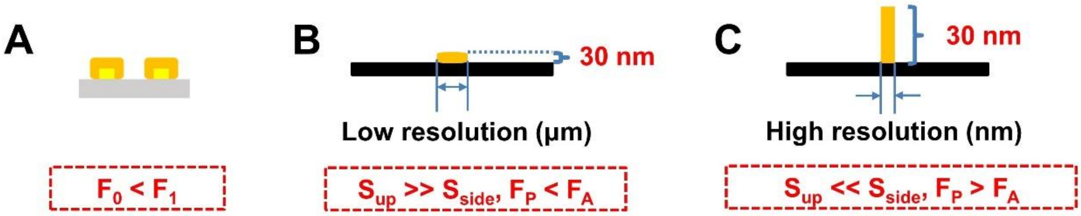

Figure 4.1 Illustration of the research gap for the original structure template. (A) Illustration of the template after electrodeposition of target materials. (B) Microscale Au template. (C) Nanoscale Au template.

One of the advantages of ERT is the reuse of a template for the electroplating process, which reduces the total cost of fabrication. The protection of templates is the key point for this technology. Therefore, it is crucial to solve the problem of damaging the Au template for the fabrication of nanoscale patterns.

Furthermore, another problem for the original ERT template is the poor selectivity of the electrodeposition of target materials on the Au pattern and Si substrate. Since Si is a semiconductor, it is still conductive, especially under high current density and long deposition time. The unpatterned area, which is the Si wafer without the Au layer, may also appear in some target materials which causes the failure of pattern replication.

4.2 Illustration of SiO_2-Protecting Structure Template

Based on the comparison between peeling force and adhesion force, reducing the lateral area of the Au template can be effective in decreasing the peeling force between the target materials and the Au template. By making F_0 smaller than F_1, the adhesion force can be made larger than the peeling force, since the connection area remains the same. To achieve this, a new template has been designed with an additional insulating SiO_2 protecting layer. The entire fabrication process is illustrated in Figure 4.2. Instead of using a normal Si wafer, a Si wafer covered by a 30 nm SiO_2 layer is used for the replication template. Conventional patterning technologies are used to generate patterns on the SiO_2/Si wafer. The patterned area of SiO_2 was then etched by the drying etch method such as inductively coupled plasma reactive ion etching (ICP-RIE). The ICP power is 1500W while the RIE power is 32 W, and the etching time is 30 seconds.

After that, aa thin adhesive layer of Cr, measuring 5 nm, and a 25 nm layer of Au were thermally evaporated. The photoresist layer and extra Au can be lifted off using various organic solvents such as acetone. Through this process, the Au pattern is embedded in the SiO_2 layer. During the following ERT process, the target materials will only be electroplated onto the upper area of the Au pattern. The SiO_2 layer greatly reduces the contact interface between the target materials and the Au template. The connection area remains the same in this situation, and the adhesion force will always be larger than the peeling force, regardless of resolution.

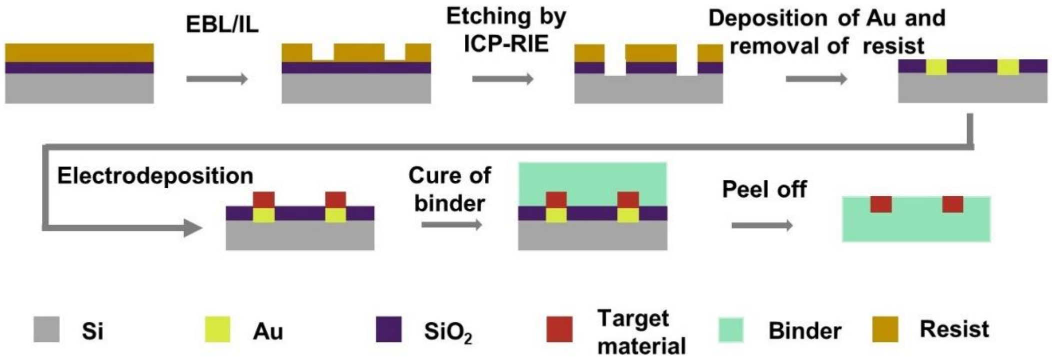

Figure 4.2 Illustration for the manufacturing process of target materials patterns using SiO2-protecting structure template.

4.3 Characterization of the Template

The surface of an Au template with a SiO2-protecting structure was characterized by AFM testing. The Au pattern is composed of parallel lines with a width of around 550 nm and a gap of 150 nm (Figure 4.3 A). As shown in Figure 4.3 (B), the surface of the Au template was almost flat, with only a slight difference in height of around 1-2 nm observed between the Au pattern and SiO2 substrate. This difference can be attributed to errors during the thermal evaporation process and is unavoidable.

The Au template was almost entirely embedded into the SiO2 layer, resulting in a great reduction in the exposed areas. For the original structure, the surface roughness of the template was also reduced, reaching a root mean square roughness (R_q) of only 1.616 nm according to the AFM results. Additional data related to surface roughness can be found in Table 4.1 below.

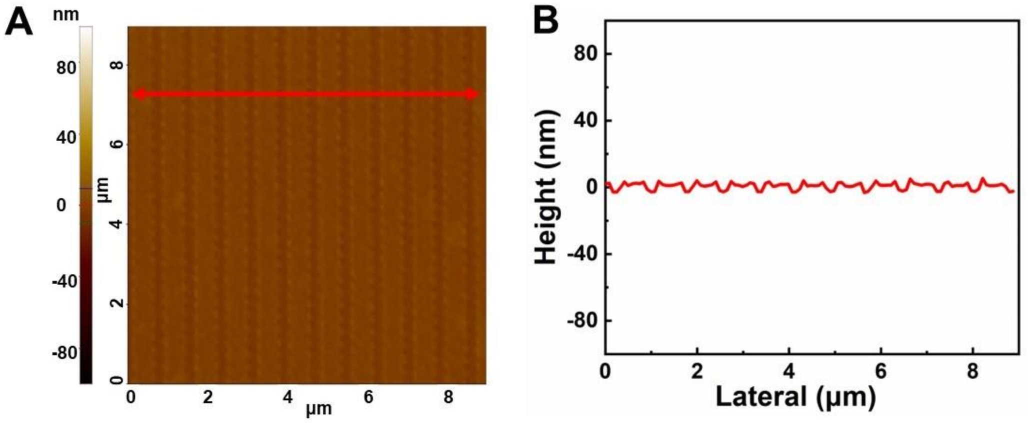

Figure 4.3 Characterization of SiO_2-protecting structure template. (A) AFM result of the Au template of lines pattern with around 550 nm width and 150 nm gap. (B) Surface profiler results of the red line in Figure 4.3 A.

Table 4.1 The surface roughness of the nano grating template characterized by AFM.

	R_{pv} (nm)	**R_q (nm)**	**R_a (nm)**	**R_z (nm)**	**R_{sk} (nm)**	**R_{ku} (nm)**
Nano lines pattern	11.259	1.616	1.283	10.468	0.031	2.973

R_{pv}: Peak-to-valley roughness; **R_q**: Root means square roughness; **R_a**: Average roughness; **R_z**: Maximum height of profile; **R_{sk}**: Skewness; **R_{ku}**: Kurtosis.

4.4 Fabrication of Micro-scale Pattern

4.4.1 Fabrication of Various Kinds of Patterns

The SiO_2-protecting structure template remains suitable for the application of micro-scale patterns. The entire process of the template fabrication is well-suited for scale-up production, as the dry etching process and thermal evaporation process are consistent and uniform. As shown in Figure 4.4, a large-scale Cu pattern up to a 4-inch scale was successfully fabricated using a single template. The deposition time was 5 minutes, and the current density was 1 mA cm^{-2}. The entire pattern was replicated without any breaks. Since the Au template is directly connected to the Si wafer, the conductivity of the entire template is not affected by the insulating SiO_2 layer. Therefore, it remains suitable for the fabrication of both continuous and isolated patterns. Figure 4.5 displays optical images of various patterns, including angular (A), lines (B-D), dots (E), connections (F-G), and arcs (H-I), ranging from 1 μm to several mm. These patterns correspond to the areas marked in Figure 4.4.

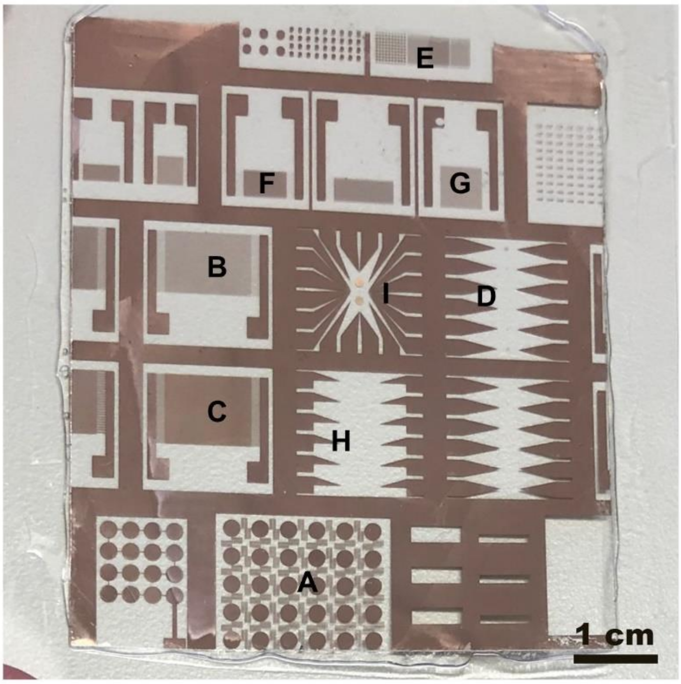

Figure 4.4 Photo of a 4-inch scale pattern fabricated using a SiO_2-protecting structure template at one time.

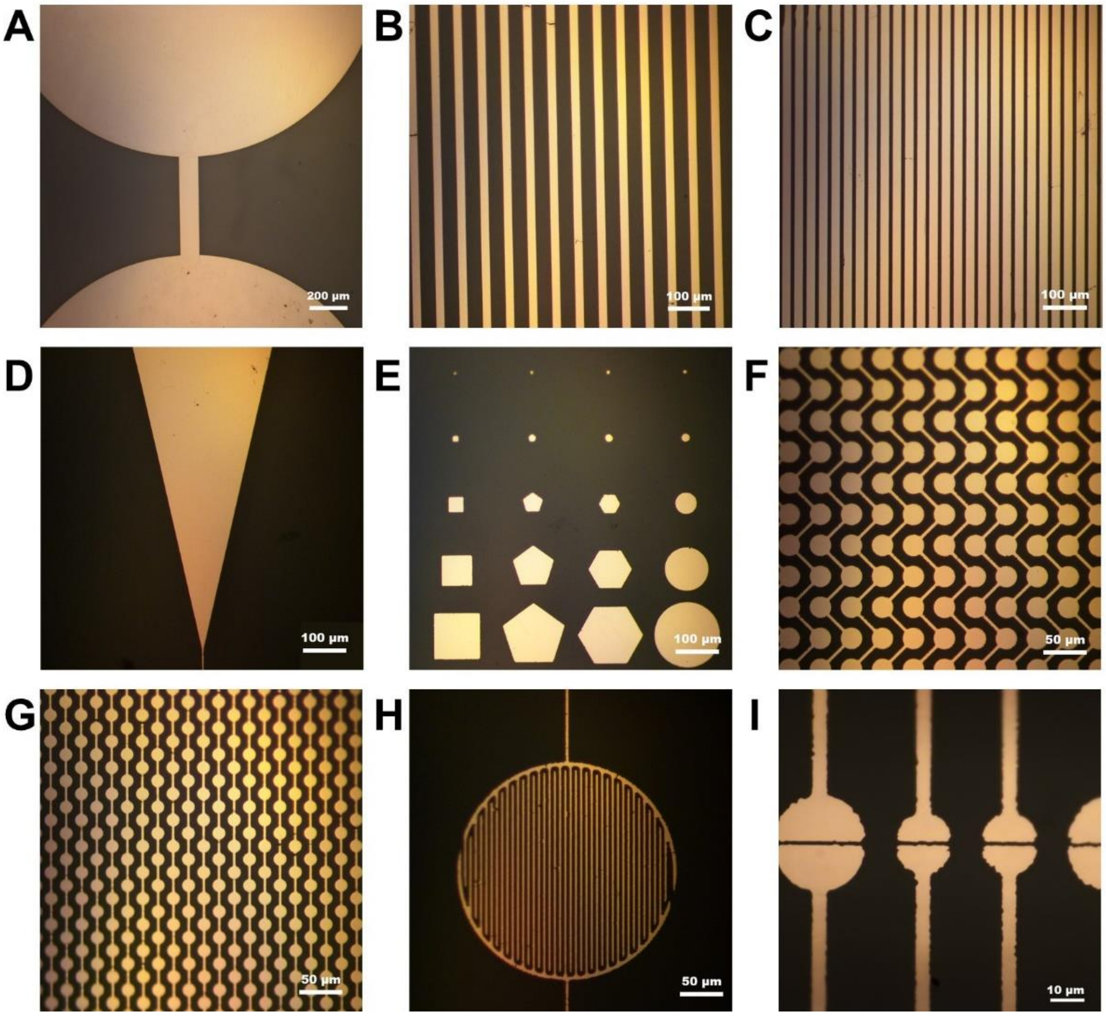

Figure 4.5 Optical images of various Cu patterns fabricated using SiO_2-protecting structure template.

4.4.2 Fabrication of Various Materials

The SiO_2-protecting structure template is also suitable for the fabrication of patterns with different materials. Here we demonstrated the fabrication of Cu, Au and Ni square dot patterns. The deposition time is 5 minutes, and the current density is 1 mA cm^{-2}. The whole pattern was unbroken as shown in the optical image no matter what kind of material it is (Figure 4.6 A-C). The relative XRD results also prove the successful deposition of these materials (Figure 4.6 D-F).

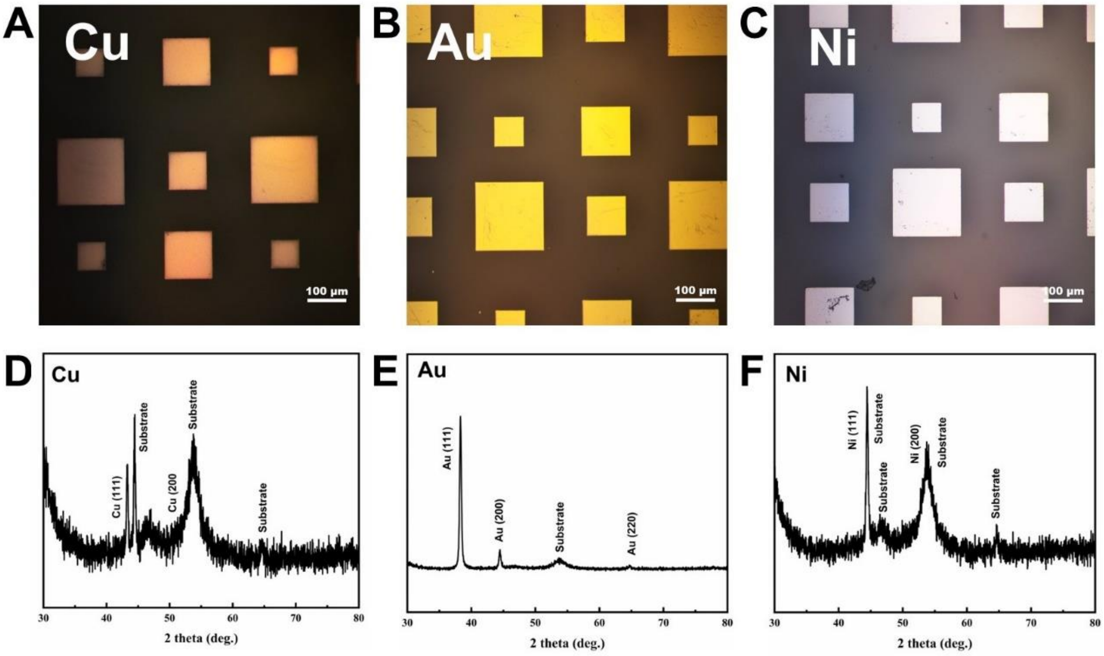

Figure 4.6 Fabrication of micro-scale patterns using various materials. Optical images of (A) Cu, (B) Au, (C) Ni square dots array. Corresponding XRD characterization results of (D) Cu, (E) Au, (F) Ni.

4.5 Fabrication of Nano-scale Pattern

For traditional nanolithography methods such as EBL, the throughput is very low due to the direct writing model. This problem could be fixed by ERT. ERT can replicate an extensive nanoscale pattern in a brief period. Here a large-scale (1.2 cm × 2 cm) nano-grating pattern was fabricated by interference lithography (IL) (Figure 4.7 A). The SEM pictures of the Au pattern is depicted in Figure 4.7 (B). The Cu grating pattern could be fabricated using this template. In a normal environment, it shows the color of the metal. Upon the irradiation of white light, the grating pattern shows various colors which proves the successful fabrication of the grating pattern.

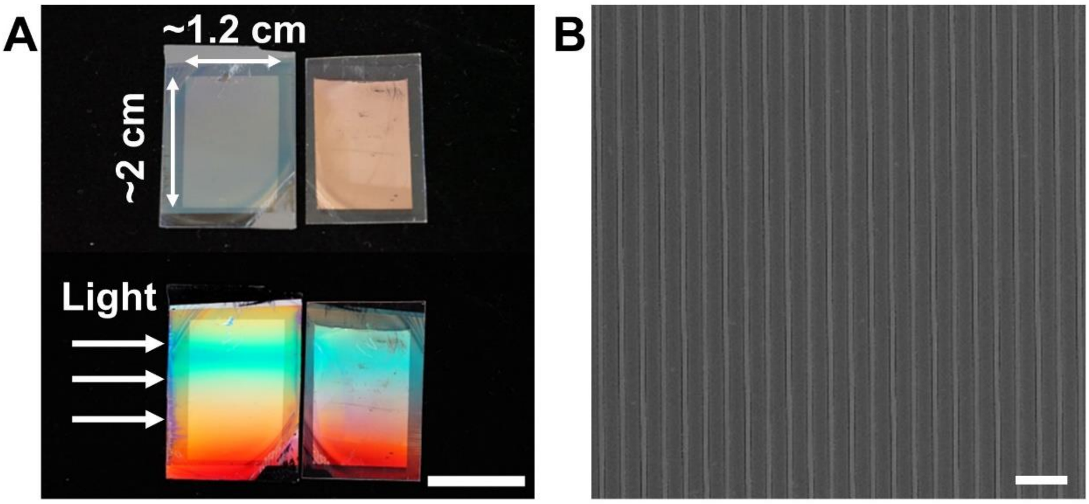

Figure 4.7 Fabrication of a nanoscale grating pattern with large-area (2 cm × 1.2 cm). (A) Photo of the nano-template and the Cu pattern transferred to PER substrate. Up: Normal environment. Down: Under white light irradiation. Scale bar: 1cm. (B) SEM image of the Au template. Scale bar: 2 μm.

Figure 4.8 reveals the optical images and SEM pictures with different magnifications of the Au template (Column A) and the Cu pattern (Column B) replicated from it. The line width of the grating pattern is around 550 nm, and the gap is around 150 nm. After the electrochemical deposition process, the line width of the Cu line pattern is around 600 nm. The deposition time is 30 seconds, and the current density is 1 mA cm^{-2}. The alteration in the line width can be ascribed to the isotropic expansion inherent in the electroplating process. No matter whether at low or high magnification, both the Au template and the Cu pattern do not show any defect. It proves the successful fabrication and transfer of using the SiO_2-protecting ERT template. The related EDX mapping are showcased in Figure 4.9 (Column A: The Au template; Column B: The Cu pattern). For the EDX result of the Cu pattern, the Au element came from the Au sputtered during the test process. The transfer process itself did not damage the Au template. The Au element for the template and the Cu element for the fabricated pattern show high conformity with the pattern. The S element came from the NOA binder layer.

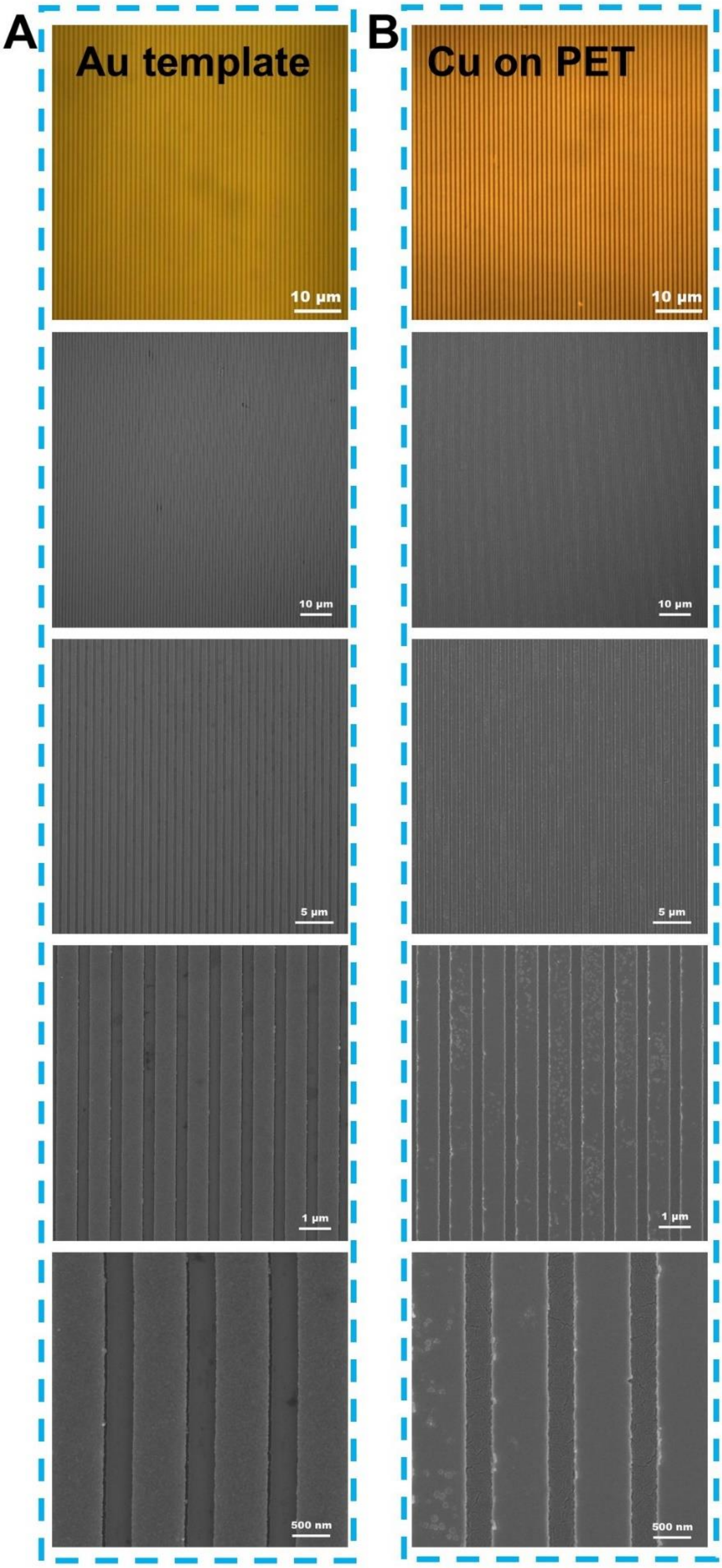

Figure 4.8 Optical images and SEM pictures under different magnifications of (A) the

Au template with nano grating pattern, and (B) the Cu pattern transferred to a PET substrate.

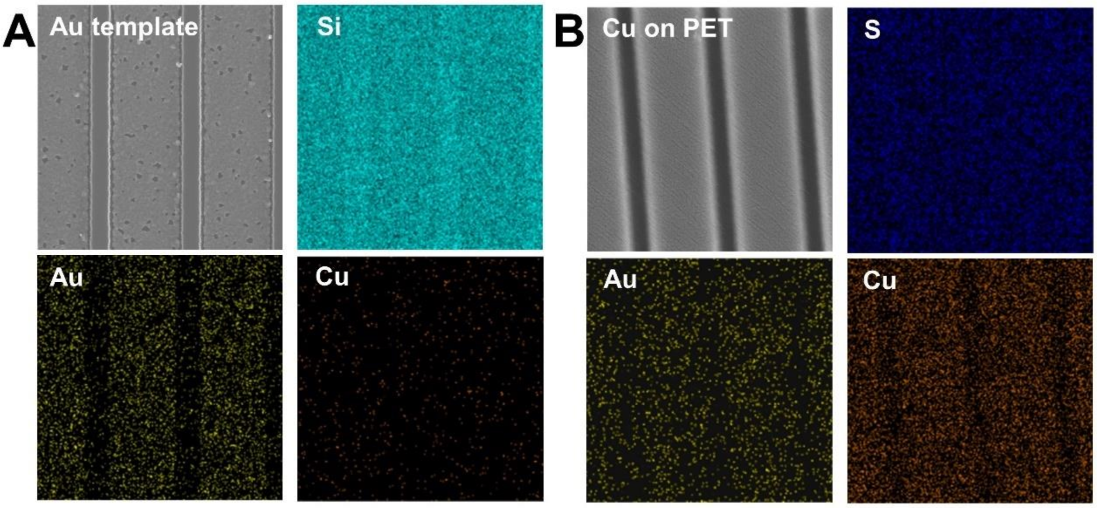

Figure 4.9 EDX results of (A) the Au template. Elements: Si, Au and Cu. (B) the Cu pattern on PET. Elements: S, Au and Cu.

To prove the successful fabrication process without damaging the Au template, the electrodeposition and transfer process was repeated over 50 times using the same Au template (Figure 4.10). The deposition time is 30 seconds, and the current density is 1 mA cm^{-2}. All of these samples show various colors under the emission of light. Only around 15 minutes were needed for the fabrication of each sample. Therefore, this replication model in ERT saves a lot of time and cost for the fabrication of nanoscale patterns.

Figure 4.10 Optical images of 50 replica samples of the Cu grating pattern fabricated by the same Au template under the emission of light.

Under the observation of SEM, it could be found that the Au template remains intact without any damage (Figure 4.11). The template was also characterized by AFM and the data relating to the surface roughness was shown in Table 4.2. The root means square roughness is only 1.571 nm which is almost unchanged compared to the original data (1.616 nm) before 50 times of fabrication.

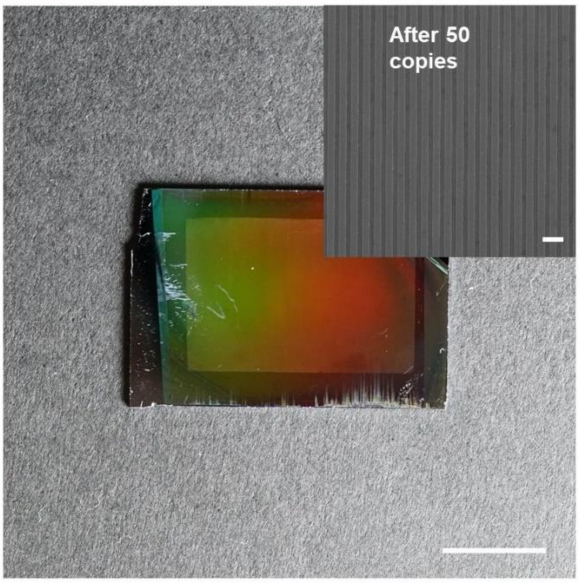

Figure 4.11 Optical image of the nanograting pattern Au template after 50 times

fabrication. Scale bar: 1 cm. Insert: The SEM images of the Au template. Scale bar: 1 μm.

Table 4.2 The surface roughness data characterized by AFM of the nano grating template after 50 times of replication.

	R_{pv} (nm)	**R_q (nm)**	**R_a (nm)**	**R_z (nm)**	**R_{sk} (nm)**	**R_{ku} (nm)**
Nano lines pattern	10.573	1.571	1.255	9.942	0.092	2.896

R_{pv}: Peak-to-valley roughness; **R_q**: Root means square roughness; **R_a**: Average roughness; **R_z**: Maximum height of profile; **R_{sk}**: Skewness; **R_{ku}**: Kurtosis.

Apart from the traditional metal materials mentioned before, the SiO_2-protecting ERT is also suitable for the fabrication of nanoscale patterns with other kinds of materials including metal oxide, conductive polymer and any other material which could be fabricated using electroplating. Here we took MnO_2 and PPy as representatives for each category. The deposition time is 30 seconds, and the current density is 1 mA cm^{-2}. SEM images and EDX results of the corresponding elements (Column A: O, M for MnO_2; Column B: C, N for PPy) were shown in Figure 4.12. They prove the successful fabrication of these two kinds of materials.

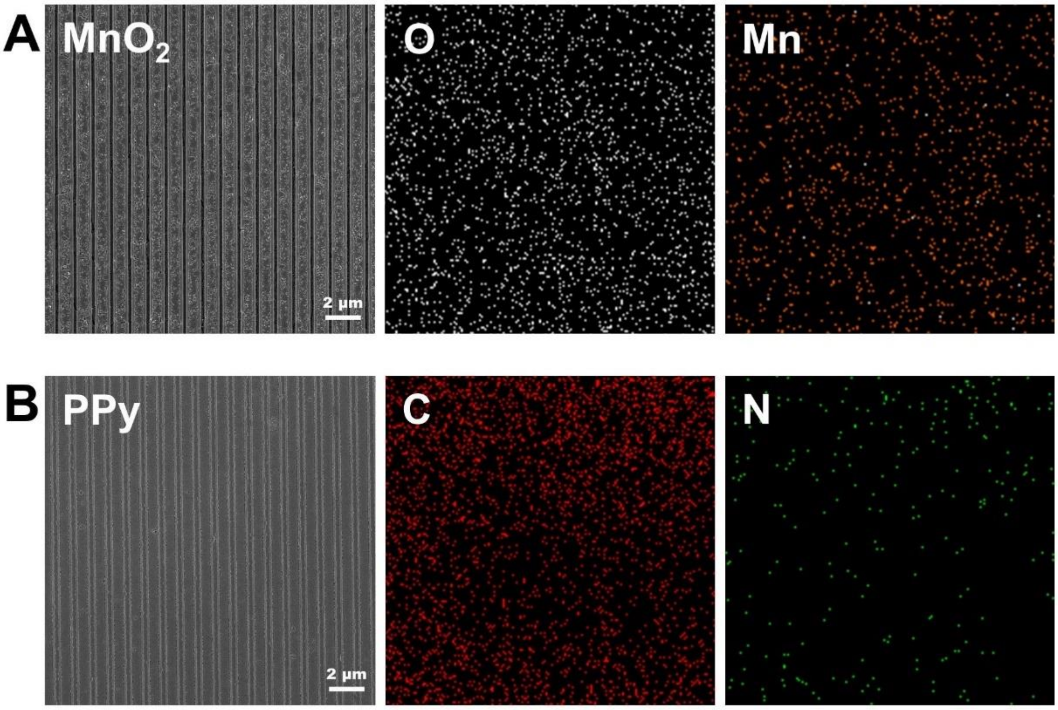

Figure 4.12 Fabrication of nanoscale manganese oxide (MnO_2) and polypyrrole (PPy) pattern through electrodeposition. (A) SEM image of MnO_2 grating pattern and the corresponding EDX result of Mn and O. (B) SEM image of PPy grating pattern and the corresponding EDX result of C and N.

The SiO_2-protecting structure template is still applicable for the fabrication of isolated nanoscale patterns such as nanodots. Figure 4.13 is the SEM pictures under different magnifications of the Au dots pattern with 150 nm diameter (Figure 4.13 A) and the Cu dots pattern (Figure 4.13 B) replicated from it. The deposition time is 30 seconds, and the current density is 1 mA cm^{-2}. The Au dots were embedded into the SiO_2 layer and the whole replicated pattern shows no damage.

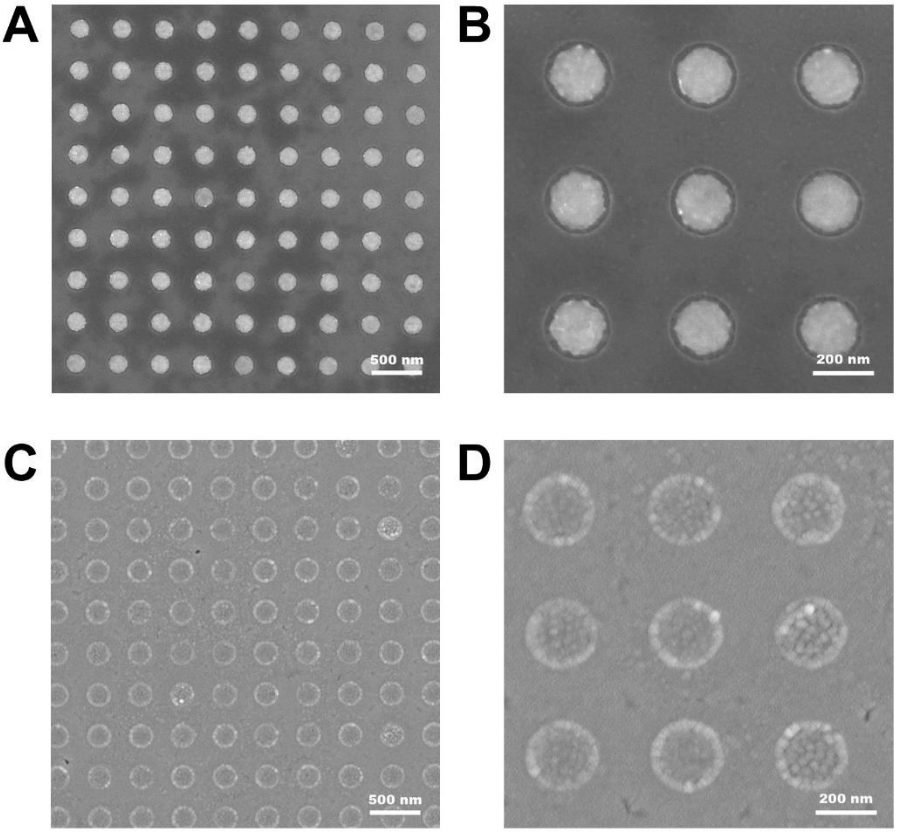

Figure 4.13 Fabrication of nanoscale dots pattern using SiO_2-protecting structure template. SEM images of (A-B) the Au dots pattern and (C-D) the Cu dots pattern replicated from the pattern.

4.6 Conclusions

The original template structure used in electrochemical replication and transfer (ERT) is not applicable to the creation of nanoscale patterns. This is because the adhesion force of the deposited materials and the Au template interface is higher than that force in the Au template and the Si substrate interface. As a result, the Au template is easily damaged during the transfer process, which is counterproductive to the goal of reducing cost and improving throughput.

To address this issue, a new template structure was proposed in this chapter. A thin SiO2 layer, which has the same thickness as the Au template, was added to the surrounding Au pattern as a protective layer during the electrodeposition and transfer process. This new structure enables the fabrication of sub-100 nm patterns using ERT, including both continuous and isolated patterns, due to the direct connection between the Au pattern and the Si substrate. The nanoscale template can be used more than 50 times, reducing costs and providing an efficient way to fabricate large-area nanoscale patterns in a short amount of time.

Importantly, this new structure has no side effects on the fabrication of large-area microscale patterns or electrodeposition of various materials, including metals, metal oxides, conductive polymers, and more.

Using our SiO_2-protecting template, it should be able to fabricate a much higher resolution theoretically. However, due to the special structure and fabrication process of the template, it is still challenging to fabricate a higher-resolution template, especially at the step of Au deposition. It is difficult to deposit the Au into a hole or groove structure. In the future, a detailed study of the fabrication parameters could be conducted and try to fabricate a higher resolution pattern. Apart from that, nanoscale patterning is essential for many characteristics such as miniaturizing electronic components, enhancing material properties, and creating devices with tailored functionalities. Further studies could be conducted on specific applications spanning electronics, photonics, biotechnology, and energy in the future.

Chapter 5: Universal Transfer Printing in ERT Using PVA Binder for Stretchable Electronic Devices

In this chapter, a polyvinyl alcohol (PVA) solution was utilized to replace the original photocurable binder (NOA 63) in ERT. The dissolvability of PVA allows for the arbitrary transfer of electrodeposited patterns to a wide range of substrates, including hard surfaces, curved surfaces, stretchable substrates, and even human skin. Furthermore, stretchable devices can be created by transferring a pattern to a pre-stretched substrate. Several applications were demonstrated, including ECG electrodes, LED light conductors, stretchable heaters, and stretchable micro-supercapacitors. Importantly, the superiorities of ERT were well-retained with the use of a PVA binder. The PVA binder is compatible with various materials such as copper (Cu), gold (Au), and silver (Ag) with resolutions ranging from 100 nm to several hundreds of micrometres. It also enables large-scale fabrication in both micro and nanoscale at one time with a high transfer yield of 99.6%.

5.1 Introduction of Stretchable Electronics

The advent of stretchable electronics has broadened the horizon for a plethora of unconventional applications, including wearable electronics[1], biosensors[4], and optical devices[6]. Over several years of study, numerous strategies have been designed to achieve stretchability in traditional electronic devices.

One approach involves the employ of materials with inherently low Young's modulus, which exhibit high flexibility and resistance to breakage. One such material is polydimethylsiloxane (PDMS) elastomer, along with other rubbery polymer materials. These materials can be utilized to creat stretchable devices, often incorporating structures such as membranes, nets, and flex circuits, as depicted in Figure 5.1.

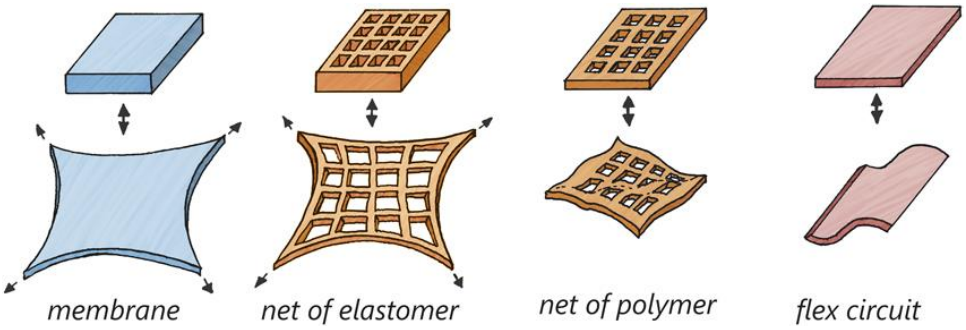

Figure 5.1 Various kinds of structures of elastomer and polymer as the substrate for stretchable devices[193].

One fundamental problem with elastomers and polymers is that they are non-conductive or have poor conductivity. However, this issue can be addressed by doping conductive materials into these stretchable substrates. For example, single-walled carbon nanotubes (SWNTs) have been successfully doped into PDMS, resulting in a conductivity of up to 57 S cm^{-2} while maintaining the original flexibility of the material. Additionally, an active matrix that combined this material with organic transistors was fabricated and maintained its performance even under 70% strain[194]. Other additives, such as Ni powder[195], silver nanowires[196], and liquid alloy EGaIn[197], have also demonstrated satisfactory performance in the field of stretchable electronics. By combining liquid metal and fiber mat fabricated by electrostatic spinning, a highly stretchable and biocompatible membrane could achieve omnidirectional stretching over

1,800% strain[2].

Despite the many ways to increase the conductivity of elastomers and polymer materials, their performance still falls short of traditional active materials like metals and semiconductors. Another approach involves constructing special structures using these active materials, such as the 'wavy' structure.

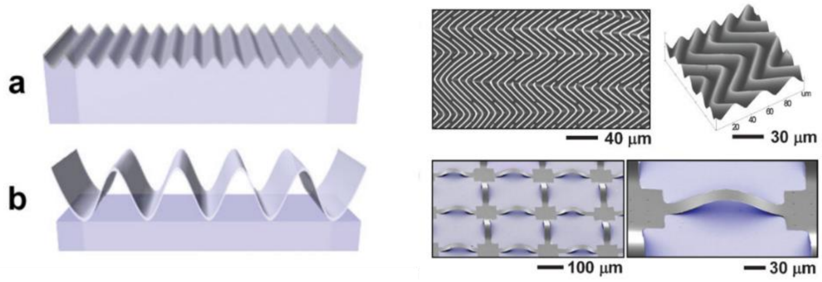

Figure 5.2 Two general types of ‘Wavy’ structures. Buckled structure of target materials (A) fully attached (B) partly attached to stretchable substrate[198].

There are generally two types of 'Wavy' structures, as depicted in Figure 5.2. In 2007, the wavy structure was first proposed by J.A. Rogers and his group[199]. They achieved this by transferring a silicon thin film membrane onto a pre-stretched PDMS substrate, which deformed in both transverse and longitudinal directions on a two-dimensional plane. This thin film exhibits an edge effect, where the edge of the film forms a one-dimensional wavy geometry. This wavy thin film holds potential for applications in integrated electronic devices. Similar structures have also been proven effective for other materials, including carbon monolayers[200] and carbon nanotubes[201].

By pre-treating the elastomer substrate, bonds can be formed between the rigid material and specific areas. For instance, as shown in Figure 5.2 (b), GaAs ribbons with silicon ribbons on the surface were fabricated on a UV-treated pre-stretched PDMS substrate. Upon exposure to UV light, the exposed area forms strong siloxane linkages (-O-Si-O-) with the GaAs ribbons. After releasing the pre-strain on the PDMS substrate, the unconnected area lifts and forms a 'Wavy' structure on the up area of the PDMS substrate instead of being embedded within it. Compared to the first buckled structure, this 'partly attached' structure can endure much higher strain (up to around 100%) without breaking the ribbons[202]. This method can be used for creating integrated circuits such as complementary metal-oxide-semiconductor (CMOS) or amplifiers[203].

Apart from these special buckles formed by pre-stretched substrates, there are also special patterns based on physics and mechanics that can achieve stretch properties. The mesh structure is one of the earliest examples explored by researchers[204] (Figure 5.3 below).

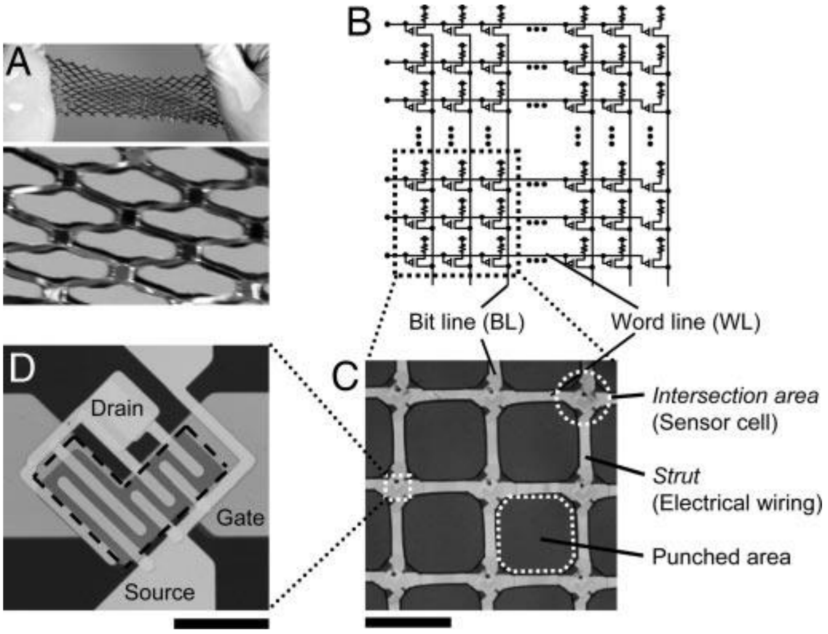

Figure 5.3 Mesh structure for stretchable pressure sensors[204].

Figure 5.3 illustrates how, despite using rigid and non-stretchable basic materials, a thin film can undergo a 25% transformation due to quadrilateral instability in mechanics. Another special structure that can deform without breaking or rupturing is the horseshoe shape. By transferring the 3D wavy structure onto a 2D plane, a unique wave shape can be achieved on the stretchable substrate. The deformation of the metal pattern on the substrate can be separated into two steps.

The first involves plastic deformation, which occurs in conjunction with the stretchable substrate. Since the size of the substrate is much bigger than that of the pattern, the metal pattern experiences uniform force from all directions. However, for the typical zigzag shape, the plastic strain at the connection turning point significantly increases (Figure 5.4). In contrast, the horseshoe shape offers a significant advantage by reducing strain from nearly 20% to around 7%. The second step is the delamination of the metal and substrate interface when the shear stress exceeds its limit. In this scenario, the metal pattern deforms freely and randomly[205].

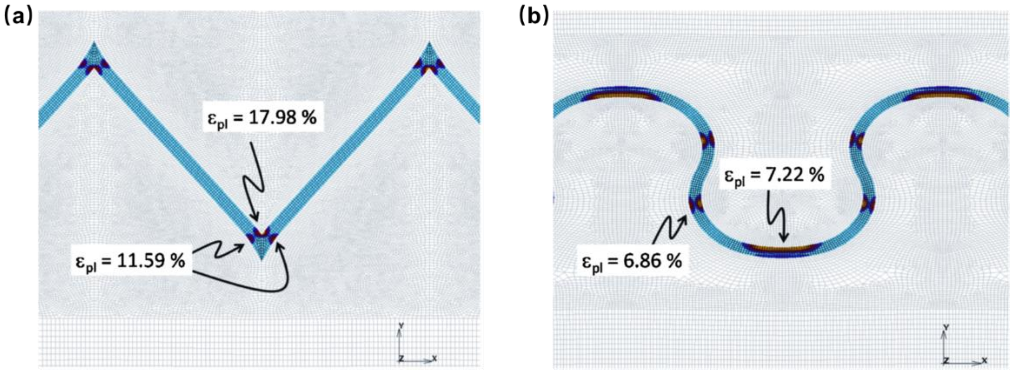

Figure 5.4 Comparison of plastic strain between (A) zigzag and (B) horseshoe

structure[205].

There are also many other structures such as microcracks. The sketch map is shown in Figure 5.5 below. It has been reported that a gold thin film with original cracks was fabricated on a PDMS substrate. The conductivity of the thin film electrode could remain unchanged even at 120% strain. The performance could be improved by electrical and thermal treatment adjustment[206].

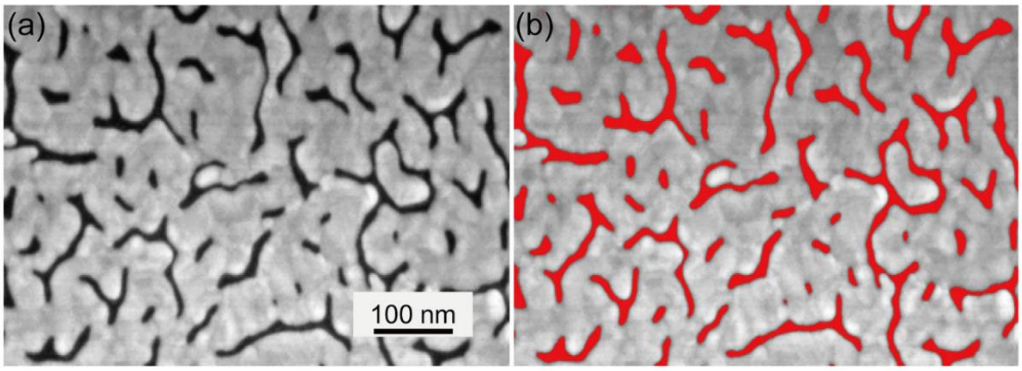

Figure 5.5 (A) SEM image of Au thin film electrode with microcracks (B) image analysis method to calculate the percentage of the microcracks[206].

The technology of patterning is integral to the process of fabricating circuits. Traditional patterning technologies, such as photolithography, electron beam lithography, and nanoimprinting lithography, have made significant advancements over the years, particularly in terms of resolution. However, these traditional methods have drawbacks including high cost, low throughput, and limited suitability for emerging special applications mentioned earlier. For instance, photolithography struggles to achieve a uniform layer of photoresist on curved surfaces or flexible substrates through spin coating. The resolution of the fabricated pattern is also compromised when other methods like dip coating are employed[207].

An emerging category of patterning technology called transfer printing offers precise and arbitrary transfer for nano- or micro-fabrication[16, 148, 153]. It demonstrates versatility across various receiver substrates, high throughput, and relatively low cost. However, achieving high fidelity of transferred patterns, especially at the nanoscale, and maintaining a high transfer yield remains challenging. Additionally, the chemical binders used for transfer or adhesion may have adverse effects on device performance and pose environmental or biological risks. Developing a biocompatible or binder-free transfer printing method suitable for arbitrary substrates continues to be a challenge.

Electrochemical release transfer (ERT), as a transfer printing method, addresses many of the aforementioned issues and meets the requirements for flexible device fabrication. However, the original binder used for pattern transfer (photocurable binder NOA 63) is not suitable for certain surfaces such as hard and curved substrates. The rigid nature of the binder makes it difficult for hard target substrates to conformably attach to or separate from the electrodeposited substrate. Moreover, applying ERT to human skin for emerging biomedical applications is impractical. Furthermore, the rigidity of the binder limits its application in fabricating stretchable devices.

5.2 Fabrication Process Using PVA as Binder in ERT

Therefore, an alternative polymer binder, a polyvinyl alcohol (PVA) solution, was used for the transfer process to replace the NOA binder in ERT. The whole fabrication process is illustrated below in Figure 5.6. Additionally, Figure 5.7 shows a photo of the transference of a Cu mesh pattern onto a substrate of a glass sheet. The design of the Au template was based on the research output in Chapter 4. The Au pattern was embedded into the SiO_2 layer (Figure 5.7 A). The first step is the same as the original method in which the target materials (e.g., Cu) are electrodeposited on the Au template with PFDT modification. The deposition time is 3 hours, and the current density is 1 mA cm^{-2}. The template was further immersed in 20% dodecyl triethoxy silane ethanol solution for 10 min and heated at 120 °C for 15 min to change from hydrophilic to hydrophobic of the SiO_2 surface (Figure 5.7 B)[208]. Then, 10% PVA solution is cast on the template by drop casting and dried at 50 °C for 3 hours. In the photo, the cyan pigment was added to the transparent PVA solution for a clear illustration (Figure 5.7 C). After that, the target materials pattern could be easily detached with the PVA layer thanks to the pre-modification of Au and SiO_2 (Figure 5.7 D). The template could then be used for the next fabrication. For the transfer process, the PVA layer, bearing the pattern, is directly affixed to the intended substrate. The receiver substrate could be pre-treated by plasma or other methods which the enhancement of adhesive force between the target materials and the receiver substrates is contingent upon the types of the substrate. Here we attached the PVA layer with a mesh pattern to a glass sheet with 5 minutes of plasma treatment as a demonstration (Figure 5.7 E). Owing to the pronounced hydrophilicity and pliability of the PVA film, achieving conformal adhesion to the intended substrate was readily accomplished. Finally, the PVA layer will be dissolved by deionized water at room temperature. No cyan colour was shown in the last picture. The Cu grid pattern could remain on the glass sheet by various adhesion forces like electrostatic force and Van der Waals' force[209-212].

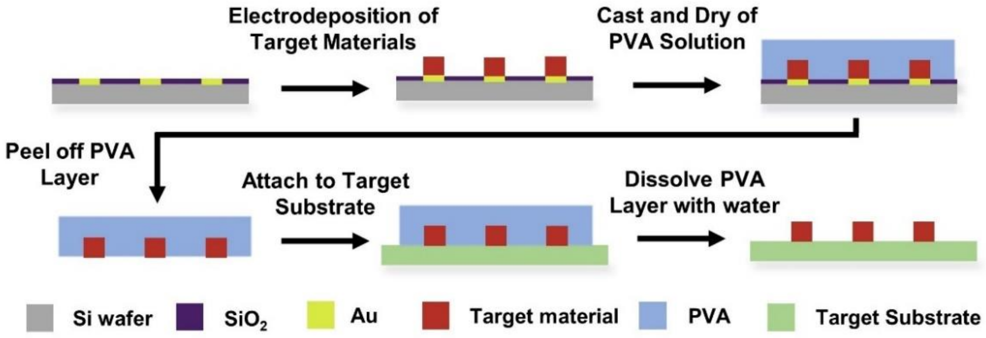

Figure 5.6 Illustration of the fabrication process of ERT using PVA as transfer binder.

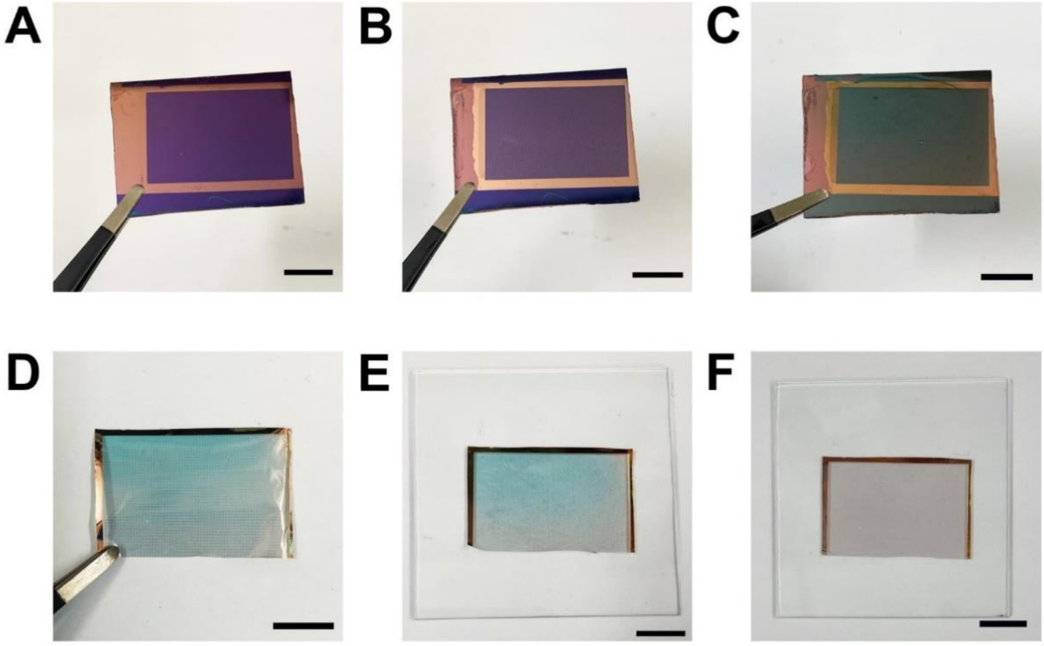

Figure 5.7 Photo of the fabrication of Cu mesh pattern and transferred to a glass sheet using PVA binder. (A) The Au mesh pattern template. (B) The template after electrodeposition of Cu. (C) The template after casting a thin layer of PVA and drying

at 50 °C. (D) Cu mesh pattern peeled off by PVA layer. (E) A PVA layer with a Cu mesh pattern was attached to the glass sheet. (F) The glass sheet with Cu pattern after dissolving the PVA layer with deionized water.

5.3 Characterization of the Transfer Process

The related optical images are depicted in Figure 5.8. The electrodeposited Cu pattern remains intact during the whole transfer process. The only problem is that the Cu may be oxidized during the drying and dissolving process using water. As showcased in Figure 5.8 (D), the color of Cu mesh is heterogeneous corresponding to the oxidation of Cu. This problem could be fixed by further treatment such as chemical etching. PVA binder may be not suitable for those water-sensitive materials.

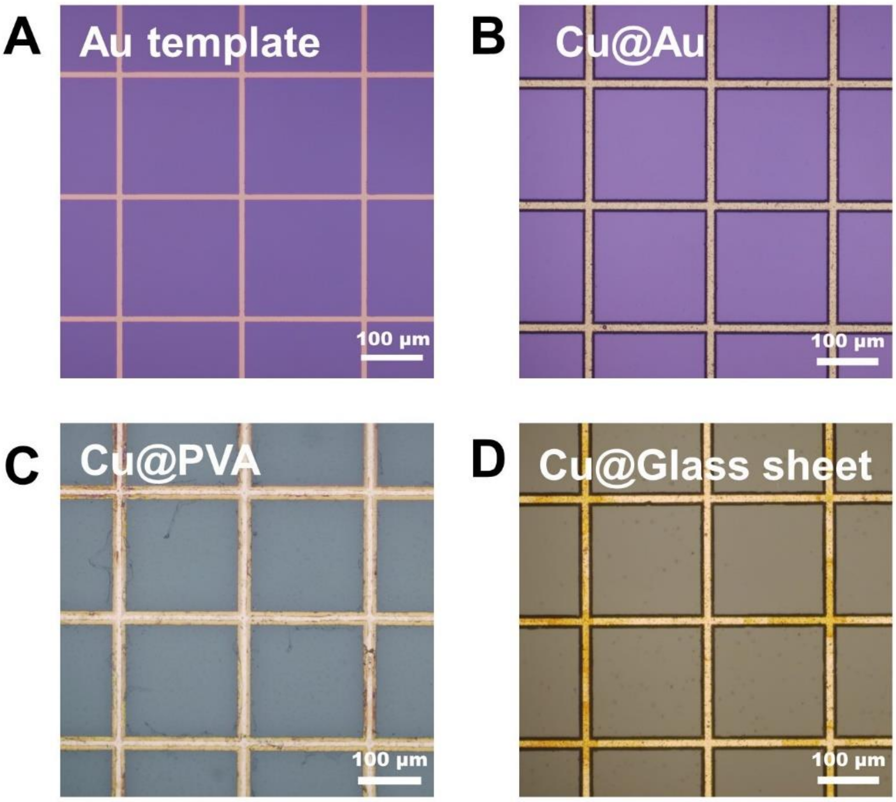

Figure 5.8 Optical image of the Cu mesh pattern fabricated and transferred to the glass sheet. (A) The Au template. (B) The Au template after electrodeposition of Cu. (C) The Cu pattern was peeled off by PVA binder. (D) The Cu pattern was transferred to a glass sheet substrate.

The transfer process was further characterized by AFM. For an efficient transfer printing technique, it is significant to make sure the pattern is unchanged after the transfer process. Compare the AFM images of the Cu pattern before (on the Au template, Figure 5.9 A) and after (on the glass sheet, Figure 5.9 B) the transfer process, there is no obvious change in the aspect of line width (~15 μm) and height (~3.5 μm). Details data were presented in Figure 5.9 (C-D) which reveals the profile change of the corresponding red line shown in the AFM images. It proves that the electrodeposited Cu pattern could be peeled off without residual on the Au pattern. Meanwhile, the deionized water used in the dissolving process will not damage the pattern and ensure transfer efficiency.

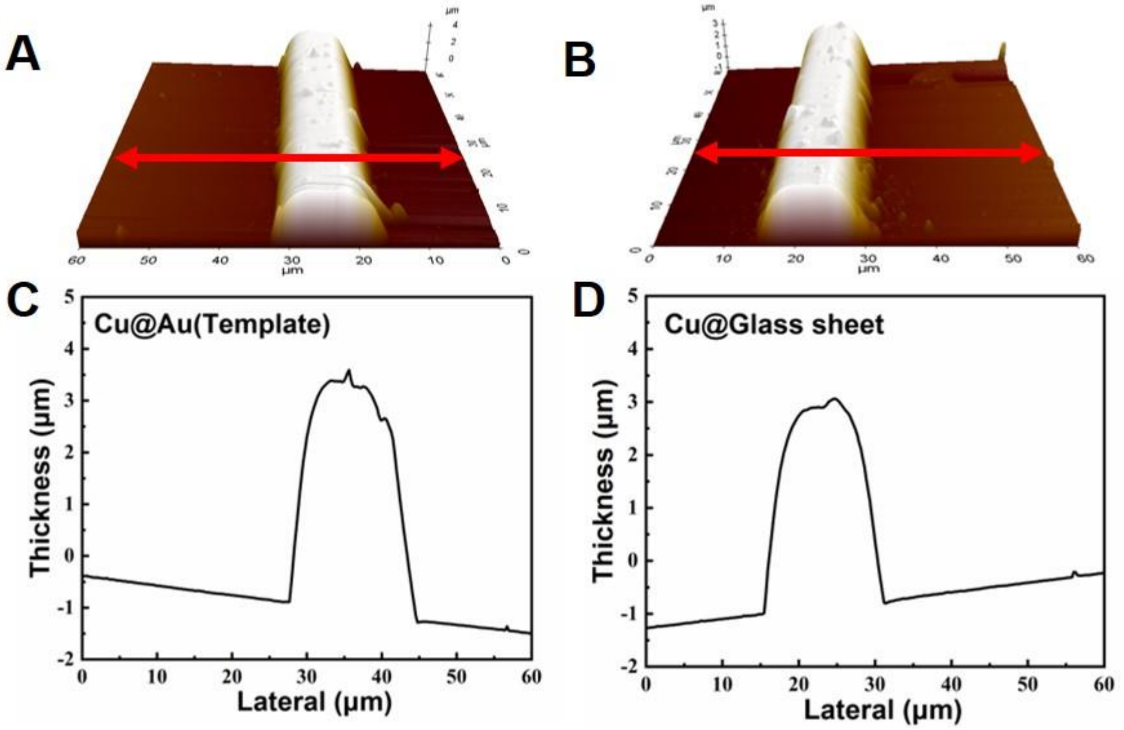

Figure 5.9 AFM test of the Cu pattern prior to and subsequent to the transfer process. (A) AFM image of the Au template after electrodeposition of Cu. (B) AFM image of the Cu pattern transferred to the glass sheet. (C) The surface profile data of the red line is in A. (D) The surface profile data of the red line is in B.

5.4 Applicability of PVA Binder

5.4.1 Various Materials and Receiving Substrates

Due to the dissolvability of PVA binder, it allows a universal transfer process for various materials and more categories of receiving substrates. Figure 5.10 shows the sensibility of Ag and Au transferred by PVA. Ag was finally transferred to a glass bottle which is a curved surface and Au was transferred to a stretchable Ecoflex film (Figure 5.10 D and H). From the optical images taken during the whole transfer process, it could be found that the whole Ag and Au pattern remained intact, and no side effects happened. The XRD result was used to further confirm the successful electrodeposition of these materials including Cu, Ag and Au (Figure 5.11). The XRD test was conducted before the dissolving process, wherein the metal patterns were incorporated into the PVA binder layer.

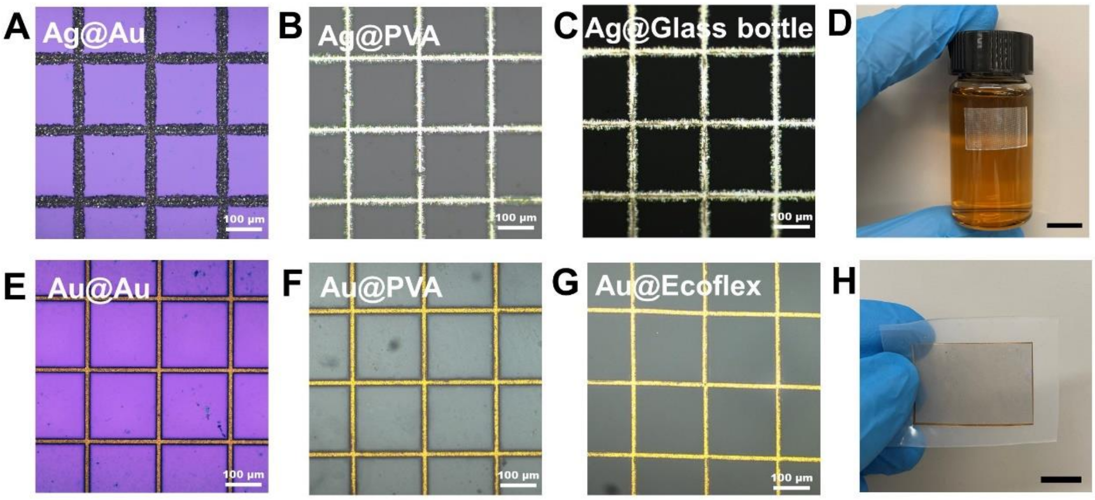

Figure 5.10 Transfer of pattern with different materials to various kinds of receiving substrates. (A) Optical image of the Au template after electrodeposition of Ag. (B) Optical image of Ag mesh pattern peeled off by PVA. (C) Optical image of Ag mesh pattern transferred to a glass bottle. (D) Photo of Ag mesh pattern transferred to a glass bottle. (E) Optical image of the Au template after electrodeposition of Au. (F) Optical

image of Au mesh pattern peeled off by PVA. (G) Optical image of Au mesh pattern transferred to a glass bottle. (H) Photo of Ag mesh pattern transferred to an Ecoflex film.

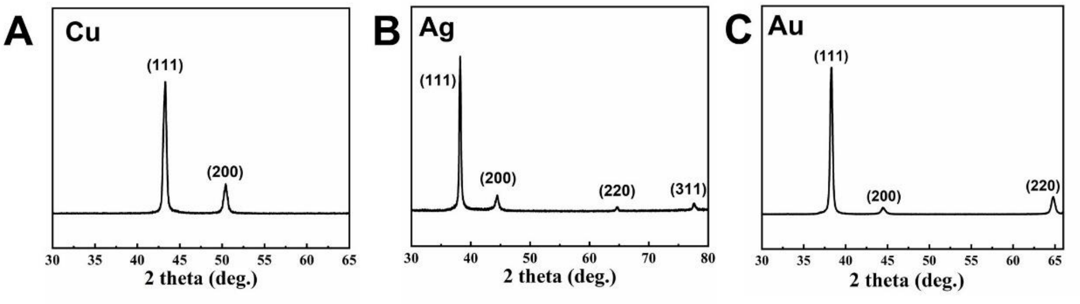

Figure 5.11 XRD result of the as-fabricated metal mesh pattern. (A) Cu. (B) Ag. (C) Au. The XRD test was conducted on the metal pattern embedded in the PVA layer before dissolving.

5.4.2 Various Patterns Reaching Nanoscale

The transfer of target materials pattern by PVA is also applicable to isolated patterns with different resolutions reaching even nanoscale. As shown in Figure 5.12 (A-B), isolated Cu dots array patterns with a size range from 3 μm to 20 μm were fabricated and replicated to PET film. The morphology of the Cu dots and the distance between each dot remained unchanged. The resolution can even reach 100 nm (gaps between the lines in Figure 5.12 D).

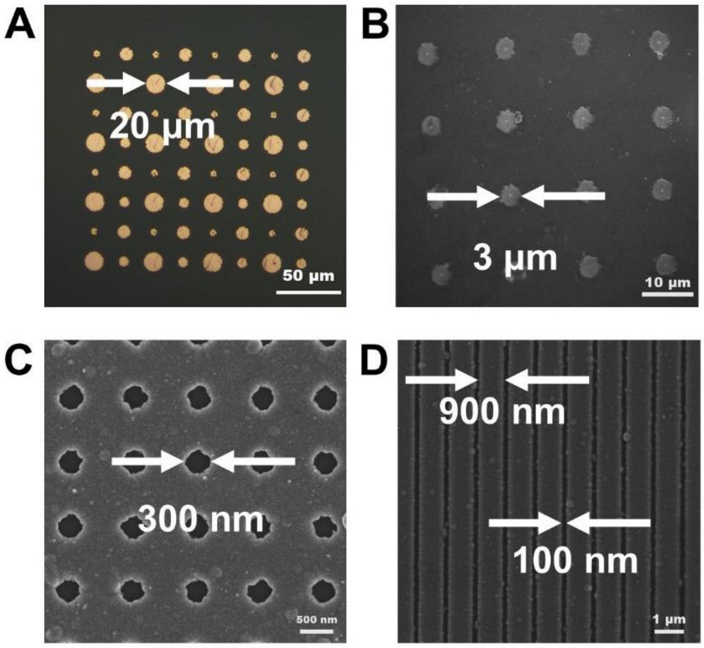

Figure 5.12 Various patterns transferred to PET film. (A) Microscale Cu dots pattern with around 5~20 µm diameter. (B) Dots pattern with 3 µm diameter. (C) Hole mesh pattern with 300 nm diameter. (D) Lines pattern with 900 nm width and 100 nm gap.

Transfer yield serves as a significant parameter in assessing the efficacy of the transfer printing methodology. The Cu nano lines pattern was fabricated and transferred to PET film by the same template in Figure 5.12 (A). The total area of the pattern is around 3 cm^2. By randomly picking up 16 areas under the observation of SEM images, the transfer yield of the nano-lines pattern could be up to 99.6% with only 2 broken lines in a total of 464 lines (Figure 5.13).

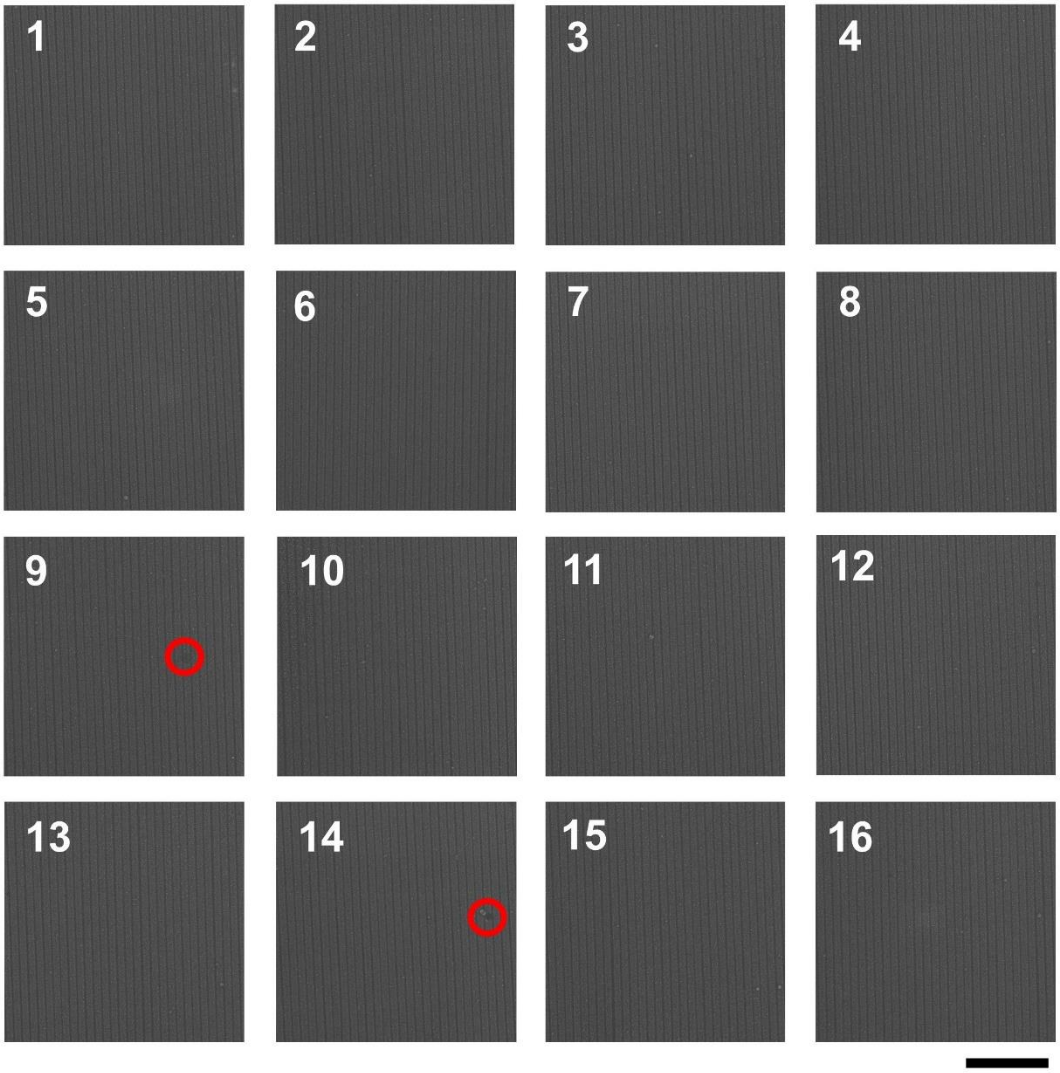

Figure 5.13 SEM images of 16 randomly picked areas in the nanoscale lines Cu pattern. Broken lines were highlighted by red circles. Scale bar: 10 μm.

Throughput constitutes another crucial element in the assessment of a lithography method's performance. ERT has been proven to be able to fabricate large-scale patterns up to a 4-inch area using NOA binder. It is also possible to realize large-scale transfer using a PVA binder. As shown in Fig. 5.14 (A-B), a 4-inch-scale Cu grid pattern could be peeled off integrally by a PVA binder. The line width is 5 μm and the gap is 100 μm.

There are 36,0000 square lattices in total for this 6 × 6 cm^2 pattern. Then, the grid pattern was transferred to a PET membrane (Figure 5.14 C-D). By detailly counting the number under the optical microscopy, only 2952 square lattices were broken. Therefore, the yield of the whole large-scale transfer process could reach 99.18%.

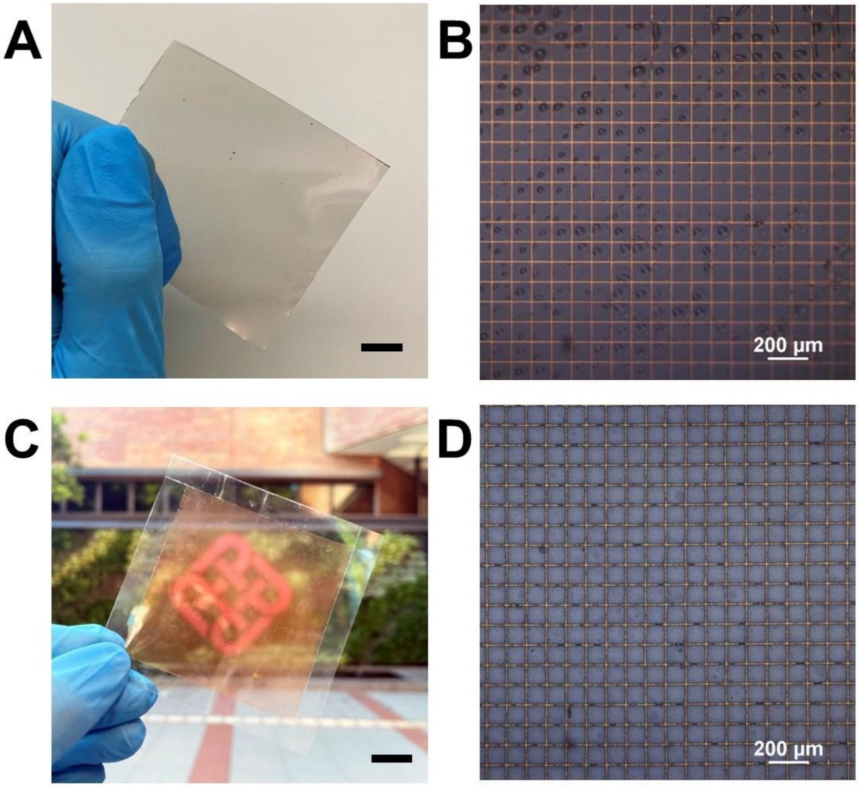

Figure 5.14 Transfer of a large-scale pattern reaching 4 inches. (A) Photo of the Cu mesh pattern peeled off by PVA binder. (B) Optical image of the Cu mesh pattern on the PVA layer. (C) Photo of the Cu mesh pattern transferred to a PET film. (D) Optical image of the Cu mesh pattern on PET film. Scale bar: 1 cm.

The corresponding SEM images of the large-scale transfer Cu grid are shown in Figure 5.15. The morphology of the Cu grid pattern was almost unchanged between the electrodeposited pattern and the transferred pattern. The pattern was embedded into the

PVA layer during the peel-off process which offers a high binding force between the Cu and PVA and increases the success rate of peeling off. After dissolving and transfer, it formed a simple three-dimensional (3D) structure on the receiver substrate (PET).

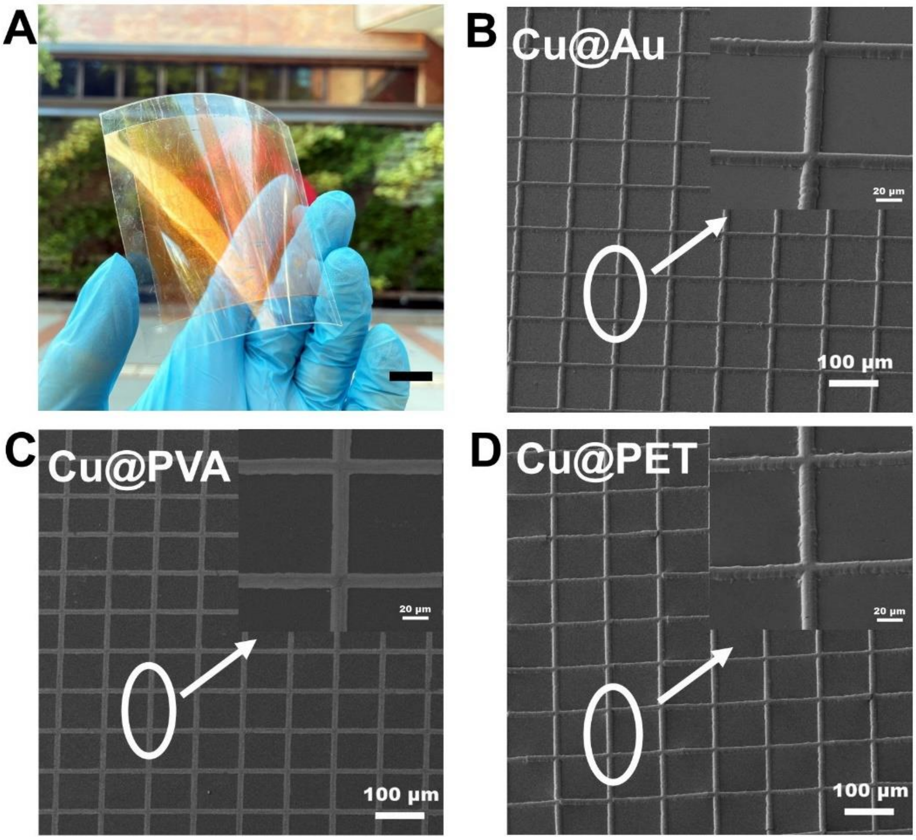

Figure 5.15 SEM images of the large-scale Cu mesh pattern during the whole fabrication process. (A) Photo of the Cu mesh pattern transferred to a PET film. Scale bar: 1 cm. (B-D) SEM images of the Cu mesh pattern during the whole fabrication process including after electrodeposition on the template, Cu pattern peeled off by PVA layer and after transferred to PET film.

5.5 Applications for Stretchable Devices

Stretchable conductors are essential constituents of stretchable electronic devices. It offers the connection between rigid and soft electronic parts to realize different functions. A stretchable conductor should be able to suffer from mechanical deformation including elongation and compression. The resistance should remain stable during the deformation process[213]. Based on the previous introduction, the buckled structure and specific pattern design such as horseshoe could be combined with the ERT process to obtain the fabrication of stretchable conductors.

5.5.1 Stretchable Conductors

Stretchable conductors form the foundational structures of stretchable devices. As the most widely used conductive material, Cu itself cannot be stretched any more. Therefore, based on the previous introduction, a specific design is necessary for the stretchability of Cu and other rigid materials.

For the classic buckled structures, the dissolvability of the PVA binder makes it easily realized by ERT. Figure 5.16 shows the fabrication process of the Cu buckled structure transferred to a stretchable polydimethylsiloxane (PDMS) substrate. First, the PDMS substrate will be pre-stretched under a certain strain (ΔL, e.g., 50%). The PDMS substrate will be treated with oxygen plasma for 5 minutes under this status to clean the surface and form polar functional groups like silanol[214]. Following the plasma treatment, the surface of PDMS transitions from hydrophobic to hydrophilic. As depicted in Figure 5.17, the contact angle of water diminishes from 111° to 15°, thereby enhancing the adhesive force between the Cu and PDMS substrates. After the surface treatment, the PVA layer with a Cu pattern will be directly attached to the pre-stretched PDMS surface. Then, the PVA layer will be dissolved in deionized water gently. After the PVA layer is dissolved, the PDMS substrate will be dried, and the strain will be released uniformly and slowly. The Cu conductors will form buckles naturally on the surface. This buckled structure enables the stretchability of Cu conductors with a maximum strain of ΔL.

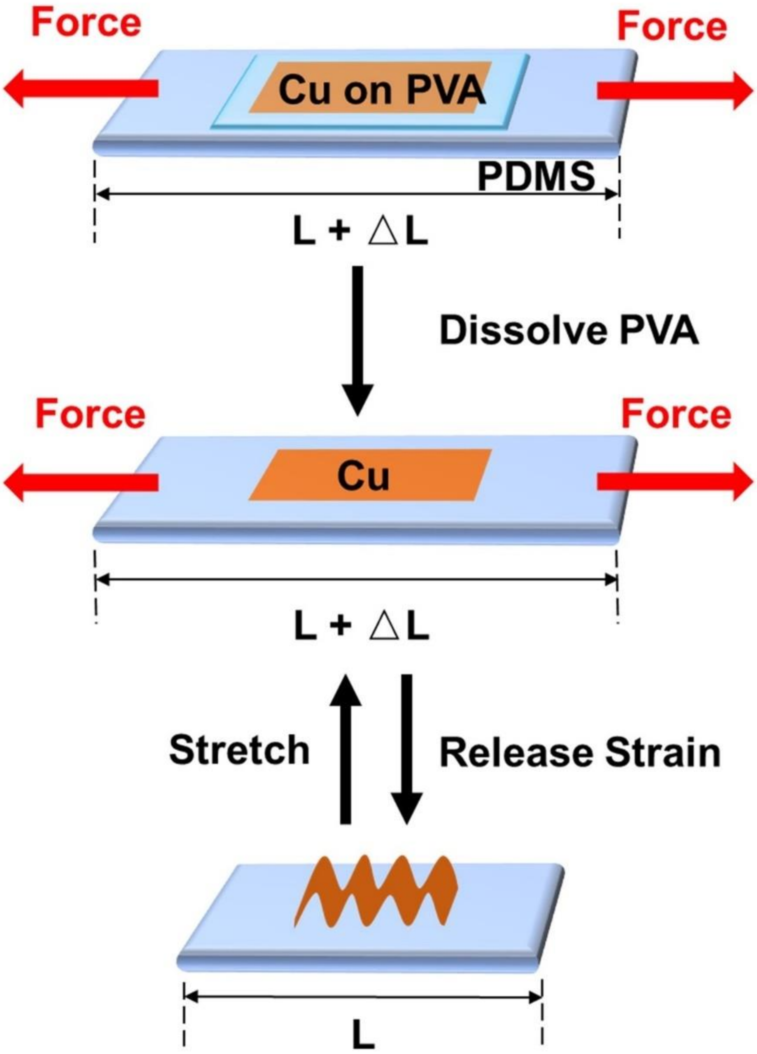

Figure 5.16 Illustration of the fabrication process of stretchable buckled conductors on PDMS.

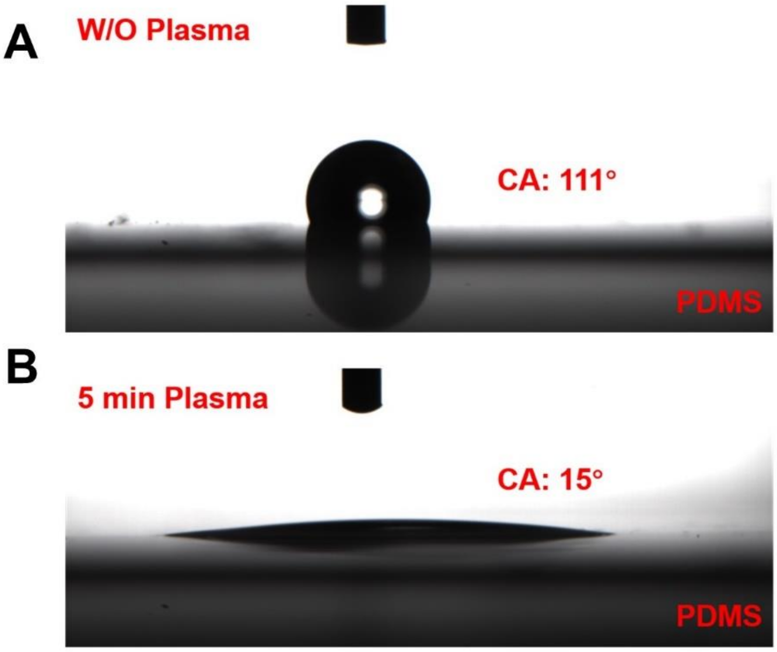

Figure 5.17 Contact angle of the PDMS substrate with/without 5 minutes of oxygen plasma treatment.

This strategy is also suitable for the normal flexible conductors by direct transfer of the pattern without pre-strain. The flexibility and stretchability of the Cu conductor fabricated by PVA binder were tested using a stepper motor linear stage as shown in Figure 5.18. The deposition time is one hour and the current density is 1 mA cm^{-2}. For both tests, the width is 2 mm, and the length is 2.5 cm for the transferred Cu conductors. For the flexibility test, the Cu conductor was bent for 3000 cycles under a bending radius of 5 mm. The resistance only increases from 1.25 Ω to 1.32 Ω with a slight change rate of 5.6%. For the stretchability test, the Cu conductor was stretched for 5000 cycles under a strain of 50%. The resistance changes from 0.21 Ω to 0.22 Ω with a small change rate of 4.8%. It proves the potential of applying ERT using a PVA binder to flexible and stretchable devices.

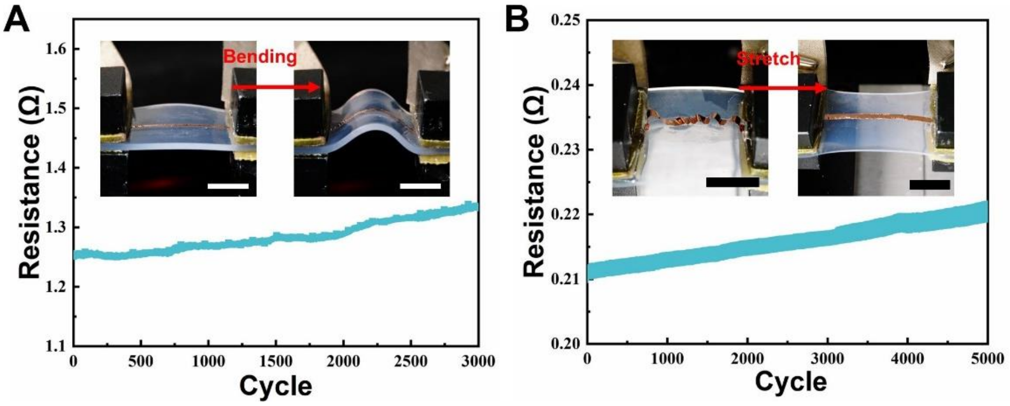

Figure 5.18 Bending and stretching tests of the Cu conductors. (A) Resistance of the Cu conductor is bent for 3000 cycles under a bending radius of 5 mm. (B) Resistance of the Cu conductor stretched for 5000 cycles under the strain of 50%. Scale bar: 1 cm.

Apart from the buckled structure, stretchability could also be realized by the intrinsic design of stretchable patterns such as horseshoe patterns. As shown in Figure 5.19 (A), an Ag horseshoe pattern was conveyed onto a PDMS substrate. It could be attached to human skin. It can also be stretched or twisted. The resistance only increases from 1.5 Ω to 3. Ω under the strain of 30%. After 100 cycles, the resistance under the stretching state was almost unchanged which proves the excellent stability.

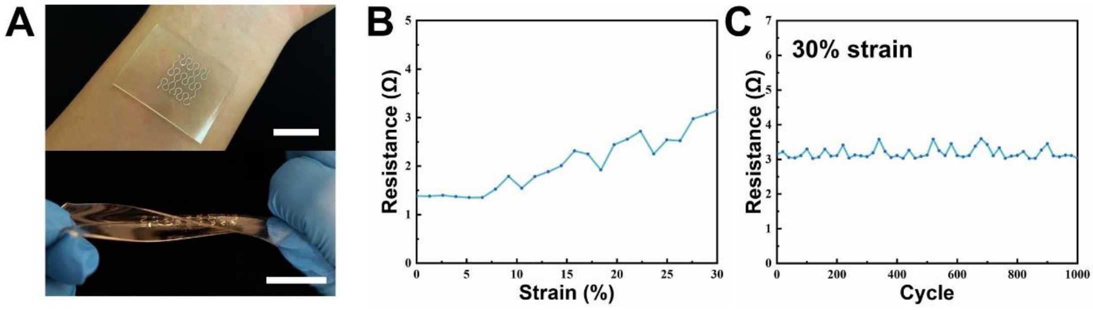

Figure 5.19 Stretchability of an Ag horseshoe pattern transferred to PDMS by ERT

using PVA binder. (A) Photo of the Ag horseshoe pattern on PDMS. Up: Attached to the human wrist. Down: Under twisting and stretching state. (B) Resistance during the stretching under a 30% strain. (C) Resistance of the Ag horseshoe pattern stretched for 1000 cycles under the strain of 30%.

5.5.2 Stretchable Devices on the Human Body

The dissolvability of PVA binder enables the arbitrary transfer even on the human body. Few amounts of PVA residue will remain on the human skin to enable the binding between the metal pattern and human skin. Combining the strategies for the fabrication of stretchable conductors, LED lights could be integrated with human fingers. The conductors form buckled structures on the finger surface (Figure 5.20 A). The light intensity will not be affected by the bending and straightening of a human finger. For the horseshoe pattern, it could be applied as stretchable electrodes for human monitoring such as ECG. Compared with the commercial electrodes, the Au horseshoe pattern transferred to the human wrist by PVA shows the same stability even after 6 hours of free motion.

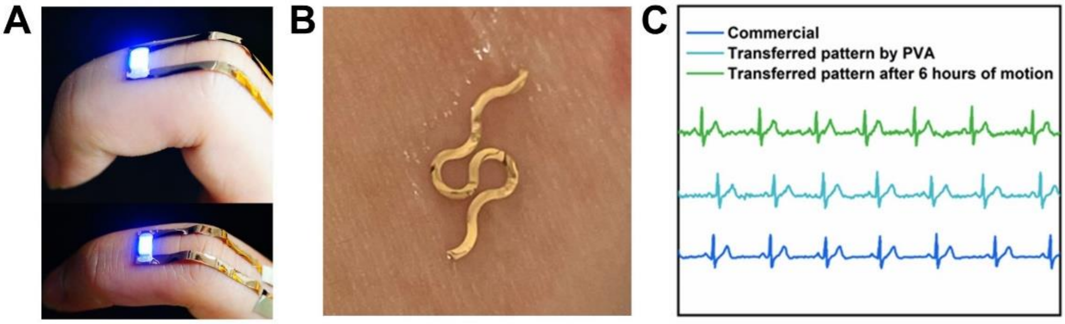

Figure 5.20 Stretchable conductors on human skin. (A) Cu conductors for LED lights

on the finger. (B) Au horseshoe pattern on the human wrist as electrodes for ECG test. (C) Comparison of ECG singles of commercial electrodes and stretchable Au horseshoe electrodes before and after free motion.

5.5.3 Stretchable Micro-Supercapacitors

To make electronic devices wearable, it is crucial not only to integrate the function groups but also the power supply components such as batteries and micro-supercapacitors (MSCs) with the human body[215]. MSCs are composed of two conductors and a separated non-conductive dielectric layer. Normally it forms a sandwich structure. It could store charge when a voltage is applied between the two plates[216]. To reduce the weight and volume of the devices on the human body, the in-plane design of interdigital electrodes was proposed[217]. The substantial energy density of MSCs presents considerable potential within the realm of wearable electronics[218]. Here stretchable MSCs with interdigital electrodes were designed and fabricated by the ERT method.

The structure is shown in Figure 5.21. The whole MSCs interdigital electrode pattern was fabricated by 10 minutes of Au deposition and 5 minutes of Cu deposition consecutively. The current density is 1 mA cm^{-2}. The Au layer serves as a current collector. The entire device will be collectively transferred to a pre-stretched PDMS substrate. Subsequent to the release of the pre-strain, the whole device will form buckles on the PDMS surface. Then, the device will be treated with oxygen plasma for 5 minutes. The Cu will be oxidized to CuO_x, which will serve as active materials.

Ultimately, the electrolyte, composed of 20-weight percent LiCl and 10-weight percent PVA in H_2O, will be directly applied to the surface of the interdigital electrode for the purpose of an electrochemical examination.

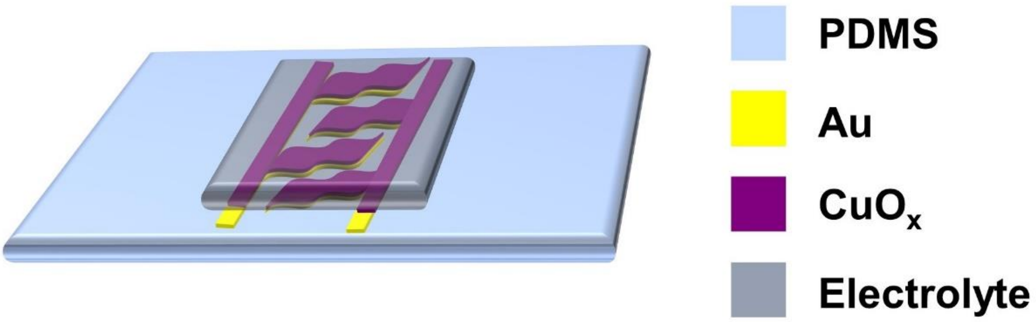

Figure 5.21 Illustration of the structure of stretchable micro-supercapacitors on PDMS substrate.

The electrochemical performance of these MSCs is shown in Figure 5.22. The cyclic voltammetry (CV) curves, which is the basic electrochemical performance, was tested under different scanning rate from 10 mV to 200 mV (Figure 5.22 A). The areal capacitances at different scanning rates were calculated according to the CV curves and shown in Figure 5.22 (B). The areal capacitance is around 0.75 under a scanning rate of 10 mV. The mechanical stretchability of the MSC was also studied (Figure 5.22 C). The whole device was stretched more than 50 times at 50 % strain. The CV curves tested before and after the stretching test were almost the same which indicated the stability of the stretchable MSC devices.

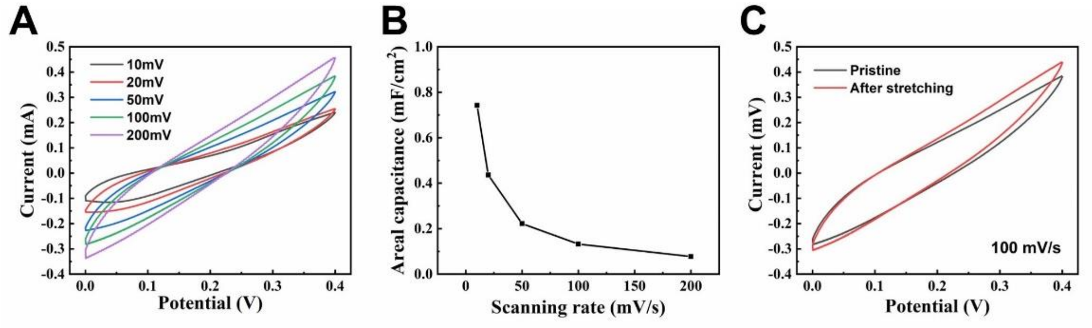

Figure 5.22 Performance of the stretchable micro-supercapacitors. (A) CV curves with different scanning rates. (B) Areal capacitance under different scanning rates. (C) Comparison of CV performance after stretching with the pristine sample. Scanning rate: 100 mV/s.

5.6 Conclusions

The ERT method has demonstrated its efficacy as a highly efficient technique for the fabrication of high-resolution patterns on flexible substrates, providing both high throughput and cost-effectiveness. To enhance the applicability of ERT, a PVA (Polyvinyl Alcohol) solution was introduced as a replacement for the original photocurable binder NOA 63. The dried PVA binder effectively peels off the electrodeposited materials from the template without causing any damage. With a success rate of up to 99.6%, large-scale transfers of patterns at both micro and nanoscale can be achieved. The versatility of ERT is demonstrated by its ability to transfer various materials, including Cu, Ag, and Au, onto different surfaces. It is applicable to hard surfaces including glass sheets, curved surfaces like glass bottles, and even stretchable substrates like Ecoflex. Other flexible substrates such as PET, PDMS, and even human skin can also be utilized. By employing a pre-strain strategy and specific pattern designs, stretchable devices can be fabricated. The flexibility and stretchability of the transferred patterns remain stable even after thousands of repetitions. The applications of ERT are wide-ranging. It has been successfully employed in the fabrication of ECG electrodes, LED lights, stretchable heaters, and stretchable micro-supercapacitors, all of which exhibit excellent stability under stretching conditions.

Despite a comprehensive investigation into the applicability of PVA as a binder in this project, the performance of stretchable electronic devices fabricated using this binder remains unsatisfactory. In future research, one direction could be to explore and compare different materials as binder layers to investigate their mechanical properties, adhesion strength, and transfer efficiency. Alternatively, the ERT method using PVA as a binder could be fine-tuned based on specific application scenarios of stretchable electronics to fabricate flexible electronic devices with outstanding performance, thereby identifying the most suitable application scenarios for devices prepared using ERT.

Chapter 6: Resolution-Confined 3D Structure Pattern and Applications Thereof in ERT

In this chapter, a modification was made to the template used for ERT to realize the fabrication of a 3D structure pattern on the flexible substrate. The 3D structure template could also restrict the decrease in resolution caused by the isotropic deposition of the electroplating process. The intended materials will be directly deposited onto the surface of Si substrates, which could also improve the reusability of the template since Si is much harder than the Au pattern and is difficult to destroy during the transfer process. The aspect ratio of the 3D structure pattern fabricated by this template could reach a maximum of 1:4, while the resolution of the pattern could reach 2 μm. The template is suitable for the fabrication of both isolated dot array patterns and interconnected patterns, including lines and meshes. To demonstrate the advantage of keeping the pattern resolution, 3D structure mesh patterns with different line widths, gaps, and heights were fabricated to chase for a high Figure of Merit which could serve as the electrodes for flexible transparent heaters. To demonstrate the specific application of 3D structures, a self-powered pressure sensor based on a triboelectric nanogenerator (TENG) was fabricated with high sensitivity, serving as the human voice monitor.

6.1 Introduction

For the original ERT method, the target materials are electrodeposited on the surface of the template. Since electroplating is an isotropic process, the resolution of the target materials pattern will decrease as the increase of deposition time. Since the resistance, which is an essential electrical parameter, will increase as the decreasing of deposition time, attaining equilibrium between the resolution and electrical performance of flexible devices presents a significant challenge. This phenomenon has been studied before, and the result is shown in Figure 6.1[26]. When the electroplating time was extended to 1.5 hours, the thickness of the electrodeposited material was around 4 µm, and the width of the line increased from 1µm to 12µm. The replication error is around 1200%. It will have serious side effects on the fabrication of high-resolution electronic devices.

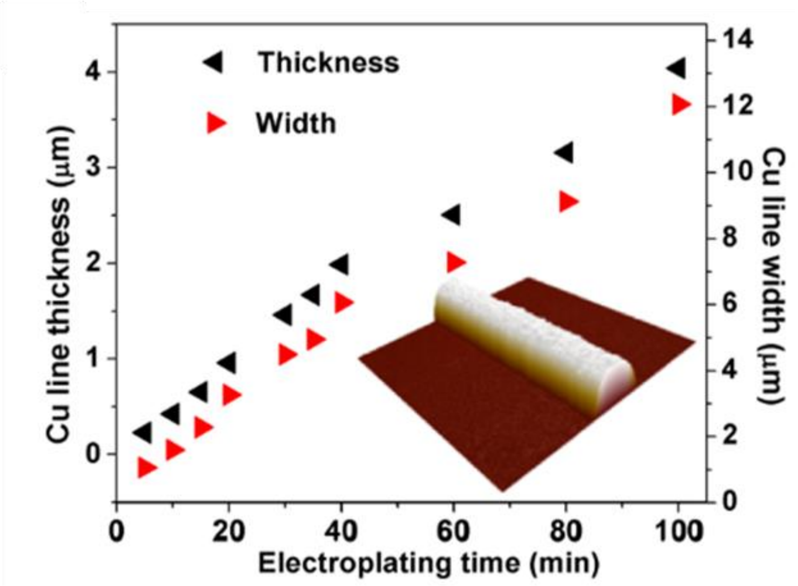

Figure 6.1 The deposition time versus pattern thickness and resolution of a Cu line pattern[26].

Another problem with the original template is that, after casting and peeling off of the binder layer, the target materials will be embedded into the binder layer[26]. AFM test was conducted on the surface of a Cu@NOA 63 sample to prove the embedded structure, as shown in Figure 6.2. Although this structure could be beneficial for most flexible electronic devices in the view of improving flexibility, it also restricts its application in some special areas such as meta-surface, pressure sensors, and so on. The ERT method should be further improved to offer more applicability for more applications.

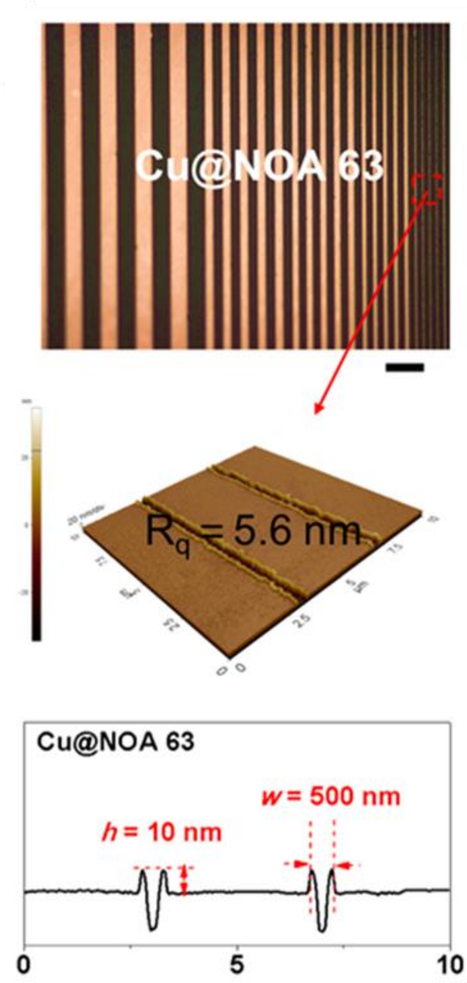

Figure 6.2 AFM test of the Cu pattern on NOA binder layer.

6.2 Illustration of 3D Structure Template for ERT

The structure of the template was modified for the purpose of fabricating a 3D structure pattern. The schematic representation of the entire fabrication process of the template, followed by the 3D pattern transfer process is shown in Figure 6.3 below. First, a conventional photolithography process was conducted on a SiO_2/Si wafer. The thickness of the SiO_2 layer could be changed for different requirements. Here a 500 nm SiO_2 was used as the demonstration. A 100 nm Cr layer was then deposited on the template by e-beam evaporation to serve as the mask during the following drying etching process. The SiO_2 and Si of the patterned area will be etched away by CF_4 and SF_6 gas, respectively. The etching depth will be the height of the 3D pattern. The fabrication of the 3D structure template will be finished after removing the residue Cr layer with a Cr etching solution. Instead of using PFDT, a silylating reagent will be used to form a SAM on the Si substrate for the pattern replication process. The template will be immersed in the 20% silylating solution for 10 minutes and then baked at 120 °C for 15 minutes. This hydrophobic layer could reduce the adhesion force between Si and the target materials fabricated during the following electrodeposition process. After the modification, the Si template will be used for the electroplating process directly. Since Si is a semiconductor while SiO_2 is an insulator, the target materials will only be electrodeposited onto the Si surface, including both the base and lateral areas of the groove. Therefore, the growth of the target materials will not change the resolution of the pattern. Finally, UV-curable binder NOA 63 will be cast onto the surface, filling the groove. The target materials will be peeled off with NOA, which is the same as the original ERT process.

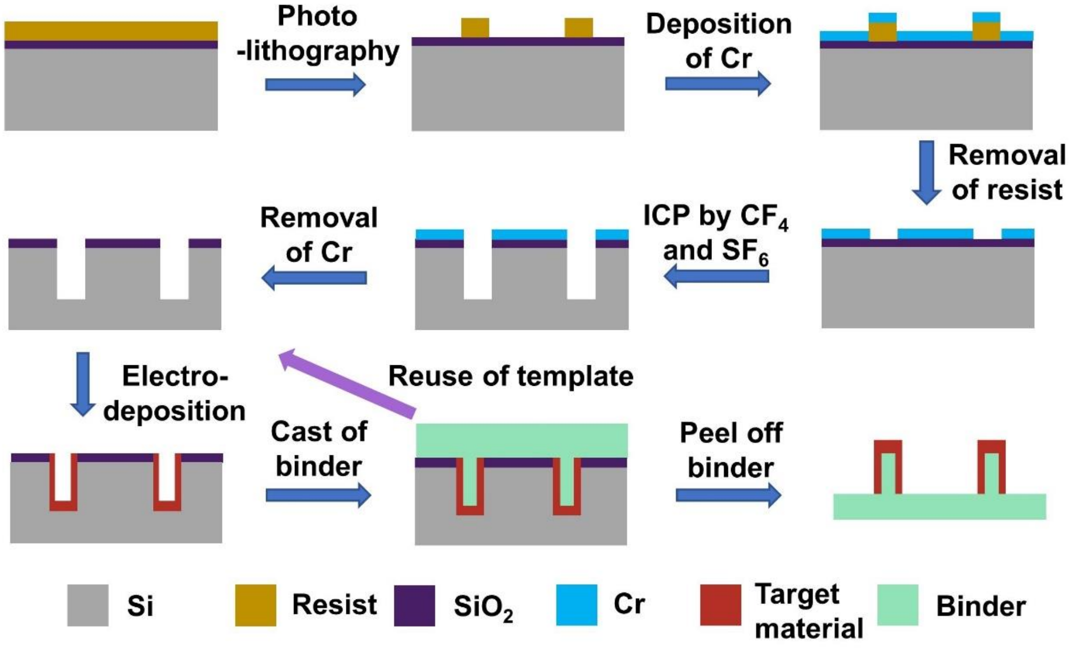

Figure 6.3 Schematic of the whole fabrication process of the template and the following 3D pattern transfer process.

6.3 Fabrication of Various 3D Patterns

6.3.1 Parallel Lines Pattern

First, a 3D template with a parallel line pattern (20 μm width and 20 μm depth) was fabricated as a demonstration. From the SEM images of the lateral sight of the template after the electrodeposition of Cu, it can be found that Cu grows along all the exposed Si surfaces, including the bottom and side walls of the groove. As the increasing of deposition time, the thickness of Cu also increases to around 1 μm when the deposition time reaches 3 hours. This structure could confine the growth of Cu in the groove area instead of increasing the line width. Although the Cu will still climb along the side wall and cause the deposition of material on the SiO_2 surface, as shown in Figure 6.4 C, this could be circumvented by augmenting the thickness of the SiO_2 layer, contingent on specific requisites.

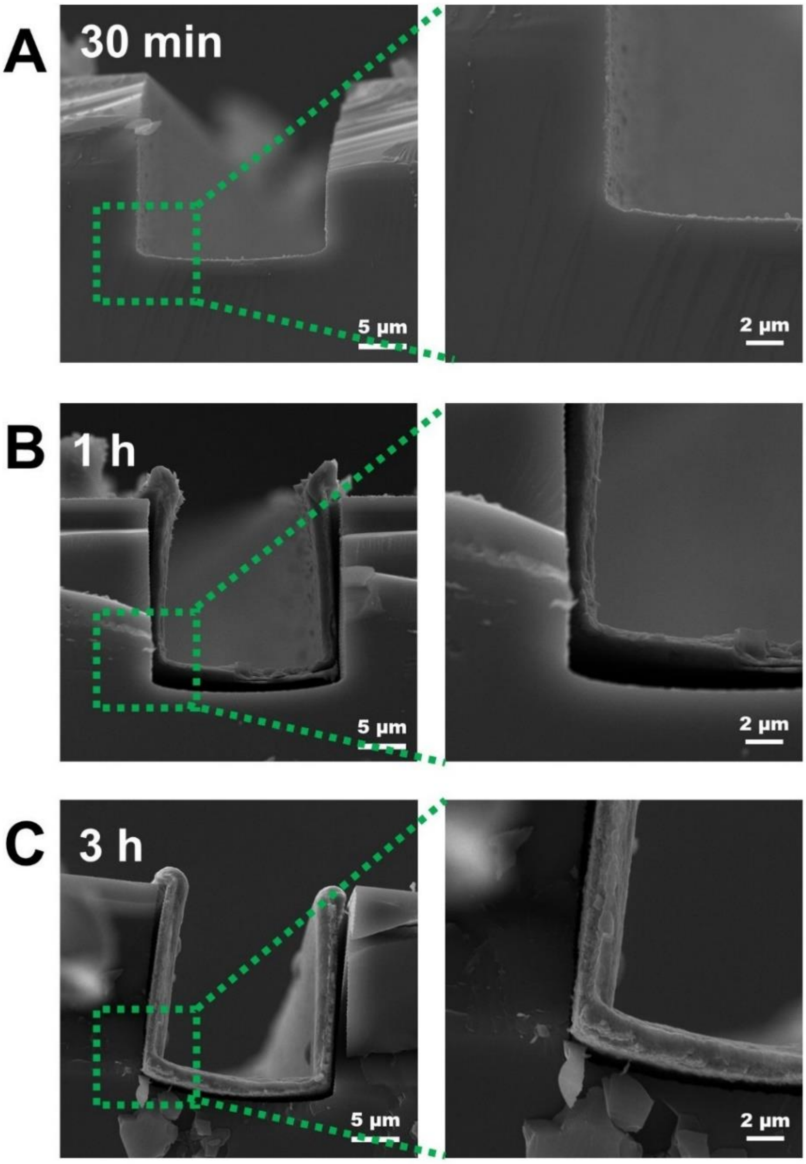

Figure 6.4 The lateral SEM images of 3D lines pattern template after different electrodeposition times. Deposition time: (A) 30 min. (B) 1 h. (C) 3 h.

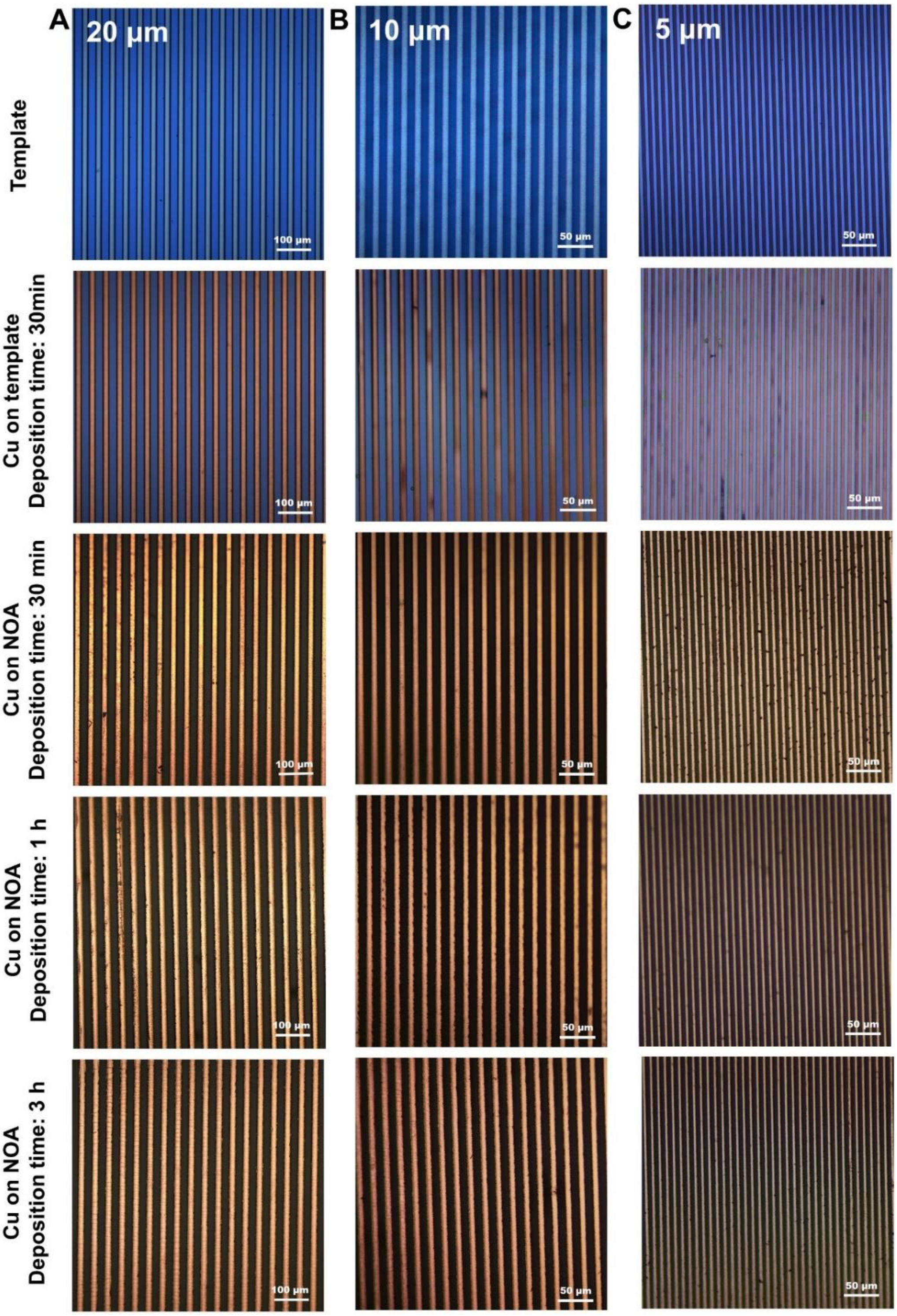

Figure 6.5 Optical images of Cu 3D lines pattern with different resolutions during of fabrication process, including template, template after deposition, peeled off by NOA binder. (A) 20 µm. (B) 10 µm. (C) 5 µm.

Lines patterns with different resolutions (20 µm, 10 µm, 5 µm) were fabricated successfully by this 3D template. Figure 6.5 shows the optical images taken during the whole process, including the pure template, the template after electrodeposition for 30 minutes and the Cu lines pattern peeled off by NOA binder with different deposition times. There is no discernible alteration in the line width after different electrodeposition times for all the resolution ranges.

The whole fabrication process is also characterized by the EDX test. The Si and O elements in Figure 6.6 A represent the SiO_2 layer, while the Cu covers the patterned area. After the transfer process, the Cu was transferred to a PET substrate using NOA as the binder. There are no Si elements, while the S represents the NOA layer.

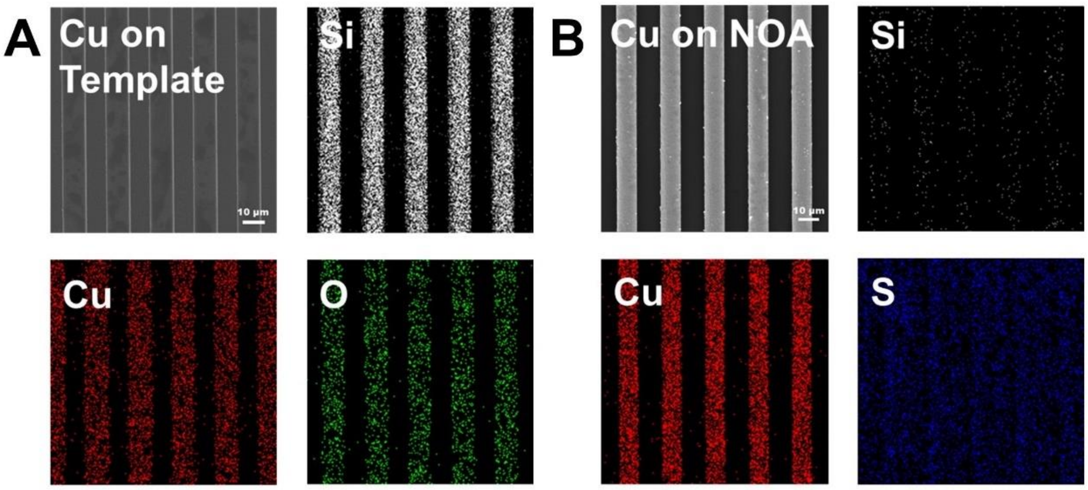

Figure 6.6 EDX results during the fabrication of lines pattern. (A) The template after electrodeposition of Cu. Elements: Si, Cu, and O. (B) Cu pattern on the NOA substate. Elements: Si, Cu, and S.

The dry-etching of Si is a mature technology. It is easy to obtain vertical 3D structures with different aspect ratios on Si substrate with a high resolution reaching the nanoscale[219, 220]. Considering the high surface energy during the peeling-off process, 3D line patterns with different aspect ratios were designed ranging from 1:1 to 1:4. The heights are all 20 μm for the line patterns with different resolutions. Figure 6.7 shows the cross-section SEM images of these Cu line patterns transferred by the NOA binder layer. The Cu (light area) covers the patterned area and the side wall of the 3D lines. As the increasing of the electrodeposition time, the thickness of the Cu layer will also increase, which corresponds to the change shown in Figure 6.4.

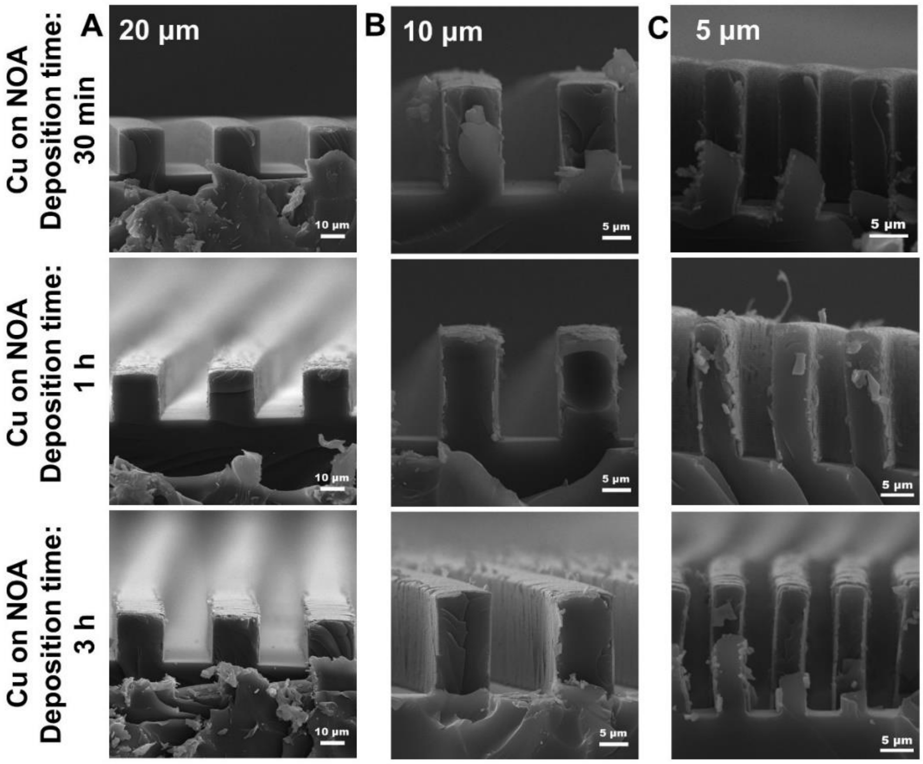

Figure 6.7 Cross-section SEM images of the line patterns with different resolutions and aspect ratios after different deposition times (30 min, 1h, and 3h). (A) Line width: 20 μm; Height: 20 μm; Aspect ratio: 1:1. (B) Line width: 10 μm; Height: 20 μm; Aspect ratio: 1:2. (C) Line width: 5 μm; Height: 20 μm; Aspect ratio: 1:4.

The resolution could be increased to 2 μm, which is also the limit of the photolithography at the lab level. As shown in Figure 6.8, the SEM images prove the successful fabrication of the 3D line pattern with 2 μm and 3 μm. The height of the pattern is around 2 μm. There are no cracks on the surface of the lines.

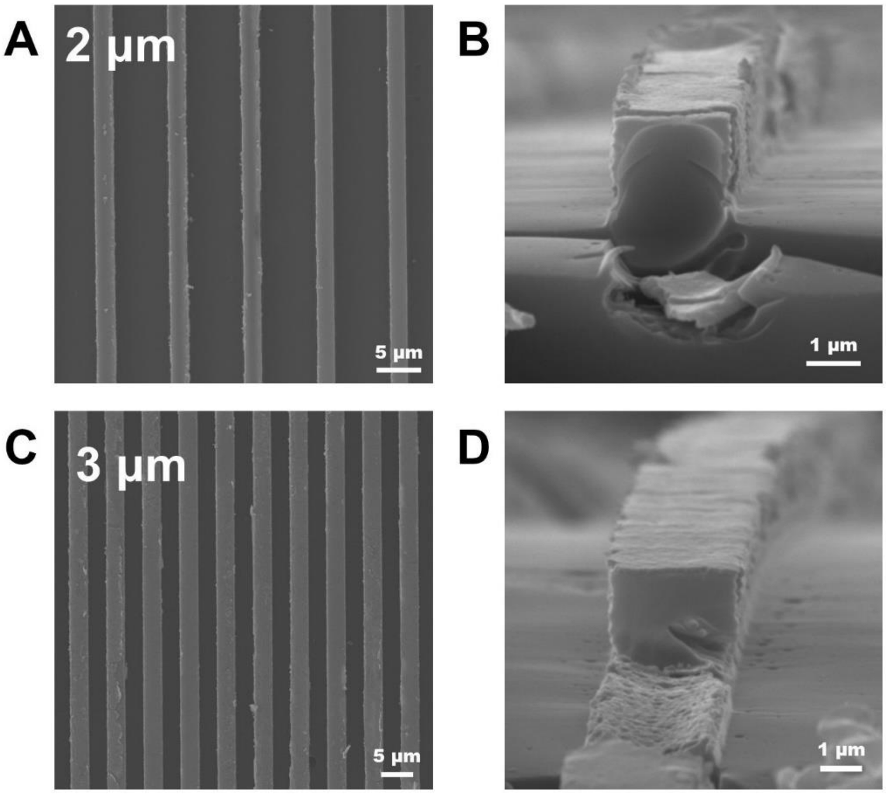

Figure 6.8 SEM images of the high-resolution line pattern. (A) 2 μm lines pattern. (B) Cross-section image. Height: 2 μm. (C) 3 μm lines pattern. (D) Cross-section image. Height: 2 μm. Deposition time: 30 minutes.

6.3.2 Fabrication of Various Materials

Apart from Cu, other materials such as Au, Ag and Ni could also be applicable, as shown in Figure 6.9. The optical images and the corresponding XRD results proved the successful fabrication of the 3D 10 μm lines pattern.

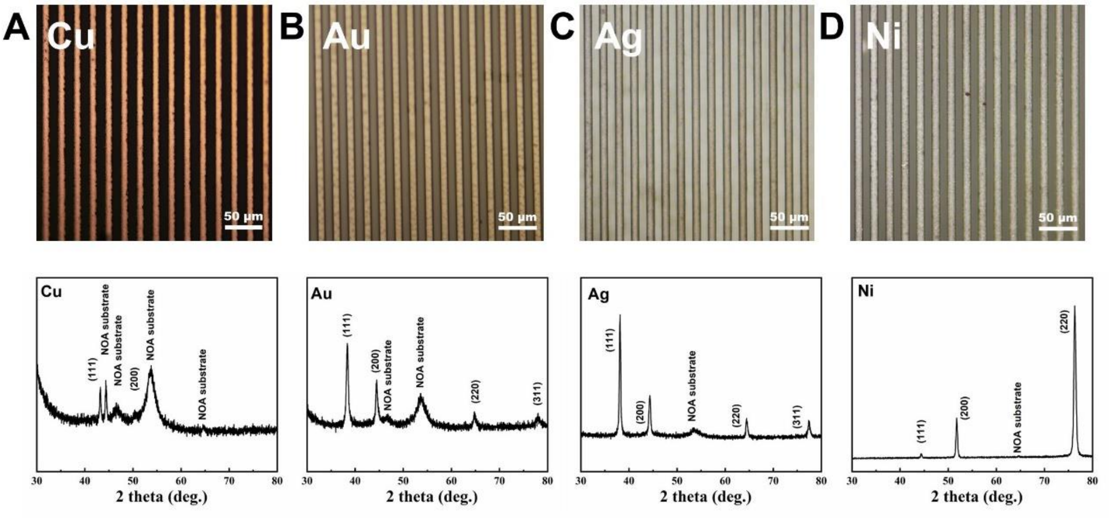

Figure 6.9 Fabrication of lines pattern with different materials and the corresponding XRD results. (A) Cu. (B) Au. (C) Ag. (D) Ni.

6.3.3 Fabrication of Isolated Patterns

Although the SiO_2 layer is an insulator, the Si layer is continuous, which is apt for the creation of isolated patterns, such as an array of dots. Figure 6.10 illustrates the fabrication of a 3D circle dots array. The optical pictures of the 3D template are showcased in Figure 6.10 A. The diameter of the circle dots is 50 µm. After different deposition times ranging from 30 min to 3 h, there is no increase in the diameter of the transferred Cu dots pattern on the PET substrate. There are also no obvious cracks shown on the transferred dot patterns, which are proven by both optical and SEM images. The cross-section SEM image shows that the thickness of the dots is around 20 µm, which means that the aspect ratio is 5:2.

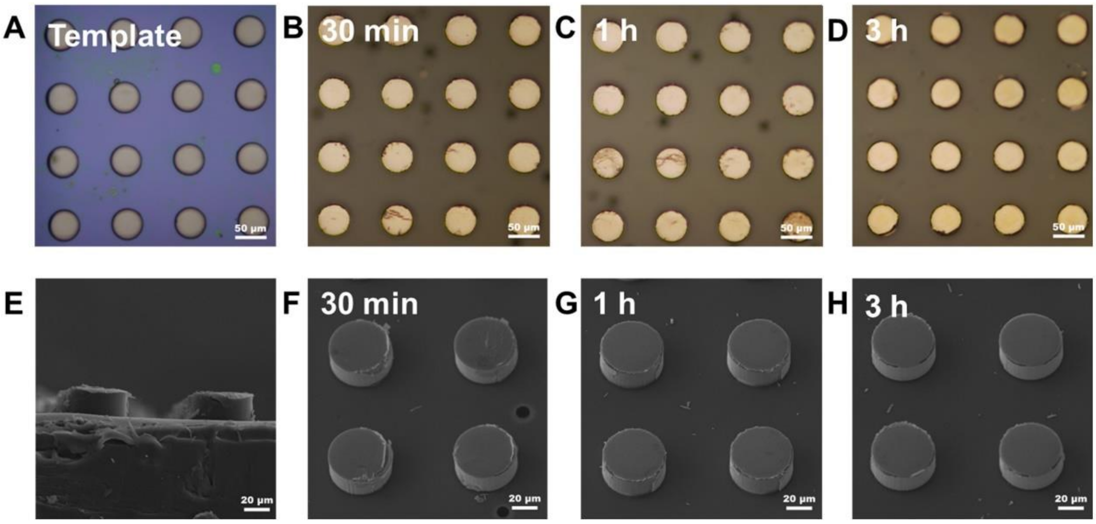

Figure 6.10 Fabrication of 3D circle dots array. (A) Template of 50 µm circle dots array pattern. (B-D) Optical images of the 3D Cu circle dots array pattern transferred to PET substrate by NOA binder. Electrodeposition time: B: 30 min; C: 1 h; D: 3 h. (E) Cross-section SEM image of the circle dots array pattern. Height: 20 µm. (F-H) SEM images of the 3D Cu circle dots array pattern transferred to PET substrate by NOA binder. Electrodeposition time: B: 30 min; C: 1 h; D: 3 h.

Apart from the circle dots array, the square dots array is also applicable. The optical images of the template and 3D Cu pattern are shown in Figure 6.11. The side length is 50 µm. There is still no change in the side length, no matter how long the deposition time is. However, different from the circle dots array, there are some cracks on the surface of the square dots. This can be ascribed to the concentration of stress at the four corners of the square pattern[221]. It is hard to avoid the shear stress during the peeling-off process. The cross-section SEM image shows that the thickness of the dots is around 20 µm, which means that the aspect ratio is 5:2.

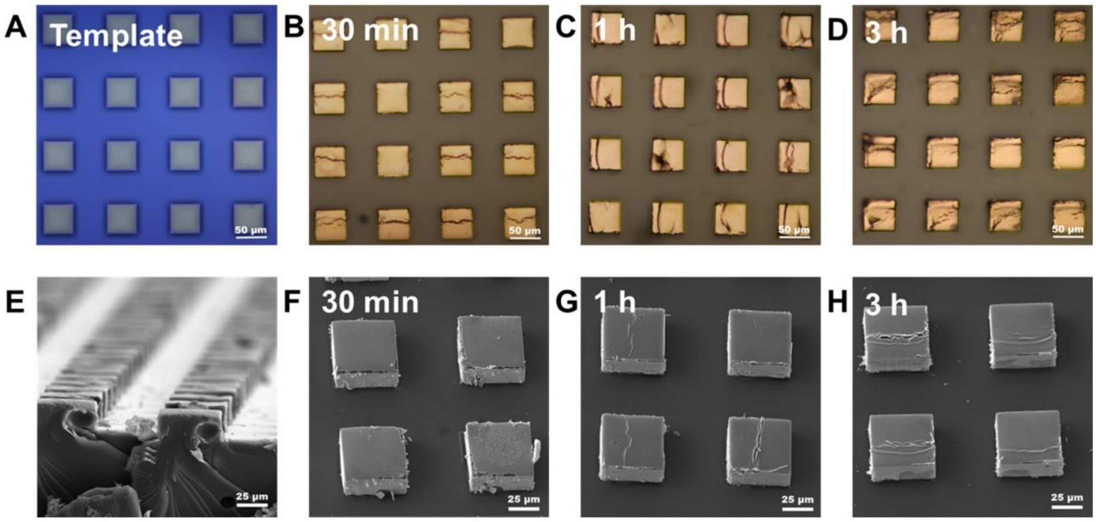

Figure 6.11 Fabrication of 3D square dots array. (A) Template of 50 μm square dots array pattern. (B-D) Optical images of the 3D Cu square dots array pattern transferred to PET substrate by NOA binder. Electrodeposition time: B: 30 min; C: 1 h; D: 3 h. (E) Cross-section SEM image of the square dots array pattern. Height: 20 μm. (F-H) SEM images of the 3D Cu square dots array pattern transferred to PET substrate by NOA binder. Electrodeposition time: B: 30 min; C: 1 h; D: 3 h.

For both the circle and square dots array pattern, the corresponding EDX results also prove the successful fabrication of a 3D Cu dots array. The Cu element only showed on the patterned array area. The S element corresponds to the NOA binder layer.

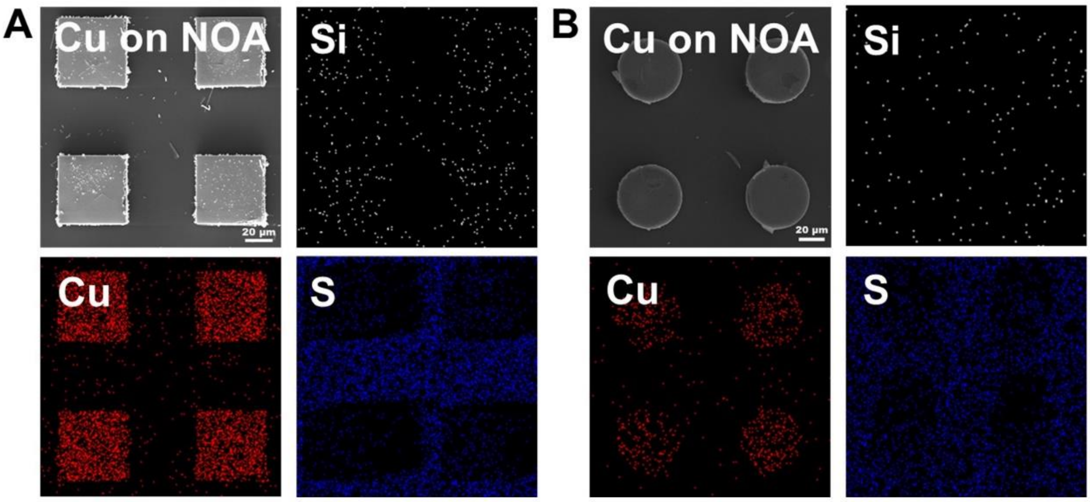

Figure 6.12 EDX results during the fabrication of dots array pattern. (A) Square dots array on NOA binder. Elements: Si, Cu, and S. (B) Circle dots array on NOA binder. Elements: Si, Cu, and S.

6.4 Application for Flexible Transparent Electrodes

6.4.1 Fabrication of 3D Mesh Pattern

Apart from basic shapes like lines and dots, it is also able to fabricate complicated patterns such as mesh patterns, which have significant potential in the field of transparent electrodes. The optical images in Figure 6.13 show the successful fabrication of a 3D Cu mesh pattern with a 10 μm line width and 200 μm line gap. As the increasing of electrodeposition time, the line width of the Cu meshes peeled off by the PET substrate is almost unchanged from the view of optical images. There are no obvious broken or cracks on the mesh pattern.

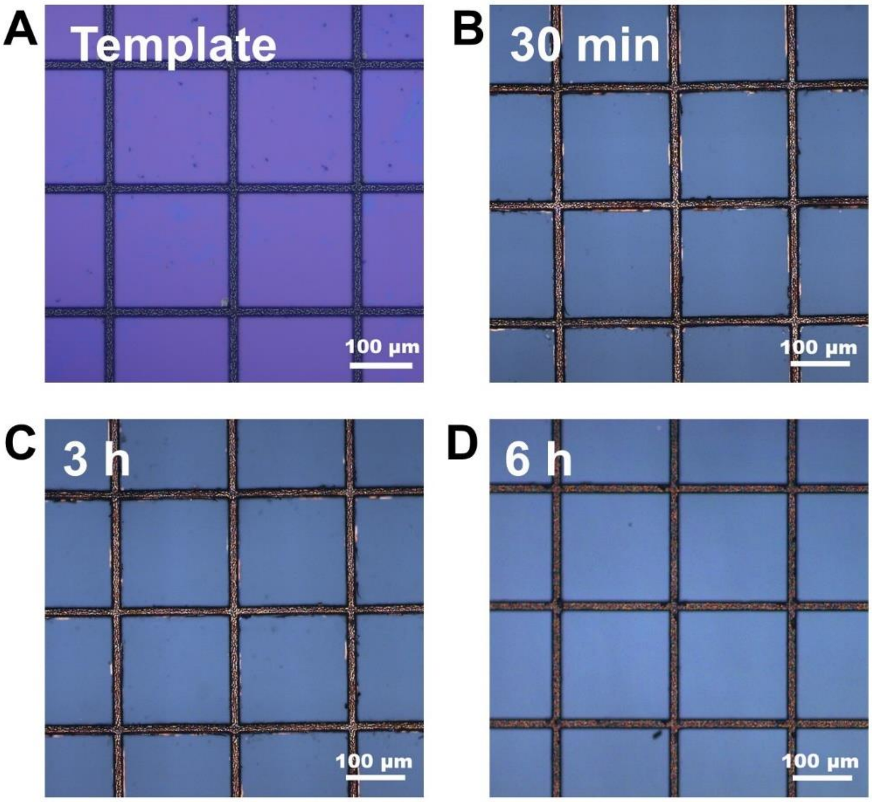

Figure 6.13 Optical images of 3D mesh pattern with 10 µm line width, 200 µm gap and 10 µm height. (A) Template. (B-D) The cu pattern on PET. Deposition time: B-30 min, C-3 h, D-6 h.

Figure 6.14 is the optical surface profiler results of the Cu mesh patterns transferred to the PET substrate with various electroplating times. The height of the mesh pattern is around 10 µm.

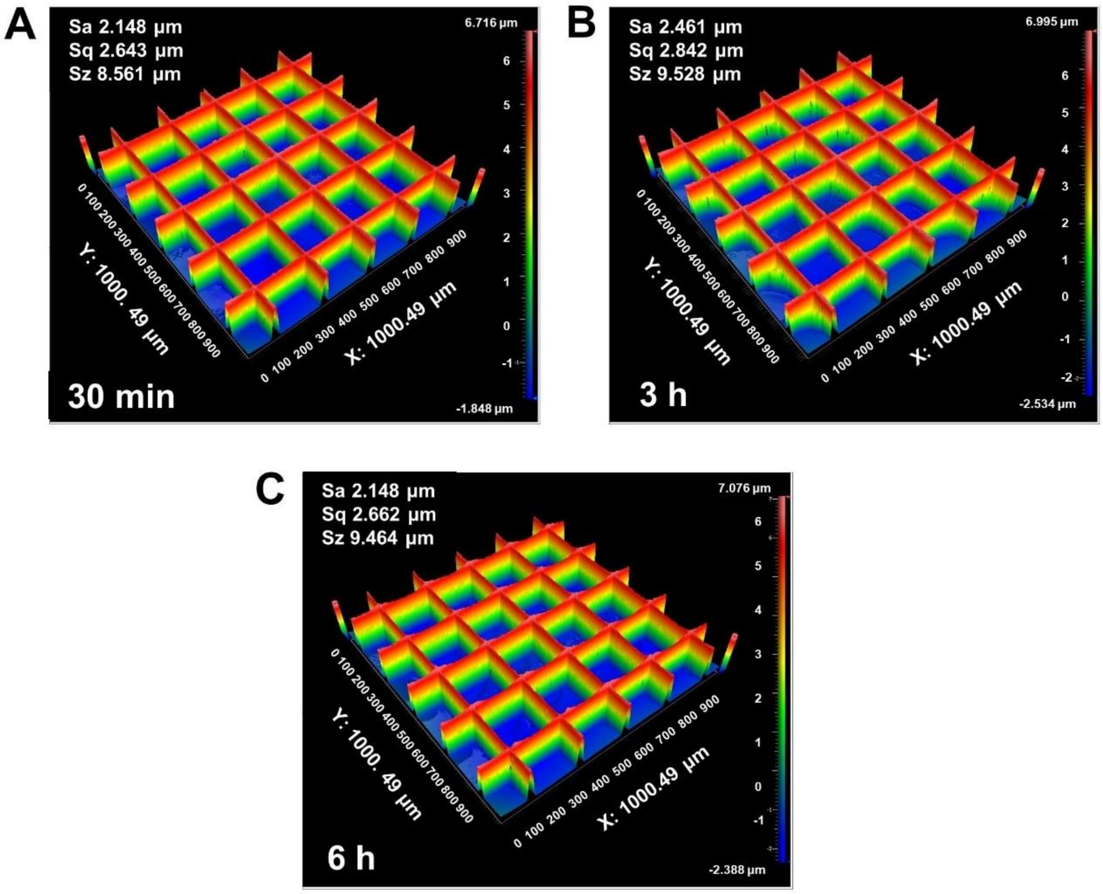

Figure 6.14 Optical surface profiler test of 3D mesh pattern with 10 μm line width, 200 μm gap and 10 μm height fabricated by different deposition times. (A) 30 min. (B) 3 h. (C) 6 h.

6.4.2 Comparison with the Original Template

The mesh pattern electrode has great advantages in the field of transparent electrodes due to the great balance between low sheet resistance and high transparency.

For the metal mesh electrode fabricated by the electroplating process, the sheet resistance will be greatly reduced as the increasing of electroplating time. However, for the original ERT template, the growth of materials is isotropic. The line width will be enlarged as the increase of deposition time as shown in the optical graphics in Figure

6.15. For the mesh pattern with a 5 µm line width and 200 µm gap, the line width increased from 5 µm to 25 µm as the deposition time was extended from 5 minutes to 3 hours.

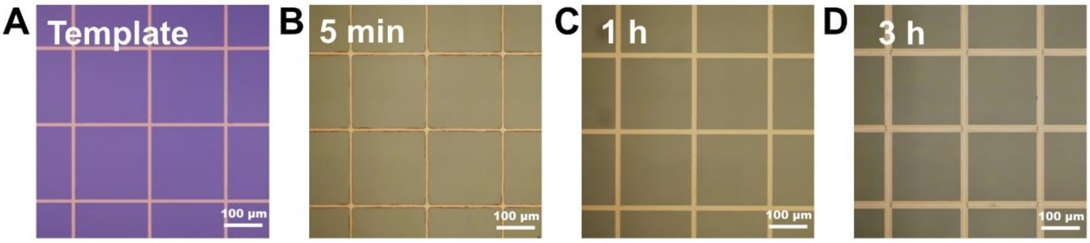

Figure 6.15 Optical images of the mesh pattern fabricated by the original template with a 5 µm line width and 200 µm gap. (A) Template. (B-D) Cu mesh pattern transferred to PET by NOA binder. Deposition time: B-30 min, C-1 h, D-3 h.

Compared with the original ERT template, the 3D structure template has great advantages in the aspect of maintaining the resolution. As showcased in Figure 6.16, for the 3D mesh pattern with the same parameters, the line width of the transferred pattern is almost unchanged even when the deposition time was increased to 6 hours.

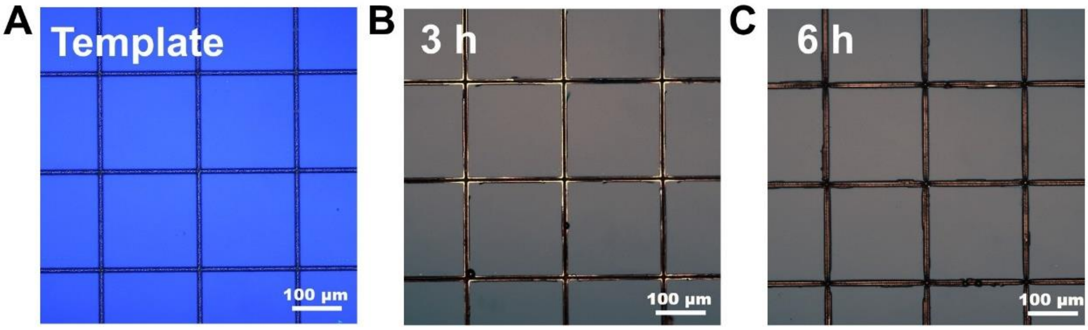

Figure 6.16 Optical images of 3D mesh pattern with 5 µm line width, 200 µm gap and 10 µm height. (A) Template. (B-C) The cu pattern on PET. Deposition time: B-3 h, C-6 h.

The transmittance of these mesh pattern electrodes could directly reflect the advantages of the 3D structure pattern (Figure 6.17). For the mesh pattern electrodes fabricated by the original ERT template, the transmittance at 550 nm wavelength decreased from 91.03% to 82.37% as the electrodeposition time increased from 5 minutes to 3 hours. For the 3D structure pattern, the transmittance is almost unchanged when the deposition time increases from 3 hours to 6 hours. The transmittance is around 86%, which is slightly lower than the mesh pattern electrodes fabricated by 5 minutes of deposition. It can be explained that the dry etching process may cause a slight growth in the line width. Furthermore, concomitant with an augmentation in deposition duration, the electrodeposited materials will still grow out of the groove area and cause a decrease in transparency. This issue could be partially mitigated by augmenting the thickness of the insulating SiO_2 layer. Predominantly, the reduction in the sheet resistance of the mesh electrodes tends to plateau when the deposition duration exceeds three hours at a current density of 1 mA cm^{-2}, as illustrated in Figure 6.18. The marginal alteration in transparency exerts minimal impact on the performance of the mesh pattern transparent electrodes.

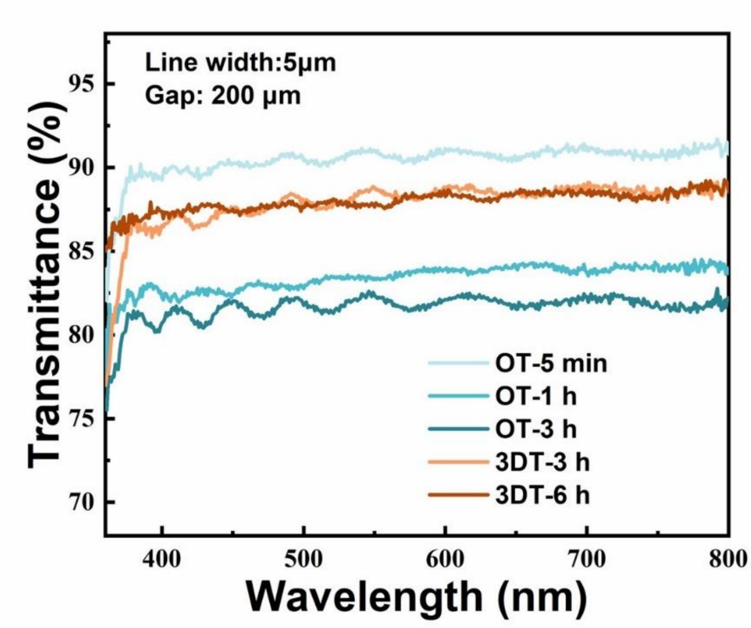

Figure 6.17 UV-vis spectra of the 5 μm mesh pattern transparent electrodes fabricated by the original template and 3D template with different deposition times.

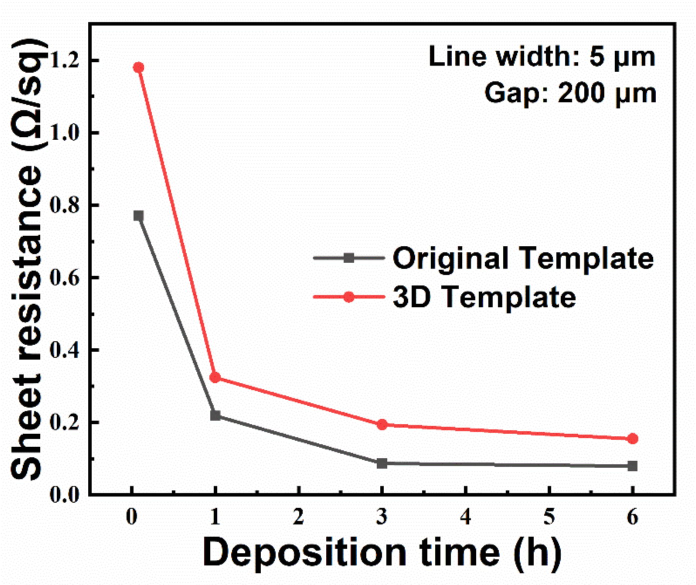

Figure 6.18 Resistance versus the electrodeposition time for the mesh electrodes fabricated by the original and 3D template. Line width: 5 μm, line gap: 200 μm.

6.4.3 Adjustment of the Figure of Merit

The evaluation of transparent electrodes is largely determined by the sheet resistance and transparency. As it is a common problem to achieve a balance between these two factors, there is a value called Figure of Merit (FoM), which could be used to evaluate the performance index of transparent electrodes. The FoM could be calculated by the equation (6.1) below:

$$FoM = \frac{188.5}{R_s\left(\frac{1}{\sqrt{T}} - 1\right)} \tag{6.1}$$

R_s represents the measured sheet resistance, and T represents the transmittance. A higher FoM value means a better performance of the transparent electrode.

For the electrodeposited mesh pattern electrodes, it can adjust the performance of the transparent electrodes by adjusting the line width, line gap, and deposition time. Due to the advantage of the 3D structure template, the influence of the deposition time could be eliminated. The deposition time could all be increased to 3 hours at a current density of 1 mA cm^{-2}. Therefore, we tried to adjust the line width and gap to achieve a higher FoM. As shown in Figure 6.19, the parameter of sample A is 5 μm width, 200 μm gap and 20 μm height, which was used to compare the influence of the height. The parameter of sample B is 3 μm width, 200 μm gap and 3 μm height, which was used to control the line width and achieve a higher transparency. The parameter of sample C is 5 μm width, 500 μm gap and 20 μm height, which was used to control the line gap and achieve a higher transparency. The parameter of sample D is 20 μm width, 500 μm gap and 20 μm height, which was used to achieve a balance between sheet resistance and transparency.

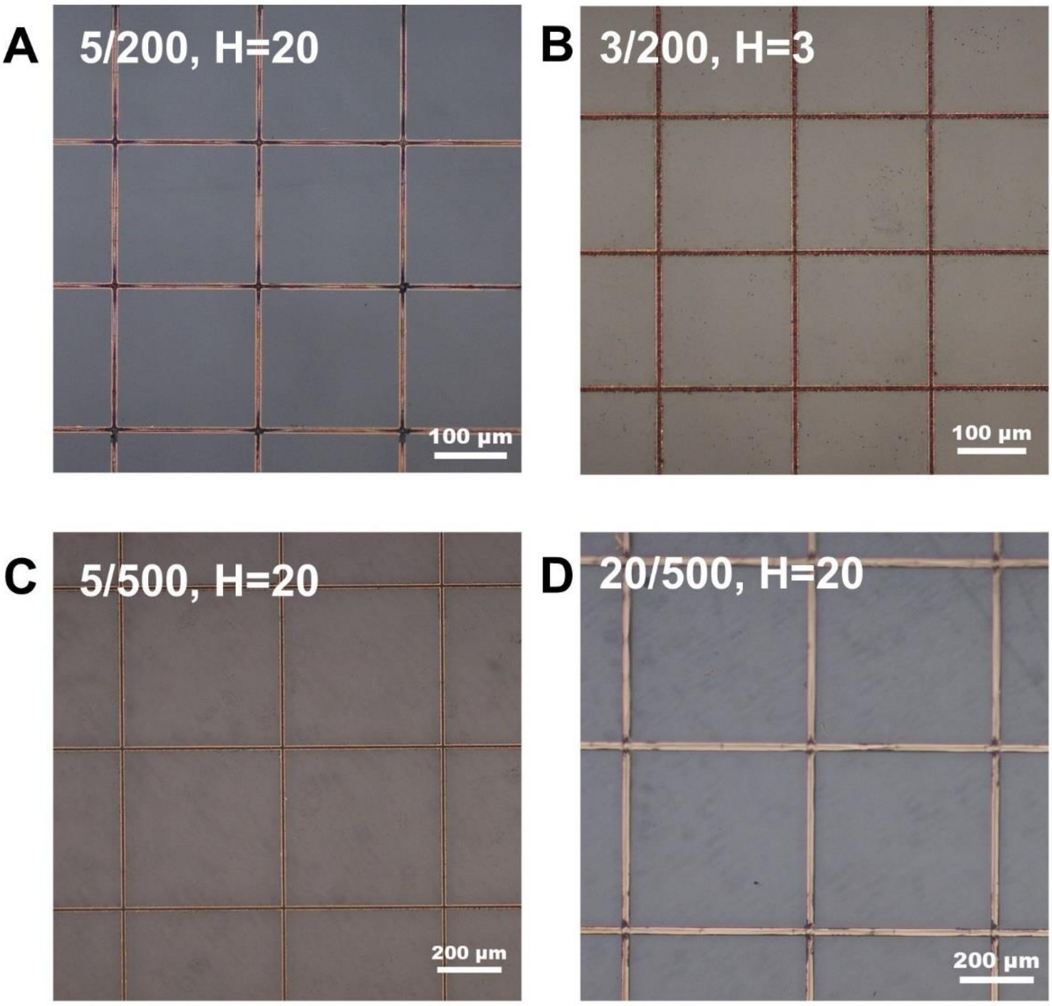

Figure 6.19 Optical images of 3D mesh pattern with different parameters. (A) Line width: 5 µm, gap: 200 µm, height: 20 µm. (B) Line width: 3 µm, gap: 200 µm, height: 3 µm. (C) Line width: 5 µm, gap: 500 µm, height: 20 µm. (D) Line width: 20 µm, gap: 500 µm, height: 20 µm.

The UV-vis spectra result of these transparent mesh pattern electrodes is shown in Figure 6.20 below, including the mesh pattern with a 10 µm line width, 200 µm line gap and 10 µm height.

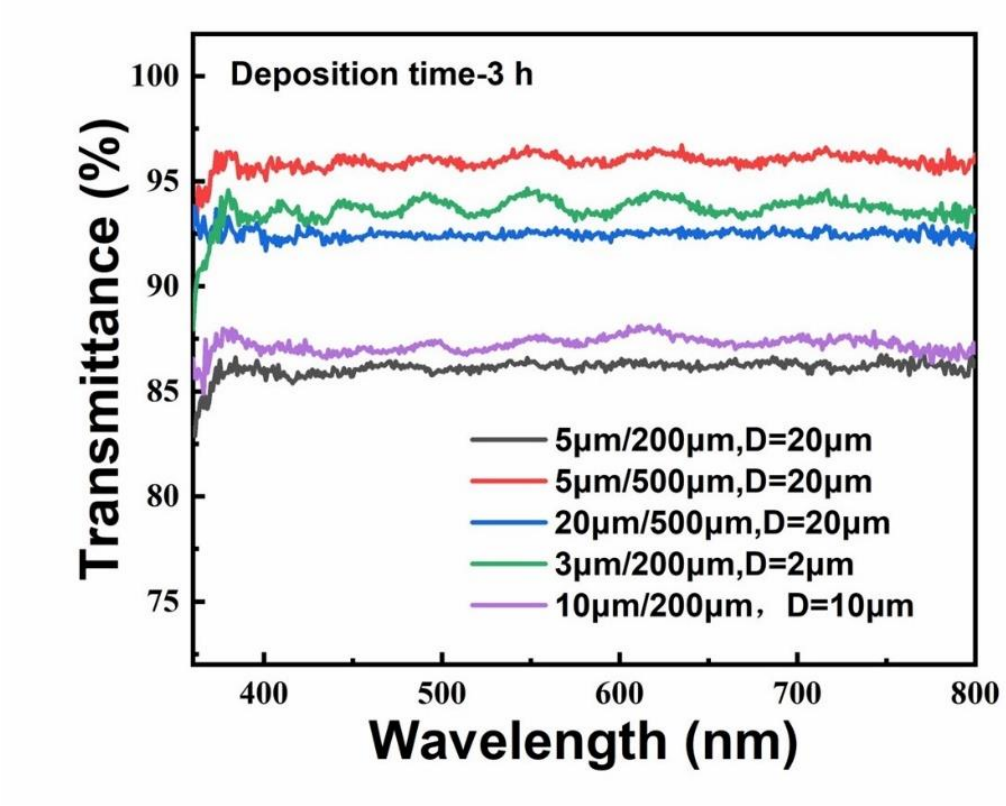

Figure 6.20 UV-vis spectra of the 3D mesh pattern with different parameters.

After collecting the sheet resistance of these transparent electrodes, the corresponding FoM values could be calculated based on equation (6.1), and the results of all the transparent electrodes fabricated before were listed in Table 6.1 below. It can be found that the transparent mesh pattern electrode with a 10 μm line width, 200 μm line gap and 10 μm height achieves the best performance among all the transparent electrodes fabricated in this project. The transmittance at 550 nm wavelength is 86.89%, and the sheet resistance is 0.0815 Ω/sq. The FoM value could reach a high value of 31774. By adjusting the parameters of line width, line gap and line height, the transmittance of the transparent electrodes fabricated by the 3D structure template could be up to 96.39%, and the lowest sheet resistance could reach 0.0799 Ω/sq. The transparent electrodes fabricated by the 3D structure template could satisfy various application environments based on real demands.

Table 6.1 Summary of the parameters, transmittance, sheet resistance and FoM of the various 3D mesh pattern transparent electrodes fabricated before.

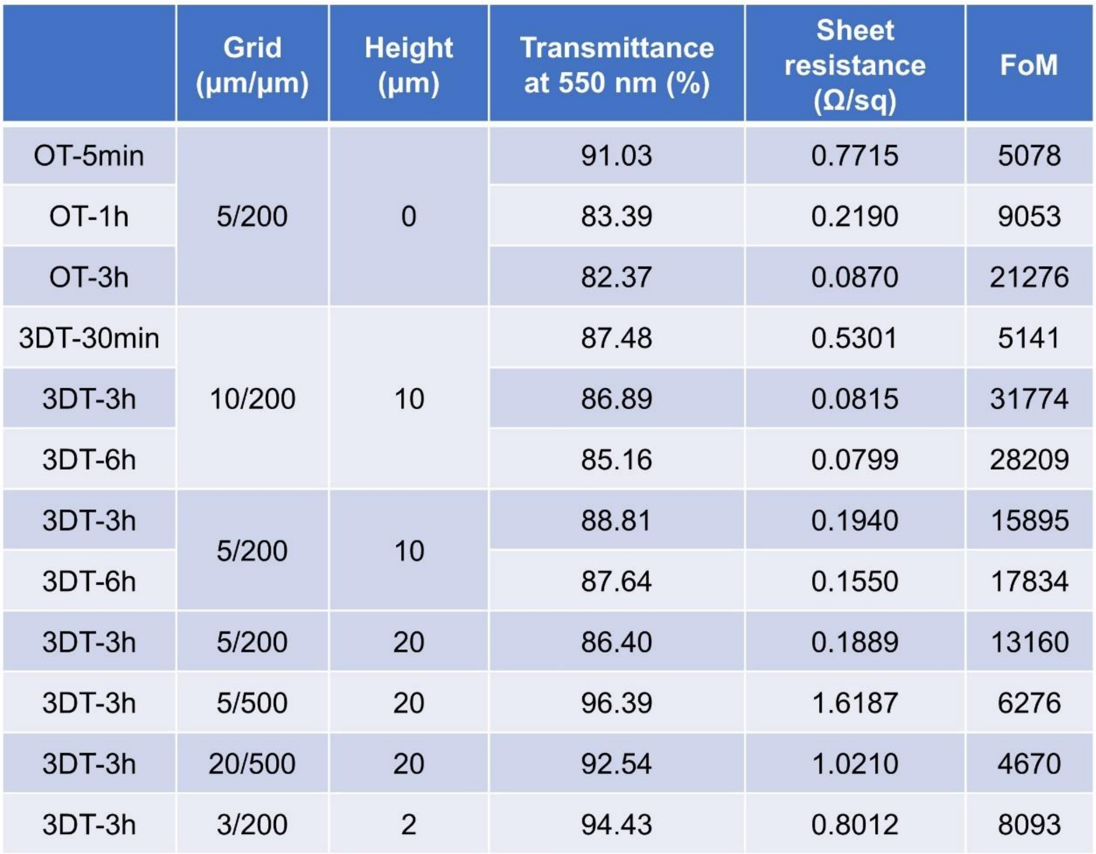

	Grid (μm/μm)	Height (μm)	Transmittance at 550 nm (%)	Sheet resistance (Ω/sq)	FoM
OT-5min	5/200	0	91.03	0.7715	5078
OT-1h			83.39	0.2190	9053
OT-3h			82.37	0.0870	21276
3DT-30min	10/200	10	87.48	0.5301	5141
3DT-3h			86.89	0.0815	31774
3DT-6h			85.16	0.0799	28209
3DT-3h	5/200	10	88.81	0.1940	15895
3DT-6h			87.64	0.1550	17834
3DT-3h	5/200	20	86.40	0.1889	13160
3DT-3h	5/500	20	96.39	1.6187	6276
3DT-3h	20/500	20	92.54	1.0210	4670
3DT-3h	3/200	2	94.43	0.8012	8093

Figure 6.21 is the comparison of optoelectronic performance between our 3D Cu mesh-based flexible transparent electrodes (FTEs) and other typical transparent electrodes (TEs) published previously, including Indium Tin Oxide (ITO)[222], Ag nanowires[223], carbon nanotubes[224], graphene[225], Ag nanofibres[226], other metal meshes[227-233]. Our 3D Cu mesh-based FTEs have better performance with higher FoM values among all the TEs.

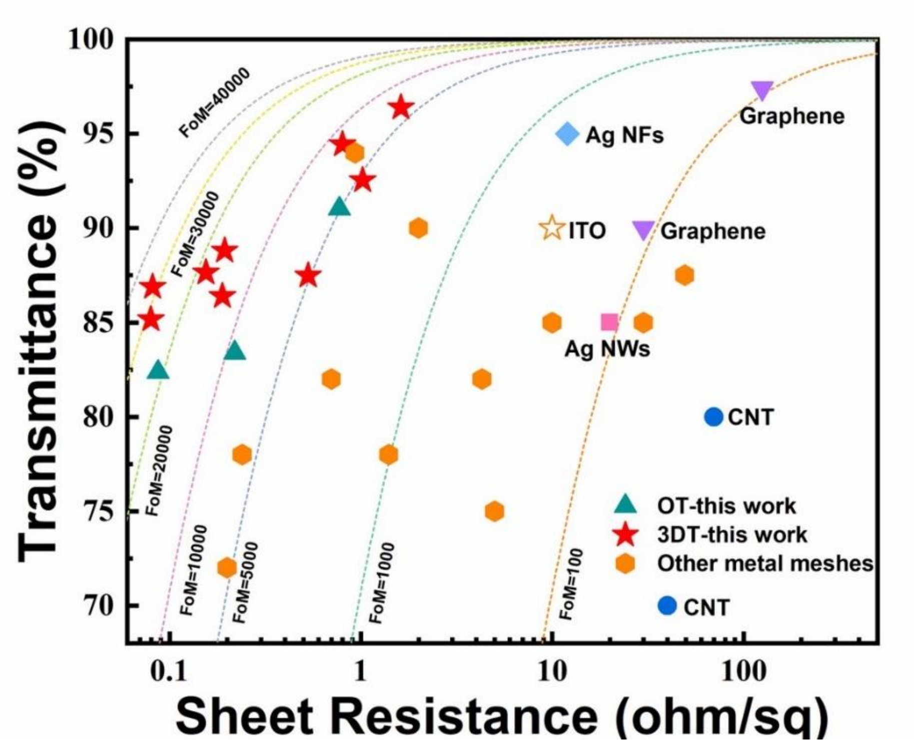

Figure 6.21 A comparative analysis of the optoelectronic performance between our 3D Cu mesh-based flexible transparent electrodes and other typical transparent electrodes previously published, inclusive of Indium Tin Oxide (ITO)[222], Ag nanowires[223], carbon nanotubes[224], graphene[225], Ag nanofibers[226], other metal meshes[227-233].

6.4.4 Applied to Flexible Transparent Heaters

The 3D metal mesh pattern could obtain good flexibility after being encapsulated by another NOA binder layer, which protects the metal from cracks during the bending process (Figure 6.22 C). The digital images in Figure 6.22 show the testing status of the encapsulated mesh pattern electrodes utilizing the bending machine at a minimal bending radius of 2 mm. The resistance change of the transparent electrodes is smaller than 1.5 even at a minimal bending radius of 2 mm after 1000 cycles.

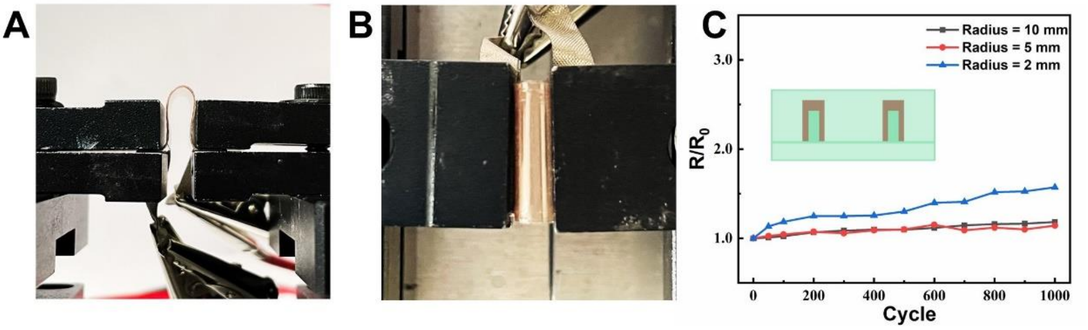

Figure 6.22 Flexibility test of the 3D mesh pattern electrode. (A) Side view a digital image of the sample under testing. (B) Top view a digital image of the sample under testing. (C) Resistance changes of the 3D mesh pattern electrode under different bending radii. Insert image: Illustration of the 3D mesh pattern electrode with NOA encapsulation.

The flexible transparent electrodes encapsulated by the NOA binder layer could be applied as the electrodes for flexible transparent heaters (FTH) as shown in Figure 6.23 A. The IR image was taken at a constant input voltage of 1.2 V. The highest temperature degree could reach 114 °C and the distribution of the heat is homogenies. Figure 6.23 B is the temperature profile of the flexible transparent heater over time at different input voltages. The temperature of the heater could be adjusted by changing the input voltage with a range from 30 °C to 114 °C with a small voltage from 0.3 V to 1.2 V. The heating process could finish within 30 seconds and remain in a stable status at the maximum temperature. The input power density could be calculated based on the maximum temperature at different input voltages as shown in Figure 6.23 C. The slope of the plot reveals the high-power efficiency of our FTH reaching 277 °C cm^2 W^{-1}.

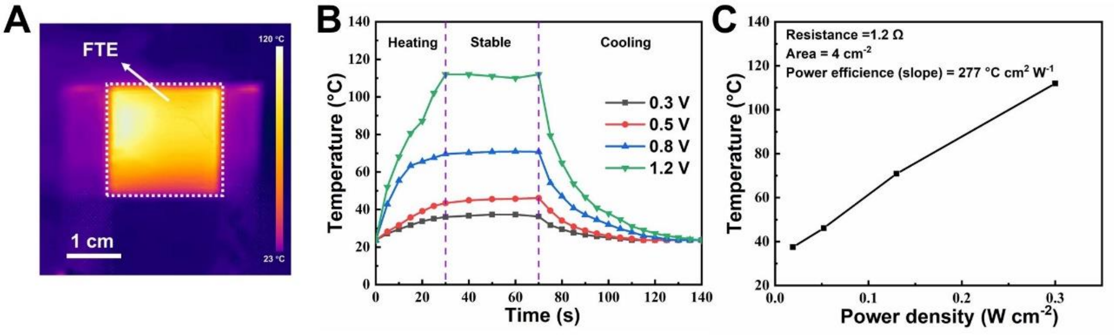

Figure 6.23 3D mesh pattern electrode-based flexible transparent heater. (A) IR image of the transparent electrode at a constant input voltage (1.2 V). (B) The temperature profile of the FTH over time, under the application of varying voltages. (C) The graph depicting the correlation between the FTH temperature at a steady state and the calculated input power density.

6.5 Application for Flexible Self-Powered Pressure Sensors

As one of the most basic and important components of IoT, flexible pressure sensors hold a pivotal role in the domain of detecting human body motion and simulating external pressure[234]. Irrespective of the underlying mechanism or material of the flexible pressure sensor, the construction of a microstructure is deemed an efficacious method to improve the compressibility and sensitivity of the sensor[235]. Diverse microstructures, including pyramids, hemispheres, pillars, and porosity, are typically fabricated using intricate methods, such as photolithography on the Si mold. However, these methods are complex and not amenable to large-scale preparation[236]. Therefore, 3D-ERT is suitable for the fabrication of flexible pressure sensors with complex microstructures due to its advantages of large-scale replication models.

6.5.1 Illustration and Mechanism

Here we fabricated a triboelectric nanogenerator (TENG) based flexible pressure sensor. The Cu electrode with microstructure was fabricated by the 3D-ERT method. The counter electrode was composed of a Cu current collector and a PDMS triboelectric layer. The structure of the whole device and the working mechanism are showcased in Figure 6.24. As the increasing of the pressure, the contact area between Cu and PDMS will increase because of the elastic property of the PDMS. Therefore, the output will change with the pressure. The deformation of PDMS will also induce a shift in capacitance, contributing to the alteration in output.

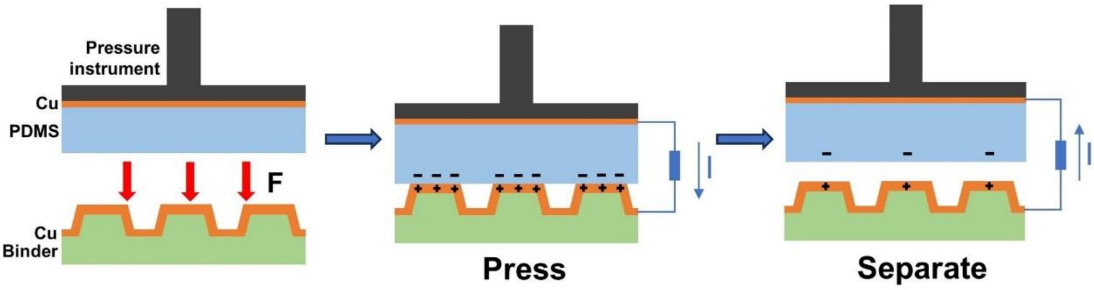

Figure 6.24 A schematic representation elucidating the operational mechanism of the self-powered pressure sensor predicated on the TENG.

6.5.2 Performance of Electrodes with Various Patterns

3D-ERT is suitable for the fabrication of various isolated patterns with different shapes and resolutions. As shown in Figure 6.25, the optical images and optical profiler results show the successful fabrication of isolated dots array pattern with 4 µm height. The shape includes a circle and a square while the resolution ranges from 20 µm to 50 µm.

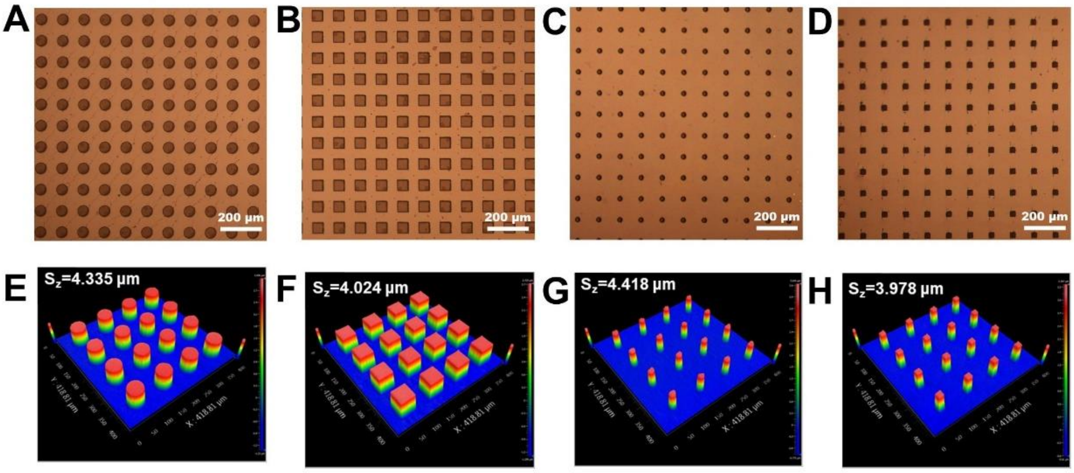

Figure 6.25 Fabrication of 3D dots array electrodes with different resolutions and shapes for pressure sensors. Optical images of the electrodes with (A) 50 µm circle, (B) 50 µm square, (C) 20 µm circle, and (D) 20 µm square. (E-H) The corresponding optical surface profiler images. The height of the dots array is around 4 µm.

Applied this microstructure array as electrodes for the TENG-based pressure sensors, they all show a good sensitivity, especially at a low-pressure range from 0 to 10 kPa (Figure 6.26 A). For the dots array with larger diameter, the sensitivity is higher which reaches around 0.6 kPa^{-1} while the sensitivity is only around 0.2 kPa^{-1} for the 20 µm dots array. The shape of the dots array has almost no influence on the sensitivity. The response time is very short reaching only 0.109 s (Figure 6.26 B).

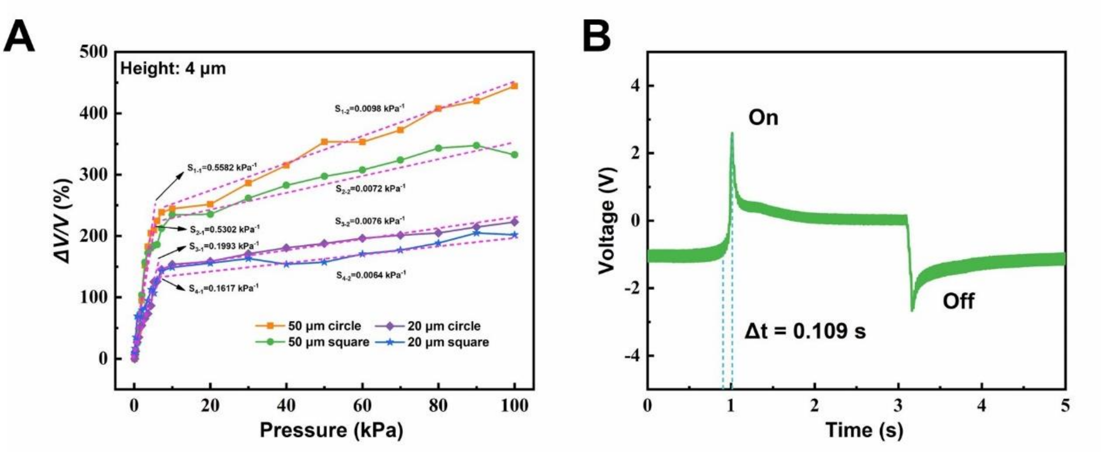

Figure 6.26 (A) The change of voltage output under different pressures for sensors with different shapes. (B) Response time for the pressure sensor.

Taking 50 μm circle dots as an example, electrodes with different heights (14 μm and 20 μm) were also fabricated (Figure 6.27 A and B). The sensitivity is almost unchanged with the increase in height. However, the higher 3D sensor has a slightly larger sensitivity range as showcased in Figure 6.27 C.

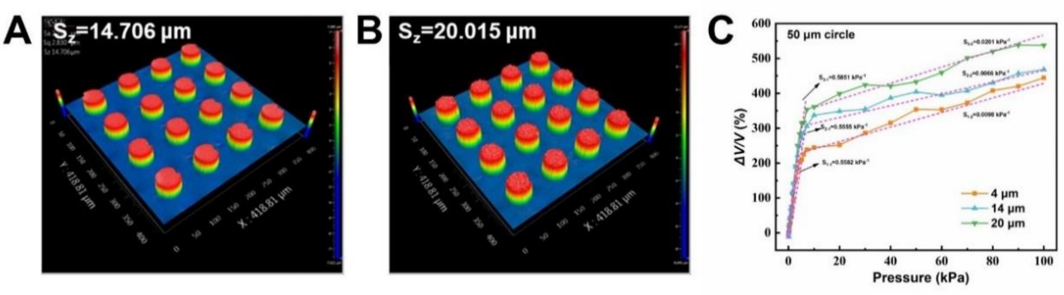

Figure 6.27 Optical surface profile images of 50 μm circle dots array with different heights. (A) 15 μm (B) 20 μm. (C) The change of voltage output under different pressures for sensors with different heights.

To further illustrate the advantage of 3D-ERT in the field of constructing complex 3D structures, a multi-step 3D dots array pattern was fabricated. The down layer is 50 μm circle dots, and the up layer is 20 μm circle dots as shown in Figure 6.28 A. The sensitivity could be increased to 2.2 kPa^{-1} at the low-pressure range while the rest part is the same as the single layer dots array pattern (Figure 6.28 B). The multi-measure range was realized in one device.

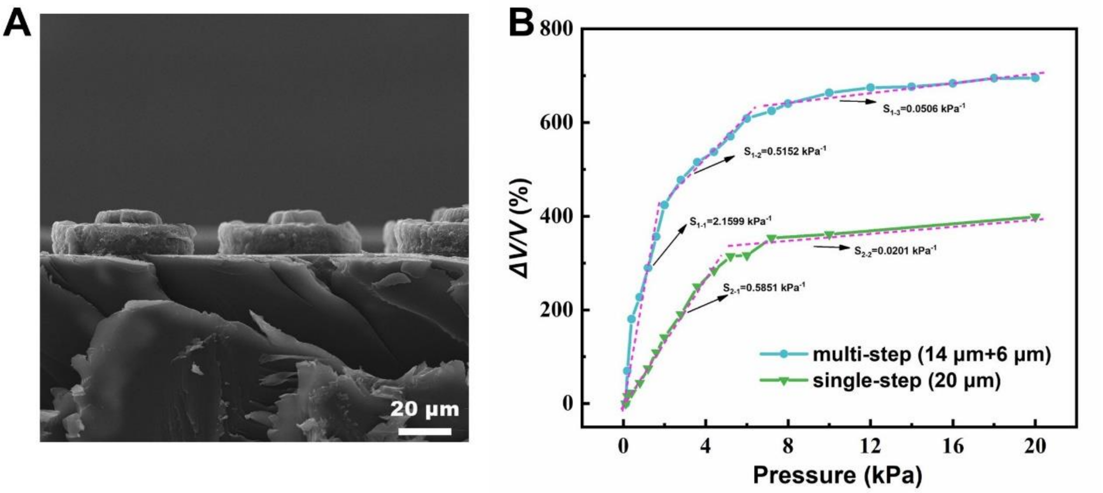

Figure 6.28 (A) Cross-section SEM image of the double layer 3D dots array electrode. (B) The comparison of the voltage output change between multi-layer and single-layer 3D dots array electrodes with the same height.

6.5.3 Flexibility and Stability

The stability of the TENG-based pressure sensor with 50 μm 3D circle dots array electrode was tested under 5 kPa pressure for 25000 s (Figure 6.29 A). The output of the voltage is almost unchanged which proves the great long-term stability. For flexibility, the electrode was bent at different radii (10 mm and 5 mm) for 1000 cycles. The resistance change of the electrodes is smaller than 2 and the voltage output at different pressures is unchanged (Figure 6.29 B).

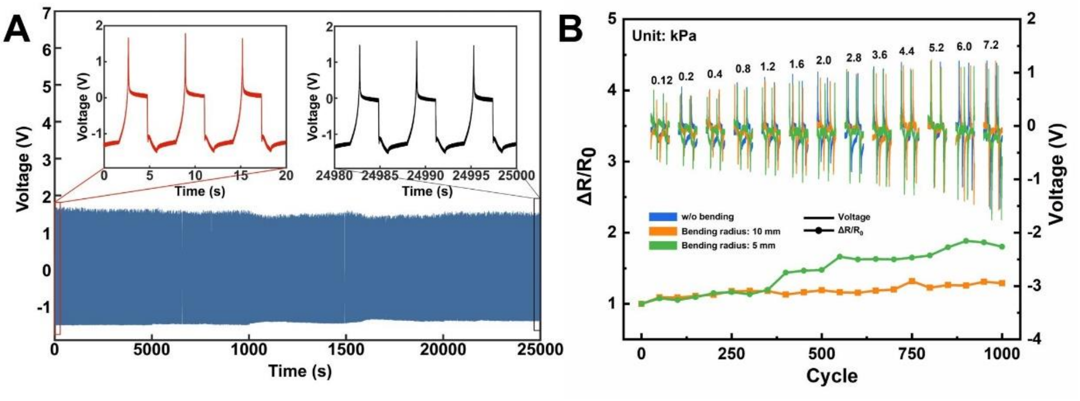

Figure 6.29 Stability of 50 μm circle dots array pressure sensor. (A) Long-term output stability under 5 kPa pressure for 25000 s. (B) Flexibility under different bending ratios in the view of resistance change and output under different pressures.

This pressure sensor could be applied for the monitoring of the monitoring of carotid artery pulse. The sensor was attached to the human neck with medical tape. The voltage output was recorded before and after 3 minutes of exercises. The BPM before exercises is around 70 while the BPM is 127 after exercises. The result is consistent with the commercial watches (Figure 6.30).

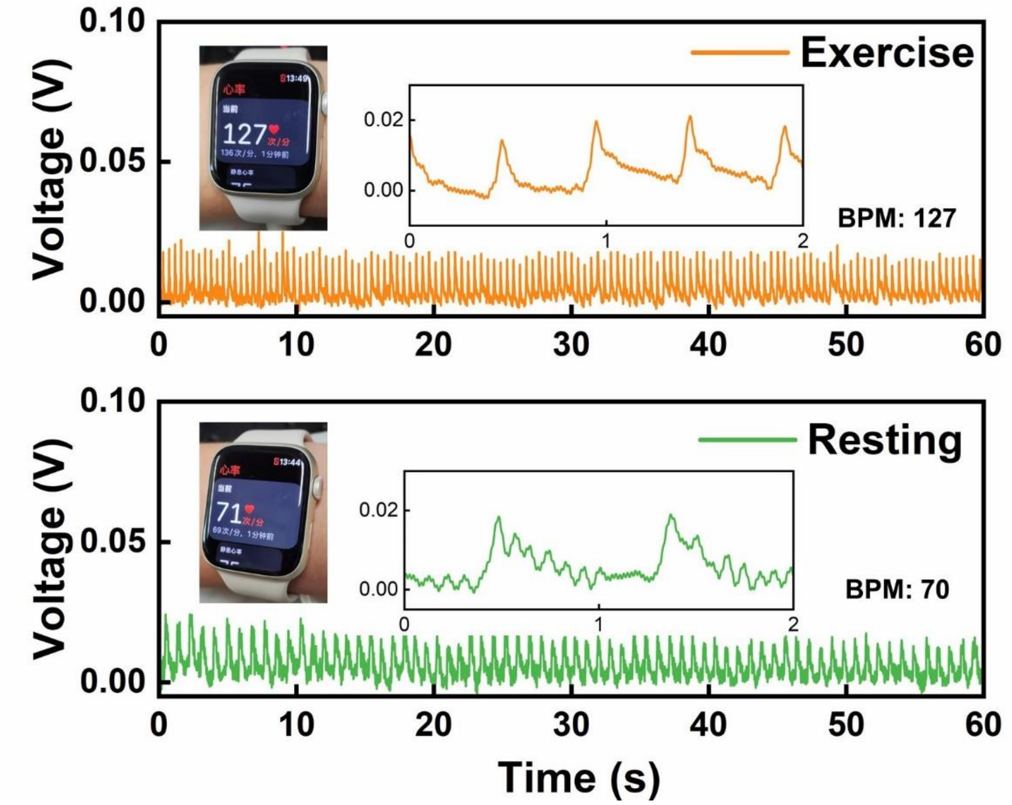

Figure 6.30 Application of the self-powered pressure sensor for monitoring carotid artery pulse waves before and after exercise.

Due to the advantage of fast replication, a 3×3 sensing array could be easily fabricated as shown in Figure 6.31 A. The voltage output could reveal the trace of the finger writing (Figure 6.31 C) and also reflect the different pressure with the same mold (Figure 6.31 D).

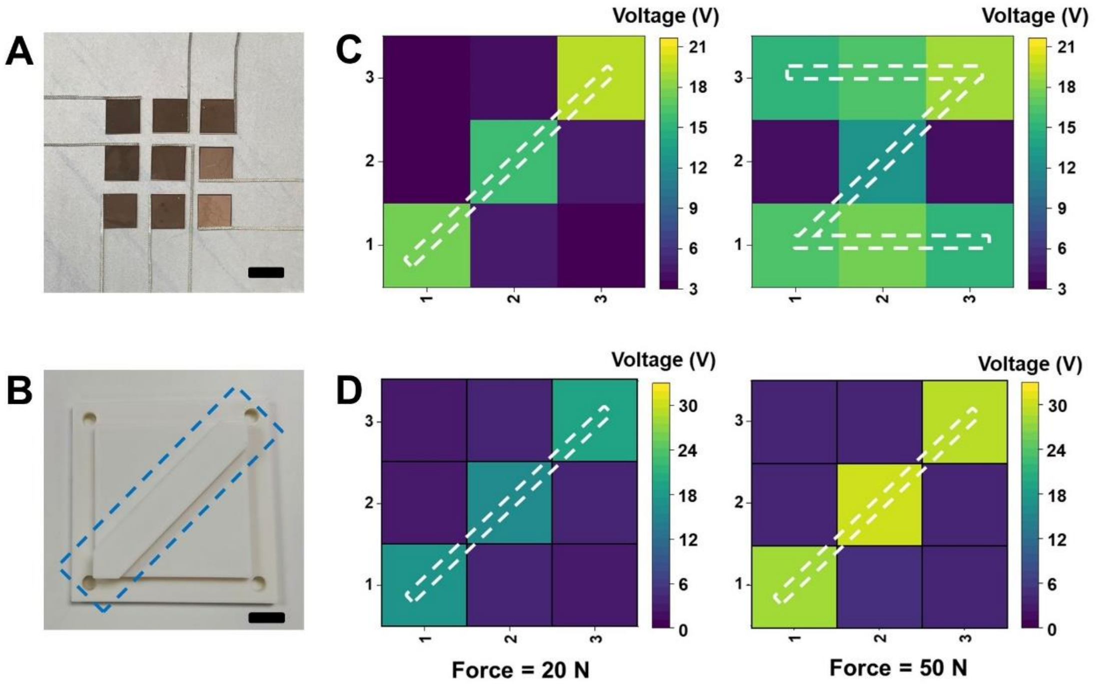

Figure 6.31 (A) Digital image of a 3×3 sensing array. (B) Digital image of a rectangle shape mold. (C) The voltage output reveals the trace of the finger writing. (D) The voltage output of the mold with different pressure.

6.6 Conclusions

Despite its powerful patterning capabilities, ERT (Electrochemical Release Transfer) still faces challenges in precisely controlling the replicated resolution due to the isotropic growth of electrodeposition. Additionally, the original ERT method cannot construct 3D structure patterns for certain applications. To overcome these limitations, a simple modification was implemented in the ERT template design. In this study, the Si surface was modified through a pre-fabrication process involving etching to create a specific 3D structure. The electroplating process was then directly performed on this modified surface. This modification allows for the fabrication of various patterns, such as continuous lines and isolated dots with different materials, using the 3D-ERT template. The growth of the pattern is restricted to the groove area of the Si substrate, ensuring a consistent resolution as the electroplating time increases. Moreover, this modified 3D-ERT method retains the advantages of ERT in terms of balancing resolution, throughput, and cost. The application of this modified 3D-ERT method in the fabrication of FTEs (Flexible Transparent Electrodes) demonstrates significant advantages. By extending the plating time without compromising resolution, the R_s of the electrodes can be greatly brought down, thereby improving transparency. By adjusting the parameters of the FTEs, a high FoM (Figure of Merit) value of 31774 can be achieved. Furthermore, the 3D-ERT method is also suitable for applications that require the construction of complex 3D structures, such as pressure sensors.

Although the 3D-ERT method is comprehensive and effective, the process of fabricating templates for 3D-ERT remains relatively complex. Direct electroplating on silicon substrates also requires further regulation and optimization of plating parameters. In future research, continuing to optimize and enhance the preparation of 3D patterns remains a worthwhile endeavour. Additionally, the fabrication of 3D nanopatterns presents greater challenges, both in terms of template preparation and the subsequent electroplating transfer process. For 3D patterns with high aspect ratios, the difficulty in achieving vertical detachment can lead to friction between the pattern and the template during transfer, resulting in pattern damage, which is a critical issue that needs to be addressed. Finally, the performance of the transparent electrodes and pressure sensors studied in the project has not yet reached its full potential. Future improvements can be achieved through further parameter adjustments and additional structural design.

Chapter 7: ERT for Electrode Fabrication: Application and Evaluation

ERT offers a significant advantage in achieving a balance between resolution, throughput, and cost, making it highly suitable for the mass production of electrodes in various applications, as demonstrated in previous chapters. In this chapter, we will discuss the potential application of ERT in the field of energy and biomedical engineering. First, we will utilize the fabrication of electrodes for TENG-based devices as a presentation and propose the concept of an ERT production line. We will compare ERT with other commonly used manufacturing methods for TENG electrodes, considering factors such as resolution, throughput, and cost, to further highlight the advantages of ERT. Additionally, we will calculate the energy consumption associated with green production. Second, we will apply the high-resolution flexible electrodes fabricated by ERT to the application of a self-powered electronic bandage. The biocompatibility of the whole device will be tested and prove the potential of ERT in the filed of biomedical engineering. The effectiveness of the electronic bandage in accelerating cell growth will be proved.

7.1 ERT for TENG Electrodes

7.1.1 Conception of ERT Production Line

Triboelectric electronics, capitalizing on the triboelectric effect and electrostatic induction, have garnered substantial interest in recent years, attributable to their extensive range of material options, compact size, cost-effectiveness, and high-power output[237, 238]. These devices possess the capability to transform ambient mechanical energy into electrical energy, thereby providing power to extant electronic devices. Additionally, they can operate as self-powered sensors that react to variations in mechanical energy[239]. With their high-voltage and low-current output, they present promising prospects in wireless sensing[240], haptic simulation[241], and electrical stimulation therapy[242].

Despite the promising versatility of triboelectric electronics, the commercialization of triboelectric-related products faces significant obstacles[243]. To further advance the performance of triboelectric electronics, standardized, low-cost, high-precision, and large-scale production processes must be developed. Although various methods have been explored, such as printed circuit board (PCB) techniques[244], laser and electron beam etching[245], and advancements in 3D printing[246], these methods have inherent limitations. Consequently, the creation of a cost-effective, highly precise, and scalable fabrication process for triboelectric electronics has become an urgent research objective.

By combining ERT with roll-to-roll manufacturing processes, we have established an effective and affordable production line for fabricating various triboelectric electronics. The detailed steps of ERT and the assembly process of triboelectric electronics are illustrated in Figure 7.1. The left part shows the fabrication of TENG electrodes using ERT, which are then transferred to PET substrates. As the PET lines move, the PET film with electrode patterns is further processed by spraying glue, covering it with fluorinated ethylene propylene (FEP film), folding, and cutting to obtain the triboelectric electronics. This process enables the large-scale preparation of flexible, high-precision triboelectric electronics with diverse structures and working modes at a low cost and in an eco-friendly manner.

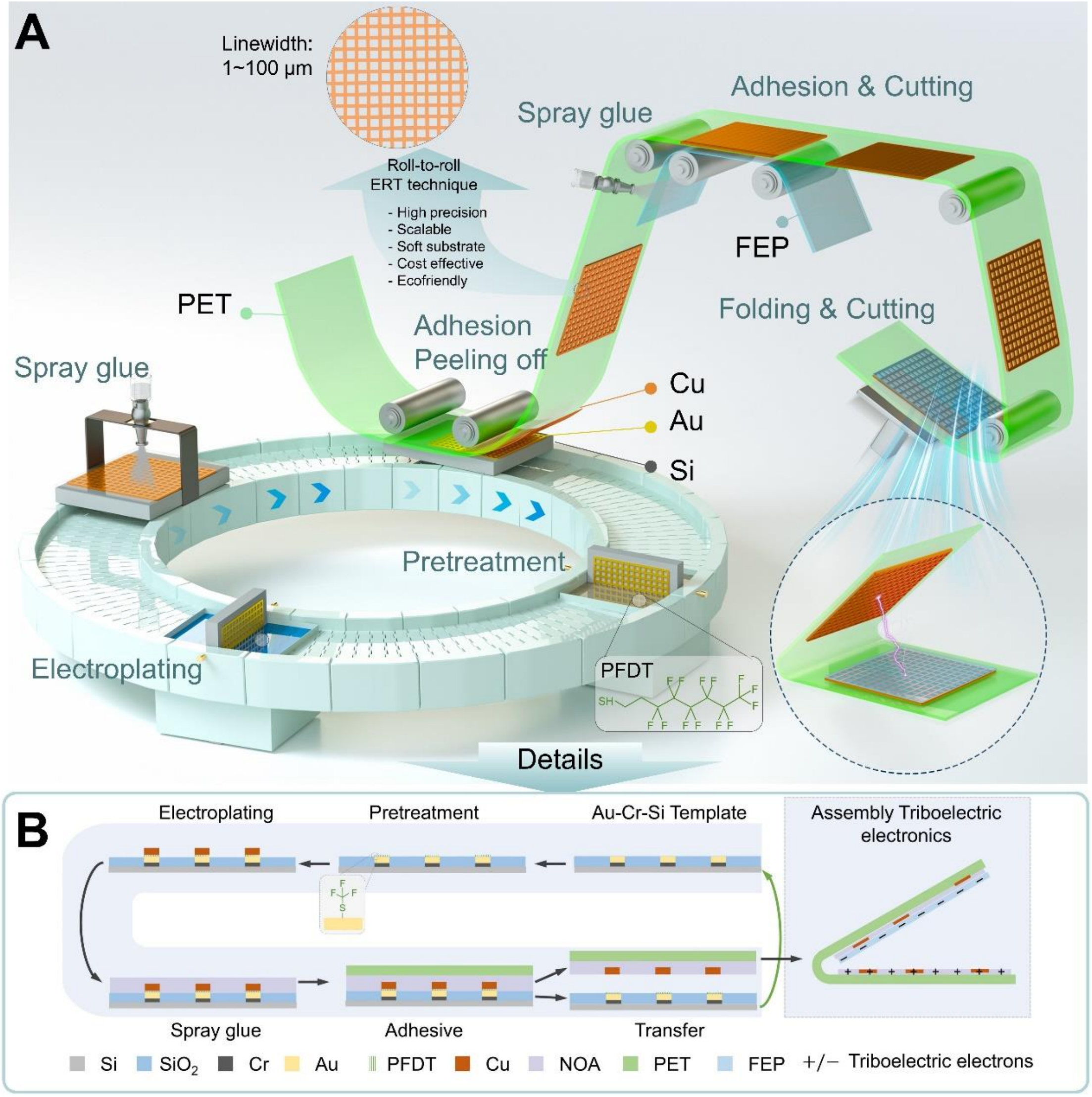

Figure 7.1 (A) Conception of ERT production line for TENG electrodes. (B) The illustration of the detailed fabrication process.

7.1.2 Comparison with Other Fabrication Techniques

A systematic evaluation of a process allows for a comprehensive exploration of its strengths and weaknesses, providing valuable insights for process optimization, identifying potential applications, and promoting sustainable development and innovation. In this section, we will conduct a systematic evaluation of the fabrication process for flexible transparent contact-separation (CS) triboelectric nanogenerators (TENGs) using the Electrochemical Release Transfer (ERT) method as an example. The CS mode TENGs designed for this evaluation consist of Cu mesh electrodes measuring 2 cm × 2 cm, with a line width of 10 μm and a gap of 100 μm, as depicted in Figure 7.2 A-C. The manufacturing process involves integrating the desired metallic mesh pattern of transparent electrodes onto a 4-inch silicon wafer, resulting in an Au-Cr-Si template. To optimize cost-effectiveness, six sets of the desired pattern can be integrated into a single template, as shown in Figure 7.2 D.

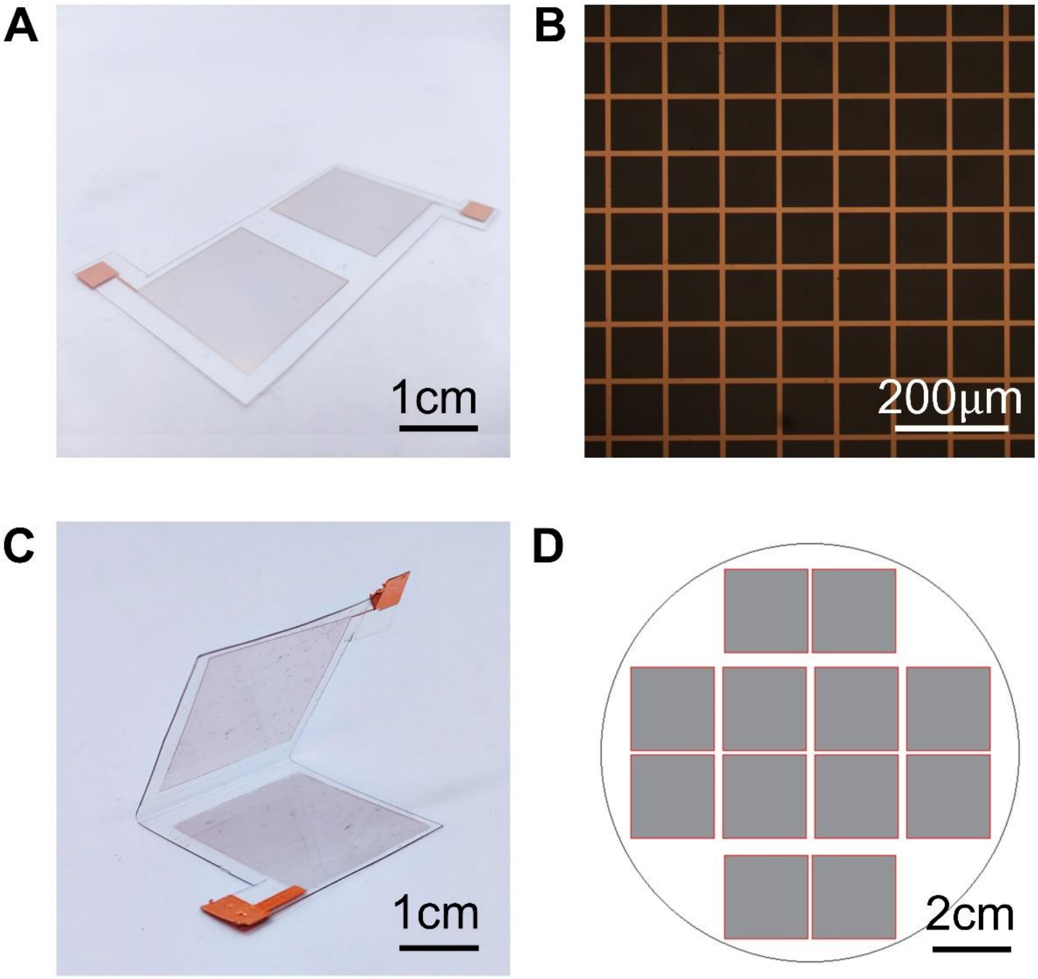

Figure 7.2 The transparent CS mode TENG composed of Cu mesh. (A) The transparent electrodes with Cu mesh for fabricating CS mode TENG. (B) The enlarged image of the transparent electrodes. (C) The assembled CS mode TENG. (D) The Au-Cr-Si template for manipulating the transparent electrodes for CS mode TENG.

After the electrochemical replication and transfer step, the template can be reused in subsequent cycles, while the transferred Cu electrodes are cut, glued, and folded to yield six flexible and transparent CS TENGs. Comprehensive details on the time, material, energy, and cost associated with each step can be found in Tables 7.1 and 7.2. When producing a small number of samples, customizing silicon-based metal templates and purchasing instrumentation can result in high costs and time requirements. Nonetheless, as the quantity of processed samples escalates, the cost and average time required to process a single sample decrease due to the recyclability of the templates, as illustrated in Figure 7.3.

Table 7.1. The time spent in each step.

Main steps	**Sub steps**	**Time/min**	**Summary/min**
Prepare Au-Cr-Si tempalte	Spin-coated with the resist AZ 5214E	2	131
	Prebake	3	
	Develop the photoresist	3	
	Dry etching and deposition of Cr-Au	120	
	Lift-off and cleaning	3	
Electrochemical replication and transfer	Plasma	5	33
	Immersed in 5mM PFDT ethanol solution	8	
	Electrodeposition	10	
	Rinsed by DI water	1	
	Dried by N_2	1	
	Casting NOA63	3	
	Cover PET film	2	
	Transfer pattern	1	
	Rinsed the template by DI water	1	
	Rinsed the template by ethanol	1	
Assembly TENG	Adhesive FEP film	0.1	0.4
	Folding	0.1	
	Cutting	0.1	
	Soldering leads	0.1	

Table 7.2. The cost spent in each step.

Type	**Sub**	**Cost/HK$**	**Summary/HK$**
Lump Sum Payment	Au-Cr-Si Template	1400	8400
	Keithley 2400 (for electroplating)	3000	
	UV lamp (for transfer)	2000	
	Other equipment (Brackets, Belt Folding, folding and cut-off parts)	2000	
Consumption of consumables (electroplating) (Single)	Electroplating solution	2	44.4825
	NOA	30	
	DI water	0.25	
	Ethanol	10	
	PET	1.36	
	N2	0.8	
	Electricity	0.0725	
Consumption of consumables (TENG) (Single)	FEP	0.113	0.631375
	Soft solder	0.042	
	Cu wire	0.472	
	Electricity	0.004375	

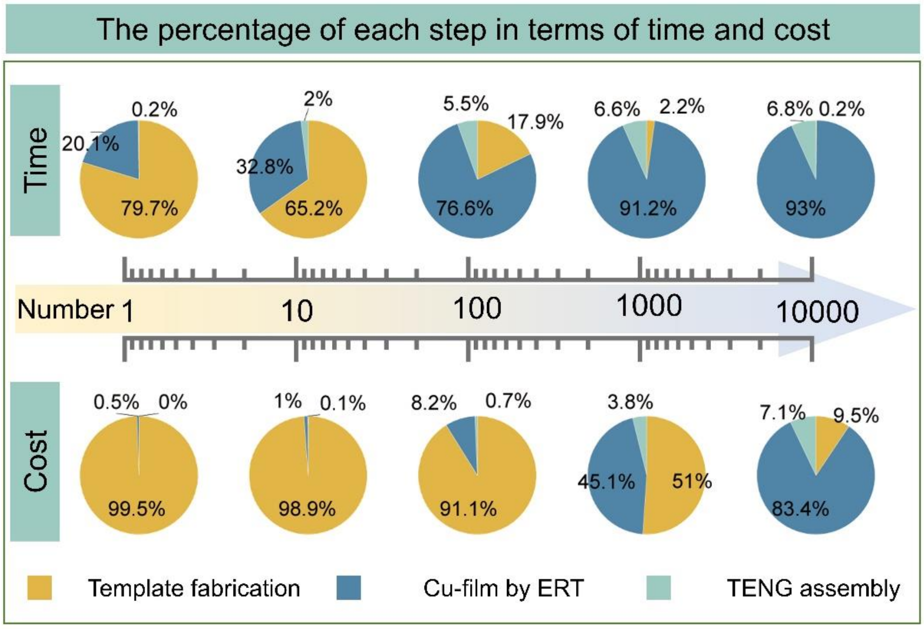

Figure 7.3 The percentage of time spent on each step for different production scales.

Ultimately, after processing over 1,000 samples, the cost of producing a transparent CS TENG was approximately HK$ 8.05, with an average processing time of 5.9 minutes per piece, as depicted in Figure 7.4 A. When compared to the conventional TENG production process, the ERT-based preparation process exhibits superior overall performance, as illustrated in Figure 7.4 B and Table 7.3.

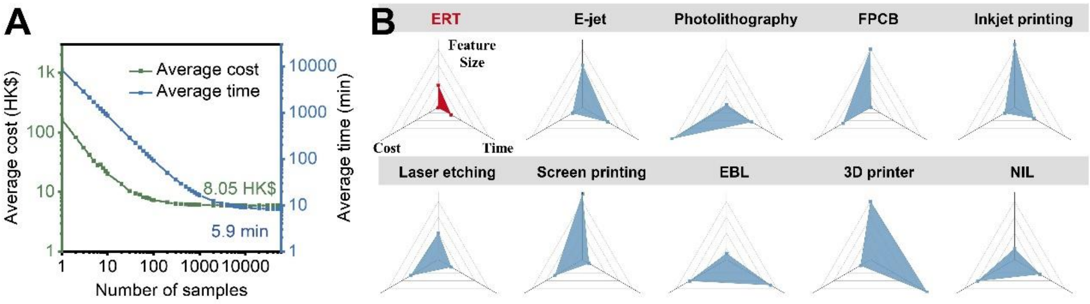

Figure 7.4 (A) Cost and average processing time per sample over the number of samples produced. (B) Radar charts illustrating feature size, average processing time, and

average production cost per square meter metallic pattern achieved through various fabrication processes.

Table 7.3 The resolution, throughput and cost of different patterning techniques.

Patterning techniques	**Feature size (μm)**	**Throughput (m^2/h)**	**Capital cost of equipment ($)**
Photolithography	0.003-10	10^{-2}-1	1M-100M
Nanoimprint lithography (NIL)	0.01-1	10^{-5}-1	500k-5M
Inkjet printing	20-100	10^{-2}-10	10k-50k
Screen printing	30-100	1-10^{3}	1k-1M
Flexible printed circuit board (FPCB)	10-100	10^{3}-10^{4}	100k-1M
Laser etching	0.1	10-100	1k-1M
Electron-beam lithography (EBL)	0.005-0.1	10^{-6}-10^{-3}	1M-5M
Electrohydrodynamic Printing (E-jet)	1	1	50k
3D printer	10-100	10^{-7}-10^{-5}	500-50k
Electrochemical replication and transfer (ERT)	0.05-100	10^{-1}-10^{2}	1k-10k

7.1.3 Performance of the TENG Electrodes

The mechanical and electrical properties of flexible triboelectric electronics are crucial to satisfy the diverse demands of various application scenarios, serving as key indicators in evaluating the suitability of the production process. In this regard, we undertook an exhaustive characterization of the mechanical and electrical properties of transparent CS TENGs composed of copper grids (line width: 10 μm; gap: 100 μm; contact area: 2 cm × 2 cm). The transparency and conductivity of TENGs fabricated using the roll-to-roll ERT method were found to be influenced by the plating time. As depicted in Figure 7.5 A, TENGs prepared by roll-to-roll ERT exhibited a conductivity of approximately 85% when the plating time was less than 90 minutes, which closely approached that of commercial flexible indium tin oxide (ITO) electrodes (90% ± 3%). In terms of conductivity, all samples, except for the one with a plating time of 5 minutes, demonstrated superior conductivity (<1 Ω sq-1) compared to ITO electrodes (10 Ω sq-1) and ranked second only to copper foil (0.02 Ω sq^{-1}) (Figure 7.5 B). The working mechanism of the triboelectric effect demonstrates that the relative motion and deformation between materials are crucial for generating triboelectric charges[247]. Consequently, the wear and bending resistance of metal electrodes play a critical role. We tested the changes in resistivity of transparent electrodes fabricated using ERT subjected to long-term horizontal sliding friction. As depicted in Figure 7.5 C, the transparent electrode produced by ERT demonstrated remarkable stability during various wear testing modes. This remarkable stability can be primarily attributed to the chemically plated metal layer, which exhibits superior adhesion properties and reduced residual stresses compared to both ITO and vapour-coated metal layers.

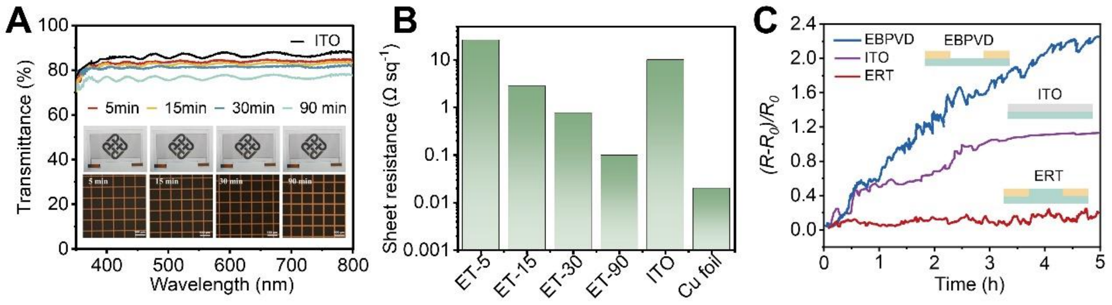

Figure 7.5 (A) The transmittance of TENGs created through roll-to-roll ERT at varying electroplating times and compared with that of a commercial ITO. (B) The sheet resistance of TENGs fabricated via roll-to-roll ERT with different electroplating times and compared with that of a commercial ITO and Cu foil. (C) The resistance changes of commercial indium tin oxide (ITO) electrodes and metal mesh electrodes produced using electron-beam physical vapor deposition (EBPVD) and ERT were measured under long-time horizontal friction.

The flexible and stable electrode structure prepared by ERT enables the design of TENGs with various structures and working modes. Figure 7.6 A showcases the utilization of ERT-prepared transparent electrodes in creating TENGs with CS mode, sliding freestanding (SFT) mode, and bending mode (Figure 7.6 B). This versatility highlights the potential of ERT in enabling the development of triboelectric devices with different configurations to suit specific application requirements.

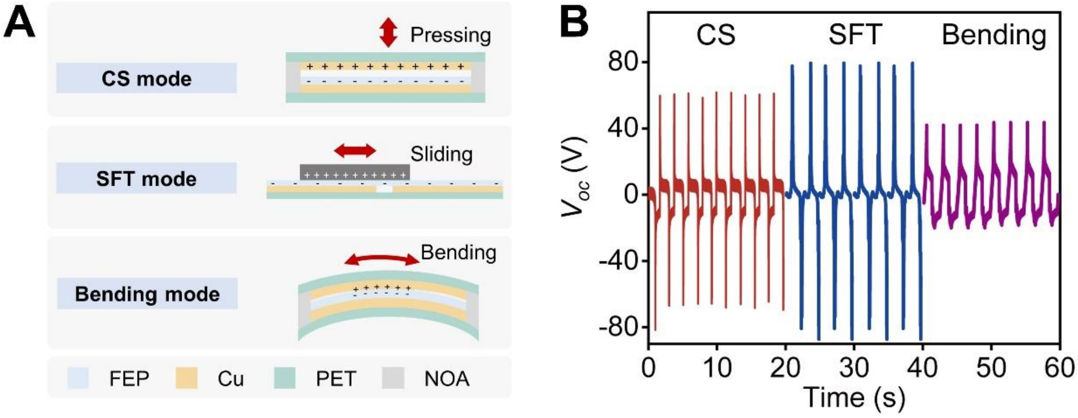

Figure 7.6 (A) The structural diagrams of TENGs with CS mode, SFT mode, and bending mode. (B) Open-circuit voltage measurements of TENGs with CS mode, SFT mode, and bending mode utilizing transparent electrodes prepared by ERT.

The subtlety of the process lies in the ability to produce multiple batches of samples from a single silicon-based gold-patterned template while ensuring consistent quality and performance across samples. To this end, we produced fifty consecutive samples with the mentioned Cu mesh and measured their triboelectric open-circuit voltage (Voc) for an extended period. The results, as shown in Figure 7.7 A and B, indicate that the Voc of different batches of TENG remains constant at 90 V. Furthermore, the long-term operation stability of different batches of TENG is excellent (3h), and the performance of the TENG electrodes fabricated by ERT with the same template is stable even after 50 times of replication. These findings demonstrate the reproducibility and stability of the ERT-based fabrication process, highlighting its potential for large-scale production of triboelectric devices with consistent quality and performance.

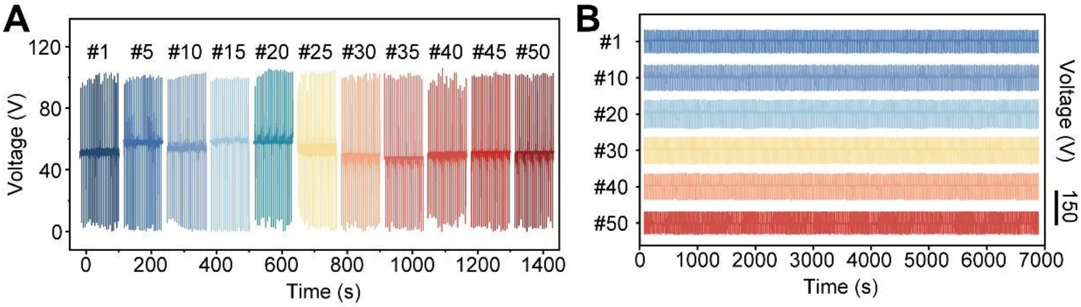

Figure 7.7 (A) The open-circuit voltage of fifty samples fabricated by the roll-to-roll ERT process. (B) The stability of fifty samples fabricated by roll-to-roll ERT process.

7.1.4 Evaluation of ERT for the Fabrication Process

As society progresses, and environmental awareness grows, there is an increasing demand for production processes that prioritize cost-effectiveness, efficiency, and environmental sustainability. To address this, researchers have proposed the concept of life cycle assessment (LCA), which evaluates the entire value chain of a product, quantifying carbon emissions resulting from energy consumption and material inputs at each stage, as illustrated in Figure 7.8[248, 249]. This methodology facilitates the recognition of potential environmental repercussions and the execution of strategies to alleviate them, facilitating the development of sustainable production processes for triboelectric devices.

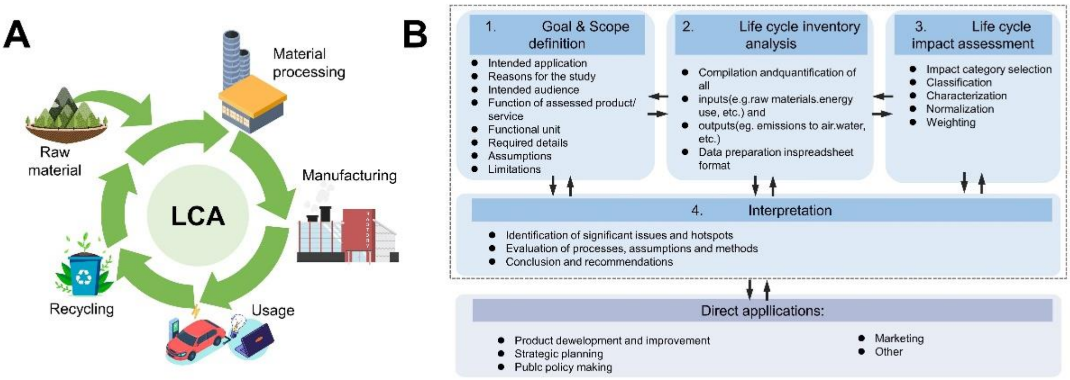

Figure 7.8 (A) The diagram of lifecycle assessment. (B) Steps in LCA studies.

Using this approach, we can evaluate the potential lifecycle impacts of triboelectric electronics manufactured using the roll-to-roll ERT technique. In this study, we focus on flexible transparent CS TENGs as an illustrative example, with the scale and detailed information remaining consistent with the aforementioned context. The number of production CS TENGs is 6E5. In the manufacturing process of a TENG device, a variety of products are employed, encompassing diverse industrial raw materials and initial bulk energy. Each of these products has its distinct lifecycle, which can be traced back. However, comprehensively assessing the entire lifecycle of a TENG device commencing from its primary raw materials would be complex and impractical. To address this challenge and mitigate infinite expansion issues, we adopted materials from the Sima Pro database and established system boundaries. Based on these boundaries, the inputs of the system were categorized into materials and energy, as shown in Table 7.4. This allows for a more streamlined and manageable evaluation of the potential lifecycle impacts of the TENG devices.

Table 7.4. The Materials and electricity spent in each step.

Main steps	Sub steps	Input				Output	
		Materials		Electricity/kW.h		Materials	Mass/g
		Name	Mass/g	Electricity	Sum		
Prepare Au-Cr-Si tempalte	Plasma	Wafer	5.49E-03	0.025	12.08533333	Resist	0.0628
	Spin coating photoresist	Resist	1.57E-02	0.003333333		None	None
	expose 405nm light	None	None	0.025		None	None
	Prebake	None	None	0.01		None	None
	Develop the photoresist	None	None	0.006666667		None	None
	Etching	CF_4	1.24E-01	0.003333333		CF_4	0.11166
	Rinsed in DI water	DI water	1.00E+01	0		DI water	9
	Coating Cr-Au	Liquid nitrogen	9.70E+03	12		Liquid nitrogen	8.7
		Au	4.73E-03			Au	0.0004396
		Cr	3.34E-04			Cr	7.05519E-05
	Ultrasonic cleaning	$NH_3.H_2O$	2.28E-02	0.012		$NH_3.H_2O$	0.020546772
		DI water	5.71E-02			DI water	0.051366931
						Template	1p
Electrochemical replication and transfer	Plasma	Template	1p	2500	4833.333		
	Immersed in PFDT	PFDT	4.00E+06	0		PFDT	19532
		Ethanol (Solvent)	1e6			Ethanol	87802.65
	Electrodeposition	$CuSO_4$	2602.77	333.333		$CuSO_4$	45000
		H_2SO_4	1000			H_2SO_4	67500
		$CuCl_2$	1.4			$CuCl_2$	13.5
	Rinsed by DI water	DI water	4e6	0		DI water	900000
	Dried by N_2	N_2	1e6	0		N_2	10485
	Casting NOA63	NOA 63	2e5	1666.6667		NOA63	41866.66667
	Cover PET film	PET	1.28e5	0		PET	29240
	Transfer pattern	None	None	333.333		None	None
	Rinsed the template with DI water	DI water	4e6	0		DI water	900000

	Rinsed the template with ethanol	Ethanol	4e6	0		Ethanol	900000
						Discarded silicon wafers	5.49E-03
						Cu-film by ERT	156107.2
Assembly TENG	Adhesive FEP film	FEP	06.79e4	12000	881000	FEP	3394.737
		Cu-film by ERT	1.56E+05				
	Folding	None	None	12000		None	None
	Cutting	None	None	12000		None	None
	Soldering leads	Soft solder	2.53e4	45000		Soft solder	1263.158
		Cu wire	2.83e5			Cu wire	14147.37
						TENG	518593.1313
Transportation	None	Cargo	200tkm	0	0	TENG-transport	518593.1313
		TENG	518593.1313	0			
TENG usage	None	TENG-transport	518593.1313	0		TENG-usage	518593.1313
				0			
TENG cycling	None	TENG-usage	518593.1313	0	0	loss	20%
				0		Recycling	40%
				0		Landfill	40%

To determine the contributions of different input materials, we analyzed the carbon footprint of each material. As shown in Figure 7.9, ethanol and FEP were identified as the primary contributors to the carbon emissions of TENGs, accounting for approximately 25.8% and 25.7%, respectively.

The significant contribution of ethanol stems from its extensive use in many production processes, serving as a solvent and cleaning solution. The higher carbon emissions of FEP can be attributed to the energy and mass consumption involved in polymer production. These findings have prompted us to explore alternative materials to diminish our dependency on polymers in the production of TENG and research the recycling processes for organic solvents, intending to mitigate carbon emissions. By identifying the major contributors to carbon emissions in the TENG manufacturing process, we can work towards developing more sustainable production processes for triboelectric devices.

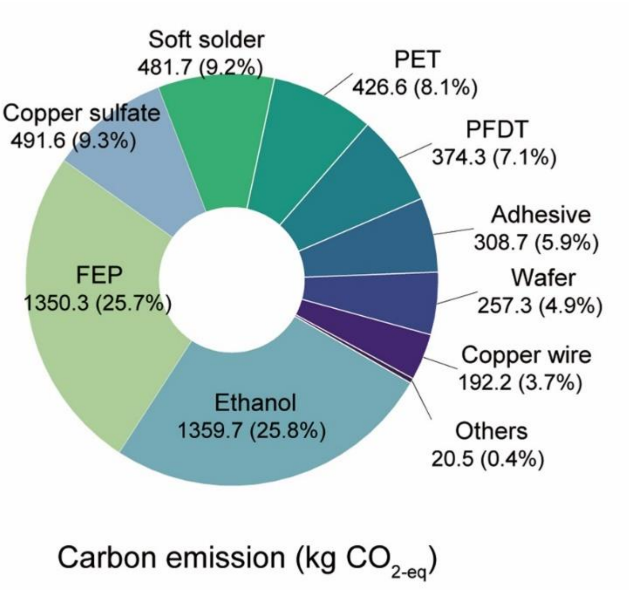

Figure 7.9 Pie Chart depicting the percentage of carbon emissions attributed to

materials used in the overall production process.

TENGs serve as environmentally friendly energy harvesting devices, offering a sustainable alternative to electricity generated from fossil fuels. As a result, the utilization of TENGs can be considered a carbon-negative process. In Figure 7.10 A, it is demonstrated that as TENG runtime increases, there is a corresponding escalation in electricity generation, accompanied by a decline in carbon emissions from the entire system. Interestingly, after the second year of usage, the carbon emissions transformed from negative to positive values. To simulate gradual degradation and loss of functionality in TENG devices, our study incorporates an attrition rate of approximately 10% per year. Ultimately, after a decade of TENG operations, the TENG system is assumed to be transported to a waste treatment facility, marking the end of its lifespan. Analyzing the carbon footprint at each step (Figure 7.10 B), it is evident that TENG assembly contributes significantly to positive carbon emissions due to the extensive use of commercially prevalent materials such as FEP, Cu wire, and soft solder. However, despite this contribution, the TENG system as a whole exhibits highly negative carbon emissions, thanks to its electricity generation capabilities. This highlights the overall environmental benefit of utilizing TENGs as an energy harvesting solution.

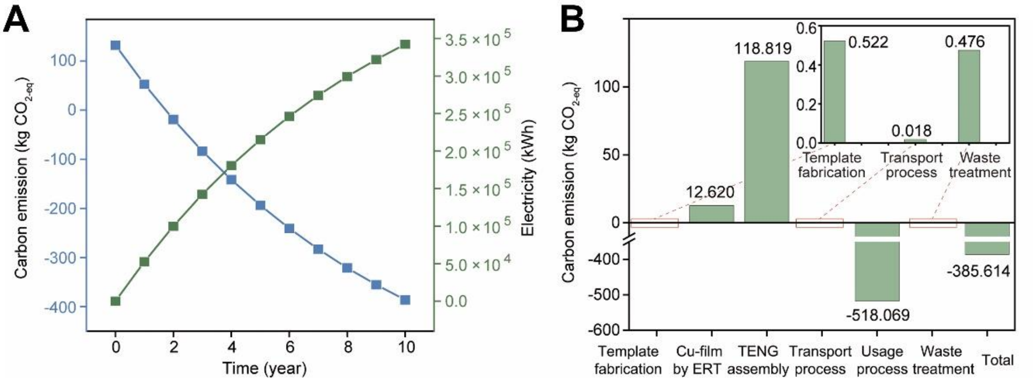

Figure 7.10 (A) Correlation between the carbon emission of the whole processes and electricity energy generation of TENGs with TENGs' runtime. (B) Carbon emission at each step and total carbon emission over a 10-year TENG usage period.

7.2 ERT for Biomedical Engineering Application

As the biggest organ of the human body, the skin is indispensable considering its function in immunoprotection, sweating, and sensing[250, 251]. However, due to its fragility, human skin could be easily damaged in daily life[252]. Depending on the size and depth of the wound, it often takes few days or even weeks for the self-healing of human skin[253]. During this period, in addition to different degrees of pain, people also need to take special care of the wound site to prevent infection caused by external bacteria, which may cause the extension of the healing time and bring more pain to the human body[254]. Therefore, it is necessary to seek an effective and practical approach which could accelerate the healing process, especially for severe trauma that is intractable to regular treatment[255].

Electrical stimulation (ES) has emerged as a transformative approach to wound healing combining electric devices and traditional biomedical treatment[256-259]. It can be divided into two main forms including current stimulation and electric field stimulation[260]. In general, electric current stimulation focuses on activating or inhibiting specific physiological processes[261], while electric field stimulation mainly influences the behaviour of cells and tissues like proliferation and differentiation[262, 263].

Among the various types of electrical stimulation, pulsed electric field (PEF) is an indispensable part which involves the application of high voltage pulses for microseconds to milliseconds to biological tissues or cells[264-266]. The main function of PEF is to induce an increase in the transmembrane potential, leading to the formation of pores in cell membranes, a phenomenon known as electroporation[267]. The non-thermal and non-invasive characteristics make PEF a safe tool in wound therapy[268]. It also has the advantages of high selectivity, short action time and high integration with continuous processing systems[269]. Short-term or low-intensity PEF can cause slight or reversible electroporation[270], which is conducive to cell growth, while long-term and ultra-high-intensity PEF may cause irreversible electroporation and induce cellular apoptosis[271]. By varying the duration and electric field strength, PEF has been proven to be a powerful tool in wound healing[268], cancer treatment[272], gene therapy[273], drug delivery[274] and disinfection[275]. However, expensive and heavy equipment is required to achieve precise control of electric fields, which hindering its application in daily wound care and treatment.

7.2.1 Structure of Electronic Bandage

In this study, we design an electronic bandage (E-bandage) with a controllable hybrid working model PEF which has a very low cost to meet the requirements for daily wound healing. The TENG power source electrodes are made of polyethylene oxide (PEO) (~35 μm) and ethyecellulose (EC) (~20 μm) and two thin layers of copper (Cu) (~100 nm) are deposited on both two electrodes by thermal evaporation which serves as the conductive layer. A PDMS square frame with 0.5 mm thickness is placed between the two electrodes as a spacer to realize the contact-separation (CS) mode (Figure 7.11 A). For the interdigital electrode, the ERT method reported by us before is utilized to realize the fabrication of a high-resolution gold (Au) electrode on the flexible NOA 63 substrate at a low cost. An additional layer of Al_2O_3 (~30 nm) is deposited on the electrode area by atomic layer deposition to eliminate possible short circuits caused by skin or tissue fluids. A conductive Cu line is used to connect the TENG power source and the Au interdigital electrode (Figure 7.11 B). Finally, serves as both the encapsulation and adhesive layer, a wet-adaptive skin proposed before covers on the top of the whole electronic device and attached to the damage skin area. This wet-adaptive skin layer has been proved to be highly comfortable during usage with ultra-stretchability, wet adhesion, permeability, and waterproof properties. Considering the low-cost characteristic of the fabrication methods, after calculation, the whole cost for an E-bandage with an active area of 1.5 × 1.5 cm^2 is only \$0.227. The detailed information is listed in Table 7.5.

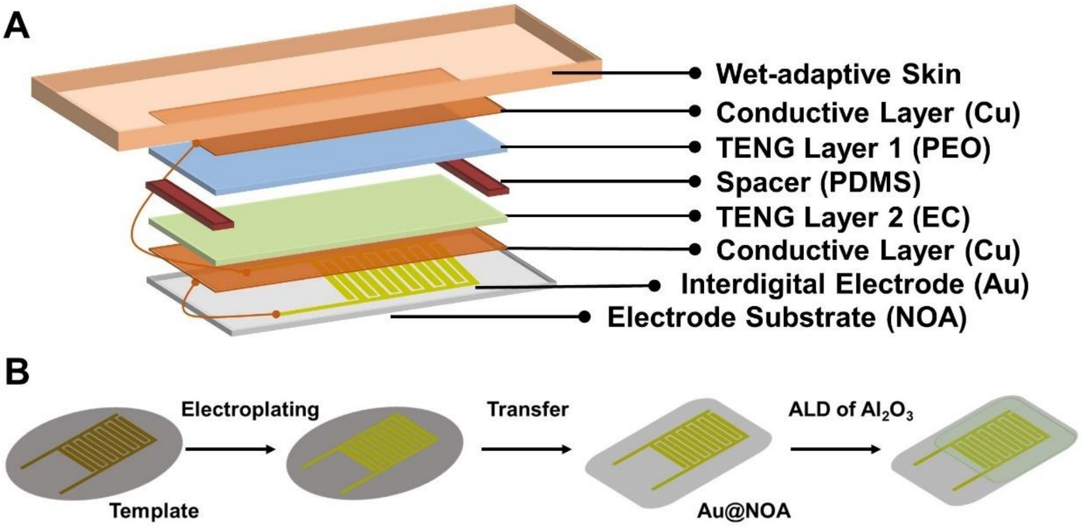

Figure 7.11 (A) Schematic Illustration of the self-powered electronic bandage structure. (B) Fabrication process of the high-resolution interdigital electrode by ERT.

Table 7.5 Cost of the E-Bandage

Type		Unit Price (\$)	Amount	Actual Price (\$)
Materials	PEO	0.09 /g	0.014 g	0.001
	EC	0.5 /g	8E-04 g	4E-4
	NOA 63	1.3 /mL	0.0225 mL	0.029
	Au	70 /g	0.002 g	0.14
	Cu	0.01 /g	8.8E-05 g	8.8E-07
	PDMS	0.07 /mL	0.3 mL	0.021
	PAA	0.9E-04 /g	0.009	8.1E-07
	SBS	2E-03 /g	0.048	9.6E-05
	DMF	6E-04 /g	0.048	2.9E-05

	THF	1.6E-03 /g	0.144	2.3E-04
Fabrication	ERT	200	1E-04	0.02
	Thermal Evaporation	15	1E-03	0.015
	Electrospinning	2E04	1E-08	2E-04
Total:				0.227

In addition to the low price and comfortable wear experience, all the materials used for this PEF E-bandage are biocompatible. The fluorescence microscope image of live/dead staining of NIH$_3$T$_3$ cells in Figure 7.12, and cell survival rate results in Figure 7.13 prove the great biocompatibility of the whole PEF E-bandage over 3 days.

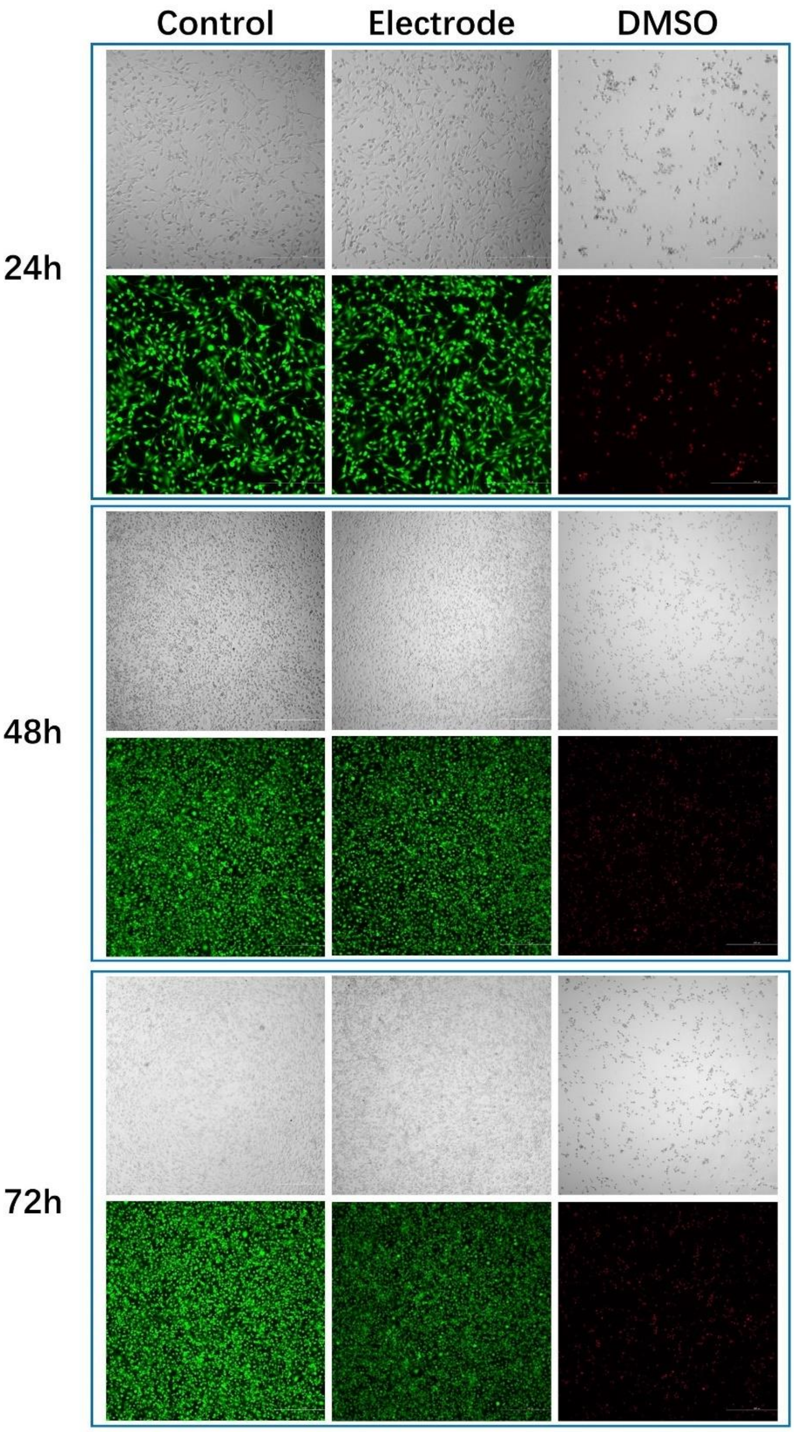

Figure 7.12 Fluorescence microscope image of live/dead staining of NIH_3T_3 cells for 24 h, 48h and 72h.

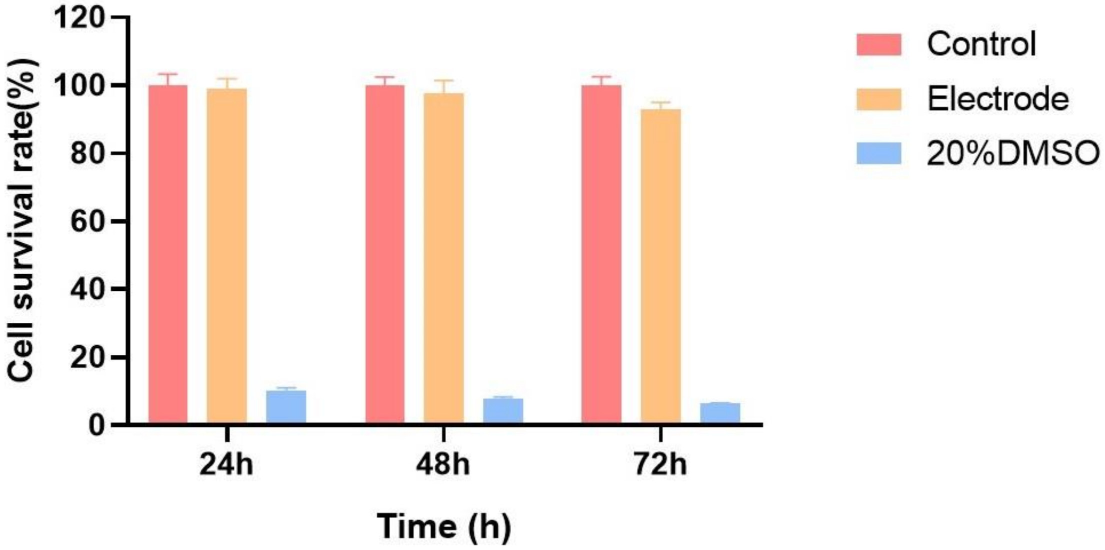

Figure 7.13 The cell survival rate of NIH3T3 cells for 24 h, 48 h and 72 h.

7.2.2 TENG Performance

The intensity and duration time are two key parameters of the PEF, which may cause different effects on cells at different ranges. For the PEF E-bandage, the intensity is adjustable, which relates to both the output voltage of the TENG power source and the parameters of the Au interdigital electrode. The TENG electrode materials, PEO and EC, have been proven to have the greatness differences of triboelectric polarities (positive for PEO while negative for EC) among various categories of biodegradable polymers. These material choices could not only increase the output voltage of the TENG power source and expand the upper limit of adjustable electric field strength but also open possibilities for other implantable devices in the future. The results of the TENG power source performance are shown in Figure 7.14 A-C. Under the small pressure (~ 4 N cm^{-2}), the open-circuit voltages (V_{oc}) could surpass 40 V. The charge density and current are very low which is beneficial for various biomedical applications due to the low heat emission. Unlike the conventional PEF, the TENG-induced PEF varies with the output voltage and shows a tendency of rapid enhancement following rapid decay. The duration time of the pulse will slightly decrease as the increase of contact frequency due to the shorter contact time while maintaining at a period of millisecond (ms) (Figure 7.14 D). The long-term stability of the TENG power source is also impressive which could maintain a stable output for over 40 hours (Figure 7.14 E).

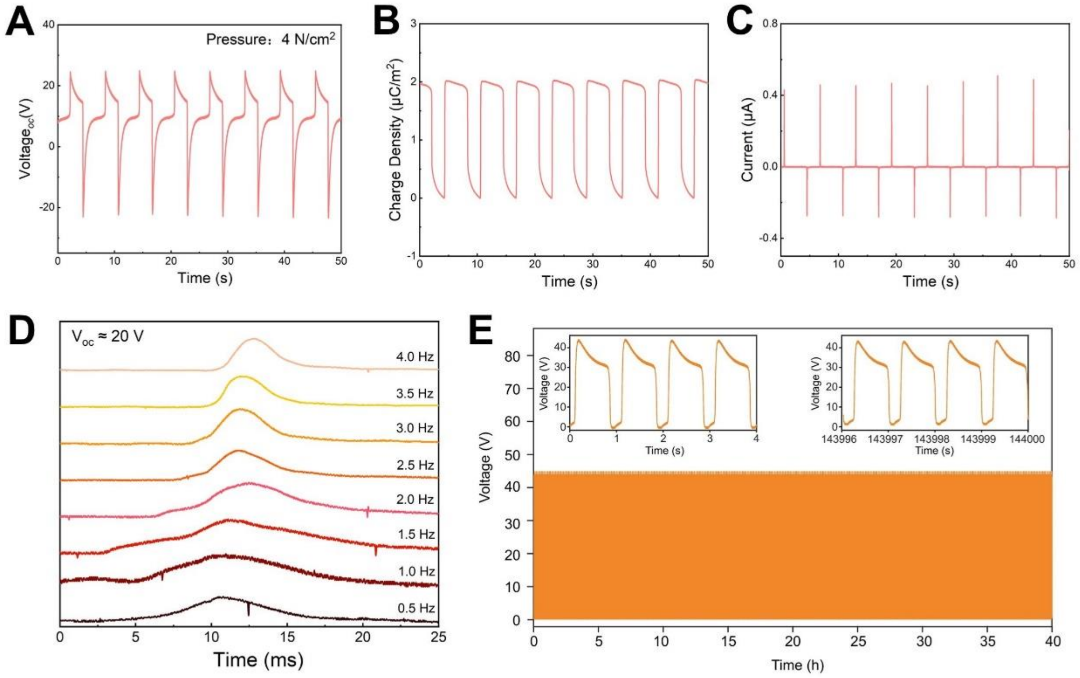

Figure 7.14 Output performance of the TENG power source composed of PEO and EC under the pressure of 4 N/cm^2. (A) The open circuit output voltage. (B) Charge density. (C) Current. (D) Output voltage under different frequencies tested by oscilloscope. (F) Long-term stability of the TENG device with a frequency of 1 Hz.

7.2.3 Electric Field Stimulation

The parameters of the interdigital electrode also have impacts on the intensity of the electric field, including width, gap and thickness. In this study, we set the width of the finger equal to the gap, ranging from 2 μm to 200 μm, as shown in the optical images in Figure 7.15. After 1 hour of electrodeposition under the current density of 1 mA cm^{-2}, the thickness of the Au electrode is around 1 μm.

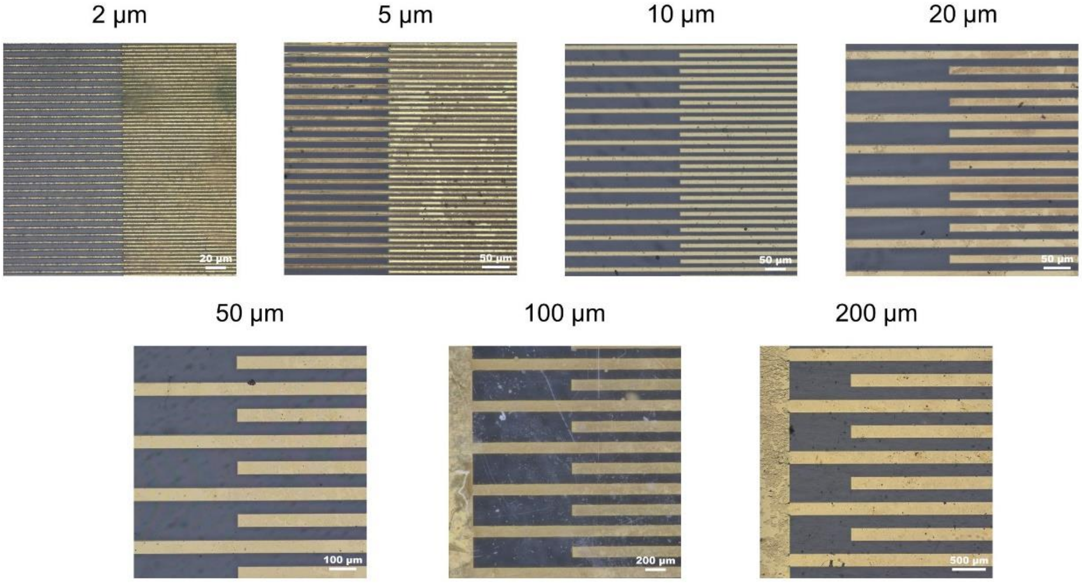

Figure 7.15 Optical images of the Au interdigital electrodes on NOA 63 substrates fabricated by ERT.

The finite element Method (FEM) is used to conduct the simulation of electric field intensity by COMSOL. The output voltage is set to be 20 V. It can be seen from the simulation diagram of the spatial distribution of electric field intensity that with the decrease of the width of the interdigital electrode, the distribution of the electric field becomes tighter and more uniform (Figure 7.16), and the maximum intensity also increases significantly (Figure 7.17). This can be attributed to the shorter decay distance of the electric field. The electrode thickness also has a remarkable influence on the electric field intensity as shown in Figure 7.18. The theoretical limits of the intensity will sharply decrease as the thickness increases from 1 μm to 50 μm. To prevent excessive electric fields from causing irreversible damage to cells, the thickness of the Au electrode is set as 1 μm in this study.

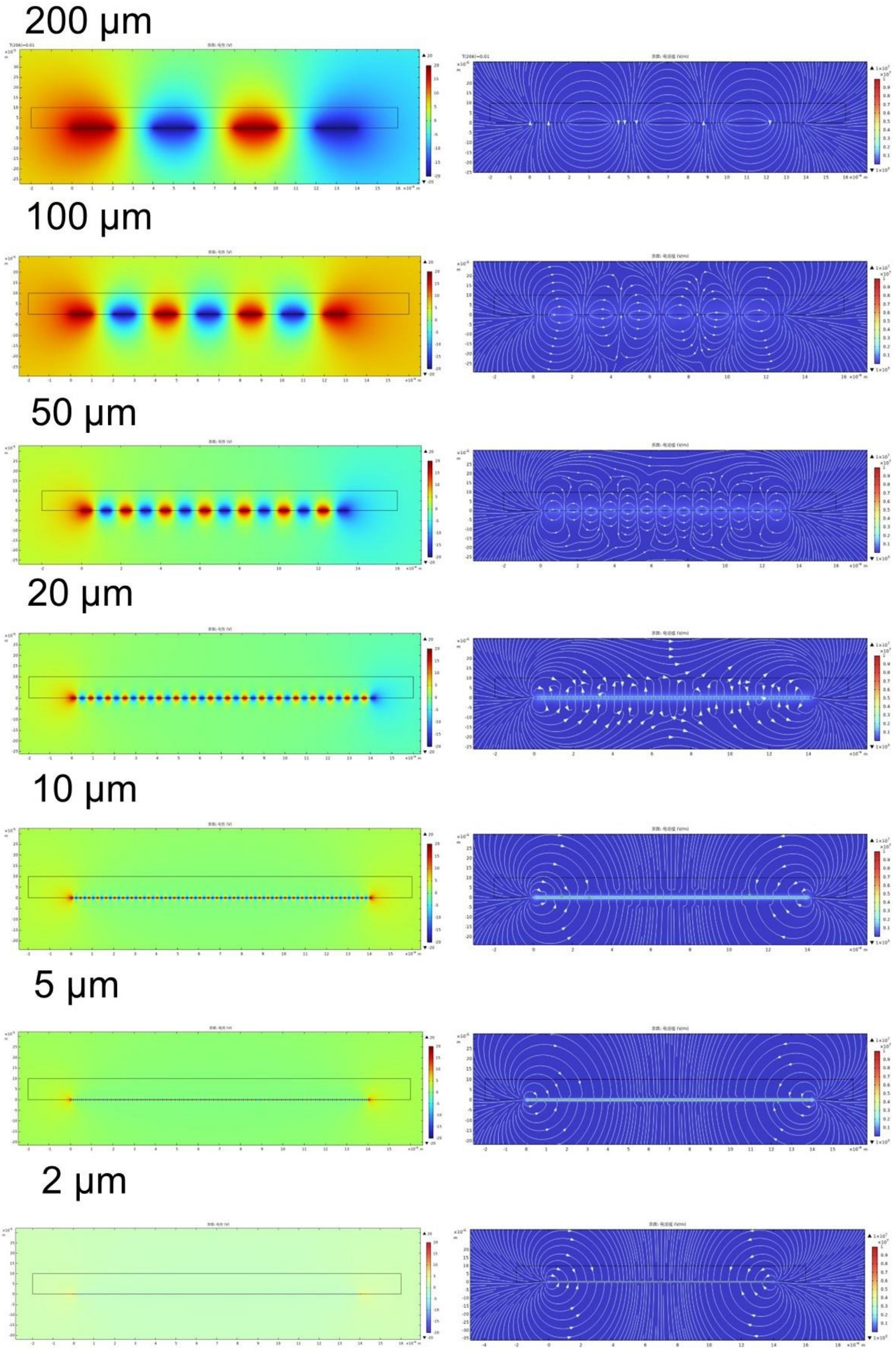

Figure 7.16 The simulation diagram of the spatial distribution of electric field intensity as the changing of the width of the interdigital electrodes.

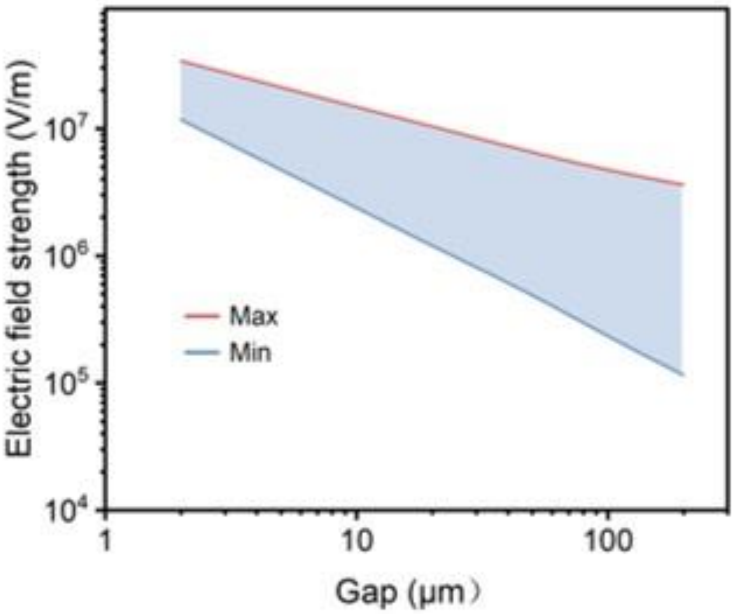

Figure 7.17 The maximum and minimum values of the electric field intensity generated by the Au interdigital electrodes with different widths under the output voltage of 20 V.

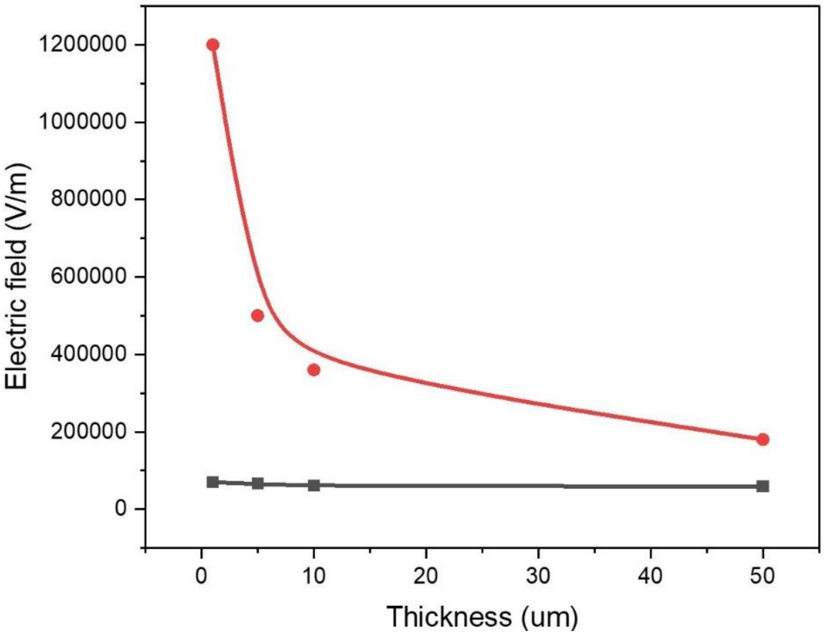

Figure 7.18 The maximum and minimum value of the electric field intensity generated by the Au interdigital electrodes with 200 μm line width and different thickness.

7.2.4 In Vitro Cell Tests

To verify the role of our E-bandage in promoting wound recovery, we first test and evaluate its capabilities for cell proliferation in vitro. An as-fabricated interdigital Au electrode on NOA substrate is placed in the cell-culture petri dish and the cells attach to the electrode side (Figure 7.19A). Considering the previous research results on PEF, the parameters of the PEF are first optimized to be 1Hz frequency, 30 times of pulse and the width of the Au electrode is 10 μm. The output voltage is fixed to be 40 V and the duration time of one pulse is around 12 ms. Four typical cells are chosen to verify the efficiency, including embryonic mouse fibroblast cell line (NIH3T3), myoblast cells (C2C12), cardiac muscle cell line (HL-1), and bone marrow mesenchymal stromal cells (BMSC). After 24 hours, the number of the four kinds of cells increases significantly. Compared to the control group without PEF stimulation, the cell proliferation rates of the four PEF groups increased to around 130~140% (Figure 7.19B). Next, we investigate the influence of the PEF parameters using cell NIH3T3. For the width of the electrodes, which influence the intensity of the PEF, we fabricate various electrodes with the width from 2 μm to 200 μm. The frequency is 1Hz and the pulse time is 30. The cell proliferation rate results in Figure 7.19C show that all the electrodes promote cell proliferation to varying degrees. For the cell NIH3T3, electrodes with 10 μm and 100 μm show the best performance with around 40~50% more proliferated cells than the control group. The pulse time also has a great influence on cell proliferation as shown in Figure 7.19D. The width of the electrode is 10 μm and the frequency is 1Hz.

The cell proliferation rate increases significantly with the increase of pulse time and reaches 200% when the pulse time is 200. Compared with the pulse time, the effect of frequency on cell proliferation rate was relatively small with around 20~50% more proliferated cells (Figure 7.19E).

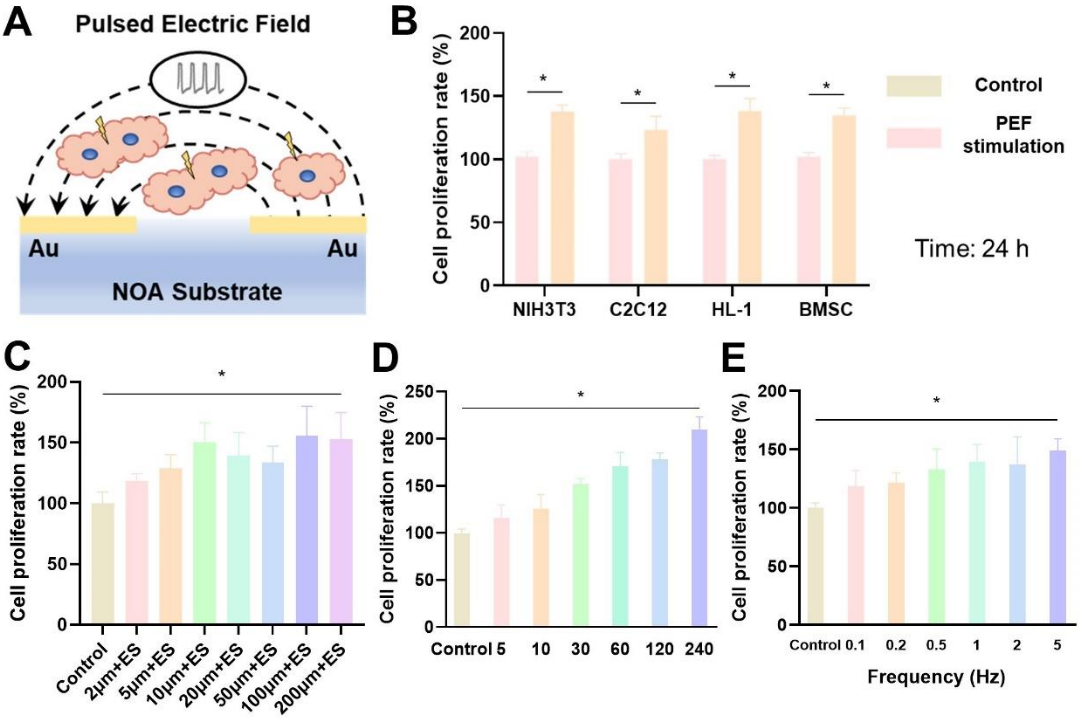

Figure 7.19 In vitro cell tests of the PEF E-bandage. (A) Schematic illustration of the in vitro tests of PEF on cells. (B) Comparison of the cell proliferation rate after 24 hours with/without PEF stimulation of NIH3T3, C2C12, HL-1 and BMSC. (C) Comparison of the cell proliferation rate after 24 hours with different electrode widths. (D) Comparison of the cell proliferation rate after 24 hours with different pulse times. (E) Comparison of the cell proliferation rate after 24 hours with different pulse frequencies.

7.3 Conclusions

This chapter presents the potential application scenarios of ERT in the field of energy and biomedical engineering. First, the combination of ERT with the roll-to-roll fabrication technique was proposed to design a process for fabricating flexible triboelectric electronics. The triboelectric electronic devices fabricated using this process exhibit excellent mechanical and triboelectric properties, in addition to enduring stability. The repeated processing of the same template ensures uniformity and stability in device output. Moreover, the LCA calculation of the entire fabrication process characterizes the production engineering involved in this process as low-carbon and environmentally friendly. Compared with other fabrication methods for TENG-based electronics, ERT shows significant advantages in rapid fabrication, sustainability, low cost, and high resolution. Second, a high-resolution interdigital electrode was fabricated by ERT and served as the key component of a self-powered electronic bandage with a pulsed electric field. The electronic bandage is highly biocompatible and has a great effect on promoting cell growth.

These findings highlight the potential of ERT in enabling the development of sustainable and cost-effective flexible devices for various applications. In this section, we have thoroughly evaluated the potential for large-scale application of ERT in the fields of energy and biomedical engineering. However, we have not delved deeper into the device performance and practical effects in specific application scenarios. In the future, more application scenarios can be explored, and deeper application levels, such as preclinical or clinical trials could be conducted to further validate the biocompatibility and functionality of electrodes fabricated by ERT in real-world applications.

Chapter 8: Conclusions and Outlook

8.1 Conclusions

In this thesis, electrochemical replication and transfer (ERT) was deeply studied and many modifications were conducted to improve the ERT process to expand the capability of ERT in the field of flexible electronics. The modifications mainly focused on the structure of the template used for the electrodeposition process and the binder material used for the transfer process. Through these improvements, the resolution limit of ERT was increased to sub-100 nm. The applicability of ERT was also expanded to stretchable electronic devices and 3D electrode-based electronics. The possibility of constructing an ERT production line was also proposed, and the related energy consumption and economic cost were also evaluated.

In Chapter 4, an additional layer of SiO_2 with 30 nm thickness was added to the original Si substrate. The Au pattern was deposited into the patterned SiO_2 layer fabricated by photolithography and dry etching method with the same thickness of SiO_2. Therefore, the template will form an embedded structure with only the upper surface of the Au pattern exposed to the environment. During the following electroplating process, the target materials will only be deposited on the upper surface of the Au pattern. The contact area between the Au pattern and the target materials is greatly reduced while that between the Au pattern and the substrate is increased. This SiO_2-protecting structure template could greatly increase the durability of the template and increase the resolution limitation of ERT to the nanoscale. Large-area nanoscale grating patterns (1.5 cm × 2 cm) with different materials were successfully fabricated for more than 50 replicas with only one template.

In Chapter 5, the UV-curable binder NOA 63 used in ERT was replaced by a PVA solution. The adhesion force of the PVA binder is also strong enough to peel off different target material patterns including Cu, Au, and Ag from the Au template. The capability of large-area fabrication and high-resolution replication were also retained. The dissolvability of PVA also allows the clean transfer of the replicated pattern to arbitrary substrates including hard surfaces, curved surfaces and stretchable substrates. The application of various stretchable electronics such as stretchable conductors and supercapacitors was demonstrated.

In Chapter 6, a 3D template and used for the electroplating process during ERT. The 3D Si template with a SiO_2-protected surface can be fabricated through a simple photolithography and dry etching process without further Au deposition on the patterned template. The growth of conductive materials is selectively proceeding on the exposed Si surface during the electrodeposition process, which replicates the 3D structures of the template conformally. Since the Si substrate is much harder than the Au pattern deposited on it, the durability of the template in ERT is also increased. The growth of target materials is confined to the 3D grooves area and prevents the changes in resolution caused by isotropic growth of target materials during electrodeposition in the case of a planar template. This 3D template could fabricate both continuous and isolated patterns with different conductive materials with various aspect ratios reaching 1:4. The 3D-ERT method has the advantage of fabricating flexible transparent electrodes which could achieve a great balance between R_s and T. The highest FoM value could reach more than 30000. Additionally, 3D-ERT is also suitable for the fabrication of complex 3D structure electrodes for pressure sensors with high sensitivity. In chapter 7, taking the fabrication of triboelectric nanogenerator (TENG) electrodes by ERT as an example, we conceived the idea of setting up the production line of ERT and characterization of the fabricated devices in terms of the electrochemical performance, flexibility, long-term stability and manufacturing stability. We also evaluated the potential consumption of energy and money in the aspect of sustainable fabrication using LCA. The application prospect in the field of biomedical engineering of ERT has also been proved through the fabrication of an electrical stimulation device in the aspect of biocompatibility and cell growth stimulation.

In summary, we conducted various modifications to the ERT method in the aspect of template design and binder choice. These improvements make ERT more applicable for the area of flexible electronics in the view of material choice, substrate choice, structure choice and resolution range. The concept of developing ERT into an actual production line was also presented. Additionally, energy and money consumption generated in the actual production and the impact on the green environment were evaluated. Finally, we proved that ERT could serve as a powerful tool in the biomedical engineering area through the fabrication of a biocompatible electrode in bioelectronic devices.

8.2 Suggestions for Future Research

After many efforts to improve the ERT, it has evolved into a potent instrument to produce diverse flexible electronics. It has great potential in the future and deserves to be explored.

First, the application of nanoscale patterns fabricated by ERT is still unexplored. Due to the limitation of lab equipment, the resolution limitation also has room for improvement.

Second, the performance of the stretchable devices (stretchable conductors and stretchable micro-supercapacitors) and the 3D electrodes (flexible transparent electrodes and pressure sensors) was still not excellent. Further optimization should be conducted to improve the performance.

Third, more application scenarios using ERT should be explored. In this thesis, we have already illustrated the potential of ERT in the fabrication of electrodes for TENG. It has a superior performance to other existing fabrication techniques including the aspect of resolution, throughput and cost. Other applications should also be conducted to evaluate the value of ERT in the field of flexible electronics. Moreover, in this study, we only test the biocompatibility of the electrodes fabricated by ERT and the basic in vitro functionality of promoting cell growth. Its functionality on biological tissue as well as various diseases needs to be further studied. In conclusion, ERT has great potential in the application of biomedical and biomaterials area, which deserves great attention in the future.

Last, the key technique of ERT is the modification of the original template to realize the reusability of the template and quick replication of the pattern. Inspired by this, other efficient patterning techniques could be modified or proposed based on this mechanism such as the modifications in transfer printing.

References

[1] M. Stoppa and A. Chiolerio. Wearable Electronics and Smart Textiles: A Critical Review. (2014) *Sensors* **14** 11957-11992.

[2] Z. J. Ma, Q. Y. Huang, Q. Xu, Q. N. Zhuang, X. Zhao, Y. H. Yang, H. Qiu, Z. L. Yang, C. Wang, Y. Chai and Z. J. Zheng. Permeable superelastic liquid-metal fibre mat enables biocompatible and monolithic stretchable electronics. (2021) *Nature Materials* **20** 859-868.

[3] W. Zeng, L. Shu, Q. Li, S. Chen, F. Wang and X. M. Tao. Fiber-Based Wearable Electronics: A Review of Materials, Fabrication, Devices, and Applications. (2014) *Advanced Materials* **26** 5310-5336.

[4] R. K. Mishra, L. J. Hubble, A. Martin, R. Kumar, A. Barfidokht, J. Y. Kim, M. M. Musameh, I. L. Kyratzis and J. Wang. Wearable Flexible and Stretchable Glove Biosensor for On-Site Detection of Organophosphorus Chemical Threats. (2017) *ACS Sensors* **2** 553-561.

[5] A. N. Yang, Y. Z. Li, C. X. Yang, Y. Fu, N. X. Wang, L. Li and F. Yan. Fabric Organic Electrochemical Transistors for Biosensors. (2018) *Advanced Materials* **30** 1800051.

[6] H. Lee, M. Kim, I. Kim and H. Lee. Flexible and Stretchable Optoelectronic Devices using Silver Nanowires and Graphene. (2016) *Advanced Materials* **28** 4541-4548.

[7] S. Choi, H. Lee, R. Ghaffari, T. Hyeon and D. H. Kim. Recent Advances in Flexible

and Stretchable Bio-Electronic Devices Integrated with Nanomaterials. (2016) *Advanced Materials* **28** 4203-4218.

[8] M. D. Levenson, N. S. Viswanathan and R. A. Simpson. Improving Resolution in Photolithography with a Phase-Shifting Mask. (1982) *IEEE Transactions on Electron Devices* **29** 1828-1836.

[9] C. Vieu, F. Carcenac, A. Pépin, Y. Chen, M. Mejias, A. Lebib, L. Manin-Ferlazzo, L. Couraud and H. Launois. Electron beam lithography:: resolution limits and applications. (2000) *Applied Surface Science* **164** 111-117.

[10] L. J. Guo. Nanoimprint lithography: Methods and material requirements. (2007) *Advanced Materials* **19** 495-513.

[11] H. Xu, V. Kosma, K. Sakai, E. P. Giannelis and C. K. Ober. EUV photolithography: resist progress in metal-organic complex photoresists. (2019) *Journal of Micro-Nanolithography Mems and Moems* **18** 011007-011007.

[12] P. van Assenbergh, E. Meinders, J. Geraedts and D. Dodou. Nanostructure and Microstructure Fabrication: From Desired Properties to Suitable Processes. (2018) *Small* **14** 1703401.

[13] S. Khan, L. Lorenzelli and R. S. Dahiya. Technologies for Printing Sensors and Electronics Over Large Flexible Substrates: A Review. (2015) *IEEE Sensors Journal* **15** 3164-3185.

[14] M. A. Meitl, Z. T. Zhu, V. Kumar, K. J. Lee, X. Feng, Y. Y. Huang, I. Adesida, R. G. Nuzzo and J. A. Rogers. Transfer printing by kinetic control of adhesion to an

elastomeric stamp. (2006) *Nature Materials* **5** 33-38.

[15]K. Sim, S. Chen, Z. W. Li, Z. Y. Rao, J. S. Liu, Y. T. Lu, S. Jang, F. Ershad, J. Chen, J. L. Xiao and C. J. Yu. Three-dimensional curvy electronics created using conformal additive stamp printing. (2019) *Nature Electronics* **2** 471-479.

[16]X. Y. Chen, W. Jian, Z. J. Wang, J. Ai, Y. Kang, P. C. Sun, Z. H. Wang, Y. J. Ma, H. L. Wang, Y. Chen and X. Feng. Wrap-like transfer printing for three-dimensional curvy electronics. (2023) *Science Advances* **9** eadi0357.

[17]Q. N. Zhuang, K. M. Yao, M. G. Wu, Z. G. Lei, F. Chen, J. Y. Li, Q. J. Mei, Y. Y. Zhou, Q. Y. Huang, X. Zhao, Y. Li, X. E. Yu and Z. J. Zheng. Wafer-patterned, permeable, and stretchable liquid metal microelectrodes for implantable bioelectronics with chronic biocompatibility. (2023) *Science Advances* **9** eadg8602.

[18]D. Lohse. Fundamental Fluid Dynamics Challenges in Inkjet Printing. (2022) *Annual Review of Fluid Mechanics* **54** 349-382.

[19]S. C. Wang, Y. Gao, Q. Y. Huang, X. Y. Guo, A. N. Yang, Y. K. Zhang, Q. N. Zhuang, D. D. Chen, L. N. Chen, X. Ju, H. Hu, S. D. Zhang, Y. Zhu, F. Yan and Z. J. Zheng. Inkjet-Printed Xerogel Scaffolds Enabled Room-Temperature Fabrication of High-Quality Metal Electrodes for Flexible Electronics. (2022) *Advanced Functional Materials* **32** 2203730.

[20]A. A. K. Farizhandi, S. Z. Khalajabadi, V. Krishnadoss and I. Noshadi. Synthesized biocompatible and conductive ink for 3D printing of flexible electronics. (2020) *Journal of the Mechanical Behavior of Biomedical Materials* **110** 103960.

[21] R. X. Yang, X. Y. Chen, Y. Zheng, K. Q. Chen, W. S. Zeng and X. Wu. Recent advances in the 3D printing of electrically conductive hydrogels for flexible electronics. (2022) *Journal of Materials Chemistry C* **10** 5380-5399.

[22] S. A. Ruiz and C. S. Chen. Microcontact printing: A tool to pattern. (2007) *Soft Matter* **3** 168-177.

[23] G. Q. Liu, M. M. Rong, H. Hu, L. A. Chen, Z. Xie and Z. J. Zheng. 3D Dip-Pen Nanolithography. (2022) *Advanced Materials Technologies* **7** 2101493.

[24] D. H. Kim, N. S. Lu, R. Ma, Y. S. Kim, R. H. Kim, S. D. Wang, J. Wu, S. M. Won, H. Tao, A. Islam, K. J. Yu, T. I. Kim, R. Chowdhury, M. Ying, L. Z. Xu, M. Li, H. J. Chung, H. Keum, M. McCormick, P. Liu, Y. W. Zhang, F. G. Omenetto, Y. G. Huang, T. Coleman and J. A. Rogers. Epidermal Electronics. (2011) *Science* **333** 838-843.

[25] N. L. Rosi and C. A. Mirkin. Nanostructures in biodiagnostics. (2005) *Chemical Reviews* **105** 1547-1562.

[26] Z. J. Chen, X. Lu, H. X. Wang, J. Chang, D. R. Wang, W. S. Wang, S. W. Ng, M. M. Rong, P. Li, Q. Y. Huang, Z. F. Gan, J. W. Zhong, W. D. Li and Z. J. Zheng. Electrochemical Replication and Transfer for Low-Cost, Sub-100 nm Patterning of Materials on Flexible Substrates. (2023) *Advanced Materials* **35** 2210778.

[27] H. H. Hsiao, C. H. Chu and D. P. Tsai. Fundamentals and Applications of Metasurfaces. (2017) *Small Methods* **1** 1600064.

[28] S. Kasani, K. Curtin and N. Q. Wu. A review of 2D and 3D plasmonic nanostructure array patterns: fabrication, light management and sensing applications. (2019)

Nanophotonics **8** 2065-2089.

[29] W. Zhu, X. Y. Ma, M. L. Gou, D. Q. Mei, K. Zhang and S. C. Chen. 3D printing of functional biomaterials for tissue engineering. (2016) *Current Opinion in Biotechnology* **40** 103-112.

[30] M. Muthu, R. Pandey, X. Z. Wang, A. Chandrasekhar, I. A. Palani and V. Singh. Enhancement of triboelectric nanogenerator output performance by laser 3D-Surface pattern method for energy harvesting application. (2020) *Nano Energy* **78** 105205.

[31] A. Alkhateeb, C. Catal, G. Kar and A. Mishra. Hybrid Blockchain Platforms for the Internet of Things (IoT): A Systematic Literature Review. (2022) *Sensors* **22** 1304.

[32] M. J. Cima. Next-generation wearable electronics. (2014) *Nature Biotechnology* **32** 642-643.

[33] A. S. Farooq and P. Zhang. A comprehensive review on the prospects of next-generation wearable electronics for individualized health monitoring, assistive robotics, and communication. (2022) *Sensors and Actuators a-Physical* **344** 113715.

[34] H. Zarrin, S. Sy, J. Fu, G. P. Jiang, K. Kang, Y. S. Jun, A. P. Yu, M. Fowler and Z. W. Chen. Molecular Functionalization of Graphene Oxide for Next-Generation Wearable Electronics. (2016) *ACS Applied Materials & Interfaces* **8** 25428-25437.

[35] S. Diridollou, F. Patat, F. Gens, L. Vaillant, D. Black, J. M. Lagarde, Y. Gall and M. Berson. In vivo model of the mechanical properties of the human skin under suction. (2000) *Skin Research and Technology* **6** 214-221.

[36] G. Park, H. J. Chung, K. Kim, S. A. Lim, J. Kim, Y. S. Kim, Y. Liu, W. H. Yeo, R.

H. Kim, S. S. Kim, J. S. Kim, Y. H. Jung, T. I. Kim, C. Yee, J. A. Rogers and K. M. Lee. Immunologic and Tissue Biocompatibility of Flexible/Stretchable Electronics and Optoelectronics. (2014) *Advanced Healthcare Materials* **3** 515-525.

[37] J. Vanfleteren, M. Gonzalez, F. Bossuyt, Y. Y. Hsu, T. Vervust, I. De Wolf and M. Jablonski. Printed circuit board technology inspired stretchable circuits. (2012) *MRS Bulletin* **37** 254-260.

[38] C. F. Murphy, G. A. Kenig, D. T. Allen, J. P. Laurent and D. E. Dyer. Development of parametric material, energy, and emission inventories for wafer fabrication in the semiconductor industry. (2003) *Environmental Science & Technology* **37** 5373-5382.

[39] J. R. Chen. Characteristics of fire and explosion in semiconductor fabrication processes. (2002) *Process Safety Progress* **21** 19-25.

[40] P. F. Moonen, I. Yakimets and J. Huskens. Fabrication of Transistors on Flexible Substrates: from Mass-Printing to High-Resolution Alternative Lithography Strategies. (2012) *Advanced Materials* **24** 5526-5541.

[41] K. Jain, M. Klosner, M. Zemel and S. Raghunandan. Flexible electronics and displays: High-resolution, roll-to-roll, projection lithography and photoablation processing technologies for high-throughput production. (2005) *Proceedings of the IEEE* **93** 1500-1510.

[42] M. Golio. Fifty Years of Moore's Law. (2015) *Proceedings of the IEEE* **103** 1932-1937.

[43] R. R. Schaller. Moore's Law: Past, present, and future. (1997) *IEEE Spectrum* **34**

52-59.

[44] G. E. Moore. Cramming more components onto integrated circuits (Reprinted from Electronics, pg 114-117, April 19, 1965). (1998) *Proceedings of the IEEE* **86** 82-85.

[45] J. T. M. Stevenson and A. M. Gundlach. The Application of Photolithography to the Fabrication of Microcircuits. (1986) *Journal of Physics E-Scientific Instruments* **19** 654-667.

[46] R. Walczak, P. Sniadek and J. A. Dziuban. SU-8 photoresist as material of optical passive components integrated with analytical microsystems for real-time polymerase chain reaction. (2011) *Optica Applicata* **41** 873-884.

[47] S. J. Fonash. An Overview of Dry Etching Damage and Contamination Effects. (1990) *Journal of the Electrochemical Society* **137** 3885-3892.

[48] G. S. Oehrlein. Dry Etching Damage of Silicon - a Review. (1989) *Materials Science and Engineering B-Solid State Materials for Advanced Technology* **4** 441-450.

[49] L. F. Thompson. An Introduction to Lithography. (1983) *ACS Symposium Series* **219** 1-13.

[50] Y. T. Xie, S. H. Ouyang, D. P. Wang, W. Y. Lee, Z. A. Bao, J. R. Matthews, W. J. Niu, R. A. Bellman, M. Q. He and H. H. Fong. High performance top contact fused thiophene-diketopyrrolopyrrole copolymer transistors using a photolithographic metal lift-off process. (2015) *Organic Electronics* **20** 55-62.

[51] P. Maraghechi, K. Cadien and A. Y. Elezzabi. A Novel Nanofabrication Damascene Lift-Off Technique. (2011) *IEEE Transactions on Nanotechnology* **10** 822-826.

[52] D. Berkoh and S. Kulkarni. Challenges in Lift-Off Process Using CAMP Negative Photoresist in III-V IC Fabrication. (2019) *IEEE Transactions on Semiconductor Manufacturing* **32** 513-517.

[53] L. Rassaei, P. S. Singh and S. G. Lemay. Lithography-Based Nanoelectrochemistry. (2011) *Analytical Chemistry* **83** 3974-3980.

[54] J. C. C. Lo, S. W. R. Lee, J. S. Wu, J. K. Kim and M. M. F. Yuen. Chip-on-chip 3D optical interconnect with passive alignment. (2004) *54th Electronic Components & Technology Conference, Vols 1 and 2, Proceedings* 2015-2019.

[55] Y. Mimura, T. Ohkubo, T. Takeuchi and K. Sekikawa. Deep-Uv Photolithography. (1978) *Japanese Journal of Applied Physics* **17** 541-550.

[56] U. K. Sengupta. Krypton Fluoride Excimer-Laser for Advanced Microlithography. (1993) *Optical Engineering* **32** 2410-2420.

[57] W. de Boeij, G. Dicker, M. de Wit, F. Bornebroek, M. Zellenrath, H. J. Voorma, B. Smeets, R. Toussaint, B. Paarhuis, M. de Jong, D. Hellweg and K. Kornitzer. Extending KrF lithography beyond 80nm with the TWINSCAN XT:1000H 0.93NA scanner. (2008) *Lithography Asia 2008* **7140** 324-334.

[58] R. Sandstrom. Argon Fluoride Excimer Laser Source for Sub-0.25 Mm Optical Lithography. (1991) *Optical/Laser Microlithography IV* **1463** 610-616.

[59] S. Owa and H. Nagasaka. Immersion lithography; its potential performance and issues. (2003) *Optical Microlithography XVI, Pts 1-3* **5040** 724-733.

[60] D. O. S. Melville, A. E. Rosenbluth, A. Waechter, M. Millstone, J. Tirapu-Azpiroz,

K. Tian, K. Lai, T. Inoue, M. Sakamoto, K. Adam and A. Tritchkov. Computational lithography: Exhausting the resolution limits of 193-nm projection lithography systems. (2011) *Journal of Vacuum Science & Technology B* **29**

[61]K. J. Dong, H. Yang, X. Y. Zhang, X. J. Zhang, Y. J. Wang and D. G. Xu. Optimization Design of High-Frequency Electronic Ballast for UV-Lamps Applied in Sewage Treatment. (2017) *Iecon 2017 - 43rd Annual Conference of the IEEE Industrial Electronics Society* 1369-1374.

[62]C. Q. Wang, G. E. Stein, A. W. Bosse and W. L. Wu. Line Edge Roughness of Directed Self-Assembly PS-PMMA Block Copolymers - A Candidate for Future Lithography. (2011) *Frontiers of Characterization and Metrology for Nanoelectronics: 2011* **1395** 305-308.

[63]T. M. Bloomstein, V. Liberman, M. Rothschild, D. E. Hardy and R. B. Goodman. Optical materials and coatings at 157 nm. (1999) *Emerging Lithographic Technologies III, Pts 1 and 2* **3676** 342-349.

[64]T. Sasaki, Y. Mori, M. Yoshimura, Y. K. Yap and T. Kamimura. Recent development of nonlinear optical borate crystals: key materials for generation of visible and UV light. (2000) *Materials Science & Engineering R-Reports* **30** 1-54.

[65]X. Fu, Y. Huang, L. Hu, H. B. Xie and W. Y. Chen. Flow behavior control in immersion lithography. (2017) *Flow Measurement and Instrumentation* **53** 190-203.

[66]B. W. Smith, A. Bourov, Y. F. Fan, L. Zavyalova, N. Lafferty and F. Cropanese. Approaching the numerical aperture of water - Immersion lithography at 193nm. (2004)

Optical Microlithography XVII, Pts 1-3 **5377** 273-284.

[67] S. Owa and H. Nagasaka. Immersion lithography: its history, current status, and future prospects. (2008) *Lithography Asia 2008* **7140** 265-276.

[68] J. Mulkens, D. Flagello, B. Streefkerk and P. Graeupner. Benefits and limitations of immersion lithography. (2004) *Journal of Microlithography Microfabrication and Microsystems* **3** 104-114.

[69] G. J. Rademaker, A. Le Pennec, T. J. Giammaria, K. Benotmane, H. Pham, C. Bouet, M. G. G. Cacho, M. Argoud, M. L. Pourteau, A. Paquet, A. Gharbi, C. Navarro, C. Nicolet, X. Chevalier, K. Sakavuyi, P. Nealey and R. Tiron. Establishing a sidewall image transfer chemo-epitaxial DSA process using 193 nm immersion lithography. (2020) *Advances in Patterning Materials and Processes XXXVII* **11326** 163-174.

[70] C. Sanchez, G. Cristóbal, G. Bueno, S. Blanco, M. Borrego-Ramos, A. Olenici, A. Pedraza and J. Ruiz-Santaquiteria. Oblique illumination in microscopy: A quantitative evaluation. (2018) *Micron* **105** 47-54.

[71] O. W. Otto, J. G. Garofalo, K. K. Low, C. M. Yuan, R. C. Henderson, C. Pierrat, R. L. Kostelak, S. Vaidya and P. K. Vasudev. Automated Optical Proximity Correction - a Rules-Based Approach. (1994) *Optical/Laser Microlithography VII* **2197** 278-293.

[72] A. Gu and A. Zakhor. Optical proximity correction with linear regression. (2008) *IEEE Transactions on Semiconductor Manufacturing* **21** 263-271.

[73] G. D. Chen, S. K. Li and X. Z. Wang. Efficient optical proximity correction based on virtual edge and mask pixelation with two-phase sampling. (2021) *Optics Express*

29 17440-17463.

[74] J. F. Chen, H. Y. Liu, T. Laidig, C. Zuniga, Y. Cao and R. Socha. Development of a computational lithography roadmap. (2008) *Optical Microlithography XXI, Pts 1-3* **6924** 473-484.

[75] T. Takigawa, K. Gronlund and J. Wiley. Extension of Optical Lithography by Mask-Litho Integration with Computational Lithography. (2010) *Photomask and Next-Generation Lithography Mask Technology XVII* **7748** 240-250.

[76] C. F. Yu, M. C. Lin, M. T. Lai, L. T. H. Hsu, A. G. Chin, S. C. Lee, A. Yen, J. Wang, E. S. Chen, D. Wu, W. H. Broadbent, W. Huang and Z. G. Zhu. Inspection of advanced computational lithography logic reticles using a 193-nm inspection system. (2010) *Photomask Technology 2010* **7823** 655-661.

[77] J. M. Zhou, Y. P. Zhang, P. Engblom, M. Hyatt, E. Wu, M. Snajdr, A. Devilliers, Y. A. He, C. Hickman, P. Liu, D. de Lang, B. Geh, E. Byers and S. Light. Improving Aberration Control with Application Specific Optimization Using Computational Lithography. (2010) *Optical Microlithography XXIII* **7640** 208-219.

[78] V. V. Ivin, K. D. Lucas, T. M. Makhviladze, V. V. Manuilov and M. G. Medvedeva. Extension of the traditional optical model for investigation into the EUV projection lithography capabilities. (1998) *Emerging Lithographic Technologies II* **3331** 646-654.

[79] J. M. Sasian. New developments in the design of ring-field projection cameras for EUV lithography: passive pupil correction. (1998) *International Optical Design Conference 1998* **3482** 658-663.

[80] P. J. Silverman. Extreme ultraviolet lithography: overview and development status. (2005) *Journal of Microlithography Microfabrication and Microsystems* **4** 011006-011006.

[81] K. H. Ko, G. J. Kim, M. Yeung, E. Barouch, M. J. Kim, S. S. Kim and H. K. Oh. Aerial Image of Mesh Supported Extreme Ultra-Violet Pellicle. (2014) *Extreme Ultraviolet (Euv) Lithography V* **9048** 601-608.

[82] A. Mallik, W. Vansumere, J. Ryckaert, A. Mercha, N. Horiguchi, S. Demuynck, J. Bömmels, T. Zsolt, G. Vandenberghe, K. Ronse, A. Thean, D. Verkest, H. Lebon and A. Steegen. The need for EUV lithography at advanced technology for sustainable wafer cost. (2013) *Extreme Ultraviolet (Euv) Lithography IV* **8679** 803-812.

[83] B. Q. Wua and A. Kumar. Extreme ultraviolet lithography: A review. (2007) *Journal of Vacuum Science & Technology B* **25** 1743-1761.

[84] V. Banine and J. Benschop. EUV lithography: Main challenges. (2004) *Micro- and Nanoelectronics 2003* **5401** 1-7.

[85] H. J. Levinson and T. A. Brunner. Current Challenges and Opportunities for EUV Lithography. (2018) *International Conference on Extreme Ultraviolet Lithography 2018* **10809** 5-11.

[86] K. Ronse. Assessing the challenges of EUV lithography. (2007) *Solid State Technology* **50** 64-64.

[87] L. Neim, B. W. Smith and G. Fenger. EUV Mask Polarization Effects on Sub-7nm Node Imaging. (2020) *Extreme Ultraviolet (Euv) Lithography XI* **11323** 264-280.

[88] Z. Belete, E. Baer and A. Erdmann. Modeling of block copolymer dry etching for directed self-assembly lithography. (2018) *Advanced Etch Technology for Nanopatterning VII* **10589** 177-188.

[89] M. Fernández-Regúlez, L. Evangelio, M. Lorenzoni, J. Fraxedas and F. Pérez-Murano. Sub-10 nm Resistless Nano lithography for Directed Self-Assembly of Block Copolymers. (2014) *ACS Applied Materials & Interfaces* **6** 21596-21602.

[90] S. Gottlieb, M. Lorenzoni, L. Evangelio, M. Fernández-Regúlez, Y. K. Ryu, C. Rawlings, M. Spieser, A. W. Knoll and F. Perez-Murano. Thermal scanning probe lithography for the directed self-assembly of block copolymers. (2017) *Nanotechnology* **28** 175301.

[91] M. J. Maher, C. T. Rettner, C. M. Bates, G. Blachut, M. C. Carlson, W. J. Durand, C. J. Ellison, D. P. Sanders, J. Y. Cheng and C. G. Willson. Directed Self-Assembly of Silicon-Containing Block Copolymer Thin Films. (2015) *ACS Applied Materials & Interfaces* **7** 3323-3328.

[92] Z. Y. Deng and S. Y. Liu. Emerging trends in solution self-assembly of block copolymers. (2020) *Polymer* **207** 122914.

[93] S. N. Das. Debroglie Wave Theory and the 2-Wave Description of Matter. (1992) *Nuovo Cimento Della Societa Italiana Di Fisica B-General Physics Relativity Astronomy and Mathematical Physics and Methods* **107** 1185-1192.

[94] W. Chen and H. Ahmed. Fabrication of 5-7 Nm Wide Etched Lines in Silicon Using 100 Kev Electron-Beam Lithography and Polymethylmethacrylate Resist. (1993)

Applied Physics Letters **62** 1499-1501.

[95] A. A. Tseng, K. Chen, C. D. Chen and K. J. Ma. Electron beam lithography in nanoscale fabrication: recent development. (2003) *IEEE Transactions on Electronics Packaging Manufacturing* **26** 141-149.

[96] R. F. Pease and S. Y. Chou. Lithography and other patterning techniques for future electronics. (2008) *Proceedings of the IEEE* **96** 248-270.

[97] Y. F. Chen. Nanofabrication by electron beam lithography and its applications: A review. (2015) *Microelectronic Engineering* **135** 57-72.

[98] A. E. Grigorescu and C. W. Hagen. Resists for sub-20-nm electron beam lithography with a focus on HSQ: state of the art. (2009) *Nanotechnology* **20** 292001.

[99] H. Namatsu, Y. Takahashi, K. Yamazaki, T. Yamaguchi, M. Nagase and K. Kurihara. Three-dimensional siloxane resist for the formation of nanopatterns with minimum linewidth fluctuations. (1998) *Journal of Vacuum Science & Technology B* **16** 69-76.

[100] M. M. Ahmed and H. Ahmed. Novel electron beam lithography technique for submicron T-gate fabrication. (1997) *Journal of Vacuum Science & Technology B* **15** 306-310.

[101] Y. Chen, D. Macintyre and S. Thoms. Electron beam lithography process for T- and Γ-shaped gate fabrication using chemically amplified DUV resists and PMMA. (1999) *Journal of Vacuum Science & Technology B* **17** 2507-2511.

[102] E. A. Dobisz and C. R. K. Marrian. Control in sub-100 nm lithography in SAL-601. (1997) *Journal of Vacuum Science & Technology B* **15** 2327-2331.

[103] L. E. Ocola, C. J. Biddick, D. M. Tennant, W. K. Waskiewicz and A. E. Novembre. Negative chemically amplified resist characterization for direct write and SCALPEL nanolithography. (1998) *Journal of Vacuum Science & Technology B* **16** 3705-3708.

[104] S. Manako, Y. Ochiai, H. Yamamoto, T. Teshima, J. Fujita and E. Nomura. High-purity, ultrahigh-resolution calixarene electron-beam negative resist. (2000) *Journal of Vacuum Science & Technology B* **18** 3424-3427.

[105] H. Sailer, A. Ruderisch, W. Henschel, V. Schurig and D. P. Kern. High resolution electron beam lithography using a chemically amplified calix[4]arene based resist. (2004) *Journal of Vacuum Science & Technology B* **22** 3485-3488.

[106] B. Q. Sun, P. Zhang, T. Zhang, S. F. Shangguan, S. Wu and X. H. Ma. Single step electron-beam lithography archiving lift-off for T-gate in high electron mobility transistor fabrication. (2020) *Microelectronic Engineering* **229** 111337.

[107] Z. M. Jing, Q. Li, Y. Bai, Y. Li and Z. Y. Zhang. Circular dichroism of spatially complementary chiral nanostructures. (2020) *Nanotechnology* **31** 445302.

[108] S. Y. Chou, P. R. Krauss and P. J. Renstrom. Imprint of Sub-25 Nm Vias and Trenches in Polymers. (1995) *Applied Physics Letters* **67** 3114-3116.

[109] S. Y. Chou, P. R. Krauss and P. J. Renstrom. Imprint lithography with 25-nanometer resolution. (1996) *Science* **272** 85-87.

[110] S. Y. Chou, P. R. Krauss and P. J. Renstrom. Nanoimprint lithography. (1996) *Journal of Vacuum Science & Technology B* **14** 4129-4133.

[111] M. C. Traub, W. Longsine and V. N. Truskett. Advances in Nanoimprint Lithography. (2016) *Annual Review of Chemical and Biomolecular Engineering,* **7** 583-604.

[112] Y. Hirai, Y. Kanemaki, K. Murata and Y. Tanaka. Novel mold fabrication for nano-imprint lithography to fabricate single-electron tunneling devices. (1999) *Japanese Journal of Applied Physics Part 1-Regular Papers Short Notes & Review Papers* **38** 7272-7275.

[113] W. M. Zhou, G. Q. Min, J. Zhang, Y. B. Liu, J. H. Wang, Y. P. Zhang and F. Sun. Nanoimprint Lithography: A Processing Technique for Nanofabrication Advancement. (2011) *Nano-Micro Letters* **3** 135-140.

[114] X. Q. Fan, H. H. Zhang, S. Liu, X. F. Hu and K. Jia. NIL - a low-cost and high-throughput MEMS fabrication method compatible with IC manufacturing technology. (2006) *Microelectronics Journal* **37** 121-126.

[115] T. Glinsner, P. Hangweier, H. Luesebrink, P. Dorsey, A. Homola and D. Wachenschwanz. Nanoimprint lithography enables patterned tracks for high-capacity hard disks. (2005) *Solid State Technology* **48** 51-54.

[116] M. Eibelhuber, T. Glinsner, T. Uhrmann and P. Lindner. Nanoimprint Lithography Enables Cost-Effective Photonics Production. (2015) *Photonics Spectra* **49** 34-37.

[117] C. Battaglia, J. Escarré, K. Söderström, L. Erni, L. Ding, G. Bugnon, A. Billet, M. Boccard, L. Barraud, S. De Wolf, F. J. Haug, M. Despeisse and C. Ballif.

Nanoimprint Lithography for High-Efficiency Thin-Film Silicon Solar Cells. (2011) *Nano Letters* **11** 661-665.

[118] G. Barbillon. Plasmonic Nanostructures Prepared by Soft UV Nanoimprint Lithography and Their Application in Biological Sensing. (2012) *Micromachines* **3** 21-27.

[119] J. Qin, L. Ding and L. Wang. In situ UV nano-imprint lithography alignment using high contrast mark. (2015) *Optics Express* **23** 18518-18524.

[120] M. Singh, H. M. Haverinen, P. Dhagat and G. E. Jabbour. Inkjet Printing-Process and Its Applications. (2010) *Advanced Materials* **22** 673-685.

[121] B. Derby. Inkjet Printing of Functional and Structural Materials: Fluid Property Requirements, Feature Stability, and Resolution. (2010) *Annual Review of Materials Research* **40** 395-414.

[122] J. K. Chen and K. D. Wise. A high-resolution silicon monolithic nozzle array for inkjet printing. (1997) *IEEE Transactions on Electron Devices* **44** 1401-1409.

[123] J. U. Park, M. Hardy, S. J. Kang, K. Barton, K. Adair, D. K. Mukhopadhyay, C. Y. Lee, M. S. Strano, A. G. Alleyne, J. G. Georgiadis, P. M. Ferreira and J. A. Rogers. High-resolution electrohydrodynamic jet printing. (2007) *Nature Materials* **6** 782-789.

[124] E. Gusarova, B. Viala, A. Plihon, B. Gusarov, L. Gimeno and O. Cugat. Flexible Screen-Printed Piezoelectric P(Vdf-Trfe) Copolymer Microgenerators for Energy Harvesting. (2015) *2015 Transducers - 2015 18th International Conference on Solid-State Sensors, Actuators and Microsystems (Transducers)* 1901-1904.

[125] D. A. Pardo, G. E. Jabbour and N. Peyghambarian. Application of screen printing in the fabrication of organic light-emitting devices. (2000) *Advanced Materials* **12** 1249-1252.

[126] Y. D. Kim and J. Hone. MATERIALS SCIENCE Screen printing of 2D semiconductors. (2017) *Nature* **544** 167-168.

[127] J. S. Yu, I. Kim, J. S. Kim, J. Jo, T. T. Larsen-Olsen, R. R. Sondergaard, M. Hösel, D. Angmo, M. Jorgensen and F. C. Krebs. Silver front electrode grids for ITO-free all printed polymer solar cells with embedded and raised topographies, prepared by thermal imprint, flexographic and inkjet roll-to-roll processes. (2012) *Nanoscale* **4** 6032-6040.

[128] C. J. Hansen, R. Saksena, D. B. Kolesky, J. J. Vericella, S. J. Kranz, G. P. Muldowney, K. T. Christensen and J. A. Lewis. High-Throughput Printing via Microvascular Multinozzle Arrays. (2013) *Advanced Materials* **25** 96-102.

[129] M. Bariya, Z. Shahpar, H. Park, J. F. Sun, Y. Jung, W. Gao, H. Y. Y. Nyein, T. S. Liaw, L. C. Tai, Q. P. Ngo, M. H. Chao, Y. B. Zhao, M. Hettick, G. Cho and A. Javey. Roll-to-Roll Gravure Printed Electrochemical Sensors for Wearable and Medical Devices. (2018) *ACS Nano* **12** 6978-6987.

[130] A. K. Assaifan. Flexographic Printing Contributions in Transistors Fabrication. (2021) *Advanced Engineering Materials* **23** 2001410.

[131] J. Lee, J. Kim, Y. Noh, H. Jeong and D. Lee. Advanced technique for achieving 10-um-width fine lines in roll-to-roll continuous gravure printing. (2021) *Precision*

Engineering-Journal of the International Societies for Precision Engineering and Nanotechnology **69** 1-7.

[132] R. R. Sondergaard, M. Hösel and F. C. Krebs. Roll-to-Roll fabrication of large area functional organic materials. (2013) *Journal of Polymer Science Part B-Polymer Physics* **51** 16-34.

[133] A. Kumar and G. M. Whitesides. Features of Gold Having Micrometer to Centimeter Dimensions Can Be Formed through a Combination of Stamping with an Elastomeric Stamp and an Alkanethiol Ink Followed by Chemical Etching. (1993) *Applied Physics Letters* **63** 2002-2004.

[134] H. Schmid and B. Michel. Siloxane polymers for high-resolution, high-accuracy soft lithography. (2000) *Macromolecules* **33** 3042-3049.

[135] M. M. Stanton, R. E. Ducker, J. C. MacDonald, C. R. Lambert and W. G. McGimpsey. Super-hydrophobic, highly adhesive, polydimethylsiloxane (PDMS) surfaces. (2012) *Journal of Colloid and Interface Science* **367** 502-508.

[136] A. C. Von Philipsborn, S. Lang, A. Bernard, J. Loeschinger, C. David, D. Lehnert, M. Bastmeyer and F. Bonhoeffer. Microcontact printing of axon guidance molecules for generation of graded patterns. (2006) *Nature Protocols* **1** 1322-1328.

[137] V. Santhanam and R. P. Andres. Microcontact printing of uniform nanoparticle arrays. (2004) *Nano Letters* **4** 41-44.

[138] S. A. Lange, V. Benes, D. P. Kern, J. K. H. Hörber and A. Bernard. Microcontact printing of DNA molecules. (2004) *Analytical Chemistry* **76** 1641-1647.

[139] C. S. Chen, M. Mrksich, S. Huang, G. M. Whitesides and D. E. Ingber. Geometric control of cell life and death. (1997) *Science* **276** 1425-1428.

[140] F. Bessueille, M. Pla-Roca, C. A. Mills, E. Martinez, J. Samitier and A. Errachid. Submerged microcontact printing (SμCP):: An unconventional printing technique of thiols using high aspect ratio, elastomeric stamps. (2005) *Langmuir* **21** 12060-12063.

[141] S. R. Coyer, A. J. García and E. Delamarche. Facile preparation of complex protein architectures with sub-100-nm resolution on surfaces. (2007) *Angewandte Chemie-International Edition* **46** 6837-6840.

[142] H. Lalo, J. C. Cau, C. Thibault, N. Marsaud, C. Severac and C. Vieu. Microscale multiple biomolecules printing in one step using a PDMS macrostamp. (2009) *Microelectronic Engineering* **86** 1428-1430.

[143] H. Y. Li, H. A. Zhang, W. Luo, R. Yuan, Y. Q. Zhao, J. A. Huang and X. Yang. Microcontact printing of gold nanoparticle at three-phase interface as flexible substrate for SERS detection of MicroRNA. (2022) *Analytica Chimica Acta* **1229** 340380.

[144] B. D. Chang, D. Zhao and H. Y. Sun. Plasma-Assisted Microcontact Printing. (2022) *ACS Applied Materials & Interfaces* **14** 23944-23950.

[145] J. Zaumseil, M. A. Meitl, J. W. P. Hsu, B. R. Acharya, K. W. Baldwin, Y. L. Loo and J. A. Rogers. Three-dimensional and multilayer nanostructures formed by nanotransfer printing. (2003) *Nano Letters* **3** 1223-1227.

[146] E. Menard, L. Bilhaut, J. Zaumseil and J. A. Rogers. Improved surface

chemistries, thin film deposition techniques, and stamp designs for nanotransfer printing. (2004) *Langmuir* **20** 6871-6878.

[147] Y. L. Loo, R. L. Willett, K. W. Baldwin and J. A. Rogers. Interfacial chemistries for nanoscale transfer printing. (2002) *Journal of the American Chemical Society* **124** 7654-7655.

[148] T. W. Park, M. Byun, H. Jung, G. R. Lee, J. H. Park, H. I. Jang, J. W. Lee, S. H. Kwon, S. Hong, J. H. Lee, Y. S. Jung, K. H. Kim and W. I. Park. Thermally assisted nanotransfer printing with sub-20-nm resolution and 8-inch wafer scalability. (2020) *Science Advances* **6** eabb6462.

[149] C. H. Lee, D. R. Kim and X. L. Zheng. Fabrication of Nanowire Electronics on Nonconventional Substrates by Water-Assisted Transfer Printing Method. (2011) *Nano Letters* **11** 3435-3439.

[150] S. Kim, J. A. Wu, A. Carlson, S. H. Jin, A. Kovalsky, P. Glass, Z. J. Liu, N. Ahmed, S. L. Elgan, W. Q. Chen, P. M. Ferreira, M. Sitti, Y. G. Huang and J. A. Rogers. Microstructured elastomeric surfaces with reversible adhesion and examples of their use in deterministic assembly by transfer printing. (2010) *Proceedings of the National Academy of Sciences of the United States of America* **107** 17095-17100.

[151] H. Y. Cheng, J. Wu, Q. M. Yu, H. J. Kim-Lee, A. Carlson, K. T. Turner, K. C. Hwang, Y. G. Huang and J. A. Rogers. An analytical model for shear-enhanced adhesiveless transfer printing. (2012) *Mechanics Research Communications* **43** 46-49.

[152] S. Jiang, S. Liu and W. H. Feng. PVA hydrogel properties for biomedical

application. (2011) *Journal of the Mechanical Behavior of Biomedical Materials* **4** 1228-1233.

[153] G. Y. Liu, Z. Tian, Z. Y. Yang, Z. Y. Xue, M. Zhang, X. D. Hu, Y. Wang, Y. K. Yang, P. K. Chu, Y. F. Mei, L. Liao, W. D. Hu and Z. F. Di. Graphene-assisted metal transfer printing for wafer-scale integration of metal electrodes and two-dimensional materials. (2022) *Nature Electronics* **5** 275-280.

[154] Y. Liu, Y. Huang and X. F. Duan. Van der Waals integration before and beyond two-dimensional materials. (2019) *Nature* **567** 323-333.

[155] M. Schleberger and J. Kotakoski. 2D Material Science: Defect Engineering by Particle Irradiation. (2018) *Materials* **11** 1885.

[156] H. J. Liu, Q. H. Thi, P. Man, X. Chen, T. R. Chen, L. W. Wong, S. Jiang, L. L. Huang, T. F. Yang, K. H. Leung, T. T. Leung, S. Gao, H. L. Chen, C. S. Lee, M. Kan, J. Zhao, Q. M. Deng and T. H. Ly. Controlled Adhesion of Ice-Toward Ultraclean 2D Materials. (2023) *Advanced Materials* **35** 2210503.

[157] G. Zabow. Reflow transfer for conformal three-dimensional microprinting. (2022) *Science* **378** 894-898.

[158] R. D. Piner, J. Zhu, F. Xu, S. H. Hong and C. A. Mirkin. "Dip-pen" nanolithography. (1999) *Science* **283** 661-663.

[159] G. Arrabito, S. Reisewitz, L. Dehmelt, P. I. Bastiaens, B. Pignataro, H. Schroeder and C. M. Niemeyer. Biochips for Cell Biology by Combined Dip-Pen Nanolithography and DNA-Directed Protein Immobilization. (2013) *Small* **9** 4243-

4249.

[160] F. S. Ielasi, M. Hirtz, S. Sekula-Neuner, T. Laue, H. Fuchs and R. G. Willaert. Dip-Pen Nanolithography-Assisted Protein Crystallization. (2015) *Journal of the American Chemical Society* **137** 154-157.

[161] Z. Q. Li, P. Guo and Y. G. Zhou. Dip-Pen Nanolithography Enabled Functional Nanomaterials and Their Applications. (2021) *Advanced Materials Technologies* **6** 2000897.

[162] G. Q. Liu, M. Hirtz, H. Fuchs and Z. J. Zheng. Development of Dip-Pen Nanolithography (DPN) and Its Derivatives. (2019) *Small* **15** 1900563.

[163] G. Q. Liu, S. H. Petrosko, Z. J. Zheng and C. A. Mirkin. Evolution of Dip-Pen Nanolithography (DPN): From Molecular Patterning to Materials Discovery. (2020) *Chemical Reviews* **120** 6009-6047.

[164] H. Ma, Z. Jiang, X. J. Xie, L. Huang and W. Huang. Multiplexed Biomolecular Arrays Generated via Parallel Dip-Pen Nanolithography. (2018) *ACS Applied Materials & Interfaces* **10** 25121-25126.

[165] P. Rath, M. Hirtz, G. Lewes-Malandrakis, D. Brink, C. Nebel and W. H. P. Pernice. Diamond Nanophotonic Circuits Functionalized by Dip-pen Nanolithography. (2015) *Advanced Optical Materials* **3** 328-335.

[166] V. Saygin, B. W. Xu, S. B. Andersson and K. A. Brown. Closed-Loop Nanopatterning of Liquids with Dip-Pen Nanolithography. (2021) *ACS Applied Materials & Interfaces* **13** 14723-14730.

[167] P. C. Chen, Y. Liu, J. S. S. Du, B. Meckes, V. P. Dravid and C. A. Mirkin. Chain-End Functionalized Polymers for the Controlled Synthesis of Sub-2 nm Particles. (2020) *Journal of the American Chemical Society* **142** 7350-7355.

[168] K. Salaita, Y. H. Wang, J. Fragala, R. A. Vega, C. Liu and C. A. Mirkin. Massively parallel dip-pen nanolithography with 55000-pen two-dimensional arrays. (2006) *Angewandte Chemie-International Edition* **45** 7220-7223.

[169] J. Z. Y. Tan, M. A. Avila-López, A. Jahanbakhsh, X. S. Lu, J. Bonilla-Cruz, T. E. Lara-Ceniceros, J. M. Andresen and M. M. Maroto-Valer. 3D direct ink printed materials for chemical conversion and environmental remediation applications: a review. (2023) *Journal of Materials Chemistry A* **11** 5408-5426.

[170] A. A. Alsharif, N. S. M. Cucuri, R. B. Mishra and N. El-Atab. 3D Printed Dry Electrodes for Electrophysiological Signal Monitoring: A Review. (2023) *Advanced Materials Technologies* **8** 2201677.

[171] C. Langdon, J. Hinojosa-Bernal, J. Munuera, M. Gomez-Chiari, O. Haag, A. Veneri, A. Valldeperes, A. Valls, N. Adell, V. Santamaria, O. Cruz-Martinez and A. M. L. Madrid. 3D printing as surgical planning and training in pediatric endoscopic skull base surgery-Systematic review and practical example. (2023) *International Journal of Pediatric Otorhinolaryngology* **168** 111543.

[172] F. Zoccali, A. Colizza, F. Cialente, A. Di Stadio, I. La Mantia, C. Hanna, A. Minni, M. Ralli, A. Greco and M. de Vincentiis. 3D Printing in Otolaryngology Surgery: Descriptive Review of Literature to Define the State of the Art. (2023) *Healthcare* **11**

108.

[173] M. P. A. M. Marijnissen and A. van der Zee. Concrete Printing in Architecture. (2017) *Material Studies–Methodologies* **2** 299-308.

[174] M. S. Karkun and S. Dharmalingam. 3D Printing Technology in Aerospace Industry - A Review. (2022) *International Journal of Aviation Aeronautics and Aerospace* **9** 4.

[175] P. Kraemer-Fernandez, S. Spintzyk, E. Wahl, F. Huettig and A. Klink. Implementation of a Full Digital Workflow by 3D Printing Intraoral Splints Used in Dental Education: An Exploratory Observational Study with Respect to Students' Experiences. (2023) *Dentistry Journal* **11** 5.

[176] A. Baigarina, E. Shehab and M. H. Ali. Construction 3D printing: a critical review and future research directions. (2023) *Progress in Additive Manufacturing* 1-29.

[177] C. Y. Liu, N. G. Huang, F. Xu, J. D. Tong, Z. W. Chen, X. C. Gui, Y. L. Fu and C. S. Lao. 3D Printing Technologies for Flexible Tactile Sensors toward Wearable Electronics and Electronic Skin. (2018) *Polymers* **10** 629.

[178] T. R. Christiani, E. Baroncini, J. Stanzione and A. J. Vernengo. evaluation of 3D printed polycaprolactone scaffolds with angle-ply architecture for annulus fibrosus tissue engineering. (2019) *Regenerative Biomaterials* **6** 175-184.

[179] N. H. M. Yusoff, C. H. Chong, Y. K. Wan, K. H. Cheah and V. L. Wong. Optimization strategies and emerging application of functionalized 3D-printed materials in water treatment: A review br. (2023) *Journal of Water Process Engineering*

51 103410.

[180] M. Mirkhalaf, Y. Men, R. Wang, Y. No and H. Zreiqat. Personalized 3D printed bone scaffolds: A review. (2023) *Acta Biomaterialia* **156** 110-124.

[181] D. Muhindo, R. Elkanayati, P. Srinivasan, M. A. Repka and E. A. Ashour. Recent Advances in the Applications of Additive Manufacturing (3D Printing) in Drug Delivery: A Comprehensive Review. (2023) *Aaps Pharmscitech* **24** 57.

[182] G. Bhargava, I. Gouzman, C. M. Chun, T. A. Ramanarayanan and S. L. Bernasek. Characterization of the "native" surface thin film on pure polycrystalline iron: A high resolution XPS and TEM study. (2007) *Applied Surface Science* **253** 4322-4329.

[183] Y. Yourdshahyan, H. K. Zhang and A. M. Rappe. n-alkyl thiol head-group interactions with the Au(111) surface -: art. no. 081405. (2001) *Physical Review B* **63** 081405.

[184] H. Häkkinen. The gold-sulfur interface at the nanoscale. (2012) *Nature Chemistry* **4** 443-455.

[185] H. Notsu, W. Kubo, I. Shitanda and T. Tatsuma. Super-hydrophobic/super-hydrophilic patterning of gold surfaces by photocatalytic lithography. (2005) *Journal of Materials Chemistry* **15** 1523-1527.

[186] C. Nicosia and J. Huskens. Reactive self-assembled monolayers: from surface functionalization to gradient formation. (2014) *Materials Horizons* **1** 32-45.

[187] R. Doering, and Y. Nishi. Handbook of semiconductor manufacturing technology. (2008) CRC Press Taylor & Francis distributor.

[188] J. U. Park, J. H. Lee, U. Paik, Y. Lu and J. A. Rogers. Nanoscale Patterns of Oligonucleotides Formed by Electrohydrodynamic Jet Printing with Applications in Biosensing and Nanomaterials Assembly. (2008) *Nano Letters* **8** 4210-4216.

[189] S. S. Shankar, L. Rizzello, R. Cingolani, R. Rinaldi and P. P. Pompa. Micro/Nanoscale Patterning of Nanostructured Metal Substrates for Plasmonic Applications. (2009) *ACS Nano* **3** 893-900.

[190] B. Z. Tian, X. L. Zheng, T. J. Kempa, Y. Fang, N. F. Yu, G. H. Yu, J. L. Huang and C. M. Lieber. Coaxial silicon nanowires as solar cells and nanoelectronic power sources. (2007) *Nature* **449** 885-889.

[191] A. Corletto and J. G. Shapter. Nanoscale Patterning of Carbon Nanotubes: Techniques, Applications, and Future. (2021) *Advanced Science* **8** 2001778.

[192] J. Y. Kim, H. Kim, B. H. Kim, T. Chang, J. Lim, H. M. Jin, J. H. Mun, Y. J. Choi, K. Chung, J. Shin, S. Fan and S. O. Kim. Highly tunable refractive index visible-light metasurface from block copolymer self-assembly. (2016) *Nature Communications* **7** 12911.

[193] D. H. Kim, N. S. Lu, Y. G. Huang and J. A. Rogers. Materials for stretchable electronics in bioinspired and biointegrated devices. (2012) *Mrs Bulletin* **37** 226-235.

[194] T. Sekitani, Y. Noguchi, K. Hata, T. Fukushima, T. Aida and T. Someya. A rubberlike stretchable active matrix using elastic conductors. (2008) *Science* **321** 1468-1472.

[195] J. S. Leng, X. Lan, Y. J. Liu, S. Y. Du, W. M. Huang, N. Liu, S. J. Phee and Q.

Yuan. Electrical conductivity of thermoresponsive shape-memory polymer with embedded micron sized Ni powder chains. (2008) *Applied Physics Letters* **92** 014104.

[196] S. Yun, X. F. Niu, Z. B. Yu, W. L. Hu, P. Brochu and Q. B. Pei. Compliant Silver Nanowire-Polymer Composite Electrodes for Bistable Large Strain Actuation. (2012) *Advanced Materials* **24** 1321-1327.

[197] S. Zhu, J. H. So, R. Mays, S. Desai, W. R. Barnes, B. Pourdeyhimi and M. D. Dickey. Ultrastretchable Fibers with Metallic Conductivity Using a Liquid Metal Alloy Core. (2013) *Advanced Functional Materials* **23** 2308-2314.

[198] D. H. Kim and J. A. Rogers. Stretchable Electronics: Materials Strategies and Devices. (2008) *Advanced Materials* **20** 4887-4892.

[199] W. M. Choi, J. Z. Song, D. Y. Khang, H. Q. Jiang, Y. Y. Huang and J. A. Rogers. Biaxially stretchable "Wavy" silicon nanomembranes. (2007) *Nano Letters* **7** 1655-1663.

[200] M. J. Schultz, X. Y. Zhang, S. Unarunotai, D. Y. Khang, Q. Cao, C. J. Wang, C. H. Lei, S. MacLaren, J. A. N. T. Soares, I. Petrov, J. S. Moore and J. A. Rogers. Synthesis of linked carbon monolayers: Films, balloons, tubes, and pleated sheets. (2008) *Proceedings of the National Academy of Sciences of the United States of America* **105** 7353-7358.

[201] D. Y. Khang, J. L. Xiao, C. Kocabas, S. MacLaren, T. Banks, H. Q. Jiang, Y. Y. G. Huang and J. A. Rogers. Molecular scale buckling mechanics on individual aligned single-wall carbon nanotubes on elastomeric substrates. (2008) *Nano Letters* **8**

124-130.

[202] Y. G. Sun, W. M. Choi, H. Q. Jiang, Y. G. Y. Huang and J. A. Rogers. Controlled buckling of semiconductor nanoribbons for stretchable electronics. (2006) *Nature Nanotechnology* **1** 201-207.

[203] D. H. Kim, J. Z. Song, W. M. Choi, H. S. Kim, R. H. Kim, Z. J. Liu, Y. Y. Huang, K. C. Hwang, Y. W. Zhang and J. A. Rogers. Materials and noncoplanar mesh designs for integrated circuits with linear elastic responses to extreme mechanical deformations. (2008) *Proceedings of the National Academy of Sciences of the United States of America* **105** 18675-18680.

[204] T. Someya, Y. Kato, T. Sekitani, S. Iba, Y. Noguchi, Y. Murase, H. Kawaguchi and T. Sakurai. Conformable, flexible, large-area networks of pressure and thermal sensors with organic transistor active matrixes. (2005) *Proceedings of the National Academy of Sciences of the United States of America* **102** 12321-12325.

[205] A. Jahanshahi, M. Gonzalez, J. van den Brand, F. Bossuyt, T. Vervust, R. Verplancke, J. Vanfleteren and J. De Baets. Stretchable Circuits with Horseshoe Shaped Conductors Embedded in Elastic Polymers. (2013) *Japanese Journal of Applied Physics* **52** 05DA18.

[206] Y. Zhao, M. Yu, Z. Y. Liu and Z. Yu. Electrical and thermal effects on electromechanical performance of stretchable thin gold films on PDMS substrates for stretchable electronics. (2019) *Journal of Applied Physics* **125** 165305.

[207] Y. Z. Zhang, J. H. Han, L. K. Zhu, M. A. Shannon and J. Yeom. Soft

lithographic printing and transfer of photosensitive polymers: facile fabrication of free-standing structures and patterning fragile and unconventional substrates. (2014) *Journal of Micromechanics and Microengineering* **24** 115019.

[208] J. B. Brzoska, I. Benazouz and F. Rondelez. Silanization of Solid Substrates - a Step toward Reproducibility. (1994) *Langmuir* **10** 4367-4373.

[209] H. Y. Zou, L. T. Guo, H. Xue, Y. Zhang, X. F. Shen, X. T. Liu, P. H. Wang, X. He, G. Z. Dai, P. Jiang, H. W. Zheng, B. B. Zhang, C. Xu and Z. L. Wang. Quantifying and understanding the triboelectric series of inorganic non-metallic materials. (2020) *Nature Communications* **11** 2093.

[210] H. Y. Zou, Y. Zhang, L. T. Guo, P. H. Wang, X. He, G. Z. Dai, H. W. Zheng, C. Y. Chen, A. C. Wang, C. Xu and Z. L. Wang. Quantifying the triboelectric series. (2019) *Nature Communications* **10** 1427.

[211] S. M. Niu, S. H. Wang, L. Lin, Y. Liu, Y. S. Zhou, Y. F. Hu and Z. L. Wang. Theoretical study of contact-mode triboelectric nanogenerators as an effective power source. (2013) *Energy & Environmental Science* **6** 3576-3583.

[212] Y. S. Zhou, Y. Liu, G. Zhu, Z. H. Lin, C. F. Pan, Q. S. Jing and Z. L. Wang. In Situ Quantitative Study of Nanoscale Triboelectrification and Patterning. (2013) *Nano Letters* **13** 2771-2776.

[213] N. Matsuhisa, X. D. Chen, Z. A. Bao and T. Someya. Materials and structural designs of stretchable conductors. (2019) *Chemical Society Reviews* **48** 2946-2966.

[214] M. J. Owen and P. J. Smith. Plasma Treatment of Polydimethylsiloxane. (1994)

Journal of Adhesion Science and Technology **8** 1063-1075.

[215] Q. Xue, J. F. Sun, Y. Huang, M. S. Zhu, Z. X. Pei, H. F. Li, Y. K. Wang, N. Li, H. Y. Zhang and C. Y. Zhi. Recent Progress on Flexible and Wearable Supercapacitors. (2017) *Small* **13** 1701827.

[216] Z. N. Yu, L. Tetard, L. Zhai and J. Thomas. Supercapacitor electrode materials: nanostructures from 0 to 3 dimensions. (2015) *Energy & Environmental Science* **8** 702-730.

[217] R. Igreja and C. J. Dias. Analytical evaluation of the interdigital electrodes capacitance for a multi-layered structure. (2004) *Sensors and Actuators a-Physical* **112** 291-301.

[218] S. Kumar, G. Saeed, L. Zhu, K. N. Hui, N. H. Kim and J. H. Lee. 0D to 3D carbon-based networks combined with pseudocapacitive electrode material for high energy density supercapacitor: A review. (2021) *Chemical Engineering Journal* **403** 126352.

[219] F. Marty, L. Rousseau, B. Saadany, B. Mercier, O. Francais, Y. Mita and T. Bourouina. Advanced etching of silicon based on deep reactive ion etching for silicon high aspect ratio microstructures and three-dimensional micro- and nanostructures. (2005) *Microelectronics Journal* **36** 673-677.

[220] R. Abdolvand and F. Ayazi. An advanced reactive ion etching process for very high aspect-ratio sub-micron wide trenches in silicon. (2008) *Sensors and Actuators a-Physical* **144** 109-116.

[221] J. C. Thompson and O. K. Bedair. Techniques to Minimize the Cost of Shape Optimization of Stress-Concentration Regions. (1991) *Optimization of Structural Systems and Industrial Systems and Industrial Applications* 129-140.

[222] J. Schneider, P. Rohner, D. Thureja, M. Schmid, P. Galliker and D. Poulikakos. Electrohydrodynamic NanoDrip Printing of High Aspect Ratio Metal Grid Transparent Electrodes. (2016) *Advanced Functional Materials* **26** 833-840.

[223] D. S. Leem, A. Edwards, M. Faist, J. Nelson, D. D. C. Bradley and J. C. de Mello. Efficient Organic Solar Cells with Solution-Processed Silver Nanowire Electrodes. (2011) *Advanced Materials* **23** 4371-4375.

[224] H. Z. Geng, K. K. Kim, K. P. So, Y. S. Lee, Y. Chang and Y. H. Lee. Effect of acid treatment on carbon nanotube-based flexible transparent conducting films. (2007) *Journal of the American Chemical Society* **129** 7758-7759.

[225] S. Bae, H. Kim, Y. Lee, X. F. Xu, J. S. Park, Y. Zheng, J. Balakrishnan, T. Lei, H. R. Kim, Y. I. Song, Y. J. Kim, K. S. Kim, B. Özyilmaz, J. H. Ahn, B. H. Hong and S. Iijima. Roll-to-roll production of 30-inch graphene films for transparent electrodes. (2010) *Nature Nanotechnology* **5** 574-578.

[226] S. Lin, X. P. Bai, H. Y. Wang, H. L. Wang, J. N. Song, K. Huang, C. Wang, N. Wang, B. Li, M. Lei and H. Wu. Roll-to-Roll Production of Transparent Silver-Nanofiber-Network Electrodes for Flexible Electrochromic Smart Windows. (2017) *Advanced Materials* **29** 1703238.

[227] A. Khan, S. Lee, T. Jang, Z. Xiong, C. P. Zhang, J. Y. Tang, L. J. Guo and W.

D. Li. High-Performance Flexible Transparent Electrode with an Embedded Metal Mesh Fabricated by Cost-Effective Solution Process. (2016) *Small* **12** 3021-3030.

[228] S. Hong, J. Yeo, G. Kim, D. Kim, H. Lee, J. Kwon, H. Lee, P. Lee and S. H. Ko. Nonvacuum, Maskless Fabrication of a Flexible Metal Grid Transparent Conductor by Low-Temperature Selective Laser Sintering of Nanoparticle Ink. (2013) *ACS Nano* **7** 5024-5031.

[229] H. Wu, D. S. Kong, Z. C. Ruan, P. C. Hsu, S. Wang, Z. F. Yu, T. J. Carney, L. B. Hu, S. H. Fan and Y. Cui. A transparent electrode based on a metal nanotrough network. (2013) *Nature Nanotechnology* **8** 421-425.

[230] B. Han, K. Pei, Y. L. Huang, X. J. Zhang, Q. K. Rong, Q. G. Lin, Y. F. Guo, T. Y. Sun, C. F. Guo, D. Carnahan, M. Giersig, Y. Wang, J. W. Gao, Z. F. Ren and K. Kempa. Uniform Self-Forming Metallic Network as a High-Performance Transparent Conductive Electrode. (2014) *Advanced Materials* **26** 873-877.

[231] H. J. Kim, S. H. Lee, J. Lee, E. S. Lee, J. H. Choi, J. H. Jung, J. Y. Jung and D. G. Choi. High-Durable AgNi Nanomesh Film for a Transparent Conducting Electrode. (2014) *Small* **10** 3767-3774.

[232] S. Kiruthika, R. Gupta, K. D. M. Rao, S. Chakraborty, N. Padmavathy and G. U. Kulkarni. Large area solution processed transparent conducting electrode based on highly interconnected Cu wire network. (2014) *Journal of Materials Chemistry C* **2** 2089-2094.

[233] H. J. Choi, S. Choo, P. H. Jung, J. H. Shin, Y. D. Kim and H. Lee. Uniformly

embedded silver nanomesh as highly bendable transparent conducting electrode. (2015) *Nanotechnology* **26** 055305.

[234] M. M. Zhu, J. C. Zhang, W. X. Xu, R. H. Xiong and C. B. Huang. Cellulose-based fibrous materials for self-powered wearable pressure sensor: a mini review. (2023) *Cellulose* **30** 1981-1998.

[235] J. Y. Wang, N. N. Yang, G. Cheng and J. Y. Ji. A sea urchin-like microstructure flexible pressure sensors for human physiological signals monitoring. (2023) *Journal of Materials Science-Materials in Electronics* **34** 930.

[236] Y. Joo, J. Byun, N. Seong, J. Ha, H. Kim, S. Kim, T. Kim, H. Im, D. Kim and Y. Hong. Silver nanowire-embedded PDMS with a multiscale structure for a highly sensitive and robust flexible pressure sensor. (2015) *Nanoscale* **7** 6208-6215.

[237] Y. L. Zi, H. Y. Guo, Z. Wen, M. H. Yeh, C. G. Hu and Z. L. Wang. Harvesting Low-Frequency (<5 Hz) Irregular Mechanical Energy: A Possible Killer Application of Triboelectric Nanogenerator. (2016) *ACS Nano* **10** 4797-4805.

[238] S. H. Pan and Z. N. Zhang. Fundamental theories and basic principles of triboelectric effect: A review. (2019) *Friction* **7** 2-17.

[239] G. Zhu, B. Peng, J. Chen, Q. S. Jing and Z. L. Wang. Triboelectric nanogenerators as a new energy technology: From fundamentals, devices, to applications. (2015) *Nano Energy* **14** 126-138.

[240] H. Y. Wang, J. Q. Wang, K. M. Yao, J. J. Fu, X. Xia, R. R. Zhang, J. Y. Li, G. Q. Xu, L. Y. Wang, J. C. Yang, J. Lai, Y. Dai, Z. Y. Zhang, A. Y. Li, Y. Y. Zhu, X. G. Yu,

Z. L. Wang and Y. L. Zi. A paradigm shift fully self-powered long-distance wireless sensing solution enabled by discharge-induced displacement current. (2021) *Science Advances* **7** eabi6751.

[241] Y. X. Shi, F. Wang, J. W. Tian, S. Y. Li, E. G. Fu, J. H. Nie, R. Lei, Y. F. Ding, X. Y. Chen and Z. L. Wang. Self-powered electro-tactile system for virtual tactile experiences. (2021) *Science Advances* **7** eabe2943.

[242] W. J. Wang, W. T. Sun, Y. F. Du, W. B. Zhao, L. J. Liu, Y. Sun, D. J. Kong, H. F. Xiang, X. X. Wang, Z. Li and Q. M. Ma. Triboelectric Nanogenerators-Based Therapeutic Electrical Stimulation on Skin: from Fundamentals to Advanced Applications. (2023) *ACS Nano* **17** 9793-9825.

[243] A. Alagumalai, O. Mahian, K. E. K. Vimal, L. Yang, X. Xiao, S. Saeidi, P. Zhang, T. Saboori, S. Wongwises, Z. L. Wang and J. Chen. A contextual framework development toward triboelectric nanogenerator commercialization. (2022) *Nano Energy* **101** 107572.

[244] C. B. Han, C. Zhang, W. Tang, X. H. Li and Z. L. Wang. High power triboelectric nanogenerator based on printed circuit board (PCB) technology. (2015) *Nano Research* **8** 722-730.

[245] D. Kim, S. B. Jeon, J. Y. Kim, M. L. Seol, S. O. Kim and Y. K. Choi. High-performance nanopattern triboelectric generator by block copolymer lithography. (2015) *Nano Energy* **12** 331-338.

[246] M. A. P. Mahmud, A. Zolfagharian, S. Gharaie, A. Kaynak, S. H. Farjana, A.

V. Ellis, J. Chen and A. Z. Kouzani. 3D-Printed Triboelectric Nanogenerators: State of the Art, Applications, and Challenges. (2021) *Advanced Energy and Sustainability Research* **2** 2000045.

[247] S. H. Wang, L. Lin and Z. L. Wang. Nanoscale Triboelectric-Effect-Enabled Energy Conversion for Sustainably Powering Portable Electronics. (2012) *Nano Letters* **12** 6339-6346.

[248] M. Fleischmann, J. M. BloemhofRuwaard, R. Dekker, E. vanderLaan, J. A. E. E. vanNunen and L. N. VanWassenhove. Quantitative models for reverse logistics: A review. (1997) *European Journal of Operational Research* **103** 1-17.

[249] M. A. Ilgin and S. M. Gupta. Environmentally conscious manufacturing and product recovery (ECMPRO): A review of the state of the art. (2010) *Journal of Environmental Management* **91** 563-591.

[250] G. K. Menon and A. M. Kligman. Barrier Functions of Human Skin: A Holistic View. (2009) *Skin Pharmacology and Physiology* **22** 178-189.

[251] N. N. Schommer and R. L. Gallo. Structure and function of the human skin microbiome. (2013) *Trends in Microbiology* **21** 660-668.

[252] S. F. Bernatchez and J. Bichel. The Science of Skin: Measuring Damage and Assessing Risk. (2023) *Advances in Wound Care* **12** 187-204.

[253] H. Sorg, D. J. Tilkorn, S. Hager, J. Hauser and U. Mirastschijski. Skin Wound Healing: An Update on the Current Knowledge and Concepts. (2017) *European Surgical Research* **58** 81-94.

[254] R. F. Pereira and P. J. Bártolo. Traditional Therapies for Skin Wound Healing. (2016) *Advances in Wound Care* **5** 208-229.

[255] E. M. Tottoli, R. Dorati, I. Genta, E. Chiesa, S. Pisani and B. Conti. Skin Wound Healing Process and New Emerging Technologies for Skin Wound Care and Regeneration. (2020) *Pharmaceutics* **12** 735.

[256] R. Z. Luo, J. Y. Dai, J. P. Zhang and Z. Li. Accelerated Skin Wound Healing by Electrical Stimulation. (2021) *Advanced Healthcare Materials* **10** 2100557.

[257] Y. J. Cheah, M. R. Buyong and M. H. M. Yunus. Wound Healing with Electrical Stimulation Technologies: A Review. (2021) *Polymers* **13** 3790.

[258] S. E. Gardner, R. A. Frantz and F. L. Schmidt. Effect of electrical stimulation on chronic wound healing: a meta-analysis. (1999) *Wound Repair and Regeneration* **7** 495-503.

[259] H. Wu, Y. Q. Wang, H. Li, Y. Y. Hu, Y. D. Liu, X. R. Jiang, H. Sun, F. Liu, A. Xiao, T. R. Chang, L. Lin, K. Yang, Z. Y. Wang, Z. Z. Dong, Y. H. Li, S. T. Dong, S. Q. Wang, J. Chen, Y. L. Liu, D. D. Yin, H. D. Zhang, M. Liu, S. S. Kong, Z. Q. Yang, X. E. Yu, Y. Wang, Y. B. Fan, L. Wang, C. J. Yu and L. Q. Chang. Accelerated intestinal wound healing via dual electrostimulation from a soft and biodegradable electronic bandage. (2024) *Nature Electronics* **7** 299-312.

[260] R. Balint, N. J. Cassidy and S. H. Cartmell. Electrical Stimulation: A Novel Tool for Tissue Engineering. (2013) *Tissue Engineering Part B-Reviews* **19** 48-57.

[261] S. Bodhak, S. Bose, W. C. Kinsel and A. Bandyopadhyay. Investigation of

bone cell adhesion and proliferation on Ti using direct current stimulation. (2012) *Materials Science & Engineering C-Materials for Biological Applications* **32** 2163-2168.

[262] T. Radman, R. L. Ramos, J. C. Brumberg and M. Bikson. Role of cortical cell type and morphology in subthreshold and suprathreshold uniform electric field stimulation. (2009) *Brain Stimulation* **2** 215-228.

[263] J. C. Weaver. Electroporation of cells and tissues. (2000) *Ieee Transactions on Plasma Science* **28** 24-33.

[264] K. H. Schoenbach, F. E. Peterkin, R. W. Alden and S. J. Beebe. The effect of pulsed electric fields on biological cells: Experiments and applications. (1997) *Ieee Transactions on Plasma Science* **25** 284-292.

[265] M. S. Wang, L. H. Wang, A. E. A. Bekhit, J. Yang, Z. P. Hou, Y. Z. Wang, Q. Z. Dai and X. A. Zeng. A review of sublethal effects of pulsed electric field on cells in food processing. (2018) *Journal of Food Engineering* **223** 32-41.

[266] E. H. Hall, K. H. Schoenbach and S. J. Beebe. Nanosecond pulsed electric fields (nsPEF) induce direct electric field effects and biological effects on human colon carcinoma cells. (2005) *DNA and Cell Biology* **24** 283-291.

[267] J. C. Weaver. Electroporation - a General Phenomenon for Manipulating Cells and Tissues. (1993) *Journal of Cellular Biochemistry* **51** 426-435.

[268] K. Cinar, S. Comlekci and N. Senol. Effects of a specially pulsed electric field on an animal model of wound healing. (2009) *Lasers in Medical Science* **24** 735-740.

[269] A. R. Ruiz-Fernández, L. Campos, S. E. Gutierrez-Maldonado, G. Núñez, F. Villanelo and T. Perez-Acle. Nanosecond Pulsed Electric Field (nsPEF): Opening the Biotechnological Pandora's Box. (2022) *International Journal of Molecular Sciences* **23** 6158.

[270] D. Parate, A. Franco-Obregón, J. Fröhlich, C. Beyer, A. A. Abbas, T. Kamarul, J. H. P. Hui and Z. Yang. Enhancement of mesenchymal stem cell chondrogenesis with short-term low intensity pulsed electromagnetic fields. (2017) *Scientific Reports* **7**

[271] E. S. Buescher and K. H. Schoenbach. Effects of submicrosecond, high intensity pulsed electric fields on living cells-intracellular electromanipulation. (2003) *Ieee Transactions on Dielectrics and Electrical Insulation* **10** 788-794.

[272] R. Nuccitelli. Application of Pulsed Electric Fields to Cancer Therapy. (2019) *Bioelectricity* **1** 30-+.

[273] S. Q. Guo, D. L. Jackson, N. I. Burcus, Y. J. Chen, S. Xiao and R. Heller. Gene electrotransfer enhanced by nanosecond pulsed electric fields. (2014) *Molecular Therapy-Methods & Clinical Development* **1** 14043.

[274] L. Caramazza, M. Nardoni, A. De Angelis, E. della Valle, A. Denzi, P. Paolicelli, C. Merla, M. Liberti, F. Apollonio and S. Petralito. Feasibility of Drug Delivery Mediated by Ultra-Short and Intense Pulsed Electric Fields. (2019) *2019 41st Annual International Conference of the Ieee Engineering in Medicine and Biology Society (Embc)* 1678-1681.

[275] A. Golberg, G. F. Broelsch, D. Vecchio, S. Khan, M. R. Hamblin, W. G. Austen,

R. L. Sheridan and M. L. Yarmush. Pulsed Electric Fields for Burn Wound Disinfection in a Murine Model. (2015) *Journal of Burn Care & Research* **36** 7-13.